2019

A STRUCTURAL AND BIOCHEMICAL STUDY ON RIC-8A, AN INTRACELLULAR GUANINE NUCLEOTIDE EXCHANGE FACTOR AND FOLDING CHAPERONE FOR THE INHIBITORY G-PROTEIN ALPHA SUBUNIT-1

Baisen Zeng

A STRUCTURAL AND BIOCHEMICAL STUDY ON RIC-8A, AN INTRACELLULAR GUANINE NUCLEOTIDE EXCHANGE FACTOR AND FOLDING CHAPERONE FOR THE INHIBITORY G-PROTEIN ALPHA SUBUNIT-1

By

BAISEN ZENG

B.S. Biochemistry and Molecular Biology, University of California-Davis, Davis, CA, 2010

Dissertation

presented in partial fulfillment of the requirements
for the degree of

Doctor of Philosophy
in Biochemistry and Biophysics

The University of Montana
Missoula, MT

January 2019

Approved by:

Scott Whittenburg, Dean of The Graduate School
Graduate School

Dr. Stephen Sprang, Mentor and Committee Chair
Department of Chemistry and Biochemistry, Division of Biological Science

Dr. Bruce Bowler, Committee Member
Department of Chemistry and Biochemistry

Dr. Klára Briknarová, Committee Member
Department of Chemistry and Biochemistry

Dr. Michael Kavanaugh, Committee Member
Department of Biomedical & Pharmaceutical Sciences

Dr. J. Stephen Lodmell, Committee Member
Department of Chemistry and Biochemistry

Zeng, Baisen, Ph.D., Fall 2018 Biochemistry and Biophysics

A Structural and Biochemical Study on Ric-8A, an Intracellular Guanine Nucleotide Exchange Factor and Folding Chaperone for Gαi1

Chairperson: Stephen Sprang

Heterotrimeric G-proteins (Gαβγ) regulate many cellular processes in the G-protein signaling pathways. The α-subunit (Gα) in the heterotrimer is activated by G-protein-coupled receptor (GPCR) as the guanine-nucleotide exchange factor (GEF), which catalyzes the GDP-release and GTP-binding reactions at Gα nucleotide-binding site, at the cell membrane. Intracellular GEFs for Gα subunits have been identified; among them, the mammalian isoform A of resistance to inhibitors of cholinesterase-8 (Ric-8A) catalyzes nucleotide exchange and functions as a folding chaperone for inhibitory Gα (Gαi1). In a nucleotide-free complex with Gαi1, Ric-8A likely assumes the GEF and chaperone roles by inducing a molten globule-like state. Tall et al. recently discovered that Casein Kinase II phosphorylates Ric-8A at two conserved sites (S435 and T440), which upon phosphorylation, elevate both the GEF and chaperone activities.

To understand the molecular mechanism under which Ric-8A interacts with Gαi1, we conducted hydrogen-deuterium exchange coupled to mass spectrometry (HDX-MS) and identified a putative protein-protein interactive site (residues 454-470) on Ric-8A. Site-directed mutagenesis generated single alanine mutants of Ric-8A along the putative Gαi1-binding sequence and tryptophan fluorescence GEF assays identified five residues (V455, T456, R458, P466, and G469) as binding "hotspot". We also solved a 2.2Å resolution, X-ray crystal structure of a 452-residue long fragment (R452) of the full-length Ric-8A. The crystal structure depicts a phosphorylated Ric-8A 1-452 molecule (pR452). Mapping sequence conservation scores and

HDX protection profile on the pR452 crystal structure provides insights about the Ric-8A, Gαi1 interaction. Low-resolution, solution structures of both R452 and pR452 were also determined using Small Angle X-ray Scattering (SAXS). Phosphorylation of R452 at S435 and T440 likely induces subtle conformational changes on the molecule. Steady-State GTPase assay results indicated that not only does R452 retain measurable GEF activity towards Gαi1, phosphorylation of R452 also elevates the GEF activity at high Ric-8A concentrations.

With information from the biochemical assessments and Ric-8A protein structures, we conclude that **(A)** Gαi1 likely binds to Ric-8A residues 454 to 470 and other under-characterized sites on Ric-8A because **(B)** R452 retains important structural elements for the GEF activity towards Gαi1 and **(C)** phosphorylation of Ric-8A induces elevated Ric-8A GEF activity which is accompanied by conformational changes.

Acknowledgment

About eight years ago, there was a voice in my head, “Hey, you! Put down that video-game and do something useful!” A cascade of events unfolded starting from that point. It has been quite a show and here are the closing credits:

Advisory Committee Members

Dr. Bruce Bowler

Recruited me to the U.M. Biochemistry and Biophysics Program | Department chair | Advisory committee chair | Expert in protein dynamics and folding | Helped me answer tough questions during all of my committee meetings, including the dissertation defense | Teaches with a lot of notes to take | Takes a lot of students | Has office inside his lab

Dr. Klára Briknarová

Taught me the basics of NMR during my recruitment interview | Always happy to see me | Very careful about science | First to tell me seven years is not too long to get a Ph.D. | Helped me make minimal media for growing seleno-methionine derivative of Ric-8A | Ask tough questions

Dr. Michael Kavanaugh

The one to go to for neuroscience-related questions but resourceful in other aspects of biochemistry and molecular biology | Boss of my close friend and student role-model, Weinan Sun | Hard to track down by emails | Good listener during my talks

Dr. J. Stephen Lodmell

Caught me off guard by asking me to draw the structures of nucleobases during a “Nucleic Acid” class pop-quiz. After failing that pop-quiz, I realized I needed to buckle up or I will not survive

graduate school | Hands down the best instructor | Brain-stormed with me for out-of-field proposal ideas | Spoke Chinese to me occasionally | Sees through my soul

Dr. Stephen Sprang

Mentor | The reason I came to Missoula. MT | Leads by actions | Literally always right, therefore, irreplaceable for everyone | Most patient and caring boss one could have | Too smart to not know, but always gives me the benefits of the doubt | Grilled me the hardest during all committee meetings, except the dissertation defense | Occasional awkward encounters in the hallway | Actually cares about science instead of fame | Spent more time editing this dissertation than anyone would | Other awesome traits I cannot elaborate here due to the page limitation

Sprang Lab Members

Dr. Tung-Chung Mou

Expert X-ray crystallographer and protein chemist | A.k.a. TC | Knows how to do and repair everything in the lab | Reliable, therefore irreplaceable in the lab | Work-above-all | I dragged him to New York at the worst time possible | Trained me | 50% responsible for solving Ric-8A crystal structure and 100% responsible for solving every other structure

Dr. Thomas Celestine

Ric-8, G-protein expert | Trained me | The king of laboratory tricks and shortcuts | Work-above-all | Saved my graduate career by switching me to the Ric-8A project

Cindee Yates-Hansen

Lab manager | Highly involved in solving Ric-8A SAXS envelopes | Optimized R452 C329S crystals | 99% responsible for ordering stuffs and lab laughter

Dr. Levi McClelland

Cytochrome *c* expert | The Ric-8, G-protein post-doc after Celestine | Former graduate student from Dr. Bruce Bowler | Optimized R452 C329S crystals | Will soon solve a Ric-8A:G-protein complex crystal structure with help from TC and Cindee | Wrestling champion who will not hurt a fly

Marlene W.

Lab technician | Aged incredibly well | Visual learner

Jake Johnston

A.k.a. Jeff/Josh/Jade | Graduate student and lab "stress monkey" | About to solve a Ric-8A:G-protein cryo-EM structure with help from TC

Other former and current Sprang Lab members

Dr. Labe Black, Dr. Sundaresh Shankar, Dr. Sascha Stump, Michael Gantz PharmD/PhD/MBA, Melissa Roseleip, the many Kevins, etc.

Synchrotron Staff

Dr. Tzanko Doukov

SLAC/SSRL beamline scientist and R&D engineer | Expert in X-ray crystallography | Wears a bandana | 50% responsible for solving Ric-8A crystal structure | First scientist I met outside of academia

Family

Weiping Zeng and Jinfeng Lu

My parents | Masters of Chinese medicine and acupuncture | Servants of God | Know American sign language

Nan Li

My wife and companion | Master of Accountancy with a CPA but refuses to do our taxes | A great cook who refuses to cook | Made chemical reagents for me | Gets bored listening to me babble about my experiments but is surprisingly insightful

Dr. Shaohua Li and Xiuying Wang

My grandmothers | Dr. Li was a Chinese medical doctor specialized in gynecology | Mrs. Wang was a worker and housewife who knew a great deal about medicine | Both passed away during my last few years in graduate school but lived productive and happy lives

Table of Contents

List of Abbreviations

(p)R452	(Phospho-) rat Ric-8A 1-452
(p)R491	(Phospho-) rat Ric-8A 1-491
(p)R530	(Phospho-) rat Ric-8A 1-530
Å	Ångström
AC	Adenylyl cyclase
AGS-3	Activator of G-protein signaling 3
AlF_4^-	Aluminum Fluoride
ARM	Armadillo
ATP	Adenosine triphosphate
cAMP	Cyclic adenosine monophosphate
CD	Circular dichroism
CKII	Casein Kinase-II
cryo-EM	Cryo-electron microscopy
D_2O	Heavy water (deuterium oxide)
DEER	Double electron-electron resonance
DSF	Differential scanning fluorimetry
E10C12	Decaethylene glycol monodecyl ether
FRET	Förster resonance energy transfer
GAP	GTPase activating protein
GDI	Guanine-nucleotide dissociation inhibitors

GDP	Guanosine diphosphate
GEF	Guanine-nucleotide exchange factors
GPCR	G-protein-coupled receptor
GST	Glutathione-S-transferase
GTP	Guanosine triphosphate
GTPγS	Guanosine 5'-O-[gamma-thio]triphosphate
Gα	G-protein alpha subunit
$G\alpha_{13}$	G-protein(13) α-subunit
Gαi1	Inhibitory G-protein α-subunit, isoform 1
Gαi1[]	Nucleotide-free Inhibitory G-protein α-subunit, isoform 1
Gαo	G-protein(o) α-subunit
Gαolf	Olfactory G-protein α-subunit
Gαq	G-protein(q) α-subunit
Gαs	Stimulatory G-protein α-subunit
Gαt	Transducin
Gβ	G-protein beta subunits
Gγ	G-protein gamma subunits
HDX-MS	Hydrogen-deuterium exchange coupled with mass-spectrometry
HEPES	4-(2-hydroxyethyl)-1-piperazineethanesulfonic acid
HSQC	Heteronuclear single quantum coherence
I3C	5-Amino-2,4,6-triiodoisophthalic acid
IMAC	Immobilized Metal Affinity Chromatography
KCl	Potassium Chloride

LC-TOF-MS	Liquid chromatography Time of Flight Mass Spectrometry
MAD	Multi-wavelength anomalous dispersion
MALDI-TOF-MS	Matrix Assisted Laser Desorption/Ionization Time of Flight Mass Spectrometry
MALS	Multi-angle light scattering
MANT	2'/3'-O-(N-Methyl-anthraniloyl)
$MgCl_2$	Magnesium Chloride
mGαi1	Myristoylated inhibitory G-protein α-subunit, isoform 1
NaCl	Sodium Chloride
NMR	Nuclear magnetic resonance
NTA	Nitrilotriacetic acid
NuMA	Nuclear mitotic apparatus protein
PEG	Polyethylene glycol
Pi	Inorganic phosphate
PKA	Protein kinase A
PMSF	Phenylmethane sulfonyl fluoride
R401	Rat Ric-8A 1-401
R425	Rat Ric-8A 1-425
R470	Rat Ric-8A 1-470
RGS-4	Regulator of G-protein signaling 4
Ric-8	Resistance to inhibitors of cholinesterase 8
Ric-8A	Resistance to inhibitors of cholinesterase 8, isoform A
Ric-8B	Resistance to inhibitors of cholinesterase 8, isoform B

SAD	Single-wavelength anomalous dispersion
SAXS	Small-angle X-ray scattering
SDS-PAGE	Sodium dodecyl sulfate–polyacrylamide gel electrophoresis
SEC	Size-exclusion chromatography or gel-filtration
TCEP	Tris(2-carboxyethyl) phosphine
TEV	Tobacco etch virus protease
tmAC	Trans-membrane adenylyl cyclase
β2AR	β2-adrenergic receptor

List of Figures

List of Tables

Chapter I: Introduction

Over forty years ago, heterotrimeric G-protein alpha subunits (Gα) were recognized as regulatory Ras-family GTPases activated by G-protein-coupled receptors (GPCR) such as β2-adrenergic receptors (β2AR) and rhodopsin. At the time, the discovery drastically changed common knowledge about regulation of cellular processes by cyclic adenosine monophosphate (cAMP), which is the secondary messenger in the signaling cascade as discovered by Sutherland et al. (109) β2AR and adenylyl cyclase (AC), however, were thought to be two domains of a large integral membrane protein. **(Figure 1-1)** We now know that Gα fills the gap between activation of β2AR by hormone (adrenaline) and the activation of trans-membrane adenylyl cyclase (tmAC), which produces cAMP from adenosine triphosphate (ATP).

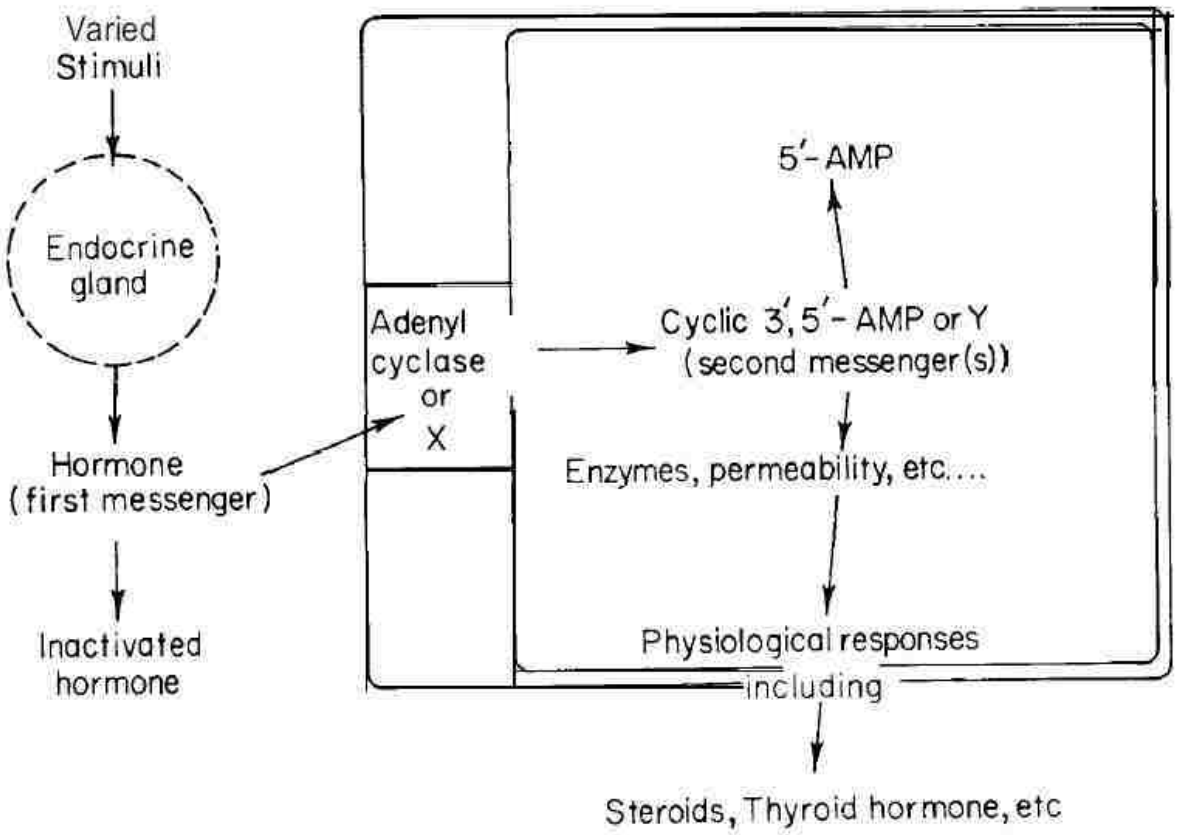

Figure 1-1. Schematic representation of the second messengers concept
(109)

As more information about the Gα family of proteins was unveiled, the scope of research on heterotrimeric G-proteins expanded because cells that express G-proteins respond to extra-cellular stimuli and regulate intra-cellular processes such as metabolism, secretion, protein expression, electrical conductivity, and cellular motility via the important Gα family of signaling protein molecules. The classical GPCR-driven G-protein activation pathway biochemistry as well as the structural changes of molecules involved thus became a more vigorous field of study in biochemical and biomedical research. After the 90's when the first X-ray crystal structures of inhibitory G-protein α-subunit, rat isoform 1 (Gαi1) and transducin (Gαt) bound to guanosine 5'-O-[gamma-thio]triphosphate (GTPγS) were solved(95, 99), even more attention was directed to the field. Alfred G. Gilman and Martin Rodbell won the Nobel Prize in Physiology or Medicine

in 1994 for the discovery and biochemical characterization of G-proteins. The structure of Gαi1, bound to GTPγS **(Figure 1-2, PDB:1GIA)** was solved the same year. (95) The structure and the transducin counterpart (99) demonstrated how the α-helical domain distinguishes Gα from other members of the Ras GTPase family of small GTPases and the molecular mechanism by which Gα binds GTP and forms an active complex. (88) Although the involvement of GTP in the G-protein signaling cascade was already discovered prior to the discovery of G-proteins (108, 110), the structural information of a nucleotide-bound Gα was novel and intriguing.

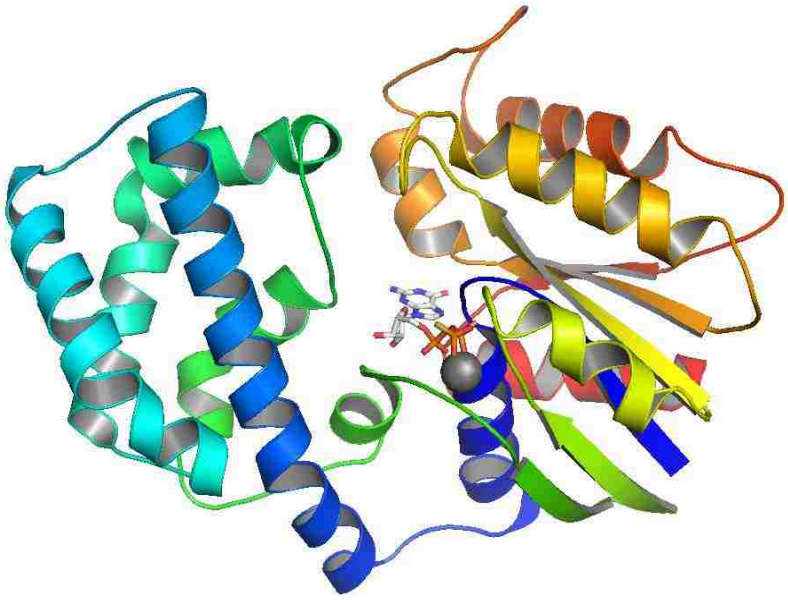

Figure 1-2. Crystal structure of rat Gαi1:GTPγS complex showing the secondary structural elements of Gαi1 in cartoon representation in rainbow colors, GTPγS in sticks, and Mg^{2+} in ball. (95) (PDB:1GIA)

1.1 Heterotrimeric G-Proteins

1.1.1 The G-protein Cycle

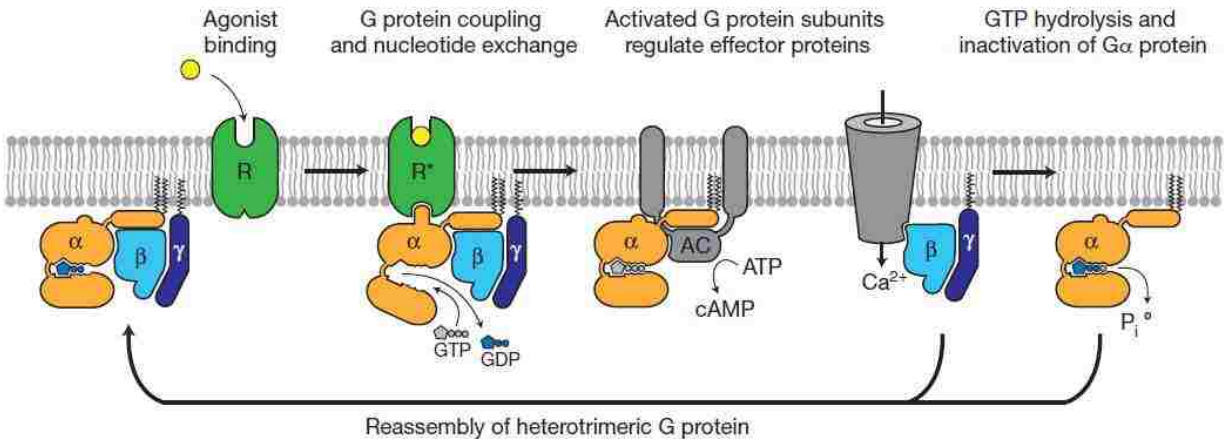

Figure 1-3. The heterotrimeric G-protein cycle.
(Starting from far-left) Inactive heterotrimeric G protein complex consisting of Gα·GDP and Gβγ, a guanine-nucleotide dissociation inhibitor (GDI), tethered to the plasma membrane, where inactive integral membrane GPCR is inserted. Binding of extracellular agonist, such as adrenalin, activates GPCR; activated GPCR interacts with the inactive G-protein heterotrimer and promotes nucleotide exchange at Gα as a guanine-nucleotide exchange factor (GEF). Interaction with GPCR leads to the formation of activated Gα·GTP, which dissociates from Gβγ. Gα·GTP and Gβγ interact with their corresponding effector molecules to perform signaling tasks. GTP is hydrolyzed into GDP and inorganic phosphate (Pi) intrinsically by the GTPase domain of Gα or with the help of a GTPase activating protein (GAP), such as regulator of G-protein signaling (RGS); Pi is released and Gα·GDP re-associates with Gβγ to form the inactive heterotrimer **(back to the beginning)**, completing one G-protein cycle. (41)

Heterotrimeric G-proteins are composed of α (~40 kDa), β(~36 kDa) and γ (~7.8 kDa) subunits. In human, there are several classes of Gα subunits including Gαs, Gαi, Gαo, Gαq, Gαt (transducin), etc.; each class is specific for interacting with different effector molecules; there are five G-protein beta subunits (Gβ) isoforms and twelve G-protein gamma subunits (Gγ) isoforms known to-date. (14) In general, a Gα subunit contains a characteristic α-helical domain and a GTPase domain (also called Ras-homology domain), which hydrolyzes bound-GTP, while the

Gβ and Gγ subunits exhibit no intrinsic GTPase activity. The activity of Gα subunits is guanine-nucleotide-dependent and is switched on (GTP-bound) and off (guanosine diphosphate, GDP, -bound) rapidly with the help of co-factors, which will be discussed in detail later. When a GPCR becomes activated by agonist, it catalyzes the exchange of GDP for GTP on Gα; the activated, GTP-bound Gα subunit dissociates from Gβγ subunits (88, 103). Specific members of Gα subunits, when activated, modulate the activity of specific effector molecules, such as tmAC, phospholipase Cβ, and nucleotide exchange factors for the small GTPase Rho, etc. (84, 88) The GTPase domain of Gα hydrolyzes the bound GTP to GDP; the now deactivated Gα subunit re-binds Gβγ to form the inactive heterotrimer, thus completing the cycle. **(Figure 1-3)** (103)

1.1.2 Regulators of G-protein Signaling: GAPs, GEFs, and GDIs

Gα signaling is regulated by altering the rate of two processes, GTP hydrolysis and guanine nucleotide exchange, which switch the Gα between the active (GTP-bound) and inactive (GDP-bound) states. Gα intrinsically hydrolyzes its bound GTP slowly and becomes deactivated. Isolated Gα subunits hydrolyze bound GTP with rate constants (k_{hyd}) between 0.1 min^{-1} (G_z) and 2 to 4 min^{-1} (G_s, G_i, G_o, G_t) at 30 °C. (80) When a GTPase activating protein (GAP) such as regulator of G-protein signaling (RGS) binds the GTP-bound Gα, it accelerates hydrolysis of the bound GTP >2000-fold by stabilizing a transition state-like intermediate. (80, 88)

Gα activity can also be regulated through means of enhancing or blocking the nucleotide exchange reaction. Just like the intrinsically slow GTPase activity, the intrinsic rate of nucleotide exchange is also slow in Gα subunits (88, 104), ranging from immeasurable (Gαq) to 0.16 min^{-1} (Gαo). (72) Nucleotide exchange in Gα subunits can be described as a two-step process, GDP release and GTP binding. Of the two, the release of GDP from Gα is considered

the rate limiting step (88, 103, 105); guanine-nucleotide exchange factors (GEF) and guanine-nucleotide dissociation inhibitors (GDI) regulate the rate of GDP release.

GEFs accelerate the rate of GDP to GTP exchange in G-proteins. (88) Until the discovery of resistance to inhibitors of cholinesterase-8 (Ric-8), a family of soluble proteins that exhibit GEF activity towards Gα subunits *in vitro*, the heptahelical, trans-membrane GPCRs were the only known GEFs for Gα and have been studied extensively. (62, 72) The other class of modulators of guanine-nucleotide exchange, GDIs, also bind specifically to the GDP-bound state of Gα subunits; instead of catalyzing the exchange reaction, GDIs inhibit the dissociation of GDP from Gα by stabilizing the GDP bound state. The Gβγ heterodimer is a GDI. (88) A new class of GDIs typified by activator of G-protein signaling 3 (AGS-3) was also discovered. Like Gβγ heterodimer, AGS-3 binds specifically to the GDP-bound state of Gα and acts as a GDI. (26, 58, 68, 78) GAPs, GEFs, and GDIs together function in precise and rapid manners to regulate G-protein signaling; in certain cases, interesting synergetic effects are observed between GEFs and GAPs.

1.1.3 Gα:GDP vs. Gα:GTP Structural Changes

As mentioned above, the identity of the guanine nucleotide (GDP or GTP) bound to Gα governs the two major conformational states of this important signaling macromolecule. At the structural level, Gα undergoes substantial structural changes as it transitions between the GDP- and GTP-bound states. Regulators and effectors of Gα show preference in interacting with specific states of Gα. The crystal structures of both states of Gαi1 and Gαt that were determined two decades ago elucidate those structural rearrangements. (93, 95, 98, 99) The crystal structures of the

RGS4:Gαi1:GDP-AlF_4^- complex as well as its Gαt counterpart even captured the transition state-like intermediate of GTP-hydrolysis. (90)

By comparing the crystal structures of GDP- and GTP-bound states of Gαi1 and Gαt, large conformational changes are observed at certain regions called the switch regions, which are designated switch I, switch II, switch III, and the Gαi1-specific switch IV. Gαi1 contains all four switches; switch I spans residues 177-187, switch II 199-219, switch III 231-242, and switch IV 111-119. Switch II and III are disordered and were not modelled in the Gαi1:GDP structure while in the Gαi1:GTPγS structure, these regions were structured and modelled successfully.

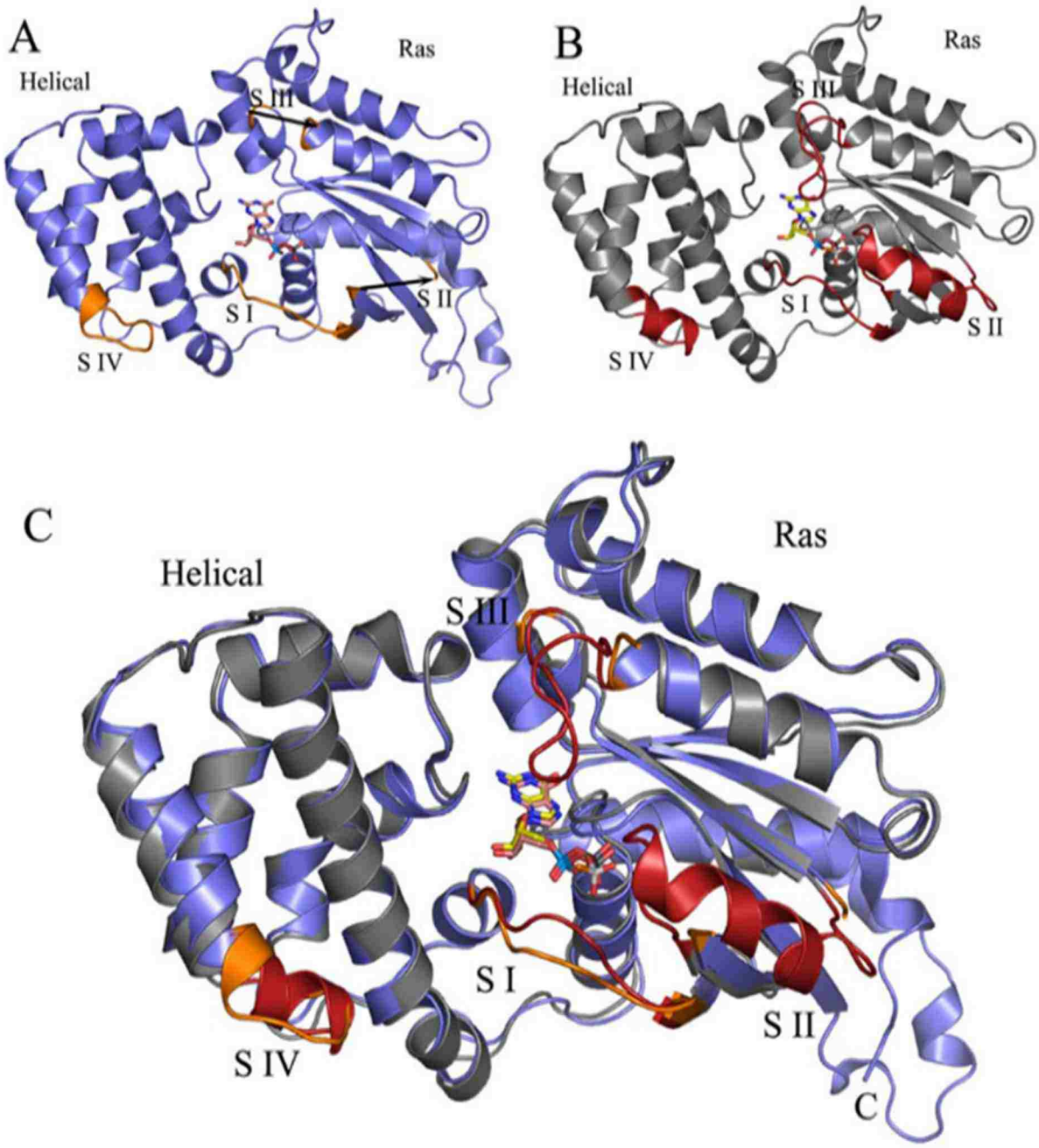

Figure 1-4 Comparison of Gαi1 structure in the GDP- and GTPγS-bound conformations
(A) Crystal structure of Gαi1·GDP (Mixon et al. 1995, PDB Code: 1GDD). Switch regions are shown in orange. **(B)** Crystal structure of Gαi1·GTPγS·Mg^{2+} (Coleman et al. 1994, PDB Code: 1GIA). Switch regions are shown in red. **(C)** Superposition of (A) and (B). Switch regions are marked as S I (switch I), S II (switch II), S III (switch III), and S IV (switch IV). The α-helical and Ras-homology (GTPase) domains are labeled. Guanine-nucleotides are shown as sticks. (58)

Switch II folds into an α-helix in the Gαi1:GTPγS structure and is stabilized by interaction with

Mg^{2+} and γ-phosphate of GTPγS. Other important sites of structural rearrangement are the N- and C-termini of Gαi1. In the Gαi1:GTPγS structure, the terminal regions are disordered but form a structured domain in the Gαi1:GDP structure. (93, 95) **(Figure 1-4)** For transducin (Gαt), the structural changes in switch regions are also observed, however, these changes do not entirely resemble those of Gαi1. Most noticeably, switch II and III of transducin seem to retain some ordered structure even in the GDP-bound form. (98, 99) The nucleotide-dependent structural changes in switch regions of G-protein α-subunits led to the speculation that the switches are responsible for effector/regulator interactions. Subsequent studies confirmed the validity of the speculation, for example, the structures of Gαi1·GDP·AlF_4^- bound to the RGS domain of RGS4, Gαi1·GDP in complex with Gβ1γ2, stimulatory G-protein α-subunit (Gαs) in complex with the soluble domain of tmAC, and most recently the receptor:G-protein complex, in which Gα maintains its contact with Gβγ while bound to a CPCR. (41, 89, 90, 92, 94)

1.1.4 Canonical GPCR-Activation of G-Protein

The canonical GPCR activation of G-proteins has been characterized to a great extent both *in vitro* and *in vivo*. (2, 14, 18, 19, 38, 41, 70) G-proteins mediate a wide range of physiological signals from the outside of the cell. The signals, which can be a change in concentration of peptides, hormones, lipids, neurotransmitters, ions, odorants, tastants, etc., or simply an influx of photons, stimulate specific GPCRs on the cell membrane. Around half of all current medications act through these receptors, among them β-blockers, antihistamines and various kinds of psychiatric medications. GPCRs pass these signals to the inside of the cell by activating specific G-proteins, especially Gα subunit in the heterotrimeric complex, triggering a series of regulatory reactions involving other proteins, nucleotides and metal ions, which result in appropriate cellular and physiological responses.

An important physiological example of GPCR activation of Gα is the initiation of fight-or-flight response in mammals. When threatened by imminent danger, the adrenal medulla of an animal produces adrenaline, among many other hormones; binding of adrenaline to the extracellular surface of β2AR activates the GPCR, which in turn activates Gαs by catalyzing the guanine-nucleotide exchange reaction on Gαs. Activated Gαs:GTP complex continues to activate tmAC, which converts ATP into cAMP, an important secondary messenger molecule. cAMP leads to the activation of protein kinase A (PKA), one of many down-stream protein targets of cAMP; the kinase in turn phosphorylates enzymes and transcription factors that are necessary to ultimately accomplish the fight-or-flight response. The complicated, yet lightning-fast physiological response is essential for survival.

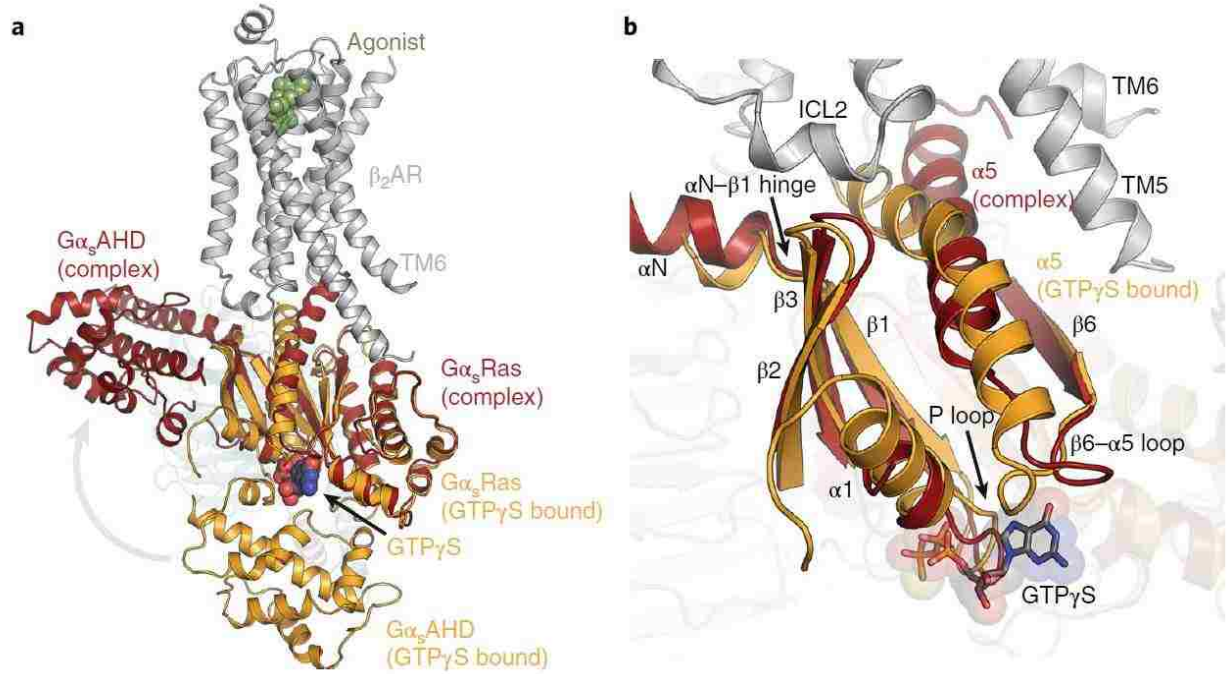

Figure 1-5 Receptor-mediated conformational changes in Gα.
(a) Structural comparison of nucleotide-free Gαs (red) coupled to β2AR (gray, PDB 3SN6) and GTPγS-bound Gαs (orange, PDB 1AZT). GTPγS is shown as spheres. Receptor-binding of Gαs induces an outward movement of the α-helical domain of Gαs (Gαs AHD) relative to its position in the GTPγS-bound state. **(b)** Structural rearrangements caused by activated GPRC-binding near the nucleotide binding site of Gαs. (41)

Recently, the fruit of almost twenty years of advancement in biotechnology, protein engineering, and biophysics was the atomic-resolution crystal structure of the activated β2AR complexed to a heterotrimeric G-protein (Gαβγ). (41) The structure illustrated a transient, but important intermediate, demonstrating for the first time in structural detail the well-understood role of GPCRs as GEFs for Gα. **(Figure 1-5, PDB:3SN6)** The structure depicts the agonist-induced conformational changes in the receptor:G-protein complex that favor GDP release by Gαs. The receptor engages the C-terminus of Gαs, causing a cascade of structural events in Gαs and eventually leading to the separation of Ras and helical domain, and forming an exit path for GDP. (41) However, Gα domain separation occurs spontaneously and frequently even in the absence of a receptor, therefore, is necessary but not sufficient for GDP release. More

substantial conformational changes that favor nucleotide release are observed using different biophysical methods. (18) Briefly, the α5 helix of Gαs inserts itself into a cavity in the activated receptor formed by outward movement of transmembrane helices TM5 and TM6. Due to the movement of α5, the β6–α5 loop and the hydrophobic core interaction between α5, β2 and β3 and α1 are perturbed. Rearrangement of the β6–α5 loop and destabilization of α1 lead to weakened binding of the purine ring and the phosphates of GDP. Interaction between the intracellular loop 2 (ICL2) of the receptor and the αN–β1 hinge region of Gαs appears to shift β1 and the adjacent P-loop that are crucial in nucleotide binding. (2) These structural rearrangements observed in the complex structure are highly conserved amongst different types of GPCRs and Gα interactions in the interruption of the contacts between α1 and α5.(19) In addition to the Ras domain, the helical domain, which distinguishes Gα from other Ras GTPases from the same family, also becomes more flexible in the receptor-bound, nucleotide-free form. (40)

1.2 Ric-8A

1.2.1 Discovery of Ric-8 and Biological Significance

G-protein signaling mechanisms are important for our current understanding of biological systems. Yet, the role(s) of intracellular regulators, especially intracellular GEFs, of G-proteins have received far less attention than trans-membrane GEFs, the GPCRs. Unlike the GPCRs, which act upon heterotrimeric complexes of G-proteins near the plasma membrane, resistance to inhibitors of cholinesterase 8 (Ric-8), 60 kDa cytosolic proteins that catalyze the release of GDP from many classes of Gα, acts exclusively on GDP-bound monomeric Gα. Ric-8 is also called "synembryn" to reflect its dual functions in synaptic transmission and early embryogenesis. (77)

1.2.1.a Synaptic Transmission

Ric-8 proteins were first identified in a *Caenorhabditis elegans* genetic screen for synaptic transmission mutants. (91) Reducing intracellular Ric-8 levels apparently alleviates toxic accumulation of acetylcholine caused by the presence of inhibitors of cholinesterase, such as aldicarb. **(Figure 1-6)** It was later discovered that the highly-conserved Ric-8 family of proteins controls neurotransmitter release by regulating G-protein(o) α-subunit (Gαo) and G-protein(q) α-subunit (Gαq). (79) Ric-8 regulates cellular abundance of Gαq therefore also regulates Gαq-dependent neurotransmitter release; knocking-down Ric-8 thereby indirectly reduces the synaptic

concentration of acetylcholine. (32)

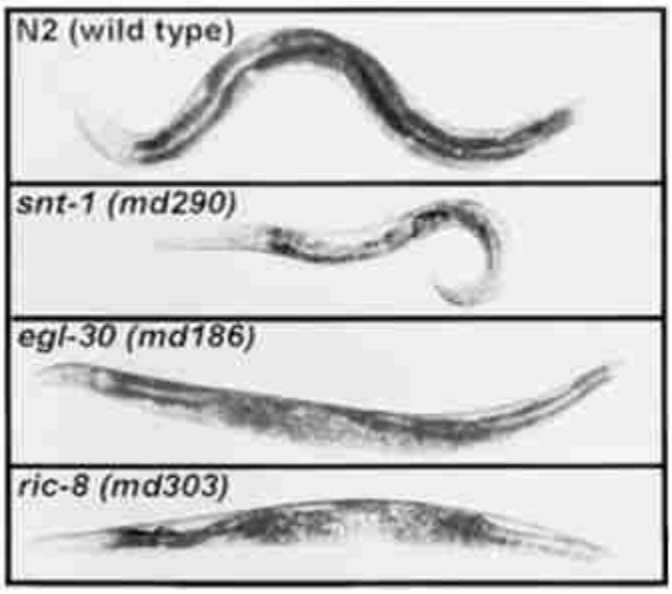

Figure 1-6 Ric-8 (ric-8) knock-down C. elegans mutants exhibit similar phenotypical defects as Gαq (egl-30) knock-down mutant in its response to inhibitors of cholinesterase, aldicarb. *egl-30* and *ric-8* mutants, in addition to being aldicarb resistant, are both bloated with eggs and exhibit decreased body flexion phenotypes that are characteristic of the subclass of aldicarb resistance mutants with defects in the Goα–Gqα signaling network. (77)

1.2.1.b Asymmetric Cell Division and Embryogenesis

In *C. elegans*, Gαo is a key component of a signaling network that regulates neurotransmitter secretion. Early studies demonstrated that reduction of Ric-8 or Gαo results in partial embryonic lethality by causing defects in centrosome movements during early embryogenesis. (79) Asymmetric cell division is of fundamental importance for the initial stage of embryogenesis. Again, in the *C. elegans* embryo model, spindle positioning has been shown to depend on heterotrimeric G-protein signaling. Reduction of Ric-8 expression results in cell division phenotypes very similar to that of Gαo knockouts. **(Figure 1-7)**

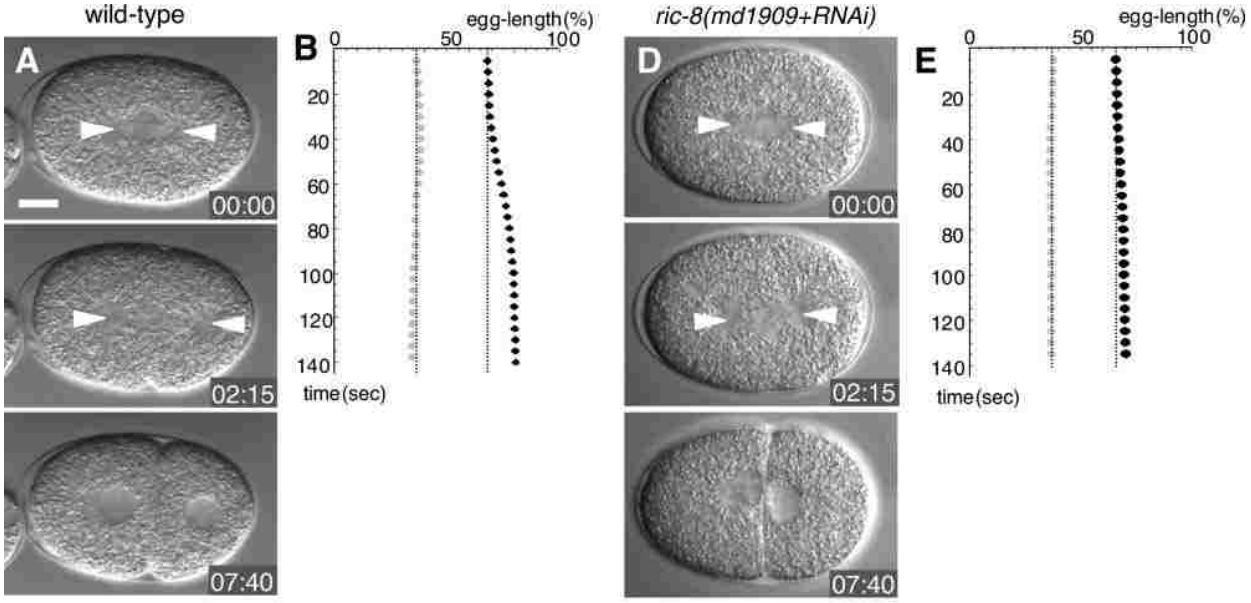

Figure 1-7 Ric-8 is required for asymmetric cell division
(A+D) WT (A) and Ric-8 RNAi-knockdown (D) embryos, elapsed time is indicated, arrowheads point to spindle poles. **(B+E)** Positions of anterior and posterior spindle poles at the end of anaphase. (64)

Ric-8 also binds Gαo:GDP preferentially, therefore is consistent with a GEF role in the worm model. (65) It was suggested that Ric-8 could also act upstream of the GoLoco protein GPR-1/2 in the sequence of events leading to Gαo activation. (64) In addition to Gαo, Gαi is also involved in asymmetric cell division through a signaling pathway that regulates microtubule pulling forces during mitotic movement of chromosomes. Other co-factors such as GPR or GoLoco domain-containing proteins, and RGS proteins are also involved. In the rat model, the GoLoco domain-containing protein LGN (GPSM2), the LGN- and microtubule-binding nuclear mitotic apparatus protein (NuMA), and Gαi1 regulate a similar process. It was demonstrated *in vitro* that Ric-8A releases Gαi1 and NuMA from NuMA:LGN:Gαi:GDP complexes and the Gαi1 released is in GTP-bound form. (63) In the Drosophila model, Frizzled and G-protein signaling act in opposition to ensure that the spindle aligns correctly. Ric-8 localizes Gαi and GPA-16 to the cell cortex to orient mitotic spindle during asymmetric cell division. (59, 60) Recently, Boularan et al. found that inhibition of Ric-8A or Gαi1 activity decreases the production of PtdIns(3)P through Vps34 therefore indirectly contributes to cytokinesis during abscission, a late-stage event in cell

division. (27) Taken together, the involvement of Ric-8 proteins in development is crucial in a G-protein-dependent manner across species.

1.2.2 G-protein, Ric-8 Biochemistry, *in vitro* and in Cell Models

In mammals, Ric-8A and Resistance to inhibitors of cholinesterase 8, isoform B (Ric-8B) isoforms have been found to act both as *in vivo* chaperones and/or *in vitro* guanine nucleotide exchange factors (GEFs) for different classes of Gα. (31, 72) For instance, Itoh et al. demonstrated that Ric-8B inhibits the ubiquitination-dependent degradation of Gαs and has *in vitro* GEF activity towards Gαs. (36, 45) Ric-8A, on the other hand, inhibits ubiquitination *in vivo* and accelerates nucleotide exchange *in vitro* for Gαi and Gαq, as seen by Tall, el al. and Sumimoto et al. (32, 72) Tall et al. also reported that manipulating Ric-8A level in embryonic stem cells affects Gαi1 expression in an mRNA-independent fashion. In cell-free expression systems, the presence of mRNA encoding Ric-8 is required to prevent accumulation of unfolded Gα. Generally, knocking-down Ric-8 in a variety of cultured cell lines reduces Gα abundance (39). Therefore, in some cases, Ric-8 regulation of Gα signaling could simply be an indirect effect of increased/stabilized Gα biogenesis. With that said, a direct GEF functional role for Ric-8 on Gα remains an open discussion because functional Gαs and Gαi can be abundantly expressed without any Ric-8 homologs in recombinant *Escherichia coli*, but co-expression of Ric-8A in insect cells significantly amplifies the production of Gαq, G-protein(13) α-subunit ($G\alpha_{13}$), and olfactory G-protein α-subunit (Gαolf). (37) Hence, it is conceivable that the cytosolic Gα levels are more strictly regulated at the protein synthesis stage in eukaryotic cells than is currently understood.

In the rat model, Ric-8A functions *in vitro* as a cytosolic GEF for Gαi1 by accelerating the release of GDP and forming a nucleotide-free Ric-8A:Gαi1 complex, which readily accepts GTP as a substrate; Ric-8A:Gαi1 complex dissociation immediately follows GTP association.(72)

(Figure 1-8)

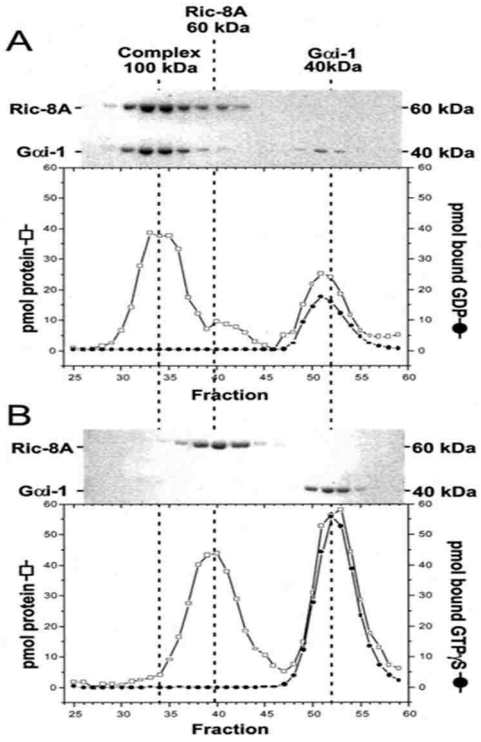

Figure 1-8 Nucleotide-free Gαi1:Ric-8A complex
Gαi1:GDP complex releases GDP slowly, Ric-8A binding to Gαi1:GDP catalyzes the release step, resulting in a stable, nucleotide-free Gαi1:Ric-8A complex. Size-exclusion chromatographic profile of samples of **(A)** excess Gαi1:GDP incubated with Ric-8A, forming a nucleotide-free Gαi1:Ric-8A complex, and **(B)** excess Gαi1:GTPγS incubated with Gαi1:Ric-8A complex, dissociating the complex. The closed circles in each chromatogram represent guanine-nucleotides (GDP or GTPγS) that are bound to Gαi1, therefore, eluted at the same elution volume as Gαi1. SDS-PAGEs of sample fractions under the curve are shown above the chromatograms. (72)

A few studies (8, 23) supported the proposal that Ric-8A binding induces local and global conformational changes as well as dynamic motions in Gαi1. Ric-8A-bound, nucleotide-free Gαi1 (Gαi1[ ]) is more accessible to trypsinolysis than Gαi1:GDP, but less so than free Gαi1[ ]. The nuclear magnetic resonance (NMR) heteronuclear single quantum coherence (HSQC) spectrum of [^{15}N]Gαi1[ ] in the Gαi1:Ric-8A complex shows a significant loss of peaks relative to that of [^{15}N]Gαi1:GDP, indicating Ric-8A-induced dynamic motions of Gαi1[ ]. Hydrogen-deuterium exchange (HDX) on Gαi1[ ] bound to Ric-8A is 1.5-fold more extensive than in Gαi1:GDP, suggesting that Ric-8A-binding possibly causes partial destabilization of Gαi1 tertiary and/or secondary structural elements, therefore increases overall solvent accessibility of

the protein. The study also concluded that the C-terminus of Gαi1 is a critical binding element for Ric-8A since the C-terminal peptide of Gαi1 not only binds Ric-8A but also inhibits full-length Gαi1 binding to Ric-8A, as it is the case for GPCR-Gα interaction.(41, 42) These findings suggest that both Ric-8A and GPCR might promote nucleotide release by similar mechanisms, acting as folding chaperones and inducing temporary unfolding to favor an unstable and dynamic nucleotide-free state of Gα. (55) However, the Ric-8A-activated Gαi1 shows large conformational changes in switch II region of Gαi1 (10), changes that are not evident in the GPCR activation scheme, suggesting that the Ric-8A-activated Gαi1 is conformationally and/or functionally different than the GPCR-activated Gαi1.

The double electron-electron resonance (DEER) spectroscopy study provided global distance constraints that identified discrete members of Gαi1 conformational ensemble in the Gαi1:Ric-8A complex. In the complex, the helical and Ras-like domains of Gαi1 move apart with displacements as large as 25 Ångströms (Å). The domain displacement appears to be different from that observed in the Gαs:β2AR complex. Moreover, the Ras domain exhibits structural plasticity at the nucleotide-binding site, the switch I and switch II regions, which are known to adopt different conformations in the GDP- and GTP-bound states of Gαi1. (23) Taken together, the data confirmed previous studies that Ric-8A induces a conformationally dynamic state of Gαi1.

1.3 Hypothesis and Goals

The dual function of Ric-8A in Gα biosynthesis *in vivo* and the apparent *in vitro* GEF activity suggests that like many other cell-signaling molecules, the Gα family of proteins are regulated elsewhere than solely near the plasma membrane. Recently published evidence about Ric-8 phosphorylation, which enhances the Ric-8 GEF activity (3), further implies an intricate alternative pathway for Gα activation remote from the plasma membrane, where signals are transduced from the exterior to the interior of a cell. Understanding the intracellular, Ric-8-regulated Gα signaling pathway could shine light on the development of alternative therapeutics targeting abnormal expression and activation of Gα in diseases.

Up to this point, no homolog of Ric-8A has been crystallized or its structure solved. Based on structural information predicted from the amino acid sequence of Ric-8A, the polypeptide consists mainly of a specific type of α-helical repeats called Armadillo (ARM) repeats.(76) Circular dichroism (CD) studies on purified Ric-8A further illustrated that the protein is well-folded in solution and indeed is >90% α-helical. (48) This dissertation aims to answer at least parts of the questions regarding the regulation of Ric-8 by Casein Kinase-II (CKII) phosphorylation (3), the structures of Ric-8 and its complex with Gα, and finally, how the two macromolecules interact.

In chapter II, a putative Gαi1 binding site on Ric-8A, as suggested by hydrogen-deuterium exchange (HDX) experiments, will be tested *in vitro* through biochemical assays. Chapter III and IV will focus on the molecular structures of Ric-8A determined by X-ray crystallography and small-angle X-ray scattering. The activation of GEF functions of Ric-8A by phosphorylation will also be further examined in these two chapters. Lastly, in chapter V, some future directions and preliminary results will be discussed.

Chapter II: A Putative Gαi1 Interactive Site on Ric-8A

2.1 Introduction

The ultimate goal for the study on Ric-8A:Gαi1 interaction is to understand comprehensively the molecular mechanism by which Ric-8A catalyzes nucleotide exchange for mature (properly folded) Gαi1 and folds nascent (freshly synthesized by ribosome) Gαi1. Using hydrogen-deuterium exchange coupled with mass-spectrometry (HDX-MS), the protein-protein binding surface of Ric-8A and Gαi1, as well as conformational changes induced by complex formation, were studied by analyzing the HDX protection profiles of pepsin-digested peptide fragments of each protein component in the complex. In this chapter, I will briefly discuss the putative protein-protein interaction sites and conformational changes on Gαi1 and on Ric-8A, extrapolated from HDX-MS results generated by our collaborators, Brian Bothner's group at Montana State University (MSU). (10) Then I will focus on characterizations, which were biochemical and biophysical experiments conducted in the Sprang lab at the University of Montana (UM), of a putative Gαi1 binding site on Ric-8A using site-directed mutagenesis, circular dichroism (CD), differential scanning fluorimetry (DSF), and fluorescence spectroscopy.

2.1.1 Insights from HDX-MS: A Putative Gαi1 Binding Site

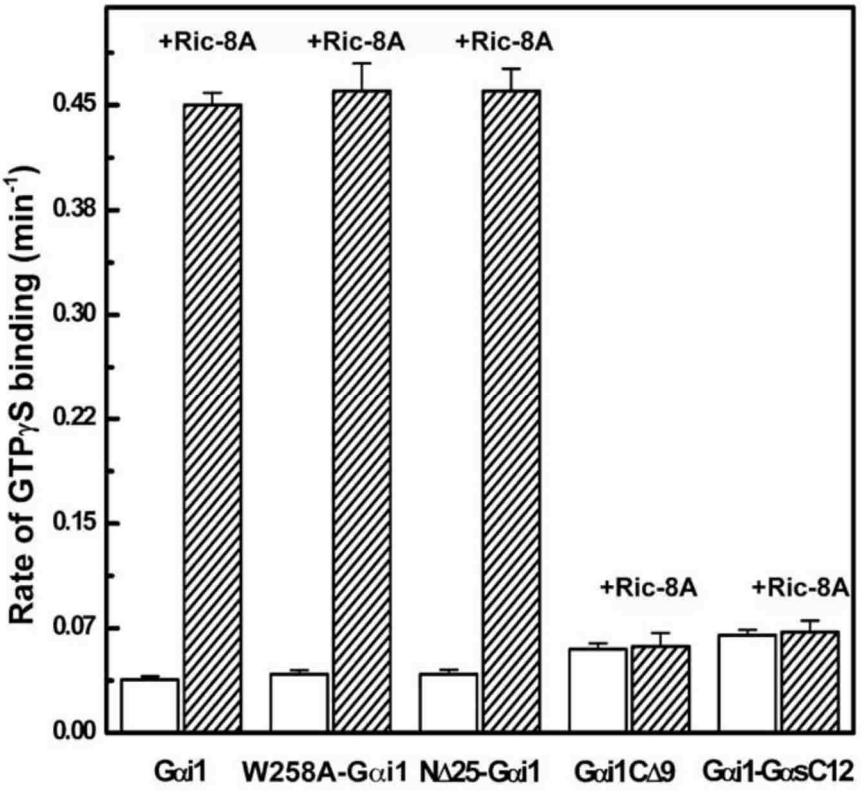

Figure 2-1 Intrinsic and Ric-8A-catalyzed GTPγS binding rates of Gαi1
Intrinsic and Ric-8A-catalyzed kinetics of binding of GTPγS to wild-type Gαi1, W258A-Gαi1, NΔ25Gαi1, Gαi1CΔ9 and Gαi1-GαsC12 were measured using a fluorescence binding assay. 400 μL of protein (1 μM) in the GDP-bound form was equilibrated for 10–15 min at 25°C in a cuvette. A 10-fold excess of GTPγS was added and fluorescence at 340 nm upon excitation at 290 nm was monitored in the absence (open bars) or presence (filled bars) of Ric-8A (1 μM). Error bars represent +/- one standard deviation apparent first-order rate constants determined in three replicates. (42)

As discussed in Chapter 1 section 1.2.2, the span of 18 residues (DAVTDVIIKNNLKDCGLF) at the extreme C-terminus of Gαi1 appears to bind Ric-8A and renders Gαi1 unresponsive to the GEF activation by Ric-8A upon partial removal or substitution with Gαs C-terminus.(42) **(Figure 2-1)** The fact that β2AR also interacts with the C-terminus of Gαs (41) suggests that Ric-8A might promote GDP release for Gαi1 through similar mechanism as β2AR does for Gαs. For Ric-8A, however, no information about Gαi1 binding site(s) were available until recently.

Without direct crystallographic structural information about the complex, we turned to HDX-MS for more insights about the Gαi1-Ric-8A interaction.

In an HDX-MS experiment, protein samples were diluted rapidly into heavy water (D_2O); labile hydrogens, for example those on the solvent accessible peptide amide bonds, exchange almost instantaneously for deuterium. If the amides are hydrogen-bonded or protected, HDX will proceed more slowly. (107) For single-component HDX experiments, the extent and time frame of protection from HDX provide information about protein dynamics and how local structural elements fold. For multi-component systems, for instance the Ric-8A and Gαi1 complex, HDX is useful for revealing potential binding interfaces, which are lined with presumably protected amide hydrogens. It is therefore possible to obtain valuable structural information about the protein-protein interaction without information from a high-resolution crystal structure of the protein complex. HDX also avoids misleading crystallographic artifacts, such as non-physiological crystal contacts or oligomerization states, in X-ray crystal structures.

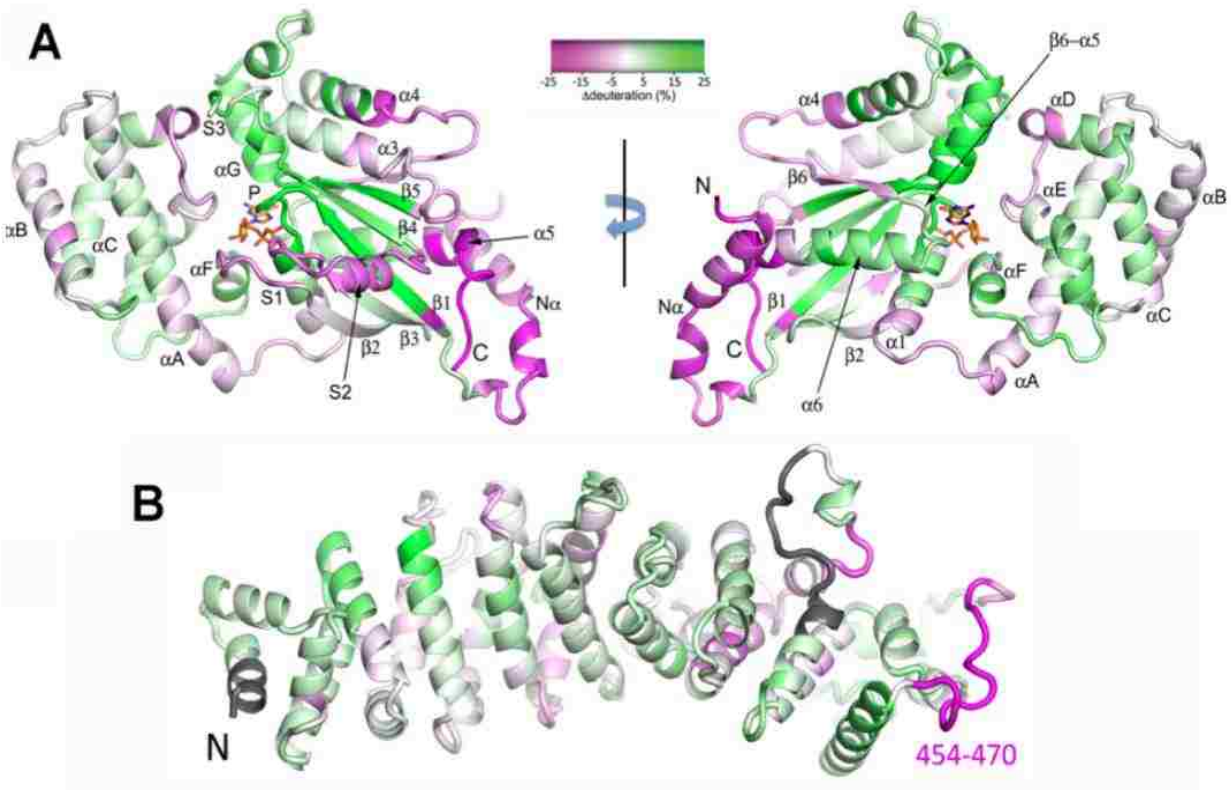

Figure 2-2 HDX protection profile of Gαi1 and Ric-8A in the complex
(A) HDX-MS of Gαi1 and **(B)** Ric-8A showing both protection (magenta) and deprotection (green) regions in the complex compared to free-Gαi1 and Ric-8A, respectively. HDX protection profiles were color-rendered on the crystal structure of Gαi1:GDP (1GDD) and a Rosetta (Bradley et al. 2005) model of Ric-8A. (10)

In a collaborative effort with Brian Bothner's group at MSU, we completed the HDX-MS experiments for Gαi1:GDP, Gαi1:Ric-8A complex, and Ric-8A. In aggregate, overlapping peptide fragments recovered from pepsinolysis represent the entire amino acid sequence of Gai1 and 87% of that of Ric-8A for the three species mentioned above. Throughout its primary structure, Ric-8A is highly susceptible to HDX, with nearly half of the observed peptide segments incorporating deuterium at 60% of exchangeable sites. Upon binding to Gai1, Ric-8A undergoes changes in accessibility to HDX throughout its amino acid sequence **(Figure 2-2)**. Many Ric-8A-derived peptides show 5–15% changes in deuteration relative to free Ric-8A at successive amino acid repeats, suggestive of distributive conformational changes. (10) Notably, a

seventeen-residue span near the C-terminus of Ric-8A is highly protected (25% decrease in deuteration) from HDX when Ric-8A is complexed to Gαi1. **(Figure 2-2)** Although it is not the only region protected, the immediate hypothesis is that the protected region (residues 454-470 with the amino acid sequence "PVTGRVEEKPPNPMEGM") on Ric-8A forms intimate contacts with Gαi1. With that said, Ric-8A conformational changes induced allosterically by Gαi1 can be alternative sources of observed HDX protection and deprotection, instead of direct protein-protein contacts.

2.1.2 Experimental Designs to Test the Putative Gαi1 Binding Site

To test the hypothesis that Ric-8A 454-470 is a Gαi1 binding site, I first performed an alanine screen by site-directed mutagenesis to create seventeen single alanine mutants, using the Ric-8A 1-491 construct (R491) as a template, through residues 454-470. With the hope to identify functional and binding "hotspots" on Ric-8A for Gαi1, I tested these mutants for their ability to **(a)** facilitate nucleotide exchange for Gαi1 and **(b)** form complexes with Gαi1. Three different experimental approaches were adopted to assess the GEF activities of Ric-8A alanine mutants, a tryptophan fluorescence GTPγS-binding assay, a 2'/3'-O-(N-Methyl-anthraniloyl) (MANT) fluorescence MANT-GTPγS-binding FRET assay, and a conventional ^{35}S-GTPγS filter binding assay. Data obtained from the tryptophan fluorescence GTPγS-binding assays were the most comprehensive, therefore, should be considered the primary data set for assessment of the GEF activities of the Ric-8A mutants. Using size-exclusion chromatography, the Ric-8A:Gαi1 complex-formation profile of each Ric-8A alanine mutant was assessed. As a quality control, thermal stability of all mutant Ric-8A 1-491 protein products was tested by heat denaturation using circular dichroism(CD) and differential scanning fluorimetry (DSF).

Three major protein constructs were selected for the GEF functional assays, Ric-8A 1-491 (R491), Gαi1 W258A (Gαi1), and myristoylated Gαi1 (mGαi1). As described previously (42), R491 appears to be the shortest fragment of the rat Ric-8A construct to retain maximum GEF activity of, if not better than, the full-length protein; therefore, is adequate for the purpose of the assays. The structure and functions of the *E. coli*-expressed Gαi1 W258A (Gαi1) have been studied extensively by the Sprang lab in the past (42, 52, 58), therefore, it is an appropriate construct for un-post-translationally modified Gαi1. The tryptophan-258 to alanine mutation does not affect any major functions of Gαi1 **(Figure 2-1)**; among the three tryptophan residues in rat Gαi1, W211 in switch II region undergoes the largest change in its fluorescence environment upon GTP-binding (73, 102, 104), therefore, the W258A mutation only improves signals for the tryptophan fluorescence assays. (42) It is also a legacy mutant designed to improve packing interactions between Gαi1 molecules in crystals. The myristoylated Gαi1 (mGαi1) construct, engineered by Linder et al., is the only post-translationally modified Gαi1 available. It harbors an internal His-tag, which does not affect the functions of the protein (96), for easy purification and enabling N-terminal myristoylation of the G-protein. Additionally, a short peptide encompassing Ric-8A residues 454-470 and a GST-fusion construct of Ric-8A 399-491 were purchased and created, respectively. The 454-470 peptide was used for pull-down assays; the GST-Ric-8A 399-491 was assayed both for its own GEF activity and inhibition of GEF activity of R491 towards Gαi1. Both Gαi1 and mGαi1 were used in the tryptophan fluorescence assays; only Gαi1 was used in the complex-formation/size-exclusion assays, the peptide competition pull-down assays, and the GST-Ric-8A 399-491 assays; only mGαi1 was used in both the FRET assay and ^{35}S-GTPγS isotope assay.

2.2 Results and Discussion

2.2.1 HDX-MS Reveals Putative Binding Sites on Gαi1 and Ric-8A

By comparing the HDX protection profiles of Gαi1:GDP and Gαi1:Ric-8A complex **(Figure 2-2)**, we propose a large, putative protein-protein interactive surface on Gαi1 that includes structural elements at the helical and Ras domain interface, Switch I and II, and the termini. HDX protection of the Gαi1 C-terminus confirms the previous finding that it may directly contact Ric-8A. It is conceivable that in the complex, Ric-8A disrupts structured regions near the GDP-binding site of Gαi1, destabilizes the interface between the Ras and helical domains, facilitates domain separation and eventually leads to GDP release. It appears that the Ric-8A-induced Gαi1 conformational changes and solvent exposure are reversible by GTP-binding and Ric-8A dissociation.

On the side of Ric-8A, HDX of the complex identifies an extensively deprotected sequence corresponding to peptide fragment from residue 419 to the C-terminus (residue 491) of the Ric-8A construct used in the study. The C-terminal segment of Ric-8A in the complex exhibits a 10–15% increase in deuteration relative to free Ric-8A. The pattern, however, is interrupted by a highly protected (25% decrease in deuteration) peptide comprising residues 454–470. The 17-residue peptide, which is rich in proline and acidic residues, as well as regions flanking it, are highly conserved in its primary amino acid sequence among vertebrates. **(Figure 2-3)** Based on the secondary structure analysis of a library of Ric-8A homologs, this peptide is predicted to be largely unstructured. (10)

Figure 2-3 Multiple sequence alignment of vertebrate Ric-8A homologs
Residues within the putative binding site (residues 454-470) are highly conserved among vertebrate species. (NCBI MSA Tool)

Overall, HDX-MS confirms that like the GPCRs, Ric-8A binds the C-terminus of Gαi1. (38) Yet distinct from GPCRs, Ric-8A also interacts with Switches I and II and possibly at the Ras-helical domain interface. These extensive interactions provide both allosteric and direct catalysis of GDP unbinding/release and GTP binding. (10) The noticeable protection of the peptide comprising Ric-8A residues 454–470 in the complex implies that the segment is a possible Gαi1 binding site. To test this hypothesis, we created seventeen single-residue mutants and assayed the GEF activity of each using a tryptophan fluorescence assay that monitors the exchange of GDP for GTPγS at Gαi1. All mutants expressed and purified similarly to WT R491 except for M470A mutant, which behaved poorly during the last step of the purification.

For each WT or mutant Ric-8A, two types of assays were performed to measure different aspects of the guanine-nucleotide exchange reaction. **(Figure 2-4)** I first measured the GEF-stimulated initial rate of Gαi1 nucleotide exchange by adding GTPγS and Ric-8A simultaneously to GDP-bound Gαi1. This assay is termed the "nucleotide exchange" assay because it measured the rate of the entire nucleotide exchange reaction; both GDP-release and GTPγS-binding steps were assayed. I then measured the initial rate of GTPγS-binding to nucleotide-free Gαi1 in complex

with Ric-8A. The rate of GTPγS-binding reaction was not combined with that of the GDP-release step because the second assay only measured the rate of GTPγS-binding reaction. I refer to the second assay as the "GTP-binding" assay. I expect the results from these two assays to differ for the same Ric-8A WT or mutant since the "GTP-binding" assay only measured 2nd half of the reaction **(Figure 2-4)**. For instance, if GDP-release were the rate-limiting for the full reaction, the "nucleotide exchange" assay should always proceed slower than the "GTP-binding" assay because the rate-limiting step was skipped in the "GTP-binding" assay.

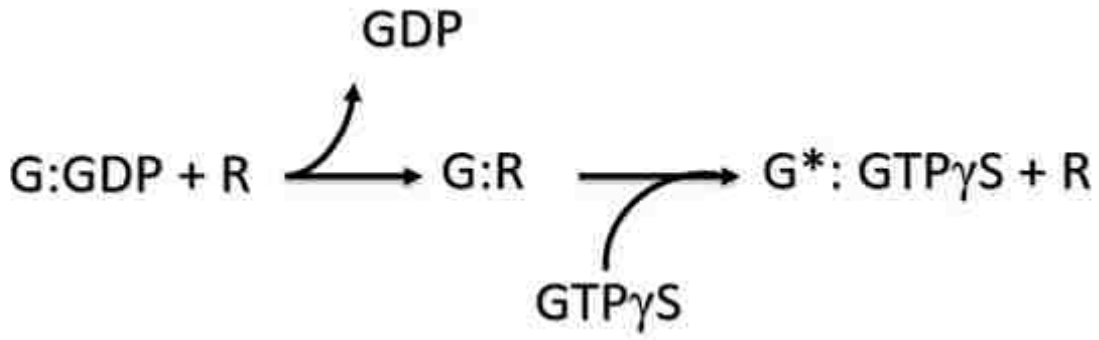

Figure 2-4 A simple schematic of Ric-8A catalyzed Gαi1 nucleotide exchange
G=Gαi1, GDP=guanosine-5'- diphosphate, R=Ric-8A, GTPγS= guanosine 5'-O-[gamma-thio]triphosphate, G:GDP=GDP-bound Gαi1 (inactive), G:R=Ric-8A-bound Gαi1(nucleotide-free), G*:GTPγS= GTPγS-bound Gαi1 (active)

2.2.2 Mutagenesis and Protein Expression and Purification

As mentioned above, the C-terminal region (residues 454-470) of Ric-8A is a putative Gαi1 binding site. In order to test the hypothesis, we performed an alanine scan by making point-mutations along the putative binding sequence. All seventeen mutant Ric-8A plasmids were sequenced and protein expression confirmed by Western Blot analysis. **(Figure 2-5)** Established protein expression and purification protocols for Ric-8A WT (42) were sufficient to purify most Ric-8A mutants except V455A, T456A, K462A, and M470A, which exhibited minor to medium

solubility issues during the routine purification process. To accommodate these mutants, the purification protocol was altered. (See Materials & Methods)

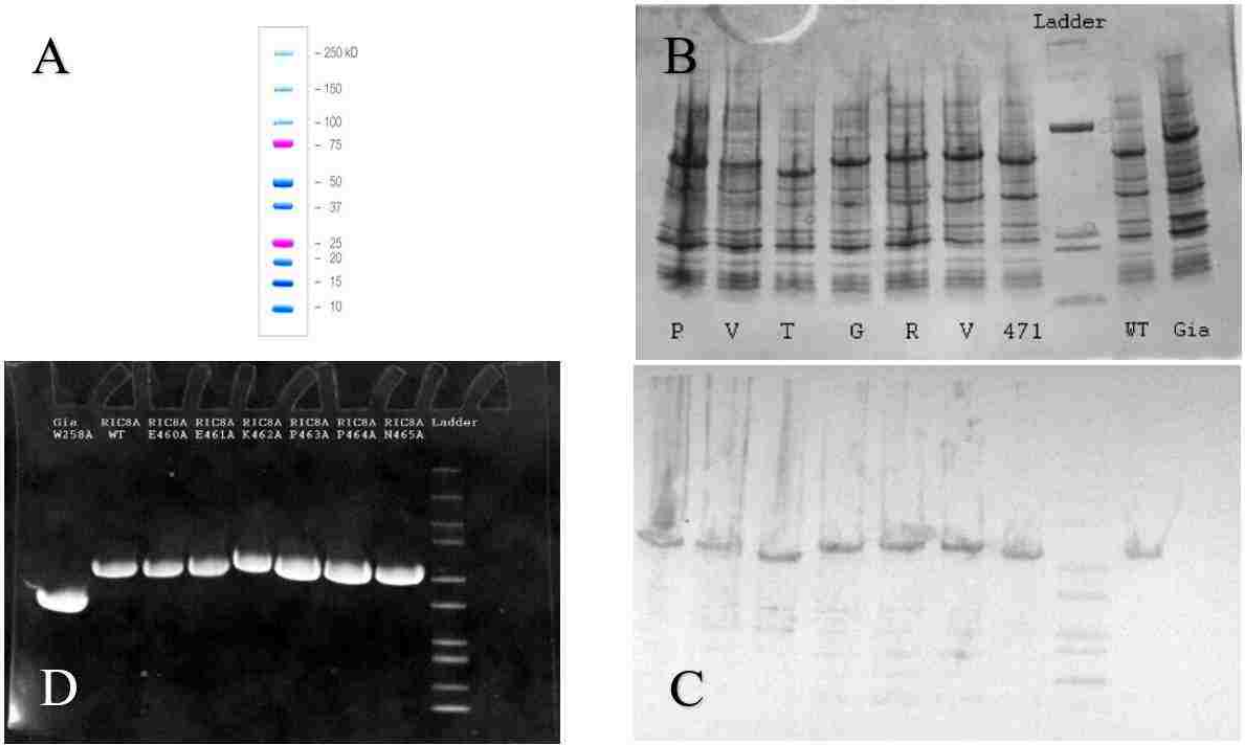

Figure 2-5 Expression and purification of representative R491 mutants
(A), SDS-PAGE protein standards. **(B)** SDS-PAGE (stained with Coomassie dye) results showing whole cell lysate of representative Ric-8A mutants, P454A, V455A, T456A, G457A, R458A, V459A, and R470. **(C)** Western-Blot of the SDS-PAGE on top-right panel blotted with 6x-His Tag Monoclonal Antibody (Invitrogen), followed by an HRP-conjugated goat anti-mouse IgG (Fc) secondary antibody (Invitrogen) and detected by Immun-Blot® Opti-4CN™ Colorimetric Kits (Bio-Rad). **(D)** SDS-PAGE analysis of purified R491 mutants used to perform experiments.

His-tagged constructs of R491, Ric-8A 1-470 (R470), Ric-8A 1-452 (R452) in pET28a vector all expressed in large quantities (>100 mg/Liter of cells) in BL21 DE3 RIPL *E. coli* using the protocol described in the method section of this chapter. Purification of R470, R452, and Ric-8A 1-425 (R425) were also straightforward using the standard R491 purification protocol with minor adjustments to accommodate less stable truncation mutants such as R452. Typical yield after the

anion exchange step of the purification, where the samples were more than 95% homogeneous, was about 50 mg TEV-digested, purified, monomeric recombinant protein per liter of cells.

All mutants but M470A were successfully purified by anion-exchange and size-exclusion chromatography (SEC). M470A precipitated heavily on the size-exclusion column. The original gel-filtration buffer (50mM HEPES pH 8.0, 150mM NaCl, 2mM β-mercaptoethanol, 0.01% Decaethylene glycol monodecyl ether (E10C12)) and assay buffer for the tryptophan fluorescence assay (50mM HEPES pH 8.0, 10mM $MgCl_2$, 150mM NaCl, 2mM β-mercaptoethanol, 0.01% E10C12) (42) were eventually changed (gel-filtration: 50mM HEPES 8.0, 150mM NaCl, 1mM TCEP; assay: 50mM HEPES 8.0, 10mM $MgCl_2$, 150mM NaCl, 1mM TCEP) for all protein samples used in the study; E10C12 was removed altogether from the recipes. The removal of detergent from the SEC running buffer drastically improved sample solubility in solution for Ric-8A mutants and did not affect the tryptophan fluorescence assay. Gαi1 and mGαi1 were expressed and purified as previously described (see materials and methods) without complications. **(Figure 2-6)**

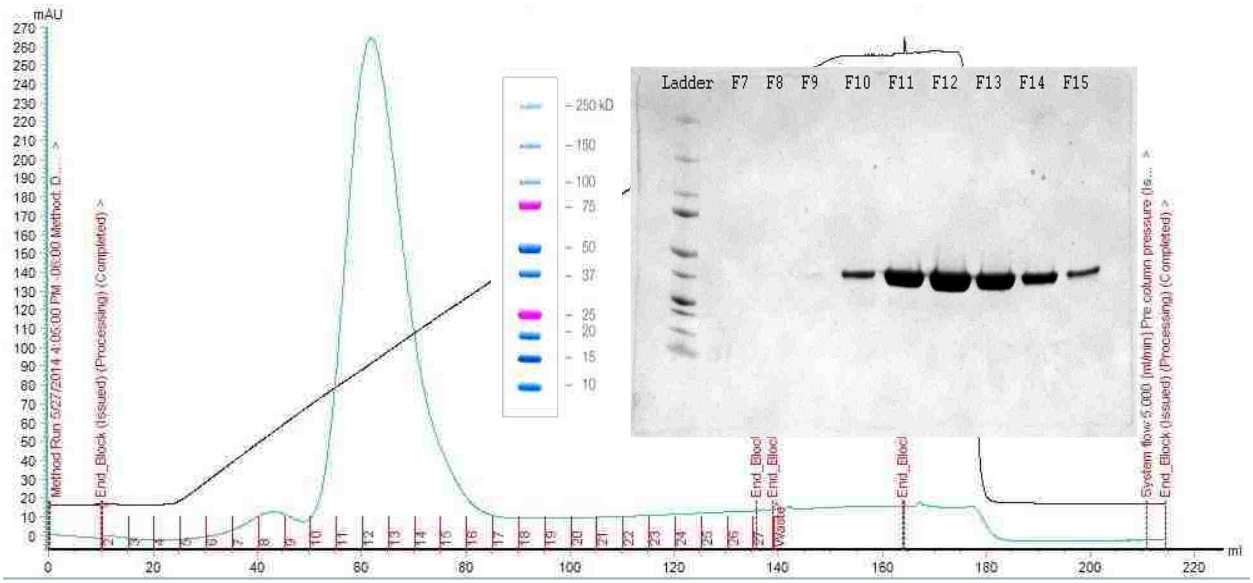

Figure 2-6 Anion exchange chromatography profile of mGαi1
Samples run on the SDS-PAGE **(inset)** correspond to fractions under the peak.

2.2.3 Thermal Stability of Secondary Structural Folds of Ric-8A Mutants

Using differential scanning fluorimetry as well as circular dichroism spectrometry, we found that most of the mutants were slightly destabilized. CD spectra of Ric-8A WT and mutants exhibited no noticeable difference in the initial scan, indicating similar secondary structural features (mainly α-helical) for all protein samples at 4°C, consistent with previous findings. (42, 48) **(Figure 2-7)** While wild type Ric-8A and mutants with wild-type-like GEF activities underwent cooperative denaturation at ~40 °C, a few mutants appeared to start precipitating heavily at that temperature. After unfolding, no significant refolding was observed after cooling the samples back to 4 °C, possibly due to the high upper temperature limit (90°C) since most mammalian proteins denature irreversibly at 90°C. Therefore, these CD experiments should be repeated using lower upper temperature limit (i.e. 60°C) to determine Ric-8A refolding capability. Nevertheless, we did not notice significant denaturation of any of the sixteen mutants during the tryptophan fluorescence assay, which was carried out at 25°C.

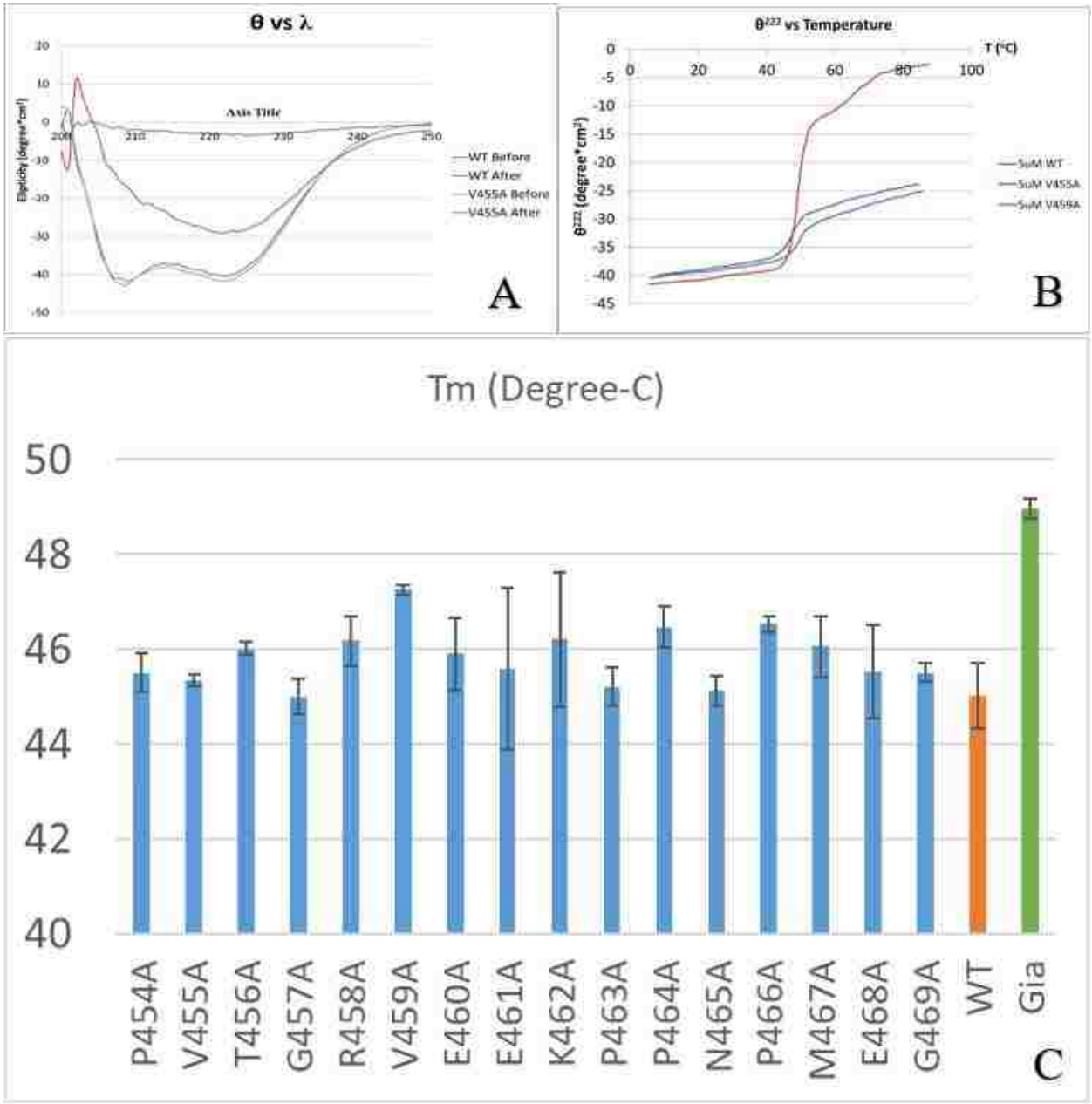

Figure 2-7 Heat denaturation of Ric-8A and Gαi1 using CD spectroscopy
(A) Full-wavelength scan from 200nm to 250nm of Ric-8A samples before and after heat denaturation. **(B)** Temperature course of ellipticity at 222nm of WT Ric-8A vs. mutant Ric-8A, showing a WT-like mutant (V459A) and a destabilized mutant (V455A). **(C)** Melting-temperatures (T_m) ensemble of all mutants of Ric-8A and Gαi1. Error bars represent the standard deviation among three replicates. See Materials and Methods for details.

All temperature denaturation experiments were performed in the buffer described in Materials and Methods section. The 1mM TCEP in the buffer interferes slightly with CD signal between

wavelengths 200nm – 205nm, however, it was not replaced with other reducing agents because the interference range does not affect the overall quality of CD spectrum or ellipticity signal at 222nm. TCEP is also the reducing agent used in the assay buffer for the tryptophan fluorescence assay, therefore, the CD spectra obtained describe closely the secondary structural properties of proteins used in the GEF assays. The noise level of some data sets deterred us from determining precisely the melting temperature of some samples (i.e. E461A, K462A); however, it is safe to conclude, at the level of secondary structure, that no Ric-8A sample was globally denatured during the nucleotide binding assays because all mutants were stable during the thermal denaturation experiments, CD or DSF **(Figure 2-8)**, up to ~30 °C with the majority remaining stable up to 35°C. Therefore, the effects on GEF activity that we observed from mutant Ric-8A's were largely due to either the loss of crucial protein-protein interaction elements or local, functional conformational change(s).

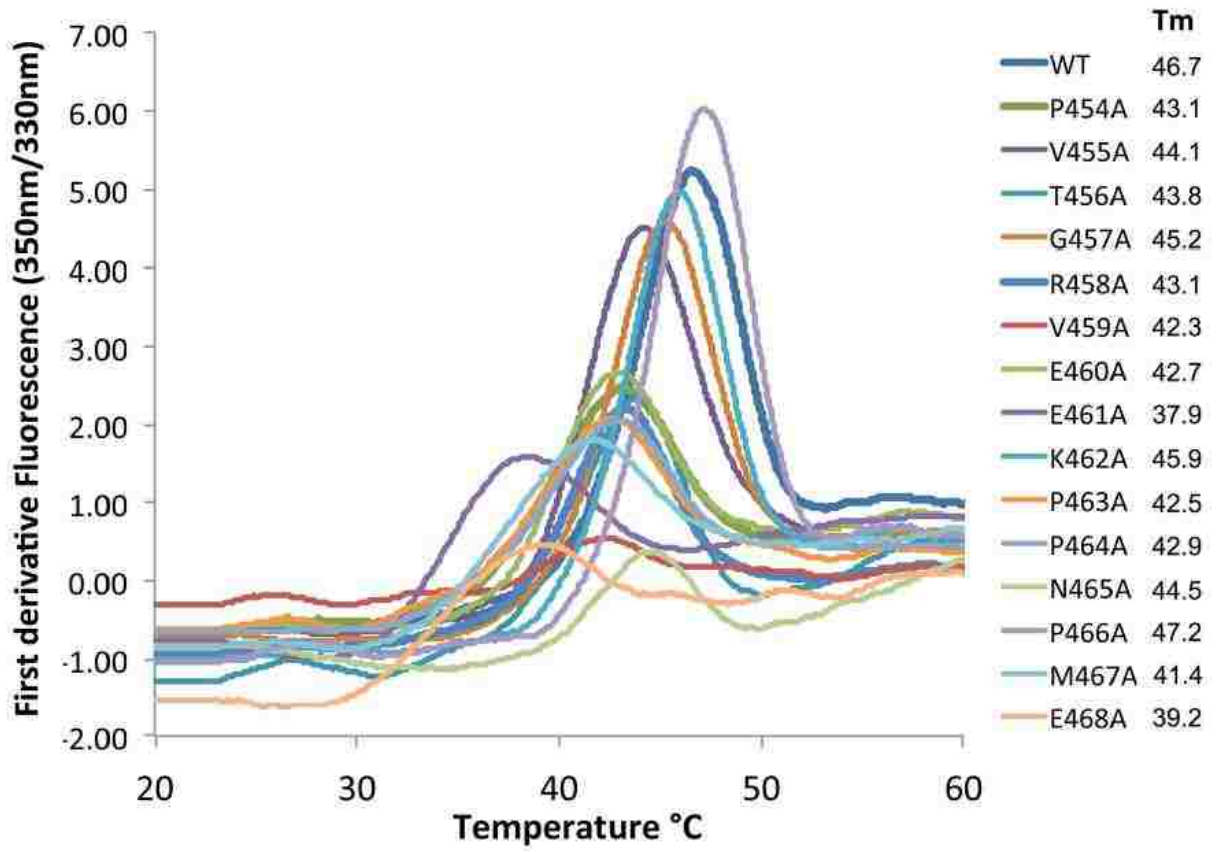

Figure 2-8 Differential scanning fluorimetry of Ric-8A and its mutants
See Materials and Methods for details. (10)

2.2.4 GEF Activity of Mutants Spanning Putative Binding Sequence

Now that all sixteen Ric-8A mutants were expressed, purified, and their thermal stability determined, it is safe to conclude that the alanine point mutations did not induce global structural perturbation on Ric-8A and the mutant proteins are suitable for functional assessments. Initially, I performed the "GTP-binding" tryptophan fluorescence assay using the unmodified Gαi1. I saw very mild effects for all mutants and was not able to draw any clear conclusion from the results. (data not shown)

After replacing unmodified Gαi1 with myristoylated Gαi1, the reduction of GEF activity in a few mutants became more pronounced and significant, compared to WT Ric-8A. **(Figure 2-9)**

Therefore, the tryptophan fluorescence assay results obtained with myristoylated Gαi1 were chosen as the primary data set and were triplicated to account for statistical variations and to ensure scientific rigor. Two alternative assay methods, which will be discussed in later sections, were attempted but the results were only used to validate the primary data set.

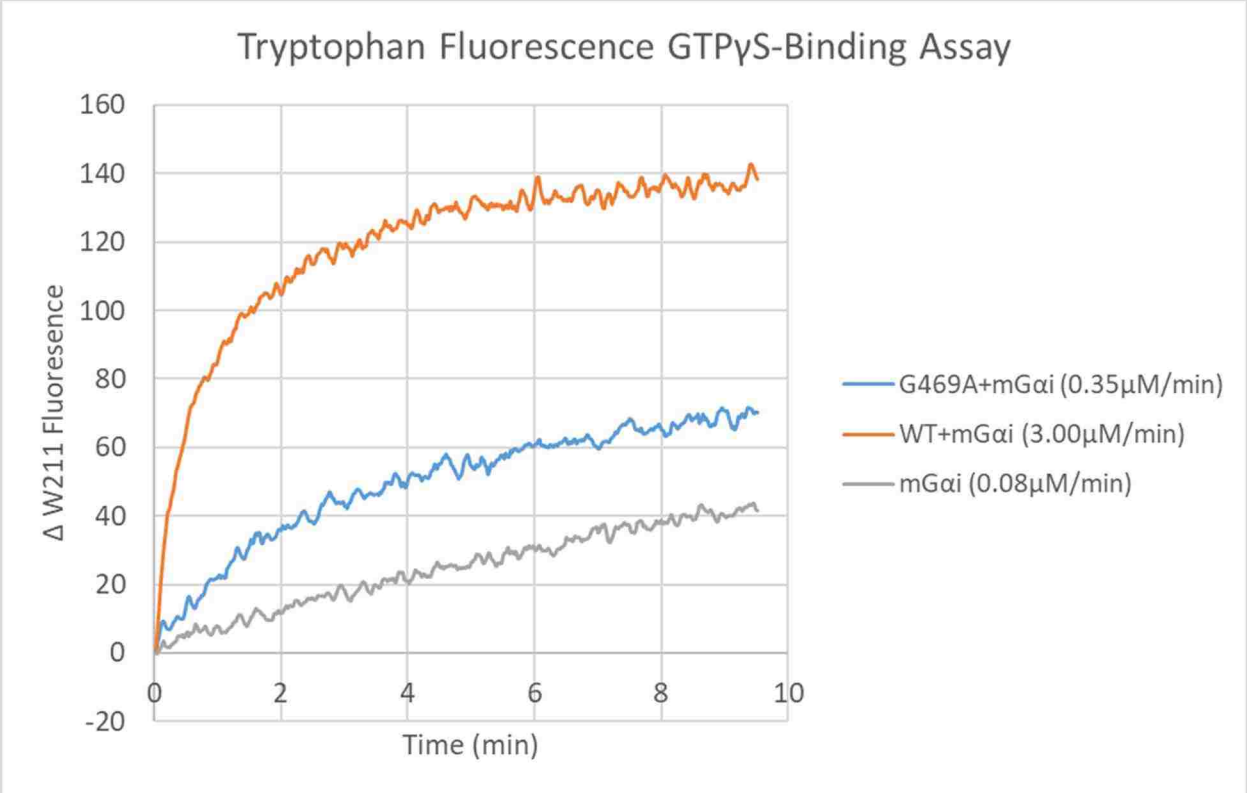

Figure 2-9 Typical mGαi1 GTPγS-binding assay time courses monitoring intrinsic tryptophan fluorescence change of residue W211 in mGαi1 upon nucleotide exchange. Initial rates of Ric-8A-stimulated or intrinsic GTPγS-binding are in parenthesis. 2μM of mGαi1 were allowed to form complex with buffer control (for intrinsic exchange rate) or 2μM of WT or G469A mutant Ric-8A 1-491 for five minutes and 20μM GTPγS was added to start the reaction. (See Materials & Methods for details.)

2.2.4a Tryptophan Fluorescence Assay

The alanine screen revealed several 'hotspots' for GEF activity, V455, T456, R458, P466 and G469. These Ric-8A mutants catalyze nucleotide exchange at a reduced initial rate corresponding to 12–20% that of WT Ric-8A. It is worth mentioning that comparable loss of

GEF activity was observed for Ric-8A 452, which does not contain the protected sequence at all. The Ric-8A 1-470 construct, which contains the putative Gαi1 binding site, showed partial recovery of GEF activity compared to the 1-452 construct (42); therefore, residues within the C-terminal segment from residue 471 to 491 might be involved in Ric-8A GEF activity or required for proper folding of 454-470. Alanine mutants at residues P454 and E468 exhibited significantly slower rates for the overall exchange reaction than for binding to the Gαi1:Ric-8A intermediate. Mutating these residues appears to favor GTPγS-binding to Gαi1:Ric-8A complex and possibly the release of Ric-8A. **(Figure 2-10, Table 2-1)**

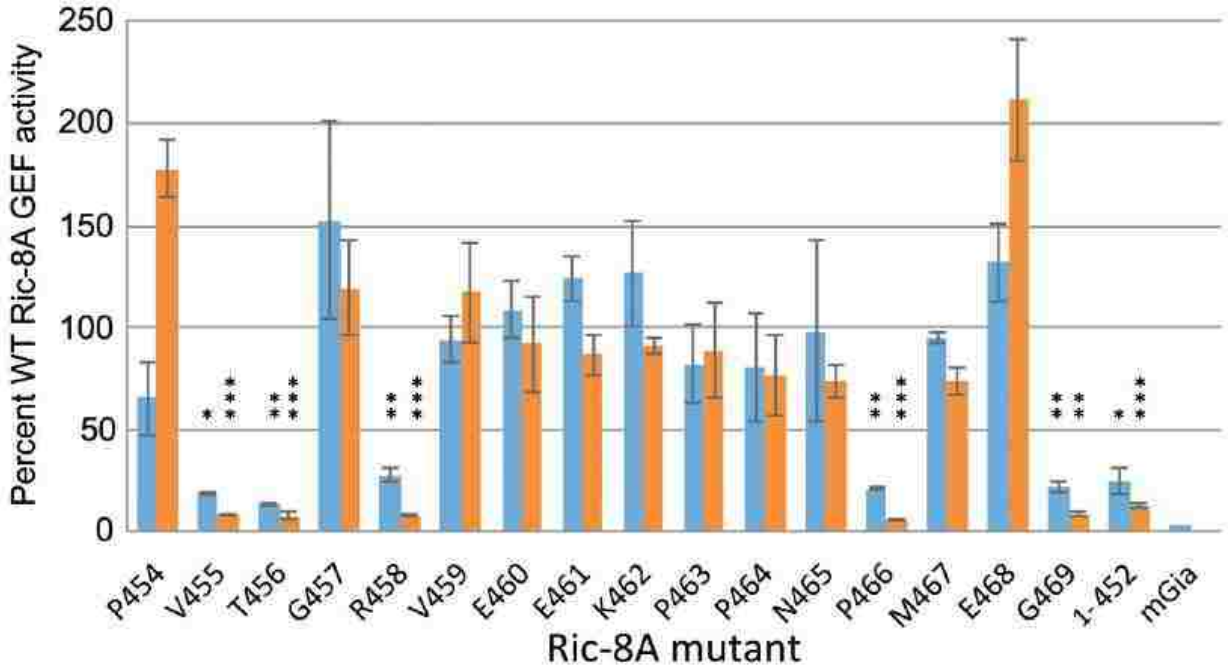

Figure 2-10 GEF activity of Ric-8A 1-491 point mutants expressed as percent of Ric-8A 491 WT activity
Blue bars ("nucleotide exchange" assays) represent the initial velocity of GDP to GTPγS exchange when Ric-8A (2μM) and GTPγS (20μM) were added simultaneously to mGαi1:GDP (2μM). Orange bars ("GTP-binding" assays) represent results of the nucleotide-binding reactions where GTPγS were added to pre-incubated, nucleotide-free mGαi1:Ric-8A (2μM) complexes. Error bars show standard deviation of three independent measurements. Asterisks above bars indicate significance of the differences: *p<0.01; **p<0.005; ***p<0.001. (10)

Ric-8A mutant	v_1* (μM/min)	v_2 (μM/min)
WT	3.84 (1.45)	4.66 (1.38)
P454A	2.88 (0.80)	5.39 (0.43)
V455A	0.82 (0.05)	0.25 (0.01)
T456A	0.59 (0.04)	0.24 (0.06)
G457A	3.47 (1.11)	6.02 (1.19)
R458A	0.63 (0.07)	0.37 (0.03
V459A	5.65 (0.68)	6.85 (1.44)
E460A	6.54 (0.83)	5.36 (1.39)
E461A	7.45 (0.65)	5.06 (0.59)
K462A	4.46 (0.92)	5.15 (0.24)
P463A	2.90 (0.69)	4.78 (1.26)
P464A	2.83 (0.94)	4.73 (1.21)
N465A	2.25 (1.03)	4.56 (0.51)
P466A	0.47 (0.01)	0.34 (0.02)
M467A	2.17 (0.06)	4.57 (0.44)
E468A	3.82 (0.55)	6.23 (0.88)
G469A	0.63 (0.08)	0.26 (0.05)
(1-452)Ric-8A	0.86 (0.22)	0.39 (0.03)

Table 2-1 Initial velocities of Ric-8A mutant guanine nucleotide exchange activity
Assays were conducted as described in Materials& Methods section. For measurement of v_1, reaction buffer (50 mM HEPES pH 8.0, 150 mM NaCl, 10 mM $MgCl_2$, and 1 mM TCEP) at 25 °C contained 2 μM mGαi1:GDP, 2 μM Ric-8A and 20 μM GTPγS (initial concentration); for measurement of v_2, 2 μM mGαi1:GDP, 2 μM Ric-8A were incubated for 5 minutes before addition of 20 μM GTPγS.
*v_1 for the reaction: mGαi1:GDP + GTPγS + Ric-8A → mGαi1:GTPγS + Ric-8A + GDP;
v_2 for the reaction: mGαi1:Ric-8A + GTPγS → mGαi1:GTPγS + Ric-8A;
Values in parentheses are the standard deviation for three independent experiments. (10)

The experimental method we adopted presents uncertainties from various sources including, but not limited to temperature, sample integrity (i.e. effective concentration of proteins), and incubation time. For example, the rate of Ric-8A activated nucleotide exchange varies with reaction temperature, the temperature of Ric-8A samples right before adding to the reaction, the age of samples (i.e. time samples spent in gel-filtration buffer before experiments), the time Ric-8A is allowed to react with Gαi1:GDP before GTPγS joins the reaction. We control for most of these factors by controlling reaction temperature and timing crucial steps of the reaction. Mostly

importantly, each mutant Ric-8A GEF activity was reported as ratios of rates catalyzed by the mutant and WT Ric-8A, which were both purified by size-exclusion chromatography the same day.

Variations among experiments decrease significantly when properly controlled. However, the initial mixing stage of the experiments appears to be the most error-prone stage among all others. This is most noticeable for fast initial binding rates. Therefore, a stopped-flow approach to assay exchange activity for the same set of mutants might help resolve the issue. Regardless, the data we collected is quite clear in determining activity knockdowns in Ric-8A mutants V455A, T456A, R458A, P466A, G469A, as well as the truncated 1-452 construct. The apparent gain of function in certain mutants requires more careful assessment with lower GEF concentrations or stopped-flow experiments to confirm.

Based on the alanine screen result, a few binding "hotspots" were proposed on the Ric-8A C-terminal region. Three residues were selected for a round of double alanine mutational study, E460, P466, and M467. We selected E460 and M467 because they were either mildly inhibitory or not inhibitory when mutated individually **(Figure 2-10)** and we were interested to see what would happen in a double alanine mutation at the two residues. P466 was selected because we know that proline residues usually do not make direct protein-protein contacts so mutating the proline to an alanine might have disrupted the Ric-8A structure locally to produce the inhibitory effect **(Figure 2-10)**. If both double mutants of P466A with E460A and M467A exhibit the same level of reduction in GEF activity as P466A single mutant, we can postulate that P466 is a structural element crucial for GEF activity of Ric-8A. Three double mutant plasmids,

E460A+P466A, P466A+M467A, and E460A + M467A, were generated using the same mutagenesis method described for single mutants. All double mutant proteins expressed but only two, E460A+M467A and P466A+M467A were purified adequately with the purification protocol optimized for single mutants. Alongside the double mutants, three charge-reversal or charge-addition single mutant plasmids, E460R, E460K, and M467E, were generated. By reverting the charge on E460, we hope to see more pronounced changes to the GEF activity than what we saw for the E460A mutant **(Figure 2-10)** if it forms ionic interaction with a positively charged residue on Gαi1. By replacing M467 with a glutamate, we introduced a negative charge at the position without changing the size of the side-chain. E460R and M467E expressed well and could be purified; but to my surprise, E460K aggregated heavily.

The mutants described above that were expressed and purified (E460A+M467A, P466A+M467A, E460R and M467E) were assayed for their GEF activity towards Gαi1 W258A, not mGαi1. The "GTP-binding" tryptophan fluorescence assays for these mutants were each performed once, therefore, the result is still preliminary and qualitative. **(Figure 2-11)** Since un-myristoylated Gαi1 was used instead of mGαi1, the single alanine mutants (E460A, P466A, and M467A) were assayed alongside for comparison. At first glance, the E460R, charge reversal mutant regained a portion of its lost GEF activity from E460A, suggesting that the glutamate residue might simply serve as a "space filler" and not participate in salt-bridge formation with basic side-chain(s). Similar comments can be made for M467E mutant since the substitution of an acidic side-chain for a neutral residue returned the GEF activity to near WT level from M467A level. The E460A+M467A double mutant, received from the mutations mild additive effect on its GEF activity, as expected. The P466A+M467A double mutant, on the other hand,

not only fully rescued the activity reduction observed for each single mutant but is a mild gain-of-function mutant by being slightly more active than WT protein. **(Figure 2-11)** These double alanine mutants and charge-reversal/addition mutants need to be assayed more carefully using mGαi1 in order to draw clear conclusions about the effects of mutations.

In conclusion, the tryptophan fluorescence assay results confirmed that the C-terminal region of Ric-8A (454-470), which was predicted to adopt a random coil secondary structure but is highly protected from HDX in the Ric-8A:Gαi1 complex, is an important peptide segment for interaction with Gαi1 and possibly comprises crucial structural elements for the GEF function of full-length Ric-8A.

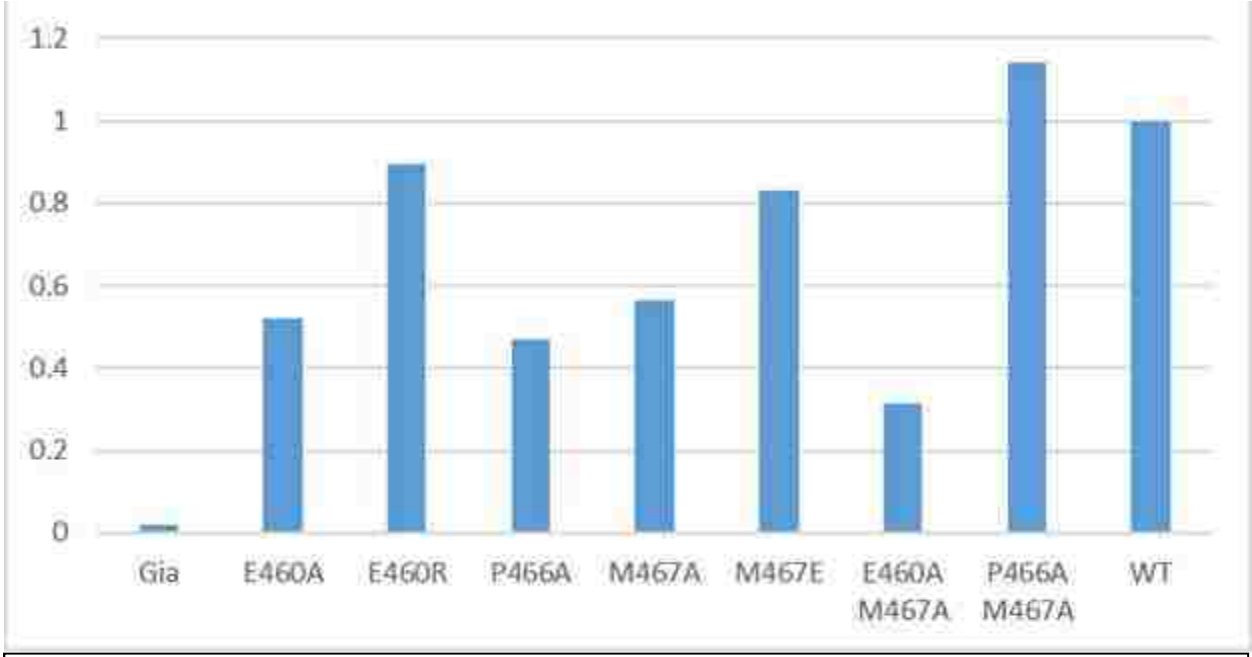

Figure 2-11 GEF activity of additional Ric-8A 1-491 mutants expressed as fraction of Ric-8A 491 WT activity using the "GTP-binding" tryptophan fluorescence assay. 2μM of Gαi1 were allowed to form complex with buffer control or 2μM of WT or mutant Ric-8A 1-491 for five minutes and 20μM GTPγS was added to start the reaction.

2.2.4b Alternative Approach-I: Filter-binding Assay with γ^{35}S-GTPγS

Although the assay method adapted here was established long ago (104), there are limitations to the tryptophan fluorescence GTPγS binding assay. For instance, the signal generated from emitting tryptophan residues is protein concentration dependent, but the major source of noise is background signal fluctuation from solution agitation and spectrometer optics, therefore, absolute noise level is almost constant for all concentrations of sample; the overall signal observed reflects the changes mainly in the fluorescence environment of W211 on switch II, which becomes ordered upon GTPγS binding, but is not a direct measurement of nucleotide-binding to Gαi1. When I attempted to perform a Gαi1:GDP concentration-dependent assay at a fixed concentration of Ric-8A to tease out kinetic parameters such as K_M and V_{max} for the nucleotide exchange reaction catalyst, Ric-8A, the results were too noisy to be interpretable at low Gαi1 concentrations (<0.5 μM) due to the Gαi1 concentration-dependent signal:noise ratio. Therefore, I attempted another well-established assay, which uses the isotope labelled nucleotide, γ^{35}S-GTPγS, as the substrate. (106)

The isotope assay involves spotting nucleotide-bound protein onto BA85 nitrocellulose membrane (Millipore Sigma) and washing the membrane so only protein:nucleotide complex bound to the membrane is counted under a scintillation counter(106). With the help of Suneela Ramineni from Prof. John Hepler's lab at Emory University, the protocol was modified for the filter-binding assay for WT Ric-8A and Gαi1. The original filter-binding assay protocol from the Hepler lab was designed for assaying inhibition of GDP-release from Gα by GDIs, which do not require NaCl for solubility in solution. For no obvious reason(s), addition of either 150mM NaCl or 0.01% E10C12 into the reaction buffer (50mM Tris pH 8.0, 1mM DTT, 1mM EDTA, 10mM $MgSO_4$) interfered with retainment of isotopes on the nitrocellulose filter discs. Therefore, the detergent (E10C12) as well as NaCl were both omitted from the reaction buffer so the assay can be performed without technical issues.

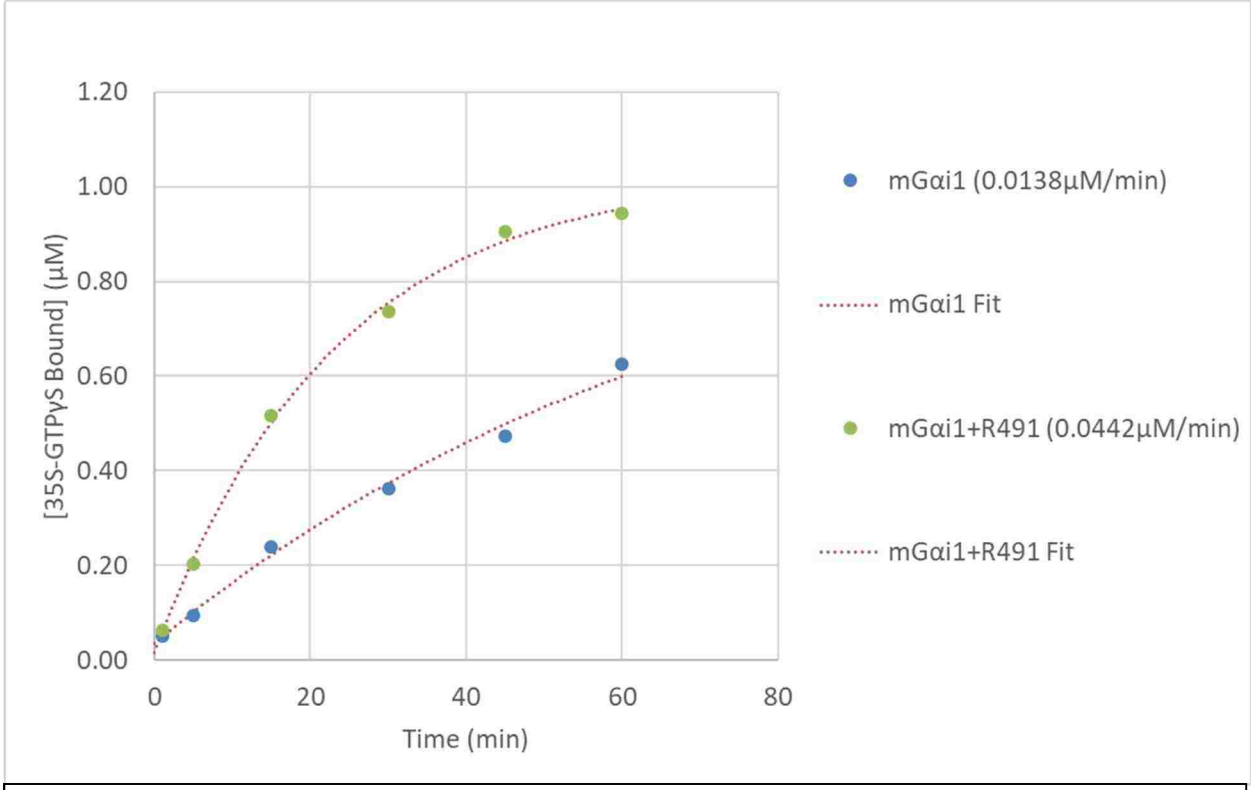

Figure 2-12 Filter-binding assay using γ-^{35}S-GTPγS as non-hydrolysable GTP analog
1.25μM of mGαi1 were added to 0.5μM Ric-8A 491 WT and 2μM GTPγS doped with (2000cpm/pmol) γ^{35}S-GTPγS in reaction buffer (50mM Tris pH 8.0, 1mM DTT, 1mM EDTA, 10mM $MgSO_4$) and multiple time points (1, 5, 15, 30, 45, 60-minutes) were taken. Initial rates of γ^{35}S-GTPγS-binding are in parenthesis. Red dotted-lines represent the single-exponential rise-to-maxima fit of the data points as described in section 2.3.4.

The assay system with γ^{35}S-GTPγS worked reasonably well for WT Ric-8A, however, the changes made to the reaction buffer composition rendered the assay unsuitable for many mutants of Ric-8A due to the absence of NaCl in the reaction buffer. Therefore, the result of the isotope assay shown here **(Figure 2-12)** could only serve as a direct proof that the fluorescence signal change observed in the tryptophan fluorescence GTPγS-binding assays correlates with GTPγS binding. The isotope assay protocol needs to be further modified in order to be applicable to the unstable Ric-8A mutants.

2.2.4c Alternative Approach-II: FRET Assay with MANT-GTPγS

I have also attempted to perform the nucleotide-binding assay using Förster resonance energy transfer (FRET). The FRET experiment is a more direct measurement of nucleotide-binding to mGαi1 than the

tryptophan fluorescence assay because the FRET efficiency will only be high enough for measurable signal to be generated if the donor and acceptor come in close proximity, as in the case of a nucleotide binding event. The fluorescence signal is emitted from the nucleotide analog, MANT-GTPγS, instead of mGαi1; therefore, the protein samples used in the reaction contribute less to the background FRET signal. In the contrary, all protein samples in the reaction mixture emit photons at 350nm when excited at 295nm in the tryptophan fluorescence assay; therefore, for the "nucleotide exchange" assays, background fluorescence should be measured by running proper negative controls and subtracted from raw data. **(Figure 2-13)**

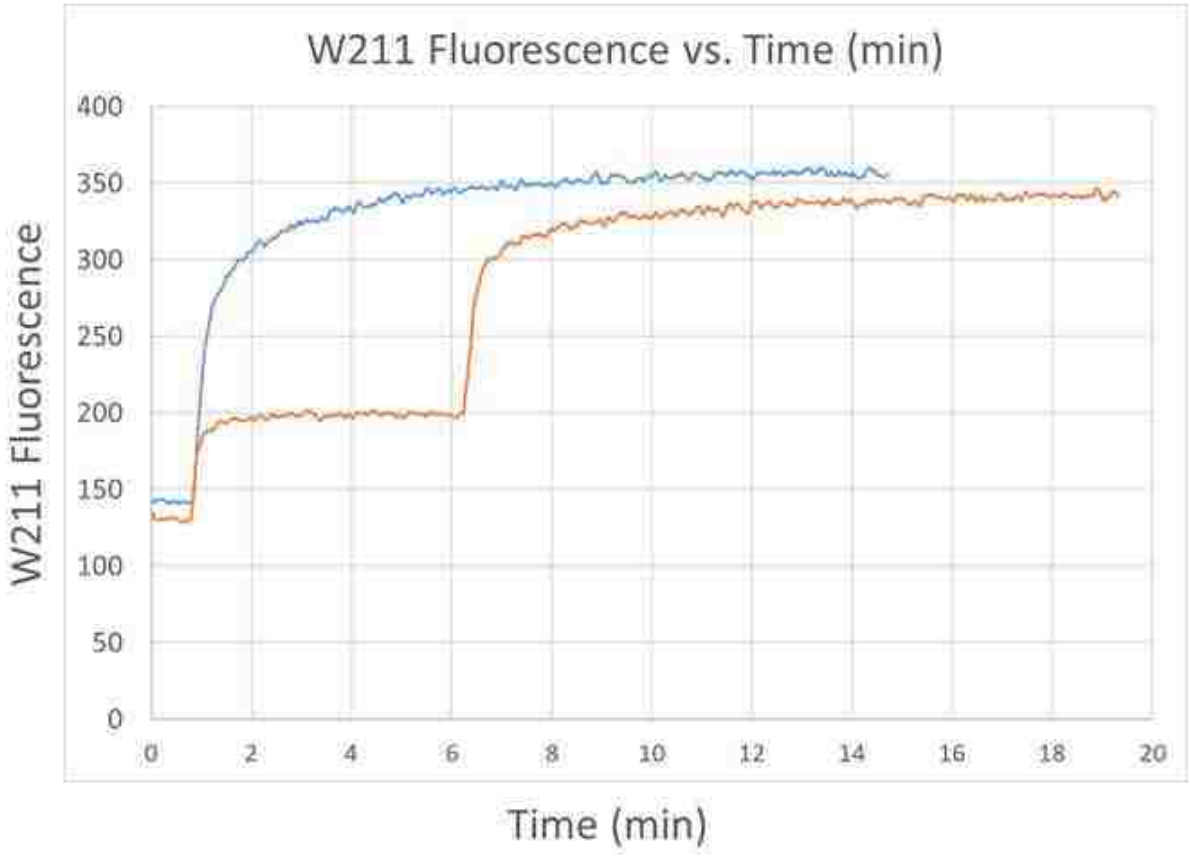

Figure 2-13 A comparison of raw data between "GTP-binding" assay and "nucleotide exchange" assay
The orange curve consists of three segments, 0 to 1 minute (2 μM mGαi1), 1 to 6 minutes (2 μM mGαi1 + 2 μM Ric-8A), and 6 to 19 minutes (2 μM mGαi1 + 2 μM Ric-8A + 20 μM GTPγS). The blue curve consists of two segments, 0 to 1 minute (2 μM mGαi1), and 1 to 15 minutes (2 μM mGαi1 + 2 μM Ric-8A+20 μM GTPγS)
Addition of protein samples (mGαi1 and Ric-8A) increases tryptophan fluorescence; therefore, a time course for a negative control (2 μM mGαi1 + 2 μM Ric-8A + 0 μM GTPγS) was measured for, and subtracted from, each "nucleotide exchange" assay.

Unfortunately, the FRET data set was not complete due to unknown complications with the R458A mutant, which was not an issue for the tryptophan fluorescence assays. In addition, the MANT-labelled substrate appears to bind mGαi1 with different binding affinity than GTPγS possibly due to the MANT group. Therefore, the MANT FRET data set was only used to compare with the tryptophan fluorescence results, which used GTPγS as the GTP analog, and was not published.

Qualitatively, the FRET assays arrived at the same conclusion as the tryptophan fluorescence assays regarding the GEF activities of Ric-8A mutants. **(Figure 2-14, 2-15, and blue bars in Figure 2-10)** For the functionally knocked-down, WT-like, and apparent gain-of-function mutants (P454A, G457A, V459A, E460A, E461A, K462A, P463A, P464A, N465A, M467A, and E468A), the FRET assay results do not always agree quantitatively with the tryptophan fluorescence assay results but the general trend of GEF activity changes caused by alanine point mutations is still clear because V455A, T456A, P466A, and G469A all exhibited severely (>75%) reduced/knocked-out GEF activities towards mGαi1 compared to WT Ric-8A, as observed by the tryptophan fluorescence assays.

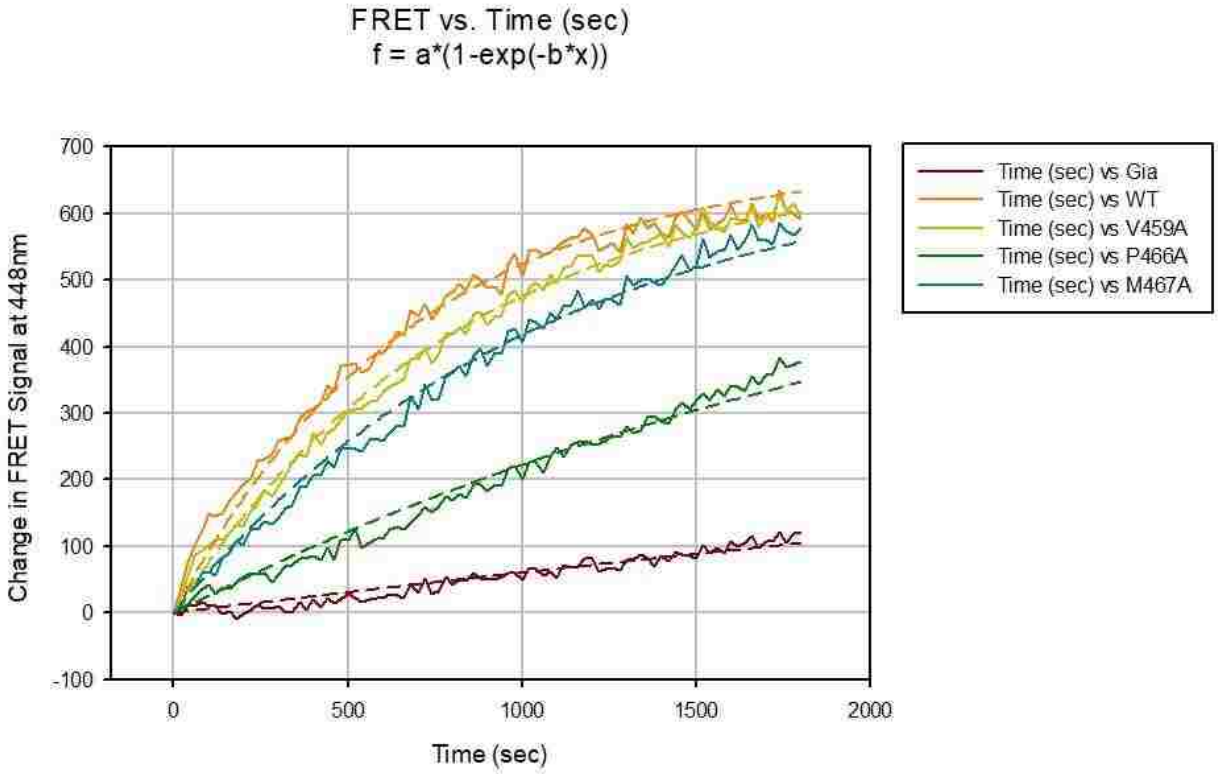

Figure 2-14 Examples of MANT-GTPγS binding curves
Each reaction mix was excited at 295 nm (tryptophan excitation wavelength) and emission recorded at 448 nm (MANT emission wavelength). 1μM Ric-8A and 5μM MANT-GTPγS were added simultaneously to 1μM mGαi1:GDP to start the reaction ("nucleotide exchange" assays).

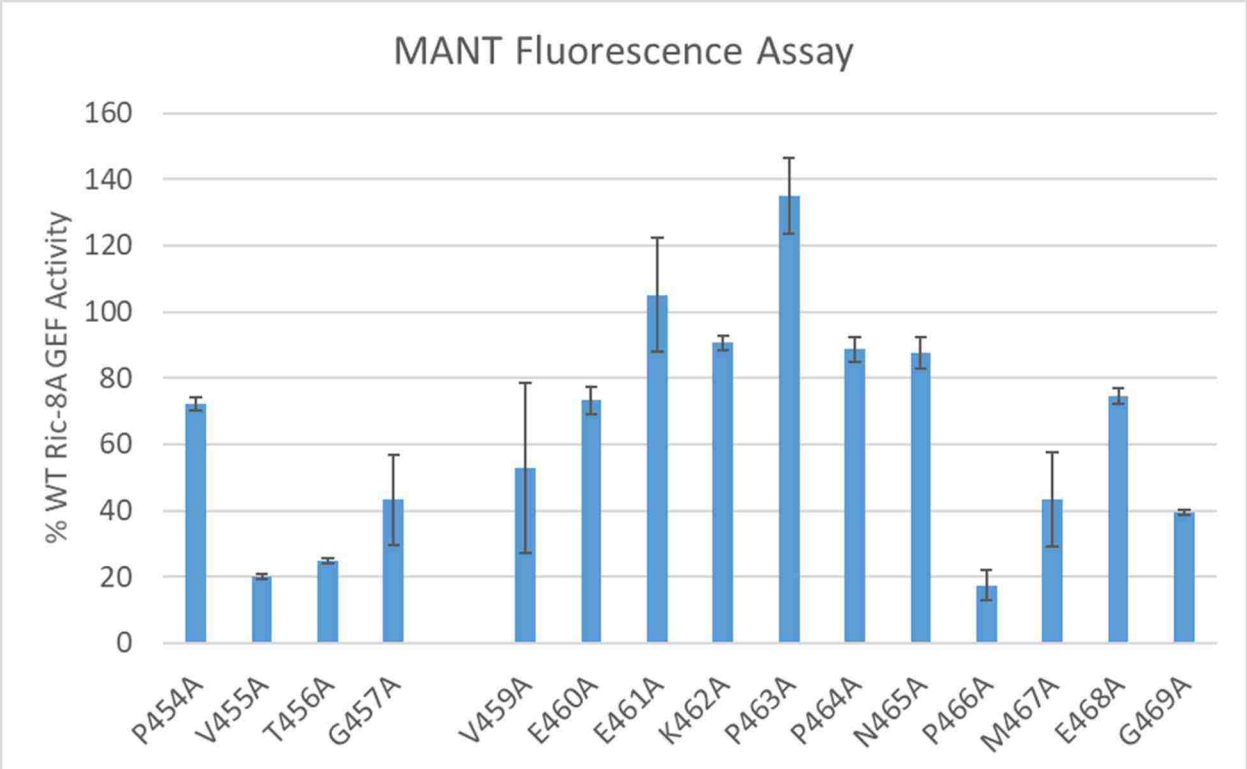

Figure 2-15 GEF activity of the same set of Ric-8A mutants using MANT-GTPγS-binding assay method

Nucleotide binding is more directly assessed since FRET efficiency would be too low to detect if the MANT group is not within maximum FRET distance to residue W211 on switch II of Gαi1. Error bars represent the standard deviation among three replicates.

Ric-8A Mutant	W.F. Ratio	W.F. Error	MANT Ratio	MANT Error
P454A	65.2	18.0	72.3	1.9
V455A	18.6	1.1	20.0	0.7
T456A	13.4	0.9	24.9	0.9
G457A	152.2	48.5	43.2	13.7
R458A	27.7	3.3	No Data	No Data
V459A	93.7	11.3	52.9	25.8
E460A	108.5	13.8	73.2	4.0
E461A	123.6	10.8	105.1	17.0
K462A	126.6	26.1	90.7	2.1
P463A	81.9	19.4	135.1	11.4
P464A	79.9	26.6	88.7	3.6
N465A	98.0	44.8	87.8	4.7
P466A	20.6	0.6	17.5	4.6
M467A	94.6	2.7	43.2	14.2
E468A	131.6	19.0	74.4	2.4
G469A	21.8	2.7	39.4	0.8
Ric-8A 452	24.5	6.2	No Data	No Data

Table 2-2 Comparison of "nucleotide exchange" assay results from tryptophan fluorescence assays and FRET assays
Data from **Figure 2-10** (blue bars) are compared with data from **Figure 2-15**. GEF activities of Ric-8A mutants are normalized and expressed in percent WT Ric-8A initial GTPγS **(W.F. Ratio)** or MANT-GTPγS **(MANT Ratio)** binding rate determined the same day. Errors represent standard deviation of three independent measurements.

2.2.5 Size-exclusion Chromatography to Assess Ric-8A:Gαi1 Complex Formation

The original hypothesis states that making single mutations along the Ric-8A sequence 454-470 hinders Ric-8A Gαi1 interaction. Since WT Ric-8A forms a stable heterodimeric complex with Gαi1 and the

complex almost does not dissociate once formed, we consistently isolate nucleotide-free Ric-8A:Gαi1 complex using size-exclusion chromatography (SEC).

The nature of the activity knockdowns is not completely characterized by the nucleotide exchange assays. By running incubated protein complex on an SEC column, we made preliminary, qualitative assessment on the ability of mutants to form complexes with Gαi1. Although some of the activity knock-out mutants also showed defects in complex-formation, the size exclusion chromatography results of the incubated product of Gαi1:GDP and Ric-8A mutants did not always agree with the nucleotide-binding assay results. (i.e. Knock-down Ric-8A mutants were not always deficient in forming complex with Gαi1) For example, G469A mutant forms Gαi1 complex just like WT Ric-8A while M467A mutant showed significantly decreased complex-formation while catalyzing nucleotide exchange similar to WT Ric-8A. **(Figure 2-16)**

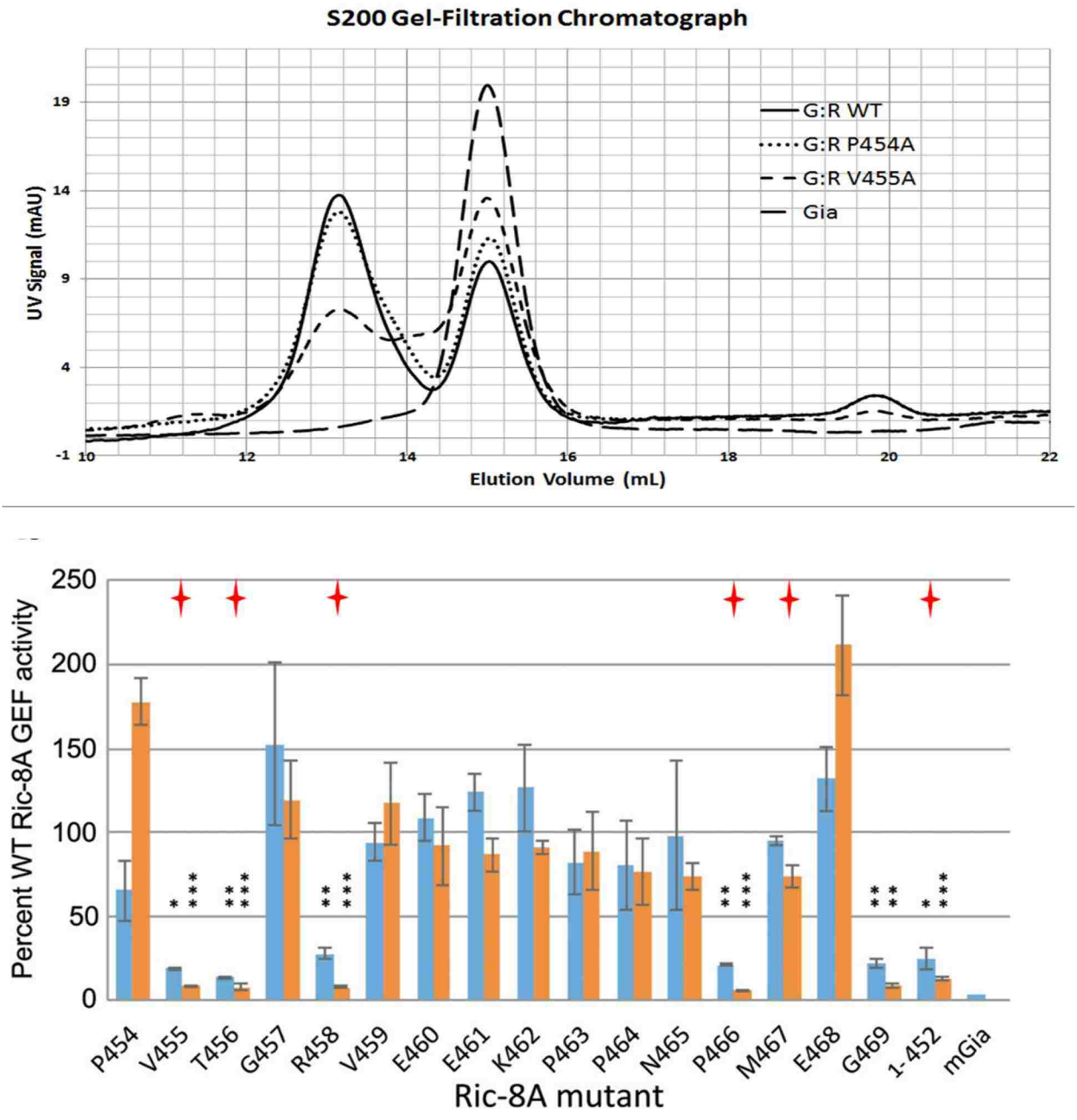

Figure 2-16 Size-exclusion chromatography to assess Ric-8A:Gαi1 complex formation
(Top) Gel-filtration traces showing the extent of complex-formation for WT or mutant Ric-8A with Gαi1. Samples of purified Gαi1 W258A and Ric-8A mutants and WT were gel-filtered separately before mixing. 5μM of Gαi1 and Ric-8A were mixed and incubated on ice for 1-2 hours before injecting into an S200 gel-filtration column for separation. Peaks at 13.2mL, 14.1mL, 15mL, and 19.8mL are identified by SDS-PAGE as Ric-8A:Gai1 complex, free Ric-8A, Gαi1, and GDP, respectively. **(Bottom)** Red stars mark mutants of Ric-8A that show deficiency in forming complex with Gαi1. (10)

2.2.6 Ric-8A 454-470 peptide and Ric-8A 399-491

The synthetic Ric-8A C-terminal peptide (up to 0.5 mM) does not appear to inhibit Gαi1:Ric-8A binding interaction significantly based on the pull-down result. On the other hand, the competitive inhibition activity can be small if 454-470 is not the only Gαi1 binding site. As reflected on the tryptophan fluorescence assay result using GST-Ric-8A 399-491 as an alternative competitive inhibitor, I observed (a) no GEF activity from the construct and (b) relatively mild inhibition effect. Taken together, the C-terminal region of Ric-8A might still be an important Gαi1 binding site, however, definitely not the only one. **(Figure 2-17, Figure 2-18)**

Figure 2-17 Pull-down assay result showing no obvious peptide competition for Gαi1 binding

---Gel Lane---

1. 100 µM peptide, Gαi1, buffer
2. 0 µM peptide, Gαi1, Ric-8A
3. 10 µM peptide, Gαi1, Ric-8A
4. 50 µM peptide, Gαi1, Ric-8A
5. 100 µM peptide, Gαi1, Ric-8A
6. 500 µM peptide, Gαi1, Ric-8A
7. ladder
8. Ric-8A loading
9. Gαi1 loading
10. Lane 6 IMAC Flow-through

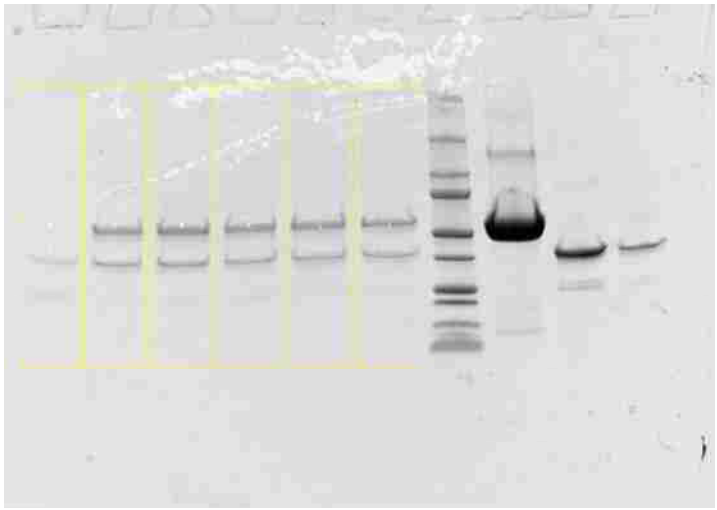

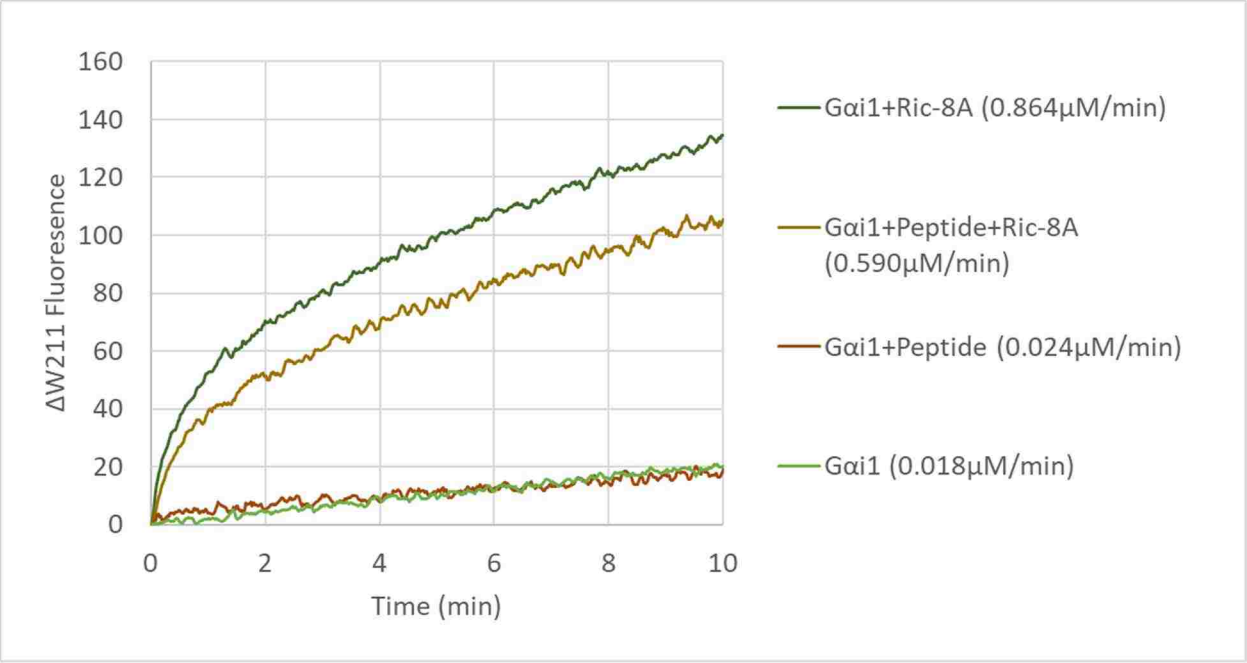

Figure 2-18 Tryptophan fluorescence GTPγS-binding assay showing minimal inhibition of Ric-8A GEF activity by GST-Ric-8A 399-491

2μM of Gαi1 W258A was preincubated with 2μM of GST-Ric-8A 399-491 or buffer negative control for 15min at room temperature with stirring. Then 2μM of His-Ric-8A 1-491 or buffer negative control were added to the mixture and incubated for 5 minutes before the addition of 20μM GTPγS to start the binding experiments.

2.3 Materials & Methods

2.3.1 Mutagenesis, Protein Expression and Purification

The W258A mutant of rat Gαi1, encoded in a Gateway pDEST15 vector (Thermo Fisher Scientific, Waltham, MA), was expressed as a tobacco etch virus protease (TEV)-cleavable, N-terminal glutathione-S-transferase (GST) fusion protein and purified as described (52). GST-fusion construct of Ric-8A 399-491 was expressed and purified using a protocol similar to that of Gαi1 W258A.

Myristoylated Gαi1, which will be referred as mGαi1 for simplicity, was expressed and purified as previously described(71, 96). Briefly, internally hexa-histidine tagged rat Gαi1 construct in pQE60 expression vector(71) was co-expressed in JM109 *E. coli* cells with yeast N-myristoyltransferase in pBB131 vector(96). Cells were grown in T7 media at 37ºC and induced at $O.D._{600}$ = 0.40 with 30 µM Isopropyl β-D-1-thiogalactopyranoside (IPTG) overnight at 30ºC. After cell lysis using an EmulsiFlex-C5 cell disruptor (Avestin) in lysis buffer (50mM Tris pH 8.0, 100mM NaCl, 5mM β-mercaptoethanol, 10µM GDP, 2mM phenylmethane sulfonyl fluoride (PMSF)) and clarification of lysate by centrifugation at 18,000 rpm in an SS34 rotor (Sorvall) for 1 hour at 4ºC, His-tagged mGαi1 was isolated from the soluble faction by a gravity Nickel nitrilotriacetic acid (NTA) (Qiagen) column and eluted with elution buffer (50mM Tris pH 8.0, 100mM NaCl, 5mM β-mercaptoethanol, 10µM GDP, 2mM PMSF, 150mM imidazole). The imidazole and NaCl were removed by dialysis (50mM Tris pH 8.0, 2mM dithiothreitol) and protein was further purified by loading onto a HiTrap Q Sepharose FF column (GE Healthcare)

and eluted with a NaCl gradient (0mM to 500mM) on an AKTA Pure FPLC system (GE Healthcare); mGαi1 elutes near 150mM salt.

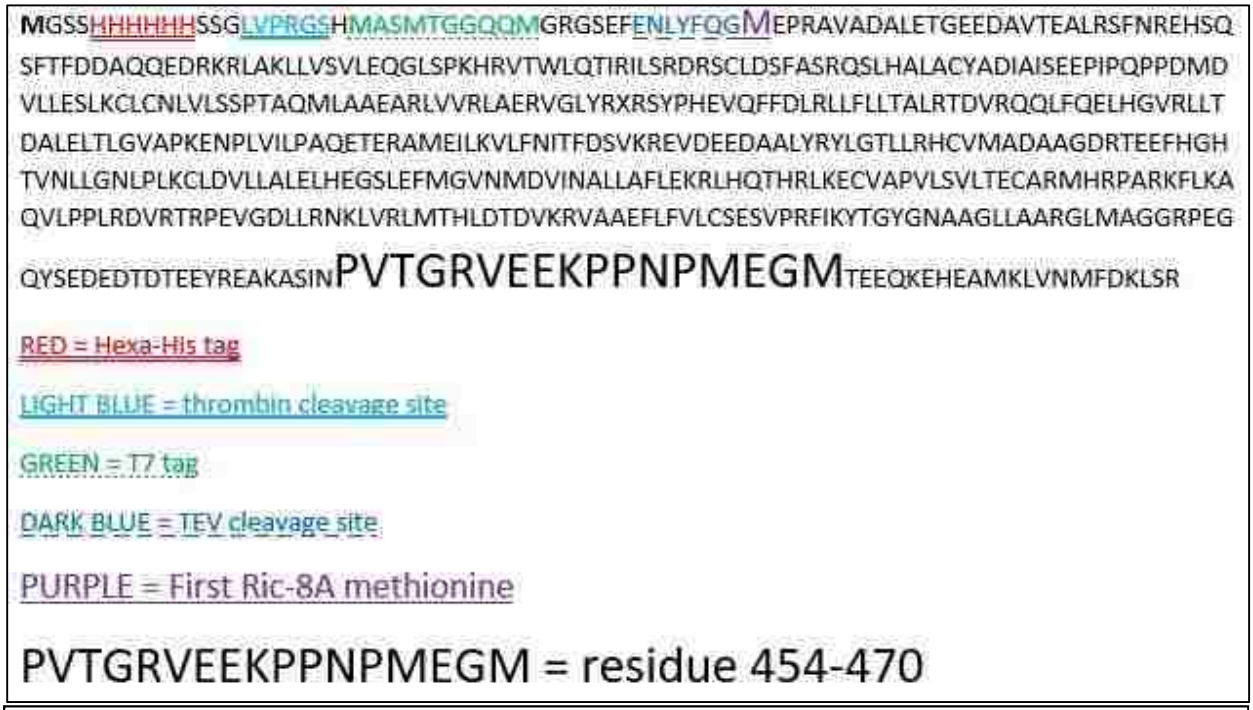

Figure 2-19 Amino acid sequence of His-tagged Ric-8A 1-491 construct in pET28a vector

The original WT plasmid that encodes the amino acid sequence of rat Ric-8A 1-491 in pET28a vector expresses an N-terminally hexa-histidine tagged protein(42) **(Figure 2-19)**. Mutants of Ric-8A were generated from the WT plasmid by using the QuikChange II XL kit (Agilent Technologies). Mutagenesis primers were designed using the QuikChange® Primer Design Program(Agilent Technologies) and purchased as synthesized, lyophilized oligos from IDT (Integrated DNA Technologies). The resulting mutant plasmids of Ric-8A 1-491 were sent for sequencing to Eurofins Operon. Sequencing results were compared to wild-type (WT) rat Ric-8A sequence in the NCBI online database using protein BLAST(NCBI).

WT and alanine single-mutant Ric-8A 1-491 proteins were expressed and purified as described previously (42) with some alterations. We used either an Avestin cell disruptor or the combination of lysozyme and DNase I to lyse cells expressing stable Ric-8A mutants or less soluble mutants, respectively. After the first step of fractionation (centrifugation of lysate) in lysis buffer (50mM Tris, pH 8.0; 250mM NaCl; 5% Glycerol; 2mM β-mercaptoethanol; 2mM PMSF), the supernatant, which contains soluble fraction of cells, was incubated for 15 minutes at 4ºC with Profinity Immobilized Metal Affinity Chromatography (IMAC) resin (Bio-Rad) in suspension with constant, gentle rocking in a flat-bottom glass culture flask. The lysate/resin mixture was poured into an empty glass gravity column (Bio-Rad) and the lysate was usually allowed to elute by gravity. For Ric-8A mutants that aggregated heavily during this step of the purification, the incubation time was reduced to 2-5 minutes and lysate was then forced to drain out by applying positive pressure to the glass column. By doing so, we suffered a loss of total yield due to shorter lysate-resin contact time but regained ability to purify less soluble proteins without heavily congesting the IMAC column with protein aggregates. After extensive wash with lysis buffer, the target proteins were eluted from the IMAC column by elution buffer (50mM Tris, pH 8.0; 250mM NaCl; 5% Glycerol; 2mM β-mercaptoethanol; 2mM PMSF; 300mM Imidazole) and immediately dialyzed in dialysis buffer, which is also Q-column buffer-A (50mM Tris pH 8.0, 5mM β-mercaptoethanol) to remove the imidazole. In certain cases, 5% glycerol and 50mM NaCl were added to the dialysis buffer to stabilize the protein for long-term storage or subsequent anion exchange chromatography purification. From this point on, all Ric-8A mutant proteins stayed soluble even at high concentrations (5 - 10 mg/mL). The dialyzed protein was then loaded onto a HiTrap Q XL anion exchange column (GE Healthcare) and eluted

with a NaCl gradient (0mM to 500mM). Ric-8A eluted at about 200mM NaCl and is already at high purity after elution from anion exchange column.

Expression, and purification steps of Ric-8A truncation mutants, R452 and R470, were similar to those of Ric-8A 1-491 and discussed in more detail in Chapter III, "Ric-8A Crystal Structure". The only difference is that the R452 and R470 samples used in this chapter were still His-tagged while proteins used for crystallization were tag-less, therefore, no TEV protease digestion was performed for any Ric-8A constructs used for experiments described in this Chapter. (See Chapter III for information about removing His-tag)

A final polishing step using a Superdex 200 10/300 GL size-exclusion chromatography column (GE Healthcare) was performed to isolate monodisperse, monomeric proteins (Ric-8A and Gαi1) from aggregated protein and to buffer exchange the sample into gel-filtration buffer (50mM HEPES, pH 8.0, 150mM NaCl and 1mM tris(2-carboxyethyl)phosphine) right before experiments.

2.3.1a Standard Conditions for Sample Quantification and Storage of Purified Samples

Unless otherwise noted, all purified protein samples mentioned in this dissertation were quantified by reading sample solution absorbance at 280nm (A280) using a NanoDrop™ 2000 spectrophotometer (Thermo Scientific). Actual protein concentrations were calculated by dividing A280 value by the estimated extinction coefficient at 280nm based on sample amino acid (and/or nucleic acid) composition and Beer's Law ($A=\varepsilon*l*c$). (67)

All protein samples used in assays or crystallogenesis experiments described in this dissertation are purified to >95% homogeneity exemplified by the sodium dodecyl sulfate–polyacrylamide gel electrophoresis (SDS-PAGE) analysis shown. **(Figure 2-6 inset)** Before flash-freezing in liquid nitrogen for long-term storage in -80ºC, Q-column-purified protein samples were concentrated to 5-10mg/mL and glycerol was added to reach 5% (v/v) final concentration if not already present in Q-column running buffers. All thawed samples were also re-purified to monodispersity and buffer exchanged into fresh gel-filtration buffer, 50mM HEPES, pH 8.0, 150mM NaCl and 1mM TCEP, using a Superdex 200 column (GE Healthcare) prior to experiments.

2.3.2 Circular Dichroism

Ric-8A WT and mutants at 5μM each in 50 mM HEPES, pH 8.0, 150 mM NaCl and 1 mM TCEP were dispensed into a 300-μl quartz cuvette with a 1 mm path length. CD spectra in the range of 210–250 nm were measured at a scan rate of 1 nm/min using a J-815 CD spectrometer (Jasco). The CD spectrum of the buffer was subtracted. The optical path and the cuvette chamber were continuously flushed with a nitrogen flow throughout the course of the experiment. Thermal denaturation experiments were carried out in the same buffer as described above. Samples were heated steadily (2 ºC/min) from 4ºC to 90ºC while monitoring the ellipticity at 222nm (θ_{222}). Once the end temperature is reached, samples were steadily cooled back to the starting temperature to determine recovery of secondary structures. Data were fitted with the "Protein Temperature Melt" function in the SigmaPlot enzyme kinetics module **(Figure 2-20)** (Systat Software) and triplicated and standard deviation shown as error bars.

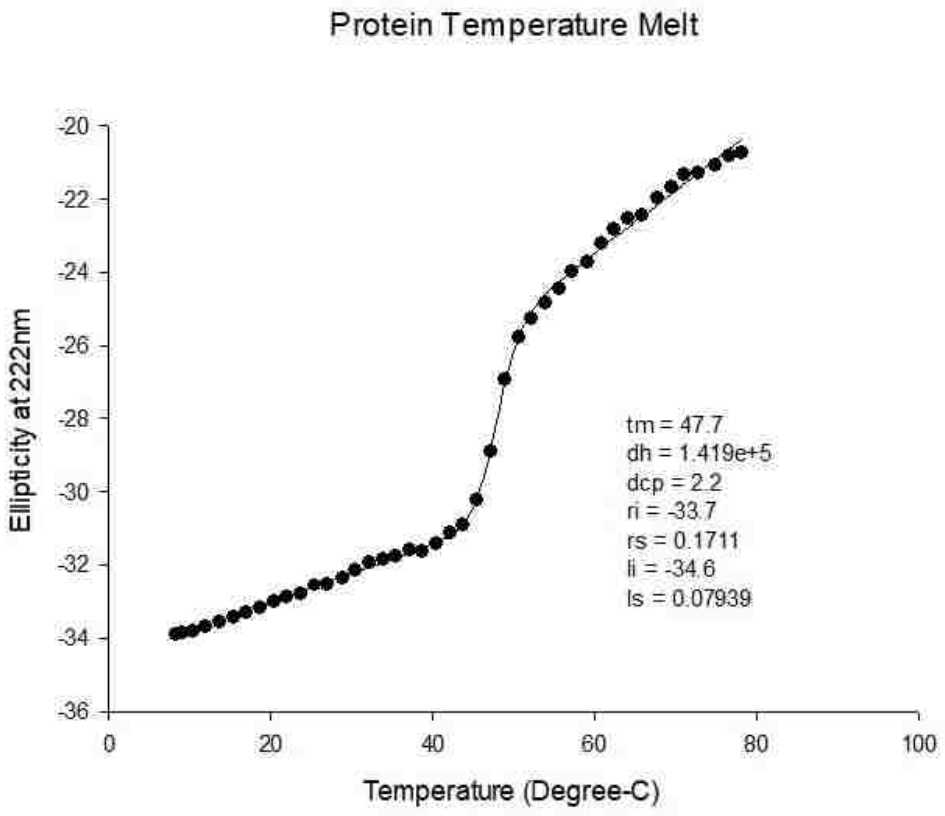

Figure 2-20 A typical CD thermal denaturation curve monitoring θ_{222}
The data is fitted with the "Protein Temperature Melt" function in the SigmaPlot enzyme kinetics module. (Systat Software)

To fit the raw data, the θ_{222} output was first normalized from θ_{222} values to fraction of protein unfolded ($f_{unfolded}$):

$$f_{unfolded} = \frac{\theta_{obs} - \theta_{folded}}{\theta_{unfolded} - \theta_{folded}} \quad (1)$$

where for every temperature point (T), θ_{obs} = observed θ_{222}, θ_{folded} = minimal θ_{222}, $\theta_{unfolded}$ = maximal θ_{222};

to correct for change in heat capacity (ΔCp),

$$\theta_{folded} = ls*T+li \quad (2)$$

where "*ls*" and "*li*" equal the slope and y-intercept of the baseline of folded species, respectively;

$\theta_{unfolded} = rs*T+ri$ *(3)*

where "*rs*" and "*ri*" equal the slope and y-intercept of the baseline of unfolded species, respectively.

$\Delta Cp = rs/ls$ *(4)*

Since

$$K_{eq} = \frac{f_{unfolded}}{1 - f_{unfolded}} \quad (5)$$

where K_{eq} = equilibrium constant of folding and

$$\Delta G = -RT \ln K_{eq} \quad (6)$$

where ΔG = Gibb's free energy of unfolding, R = the gas constant = 1.98 cal/mol, and T = the absolute temperature in Kelvin, $f_{unfolded}$ is converted to ΔG and plotted against T. The ΔG vs. T plot is fitted with

$$\Delta G=\Delta H\,(1 - T/T_M) - \Delta Cp\,((T_M - T) + T\ln\,(T/T_M)) \quad (7)$$

where ΔH = change in enthalpy, T_M = Melting temperature where $f_{unfolded}$ = 0.5. (56)

2.3.3 Differential Scanning Fluorimetry

Samples (10µL) of wild type Ric-8A(1–491) and mutants (~1 mg/ml) in 50mM HEPES, pH 8.0, 150 mM NaCl and 1 mM TCEP were dispensed into glass capillaries and placed into the sample chamber of a Prometheus NT.48 differential scanning fluorimeter (NanoTemper Technologies, Inc, Munich, Germany). Samples were subjected to a time-dependent temperature gradient over 20–75°C at a rate of 1°C/min. Fluorescence emission at 330nm and 350nm (excitation wavelength, 295 nm) was recorded at seven second intervals. The transition temperature for

thermal denaturation (T_m) is defined as the temperature at the maximum first derivative of the ratio of fluorescence emission at 350 and 330 nm (F350/F330) as determined by a polynomial fit to the temperature-fluorescence ratio curve implemented in the manufacturer's software.

2.3.4 Tryptophan Fluorescence GTPγS-Binding Assay to Assess GEF Activity

Ric-8A catalyzed binding of GTPγS to mGαi1 ("nucleotide exchange" assay) was followed by monitoring the change in intrinsic fluorescence of mGαi1 at 340nm upon exchange of GDP with GTPγS. (102) 2μM of mGαi:GDP in buffer composed of 50mM HEPES pH 8.0, 150mM NaCl, 10mM $MgCl_2$, and 1mM TCEP in a reaction volume of 500μl was allowed to equilibrate for 5min at 25°C in a quartz fluorescence cuvette (quartz SUPRASIL macro/semi-micro cell, PerkinElmer B0631132) with stirring. Ric-8A samples were equilibrated separately at 25°C simultaneously. 20μM GTPγS was added to the reaction mixture in the absence or presence of 2μM Ric-8A, and the increase in fluorescence at 340nm was monitored upon excitation at 295nm. Fluorescence measurements were conducted using an LS55 spectrofluorometer (PerkinElmer Life Sciences). The excitation and emission slit widths were set to 2.5nm. All excitation light was eliminated by the use of a 290nm cut-off filter positioned in front of the emission photomultiplier.

In the case of the "GTP-binding" assays, 2μM Ric-8A were first added to the cuvette containing 2μM mGαi:GDP and allowed to incubate for 5 min. 20μM GTPγS was subsequently added to start the nucleotide-binding reaction with the incubated product. 10-minutes time courses of GTPγS binding events were recorded and fit to a single exponential equation using SigmaPlot (Systat Software):

$$y = a*(1-e^{-kt}) \qquad (8)$$

where y = change in tryptophan fluorescence at time t; a = maximum achievable change in tryptophan fluorescence; k = rate constant, t = time in minutes.

The initial rates of change in tryptophan fluorescence were calculated by taking the first derivative of the equation at t = 0:

$v(t) = dy/dt = a*k*e^{-kt}$ *(9)*

$v(0) = a*k$ *(10)*

Rates of nucleotide exchange were then calculated by correlating maximum changes in tryptophan fluorescence with the maximum possible amount of mGαi1: GTPγS being formed in the reaction volume. The relative activity of each Ric-8A mutant was computed as the ratio of its GEF activity, v(0), to that of WT Ric-8A. For each Ric-8A mutant, relative activities were determined for each of three samples derived from the same stock solution of protein and the average relative activity and standard deviation computed. Assays were conducted over a period of several days, using the same stock of mGαi1 and WT Ric-8A, and the activity of WT Ric-8A re-determined each day from a single sample.

P-values associated with the difference between the GEF activities of mutant versus WT Ric-8A were conducted using a two-tailed Student's t-test based on the mean and variances of three determinations for the activities of each mutant and eight determinations of the activity of WT Ric-8A.

2.3.5 FRET Assay Using MANT-GTPγS

The FRET assays were performed in similar fashion as the "nucleotide exchange" tryptophan fluorescence GTPγS-binding assay except MANT-GTPγS was used as the nucleotide and fluorescence signal at 448nm, instead of 340nm, was monitored. Final concentration of samples

in the reaction were also decreased to 1μM mGαi1, 1μM Ric-8A, and 5μM MANT-GTPγS due to scarcity of MANT-GTPγS at the time the assays were performed. When 2'/3'-O-(N-Methyl-anthraniloyl)-guanosine-5'-(γ-thio)-triphosphate (MANT-GTPγS, Jena Bioscience) **(Figure 2-21)** was excited directly at λ_{ex} = 355nm and its fluorescent emission measured at λ_{em} =448nm as Gαi1 binds, a poor signal-to-background ratio was observed. (data not shown) By using W131 and W211 as a FRET donors (73, 97) for incoming MANT-GTPγS and exciting the nucleotide binding reaction at λ_{ex} = 295nm and detecting for emission at λ_{em} = 448nm, signal-to-background was significantly improved, therefore, the MANT FRET assay results were performed thrice and treated as the primary data set over the direct MANT fluorescence assay results. Data fitting and normalization were performed using identical procedures as the tryptophan fluorescence assay.

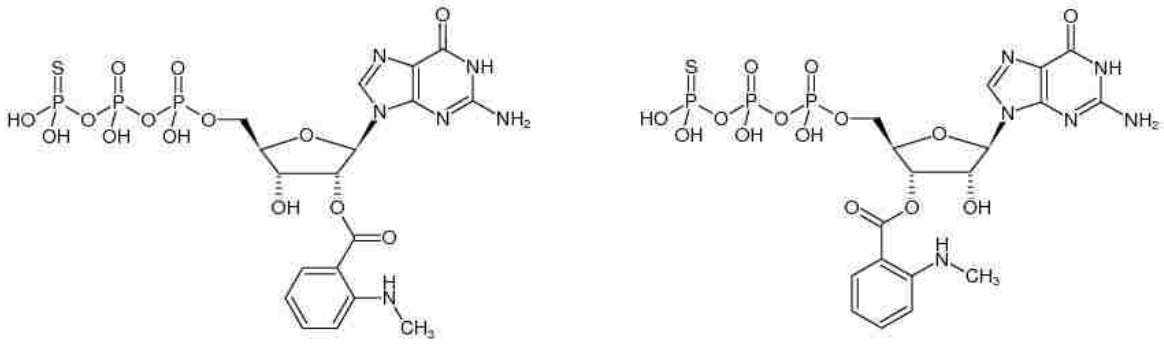

Figure 2-21 Structure of MANT-GTPγS
(Jena Bioscience Reagent Data Sheet)

2.3.6 Filter-Binding Assay Using γ^{35}S-GTPγS

Protein samples of interest were gel-filtered in reaction buffer (50mM Tris pH 8.0, 1mM DTT, 1mM EDTA, 10mM $MgSO_4$) prior to the assays. 1.25μM of mGαi1 were added to 0.5μM Ric-8A 491 WT and 2μM GTPγS doped with (2000cpm/pmol) γ35S-GTPγS and multiple time points (1, 5, 15, 30, 45, 60-

minutes) were taken and filtered through pre-washed nitrocellulose BA35 membrane discs with the aid of a 1225 sampling manifold (Millipore). The membrane discs were then washed three times with cold reaction buffer while on the vacuum manifold and completely dissolved in 2mL of 2-metholyethanol followed with 8mL of 3a70b scintillation cocktail (RPI) before counting. Each data point was duplicated by spotting and filter reaction from the same time-point twice to control for technical errors.

2.3.7 Ric-8A 454-470 Peptide and GST-Ric-8A 399-491 Competition Assays

A synthetic peptide corresponding to rat Ric-8A residues 454-470 was purchased from GenScript. To see whether the peptide competes with Ric-8A 491 for Gαi1 binding site(s), a pull-down assay was performed. 3.6μM of Gαi1 was preincubated with a range of concentrations (0 to 500μM) of the Ric-8A peptide for 15 minutes at room temperature. 1μM of His-tagged Ric-8A 491 WT or buffer control were then added to the mixture and incubated for another 15 minutes at room temperature. The incubated samples were passed through spin-columns (Thermal Fisher) packed with 200μL of Profinity IMAC resins (Bio-Rad) pre-washed with gel-filtration buffer (50mM HEPES pH 8.0, 150mM NaCl, 2mM β-mercaptoethanol, 0.01% E10C12) three times to capture His-tagged protein. The IMAC columns were then washed thoroughly with gel-filtration buffer. Protein was eluted with 30μL of elution buffer (300mM imidazole in gel-filtration buffer). The eluate as well as the loading and flow-through were analyzed by SDS-PAGE.

The GST-fusion Ric-8A 399-491 protein contains the putative Gαi1 binding site (454-470), therefore was tested for its own GEF activity as well as competitive inhibitor activity towards the GEF activity of Ric-8A 491 on Gαi1. Tryptophan fluorescence GTPγS binding assay was used for the assessment. Briefly, 2μM of Gαi1 was preincubated with 2μM of GST-Ric-8A 399-491

or buffer negative control for 15 minutes at room temperature with stirring. Then 2μM of His-Ric-8A 1-491 or buffer negative control were added to the mixture and incubated for 5 minutes before the addition of 20μM GTPγS to start the binding experiment as described earlier.

2.3.8 Size-Exclusion Chromatography to Assess Gαi1 Complex Formation

To test the Ric-8A mutants for their ability to form complex with Gαi1, one molar equivalent of Gαi1 is allowed to react and form complex with one molar equivalent of Ric-8A WT or mutant for 1 hour on ice. Analytical quantity (~1mg) of the incubated mixture is then run through a Superdex 200 10/300 GL size-exclusion chromatography column (GE Healthcare) at 0.5mL/min to assess the extent of complex-formation. Molecular weights (kDa) of protein species eluting from the column were estimated by the elution volume (mL) and a standard curve generated by running gel-filtration standard (Bio-Rad #1511901) through the same column.

Chapter III: Ric-8A Crystal Structure

3.1 Introduction

As described in Chapter I, Ric-8 appears to function as a GEF in similar fashion as the GPCRs, the nucleotide exchange reaction proceeds with the formation of a stable nucleotide-free Ric-8:Gα complex intermediate in the absence of GTP. Biophysical investigations of this complex revealed that nucleotide-free Gαi1 adopts a molten-globule-like state when bound to Ric-8A and is structurally heterogeneous.(23, 42) In the Ric-8A:Gαi1 complex, the secondary structure scaffold that supports the nucleotide binding site in the Gαi1 Ras-like domain becomes accessible to HD exchange and is therefore likely destabilized.(10) It has been lately discovered that Ric-8A phosphorylation at five casein kinase II (CKII) sites, which are highly conserved across Ric-8A phylogeny, activates both the GEF and chaperone activity of Ric-8A. (3) Thus, whereas Gα activation is regulated by exogenous GPCR agonists, cytoplasmic activation may be stimulated through a kinase activation cascade.

Little is understood about the molecular mechanism by which Ric-8 homologs catalyze nucleotide exchange on Gα and the absence of structural information about the Ric-8 family of proteins has been a major obstacle for this field of research. Although the atomic structures of a variety of Gα proteins have been determined in several conformational states (54), only computational models are available for Ric-8A. (10, 29, 48) The computational models predicted an elongated macromolecule composed primarily of α-helical Armadillo repeats, similar to importin-β, the nucleo-transporter that binds Ran-GTPase. (83) **(Figure 3-1)** Although importin-β does not catalyze nucleotide exchange for Ran, the crystal structure of importin-β:Ran complex

is the best structural model available to describe the paradigm where a protein macromolecule composed of mainly Armadillo repeats, such as Ric-8, can interact with a Ras GTPase.

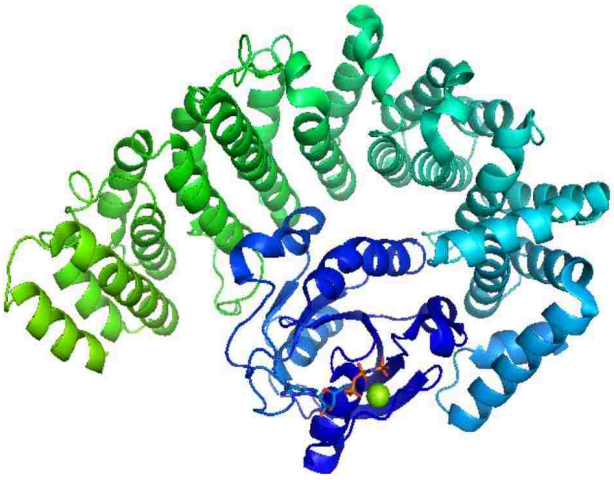

Figure 3-1 Crystal structure of importin-β:Ran complex showing importin-β Armadillo repeats, a superhelix of repeating α-helices, in GREEN to CYAN and Ran GTPase in BLUE. (83)

Very briefly, X-ray crystallography is an experimental technique that exploits the fact that X-rays are diffracted by atoms in crystals. X-rays have the proper wavelengths (~10^{-10} m) to be scattered by the electron cloud of an atom. Based on the diffraction pattern obtained from X-ray scattering off the periodic assembly of molecules or atoms in the crystal lattice, an electron density map can be reconstructed. Additional phase information must be extracted either from the diffraction data or from supplementing diffraction experiments to complete the reconstruction. A model is then progressively built into the electron density, refined against the data that generates the map.

Up to this point, structural analogs of Ric-8A have been very resistant to crystallization, possibly due to highly dynamic motions of these proteins sampling multiple conformations in solution. In this chapter, I will describe an atomic-resolution crystal structure of phospho-Ric-8A 1-452 (pR452) and our endeavor to solve the structure. This protein retains the two (of five) CKII

phosphorylation sites that are critical for GEF stimulation. (3) We show that R452 retains partial GEF activity that is stimulated by phosphorylation and forms a stable complex with Gαi1. The crystal structure of pR452, in conjunction with the results of earlier HDX-MS experiments, small angle X-ray scattering (SAXS) data and evolutionary conservation analysis, provides insight into the mechanism of Gαi1 binding, and the global structural consequences of phosphorylation. Practically, the structure will serve as a useful tool for further structural studies on Ric-8 homologs, as well as the more sought-after Ric-8:Gα complexes, by aiding construct design and providing a homology model for molecular replacement.

3.1.1 Limited Trypsinolysis Suggests a Stable Core of Ric-8A

To approach the problem of protein crystallization, a common practice is making truncation mutants of the full-length protein in the hope that a stable "core" motif or domain, which contains fewer flexible regions, will be an easier target for crystal packing and ultimately form protein crystals suitable for X-ray diffraction experiments. As described in the limited proteolysis study in Thomas 2011(42), a large portion of full-length rat Ric-8A (1-530) expressed in *E. coli* appears to be quite resistant to trypsinolysis. **(Figure 3-2A, B)** In light of that finding, multiple N- and C-terminal truncations mutants (1-491, 1-452, 1-425, 1-401, 1-373, 12-491, 38-491) were generated and their GEF activity assayed. **(Figure 3-2C, D, E)** The assay results suggest that both the N- and C-termini of Ric-8A participate in its GEF function towards Gαi1. On the N-terminus, residues N-terminal to residue 38 are needed; on the C-terminus, a peptide stretch composed of the last 40 residues contains a possible auto-inhibitory domain, which upon removal elevates the GEF activity beyond that of the full-length WT protein; the region between residues 425 to 491 appears to contain another important domain or motif. (42)

In chapter II of this dissertation, we confirmed that this region indeed contains a crucial Gαi1 interactive site, 454-470.

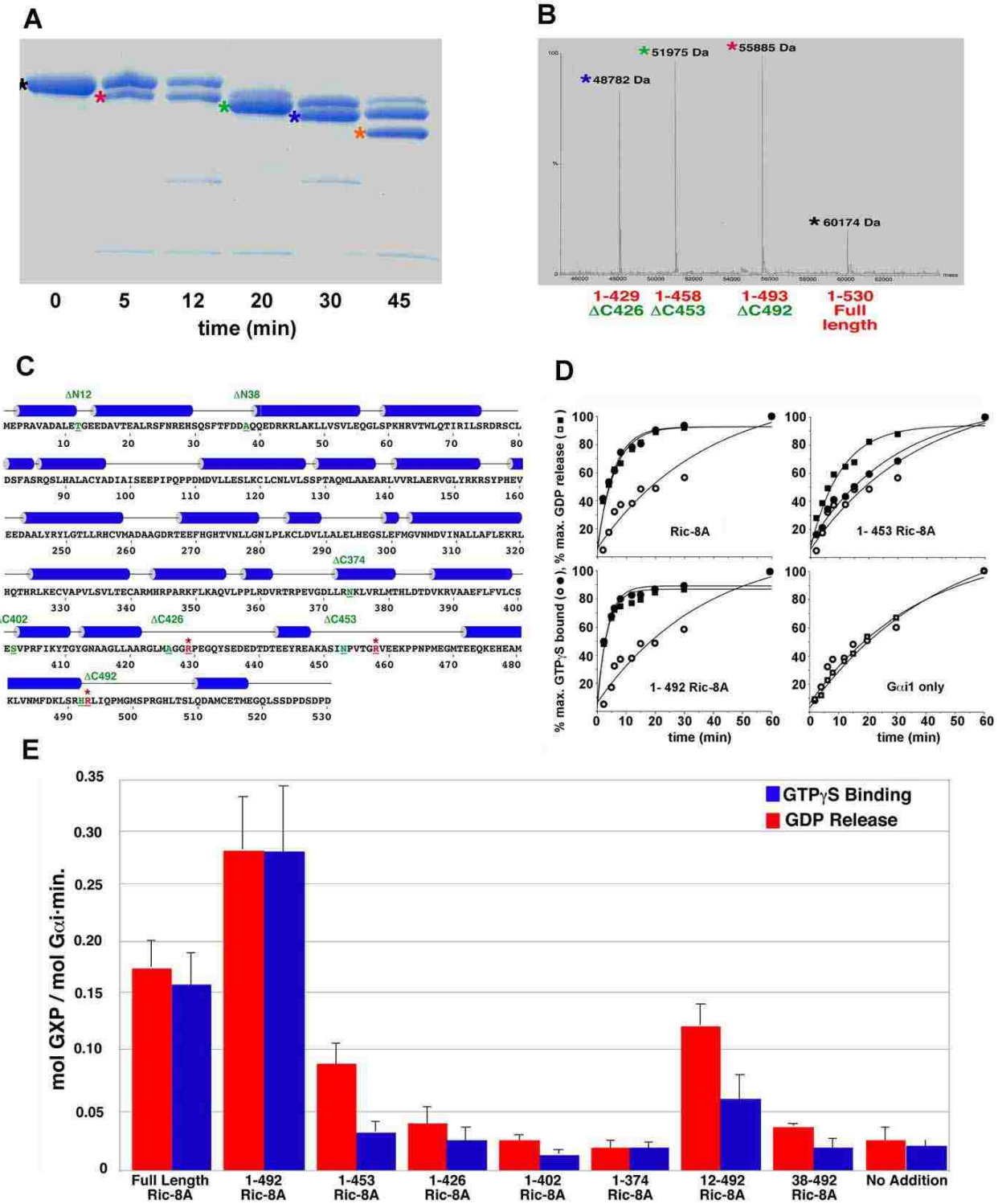

Figure 3-2 GEF activity of purified Ric-8A fragments defined by limited trypsinolysis and secondary structure analysis
(A) Coomassie-stained SDS-PAGE analysis of Ric-8A after trypsinization for the times indicated below each lane; unique fragments are identified by colored asterisks. **(B)** Electrospray mass spectrometric analysis of Ric-8A tryptic digest fragments extracted from the SDS-PAGE gel shown in panel A; peaks identified by asterisks refer to corresponding bands shown in panel A. Fragment masses (Da) are indicated at each peak position. **(C)** Amino acid sequence of rat Ric-8A; cylinders indicate helical segments predicted using JPRED. Residue codes colored red indicate sites of proteolytic cleavage (see panel A). Residue codes in green indicate N- or C-termini of recombinant Ric-8A fragments engineered to coincide approximately with proteolytic sites or predicted secondary structure boundaries: ΔC492 denotes the Ric-8A fragment comprising residues 1–492. Both N-terminal truncations ΔN12 and ΔN38 were also C-terminally truncated at residue 492 and comprised residues 12–492 and 38–492, respectively. **(D)** Kinetics of intrinsic (open symbols) or Ric-8A-stimulated (filled symbols) GDP release (squares) from, or GTPγS binding to (circles) myristoylated Gαi1 were determined by a filter binding assay using radiolabeled nucleotides. Upper left panel, Gαi1 (200 nM) nucleotide binding and release in the presence of full-length Ric-8A (200 nM); lower left panel, ΔC492Ric-8A (200 nM); upper right panel, ΔC453Ric-8A (200 nM); lower right panel, Gαi1 alone. Data for each panel are normalized to maximum GDP released or GTPγS bound in a single experiment. Data points represent the average of three experiments; standard deviation from the mean is <10%. Time course of GTPγS binding in the absence of Ric-8A, shown at lower right, is replicated in the other panels for comparison. **(E)** Histogram showing relative rates of Gαi1 GDP release (red bars) and GTPγS binding (blue bars) catalyzed by Ric-8A and Ric-8A truncation mutants (200 nM). Error bars represent +/- one standard deviation of the apparent first-order rate constants determined in three replicates. (42)

Based on this 2011 study, it is safe to conclude that Ric-8A 1-491(R491), and Ric-8A 1-425 (R425) are the smallest continuous fragments of Ric-8A that retain full, and minimal GEF activity, respectively. R425 was also identified by limited proteolysis as a unique fragment and remained undigested after 30 minutes, **(Figure 3-2A)** it is likely the "core" fragment of Ric-8A that still contains residues required for interaction with Gαi1. We started our crystal screens using R491 and moved to the shorter constructs, R470, R452, R425, and R401, without prior knowledge about the GEF/chaperon-activating phosphorylation of Ric-8A by CKII. After we had obtained small crystals for R452, which happens to still contain the two important CKII phosphorylation sites out of five sites, we were informed of the activating effects by

phosphorylation. We proceeded to perform the kinase reaction as described(1) and were able to significantly improve the size and quality of Ric-8A crystals by replacing R452 with pR452.

3.2 Results & Discussion

3.2.1 Protein Expression and Purification

3.2.1.a Ric-8A 491, 470, 452, 425, 401 Expressed and Purified to High Homogeneity

His-tagged constructs of R491, R470, R452, R425, and R401 in pET28a vector all expressed large quantities (>100 mg/Liter of cells) in BL21 DE3 RIPL *E. coli* using protocol described in the method section of this chapter. Purification of R470, R452, and R425 were straightforward using the existing R491 purification protocol with minor adjustments to accommodate less stable truncation mutants such as R452. Typical yield at the end of anion exchange step of the purification, where the samples are more than 95% homogeneous, was about 50 mg TEV-digested, purified, monomeric recombinant protein per liter of *E. coli* cells. All anion exchange column-purified samples could be flash-frozen in liquid nitrogen and stored in -80^{o}C for long term. For the purpose of functional assays or protein crystallization, flash-frozen aliquots of protein samples were quickly thawed at room temperature and passed through a size-exclusion column for effective buffer exchange and re-purification to segregate possible oligomeric species from monomers.

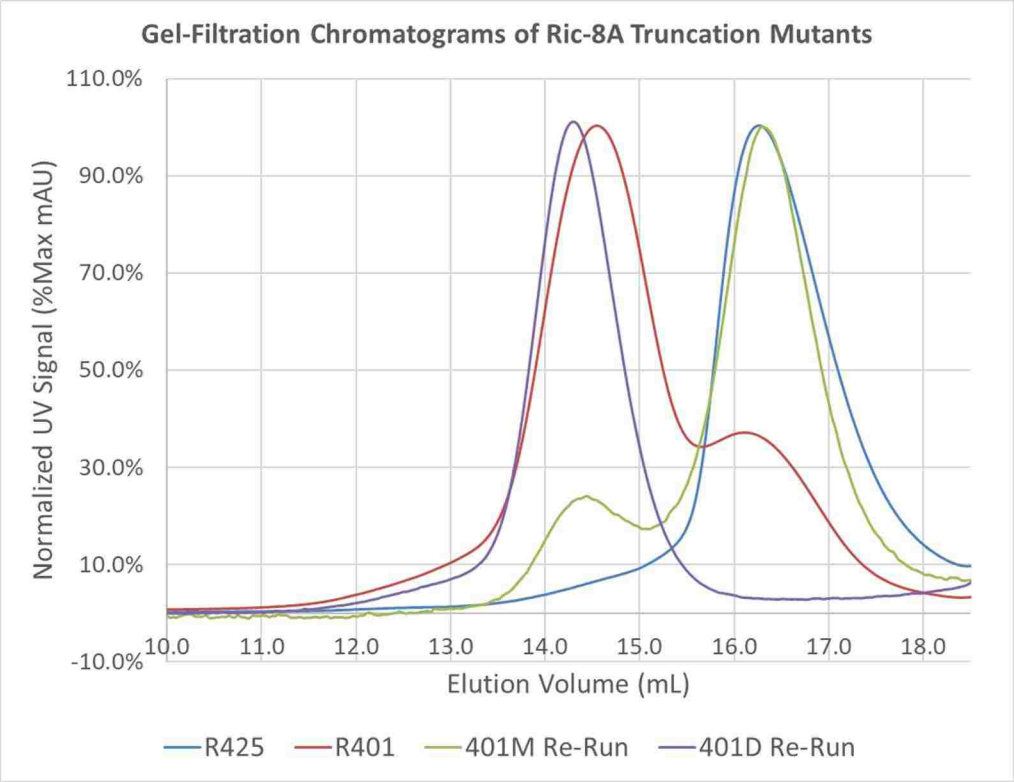

Figure 3-3 Gel-filtration chromatograms showing R401 dimerization
R425(blue), R401(red), R401 monomer(green) and R401 dimer(purple) were resolved using a Superdex 200 size-exclusion column. Sample eluted at ~16.2mL and ~14.4mL corresponded to approximately Ric-8A 401 or 425 monomers and dimers, respectively.

One interesting exception was R401, the shortest Ric-8A truncation construct I used for protein crystallization screens. A large percentage of the protein sample appeared to dimerize judged by SEC **(Figure 3-3)**. The R401 dimerization interaction also appeared resistant to SDS denaturation **(Figure 3-4)**. We speculate that due to the C-terminal truncation, a large portion (>75%) of the R401 protein preparation became mildly misfolded with part of Ric-8A hydrophobic core exposed to solvent, forming hydrophobic interactions between two monomers.

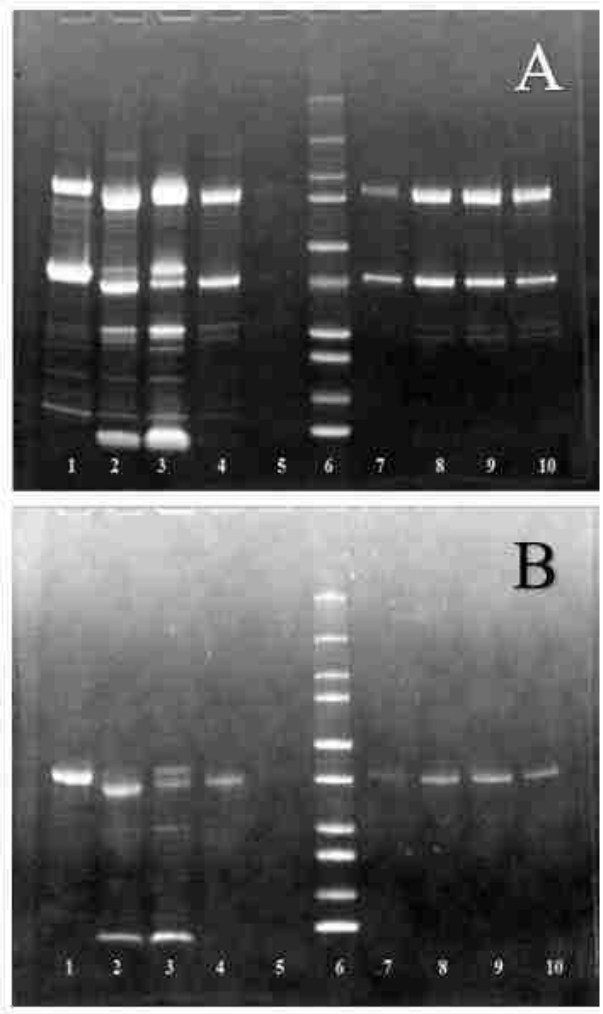

Figure 3-4 SDS-resistant R401 dimerization
(A) SDS-PAGE of R401 samples at different stages of purification, samples were mixed 1:1 with 2X SDS-PAGE sample buffer without heating. **(B)** Same set of samples boiled for 1 min in SDS-PAGE sample buffer.

Lane# and the corresponding samples ID:
1. R401 IMAC elution (over-night in cold)
2. R401 IMAC elution (dialyzed and TEV digested)
3. R401 2nd IMAC resins (post-TEV)
4. R401 2nd IMAC flow-through (post-TEV)
5. R401 Q-column flow-through
6. Ladder
7-10. R401 O-column fractions

3.2.1.b Lower Yield Obtained for Seleno-Methionine R452

To obtain important phase information for Ric-8A, which has no suitable homology model in the protein data bank (PDB) for molecular replacement (MR), multiple attempts with different expression, purification, and post-translational modification methods were made towards crystallizing a seleno-methionine derivative of R452 (SR452). SR452 was purified similarly to R452 and the increase in mass due to heavy-atom incorporation was qualitatively confirmed by Matrix Assisted Laser Desorption/Ionization Time of Flight Mass Spectrometry (MALDI-TOF-MS) (Bruker), however, the extent of heavy-atom incorporation was never quantitatively assessed by liquid chromatography Time of Flight Mass Spectrometry (LC-TOF-MS). It was

expected that by following the existing protocol we should generate pure (>99%) seleno-methionylated recombinant protein because the methiono-auxotrophic *E. coli* cells could only synthesize protein using the supplemented seleno-methionine. Possible contamination of non-auxotrophic competent cells during cell growth was controlled by adding nitrofurantoin into the growth media since the T7 Express Crystal competent cells confer resistance to nitrofurantoin (Nit^+) intrinsically. The final protein yield from each liter of cells (~5 mg) was routinely lower than that of R452 due to several factors including the use of minimal growth media and an early termination of the post-induction/expression phase, which caused lower cell mass and lower protein yield/cell, respectively. Nevertheless, sufficient quantity of sample was obtained for protein crystallization trials. Flash-freezing Q-column purified SR452 caused large (>50%) sample loss after thawing therefore was not recommended.

3.2.2 Quality Assessment of the Extent of R452 Modification by *in vitro* CK II Phosphorylation

It was crucial to confirm the extent of CK-II phosphorylation on Ric-8A. We approach the problem through multiple different methods including high-resolution anion exchange chromatography, mass-spectrometry, and a customized SDS-PAGE method.

Using a high-resolution anion exchanger, Source 15Q from GE Healthcare, we were able to distinguish phosphorylated and unmodified Ric-8A. The more negatively charged pR452 routinely elutes at higher NaCl concentration than R452, therefore, the anion exchange column run accomplishes both an analysis of protein phosphorylation status and a purification step to separate pR452 from other contaminants in the CK-II reaction. Mass analysis of R452 and pR452 showed an increase in mass of 160 Da upon treatment with CKII, consistent with phosphorylation at residues S435 and S440. **(Figure 3-5)** These are the only two CKII

phosphorylation sites within the amino acid sequence range of R452 that are shared with the intact protein. (3)

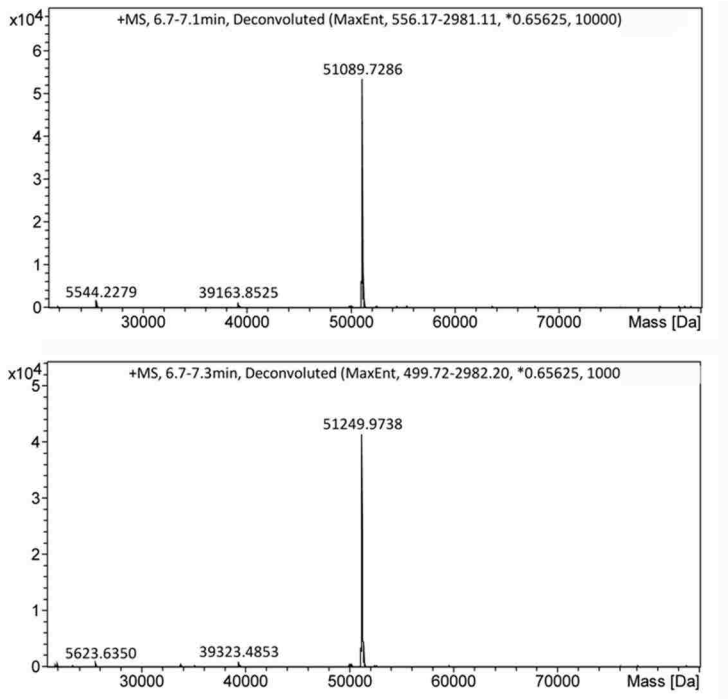

Figure 3-5 LC-TOF-MS spectra of R452 and pR452 showed an increase in mass of 160 Da upon treatment with CKII.

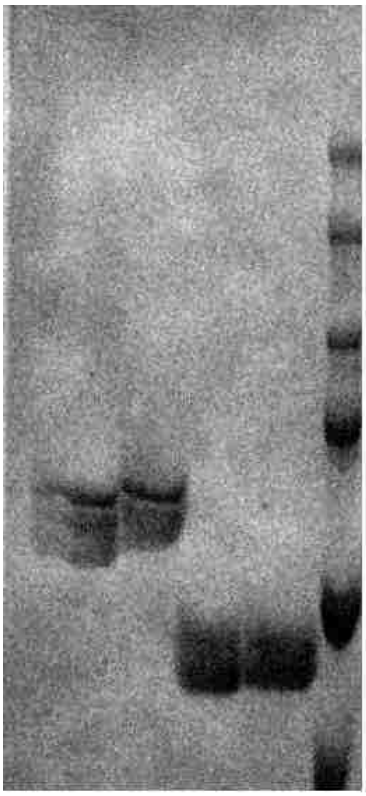

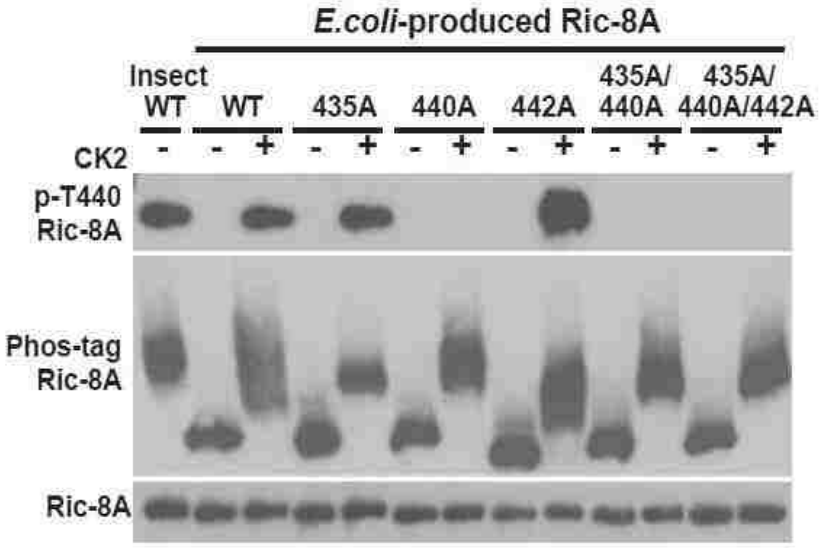

Figure 3-6 Phos-Tag SDS-PAGE results
(Left), samples run on a pre-cast Phos-Tag gel showing very mild retardation of phosphorylated proteins, pR530 and pR452, compared to their unmodified counterparts, R530 and R452, respectively. **(Bottom)**, published results from Tall lab showing large mobility shifts caused by CKII phosphorylation. (3)

According to recent publication regarding Ric-8A phosphorylation (3), there was another useful, commercially available tool to assess the extent of protein phosphorylation, the Phos-Tag series of products. In 2002, Prof. Koike's group (Hiroshima University) reported that a di-nuclear metal complex (i.e., 1,3-bis[bis(pyridin-2-ylmethyl) amino]propan-2-olato dizinc(II) complex) acts as a selective phosphate-binding tag molecule. The molecule is incorporated into biochemical methods for analysis and isolation of phosphorylated proteins (51). We performed Phos-Tag SDS-PAGE analysis on R452 and pR452 using precast gels purchased from Wako Incorporated. The results were not as satisfying as we expected. **(Figure 3-6)** The retardation of phosphorylated protein by the Phos-Tag reagent is very mild compared to what was reported. (3) Apparently Tall's group purchases the Phos-Tag reagent and poured their own gel for their SDS-

PAGE analyses. By doing that, they effectively stacked the protein samples during the stacking phase without Phos-Tag; Phos-Tag only came into effect during the resolving phase. They also heated their samples prior to experiments and ran the SDS-PAGE at a lower voltage for longer time in a modified SDS-PAGE running buffer(3). We will attempt to use Tall's method in the future because the Phos-Tag SDS-PAGE provides a quick and qualitative way to assess protein phosphorylation states during protein purification.

3.2.3 R452 Is a Viable GEF for Gαi1:GDP and Dual Phosphorylation Increases Its Potency

3.2.3.a Tryptophan Fluorescence Assays Showed Increased GEF Activity upon CK II Phosphorylation of R452 and R491

Using the "GTP-binding" tryptophan fluorescence assay method detailed in Chapter II, we examined the effect of *in vitro* phosphorylation on the GEF activity of R452. While being stirred in a quartz cuvette, 1 μM mGαi1 was pre-incubated with Ric-8A (8μM, 4 μM, 2 μM, 1 μM, 0.5 μM, and 0 μM) for 5 minutes at room temperature before the addition of 10 μM GTPγS. The intrinsic tryptophan fluorescence change was monitored, and the initial rate of nucleotide binding calculated and plotted on an initial rate vs. [Ric-8A] plot. **(Figure 3-6)**

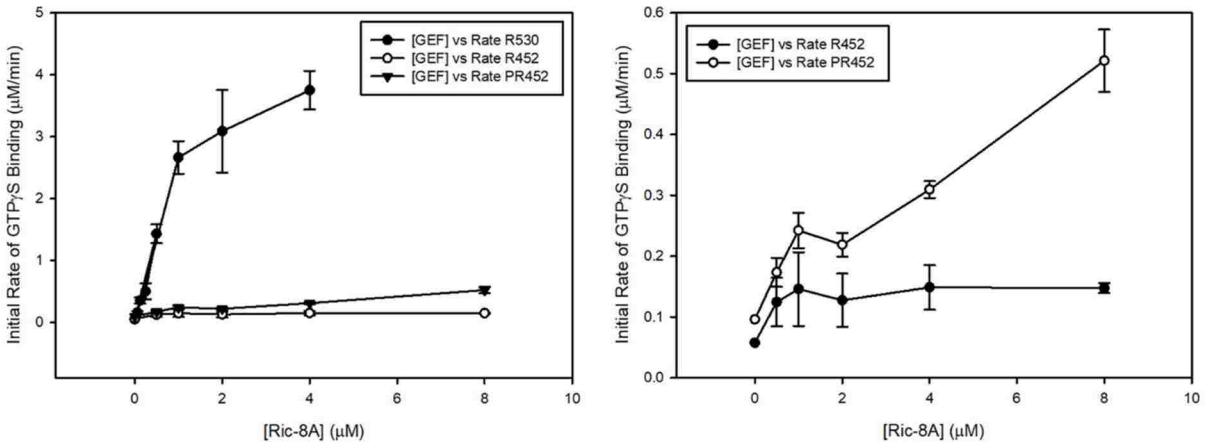

Figure 3-6 GEF-concentration-dependent functional assays using tryptophan fluorescence method to assess the effect of R452 phosphorylation. 1 μM mGαi1 was pre-incubated with Ric-8A (8μM, 4 μM, 2 μM, 1 μM, 0.5 μM, and 0 μM) for 5 minutes at room temperature before the addition of 10 μM GTPγS to start the reaction. The 8μM Ric-8A concentration time course was not measured for full-length Ric-8A (R530). **(Left)**, comparison among full-length Ric-8A, R452, and pR452. **(Right)**, comparison between R452 and pR452. Error bars represent the standard deviation among three replicates.

At low Ric-8A concentration, the difference between the GEF activities of pR452 and R452 was not significant, possibly due to the very low basal GEF activity of R452 compared to R491 or full-length Ric-8A. At high Ric-8A concentrations, we started to notice marked elevation of GEF activity caused by protein phosphorylation. R452 was a weak but still viable GEF for Gαi1; the reduction in its GEF activity compared to the longer constructs could be due to the absence of the crucial C-terminal Gαi1 interactive site(s) we characterized in Chapter II. At high GEF concentrations (4 μM and 8 μM), the Ric-8A concentrations could be equivalent to or above the K_D of Gαi1:GDP for R452 or pR452, therefore, the effect of the phosphorylation on elevating GEF activity becomes more apparent at those GEF concentrations.

3.2.3.b C-terminus of Gαi1 Inhibits GEF activity of pR452 toward Intact Gαi1

Thomas et al. 2011 demonstrated that a C-terminal peptide of Gαi1 binds to Ric-8A 1-491 and inhibits the GEF activity of Ric-8A on full-length Gαi1, therefore, the peptide could represent

the most intimate Ric-8A contact region on Gαi1(42). We then asked whether pR452 interacts with Gαi1 by recognizing the C-terminus of Gαi1, similar to previous observation with R491. If so, it was conceivable that R452 harbors at least part of the Gαi1 C-terminal recognition site, therefore, could still be a viable Ric-8A molecule to study Ric-8A: Gαi1 interaction. To answer the question, we incorporated a synthetic C-terminal peptide of Gαi1 into the GTPγS binding assay.

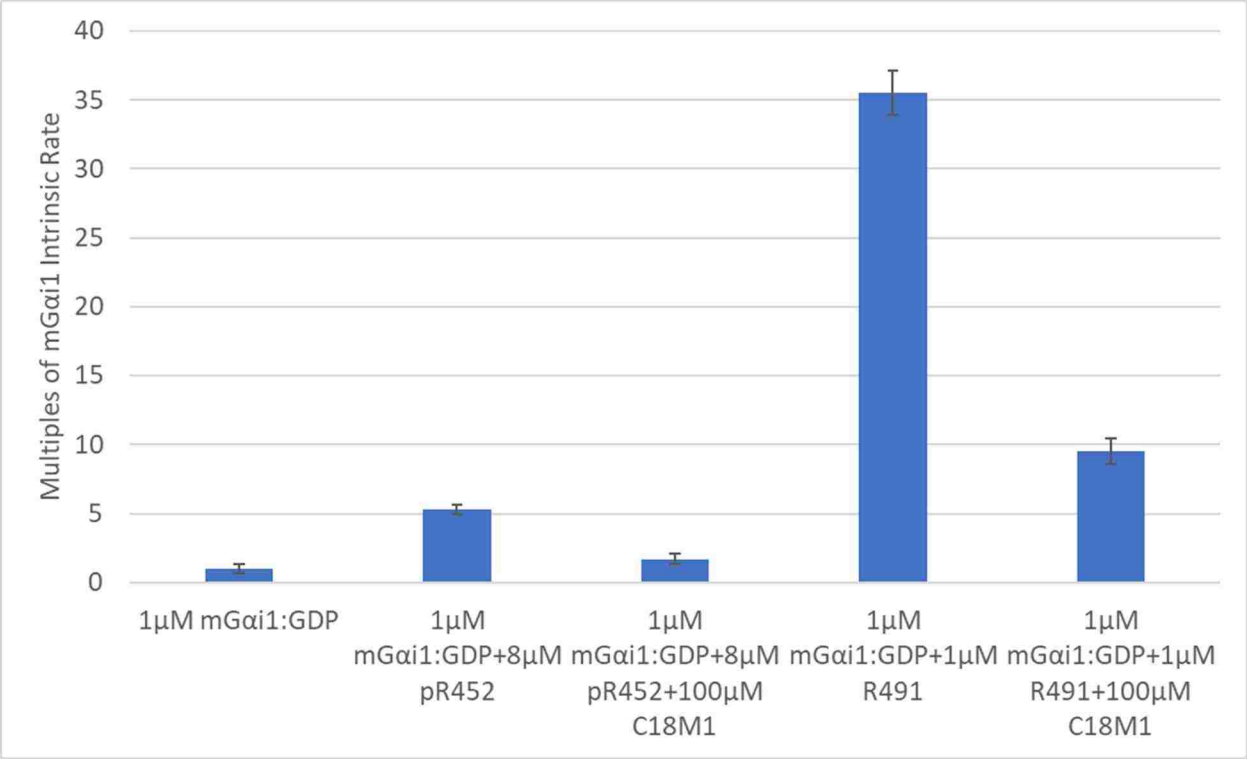

Figure 3-7 Competitive inhibition of the GEF activity of Ric-8A constructs by 100 μM C18M1 peptide
Initial rates of GTPγS binding were presented as multiples of intrinsic rate. 100μM of C18M1 peptide or equal volume of water (negative control) was pre-incubated with 1μM R491 or 8μM pR452 for 1 hour . 1μM mGαi1:GDP were added and allowed to equilibrate for 5 minutes before the addition of 10μM GTPγS to start the reaction. Error bars represent the standard deviation among three replicates.

When a modified version of the Gαi1 C-terminal peptide (see section 3.3.3 for peptide details), C18M1, is incorporated into the assay for R491, I saw similar inhibitory effect on the GEF activity as previously seen(42). Interestingly, I also saw significant inhibition of the GEF

activity of 8μM of pR452 on 1μM mGαi1 by 100μM C18M1. This indicates that the C-terminus of Gαi1 could bind to the first 452 residues of Ric-8A, therefore, at least one important protein-protein interaction surface was preserved in the R452 truncation mutant. **(Figure 3-7)**

3.2.3.c Steady-State GTPase Assay Showed Increased GEF Activity upon CK II Phosphorylation of R452

As an alternative and more sensitive approach to decipher the difference between R452 and pR452 in their GEF activities towards Gαi1, we used a steady-state GTPase assay that measured GTP hydrolysis rate of Gαi1 by counting ^{32}P-labelled inorganic phosphate generated over time in solution. The method was well-established and most recently used to assay the change in GEF activity of Ric-8A towards Gαq(3). We adopted the assay for our system of Gαi1 and Ric-8A and made some modifications.

Using radio-labelled GTP as a substrate, the steady-state GTPase assay provided a more sensitive way to assess the effect of phosphorylation on Ric-8A. A few important factors needed to be considered before interpreting the steady-state GTPase assay result. At the assay temperature (30^{o}C), the intrinsic, single-turnover GTP catalysis rate of Gαi1 was on the order of 2-3 min^{-1}, therefore, I expected the nucleotide exchange reaction to be the rate-limiting step even at high R452 or pR452 concentrations (>5 μM) based on the information from the tryptophan fluorescence GTPγS binding assay. On the contrary, for the full-length Ric-8A, I expected to see maximum steady-state GTPase rate at comparatively low GEF concentrations (<4μM) because the apparent nucleotide exchange rate was higher than the GTPase rate, making GTP hydrolysis rate-limiting instead. **(Figure 3-6)**

R452 and pR452 behaved as expected, showing elevated GTP hydrolysis rates due to CK-II phosphorylation; however, to my surprise, the assay did not reach a plateau of maximum GTP hydrolysis rate as I expected for even the highest concentration of R530 (10μM). More surprisingly, pR530 did not show the typical concentration dependent behavior as the other species; instead, I observed apparent inhibitory activity at high concentrations of pR530 (>2μM). **(Figure 3-8 top)** This result was in contradiction with what was published for the effect of phosphorylation on the Ric-8A, Gαq interaction. (3) With that said, Gαq was not only a different Ric-8A-interacting Gα subunit but also an excellent target for the steady-state GTPase assaying method due to its low maximum intrinsic GTPase rate (~0.1 min^{-1}, compared to the ~2 min^{-1} for Gαi1). As a result, plateaus in GTP hydrolysis rate were easily reached with sub-μM Ric-8A, therefore, Ric-8A concentrations higher than 2μM were not needed.

To see whether the C-terminus of Gαi1 has an effect on Ric-8A:Gαi1 interaction, I also preincubated 50μM of C18M1 peptide or water control with 10μM Ric-8A on ice for an hour prior to performing the assay. The 50μM peptide showed modest inhibitory effects on the unmodified Ric-8A constructs, however, did not show any significant inhibition on pR452 or pR530, if not slightly activating the GTPase. **(Figure 3-8 bottom)**

Some of the results I present here might seem inconsistent or even contradictory to the tryptophan fluorescence assay result in section 3.2.3.a and section 3.2.3.b. I would like to argue that the steady-state GTPase assay was a different assay than either version ("GTP-binding" or "nucleotide exchange") of the tryptophan fluorescence GTPγS-binding assay. The tryptophan fluorescence GTPγS-binding assay only measured the binding of nucleotide while the hydrolysis

assay measured both GTP binding and hydrolysis, therefore, the results of the GTPase assay included more aspects of the system being studied here. For instance, high concentrations of pR530 could possibly function to inhibit the GTPase activity of Gαi1; a GTPγS binding assay with unhydrolyzable nucleotide could not test for that while the steady-state GTPase assay could. More importantly, the "GTP-binding" tryptophan fluorescence assays involved a 5-minute incubation of the nucleotide-free, Ric-8A:Gαi1 complex in the absence of GTPγS. As suggested earlier, Gαi1[ ] in the GEF:G-protein complex is in a dynamic, molten globule-like state (23, 42); such state did not exist for a prolong period during the time course of the steady-state GTPase assays because GTP was always present to dissociate the complex immediately after formation.

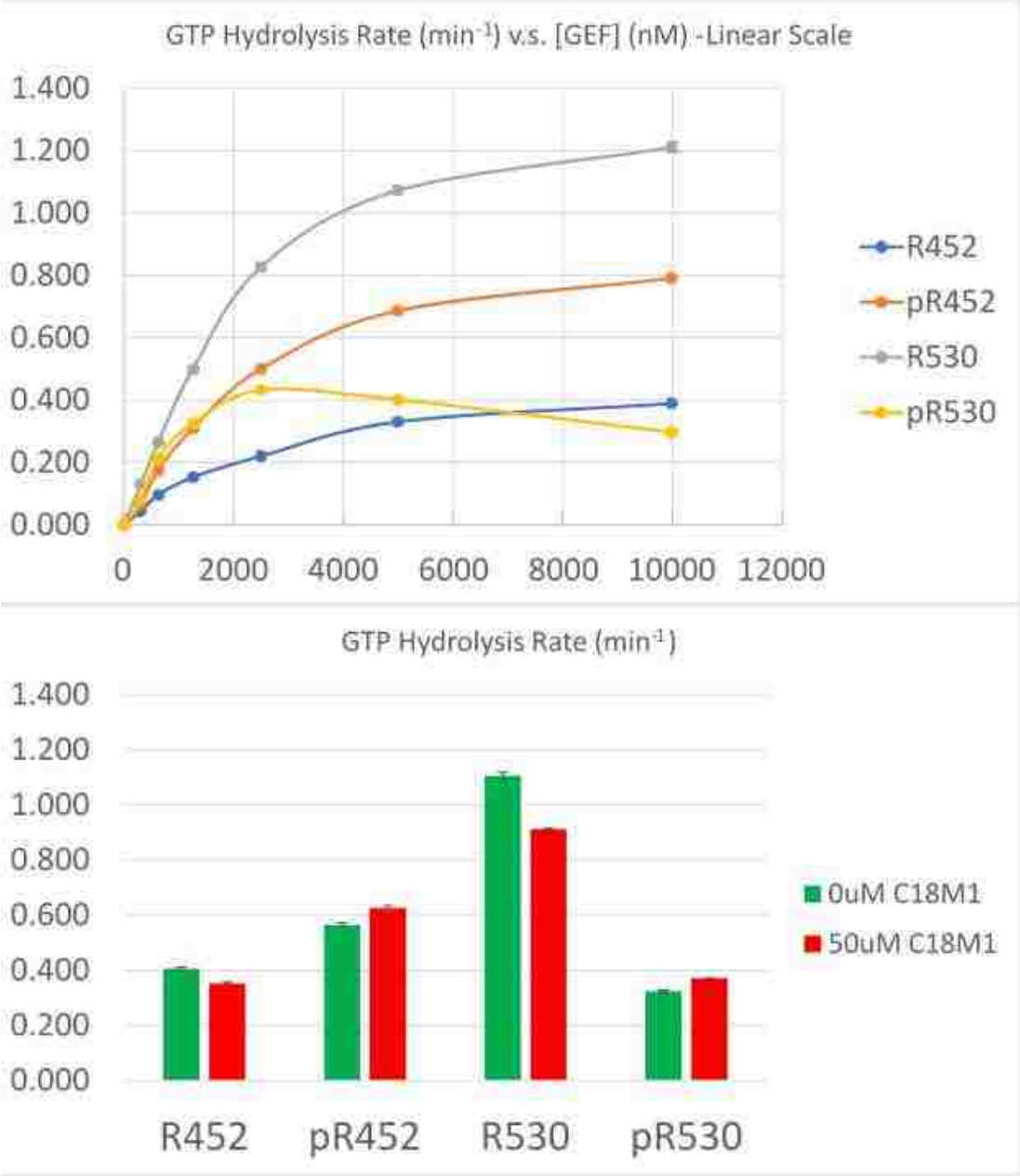

Figure 3-8 Steady-State GTPase Assay
1µM mGαi1:GDP was added to different concentrations (10µM, 5 µM, 2.5 µM, 1.25 µM, 0.625 µM, 0.3125 µM, 0 µM) of different Ric-8A's (R452, pR452, R530, pR530) and 30µM GTP (doped with γ^{32}P-GTP to >1000cpm/pmol GTP) to reach a 20µL final reaction volume in assay buffer (50mM HEPES, pH 8.0, 100mM NaCl, 1mM EDTA, 1mM TCEP, and 10mM $MgCl_2$). All reactions were allowed to proceed for 5 minutes and quenched with 180µL of cold 1 M NaH_2PO_4 pH 4.0. **(Top)** [GEF]-dependent assay results showing the difference among R452, pR452, R530, and pR530. **(Bottom)** Incorporating 50 µM C18M1 peptide into the highest [GEF] (10 µM) data points to see competitive inhibition of Ric-8A GEF activity by Gαi1 C-terminus. Error bars represent the standard deviation among three replicates.

3.2.4 CKII Phosphorylation Mildly Increases Gαi1 Binding Affinity towards Ric-8A

Surface Plasmon Resonance (SPR) is a powerful tool to measure protein-protein interactions in real-time without labelling protein samples with fluorophores; the required sample concentrations are also several orders of magnitude lower than needed for conventional methods such as ITC. During an SPR experiment, one of the interactants (ligand) is immobilized to a sensor surface, the other (analyte) is free in solution and passes over the ligand-occupied surface. When the analyte binds the ligand, an increase in mass can be reflected on change in SPR and detected by instruments, such as BiaCore system (GE Healthcare). For detailed physical theory of SPR, please refer to this video clip from https://youtu.be/o8d46ueAwXI, which explains the BiaCore SPR system interactively and concisely. More technical details can be found in the handbooks from GE.(81)

The default BiaCore X100 analysis program (GE Healthcare) fits the experimental data using a simple 1:1 kinetics binding model by default. The model fits all data curves generated from different analyte concentrations globally for each data set. For a simple 1:1 binding system such as an antigen to an antibody, the default kinetics model describes the system well; however, when using Ric-8A as the ligand and Gαi1:GDP as the analyte, the system is more complex than a simple 1:1 binding interaction. After Gαi1:GDP binds the anchored Ric-8A, Gαi1:GDP undergoes a conformational change to release GDP, therefore, the identity of the analyte (Gαi1:GDP) changes (to nucleotide-free Gαi1) as ligand-binding occurs while the model assumes otherwise. Regardless, fitting the Gαi1, Ric-8A binding curves with the 1:1 model **(Figure 3-9)** still yielded a reasonable estimation of the "on" and "off" rates, which describe the rate at which Gαi1:GDP binds to Ric-8A and Gαi1 dissociates from the complex, respectively

(Table 3-1). For the four different types of Ric-8A anchored on the Ni-NTA chip, Gαi1:GDP appeared to bind at similar rates (2610 to 3300 $M^{-1}*sec^{-1}$). Phosphorylation did not significantly affect the "on" rate of Gαi1:GDP to either R452 or R491. The dissociation curves, on the other hand, suggested an apparently slower dissociation rate ($8.94*10^{-5}$ sec^{-1}) of Gαi1 from the pR491:Gαi1 complex compared to that from R491:Gαi1 ($3.08*10^{-4}$ sec^{-1}). R452:Gαi1 dissociated slightly faster ($1.52*10^{-4}$ sec^{-1}) than pR452:Gαi1 ($1.13*10^{-4}$ sec^{-1}). Although these observations agreed with the notion that phospho-Ric-8A binds Gαi1 more tightly, therefore is a better GEF and folding chaperone for Gαi1, these k_{off} values did not represent the real dissociation rates of unexchanged Gαi1:GDP from an intermediate Ric-8A:Gαi1:GDP ternary complex. Furthermore, the k_{off} values were all slower than the k_{off} confidence limit (10^{-4} sec^{-1}) of the BiaCore X100 fitting program (86), therefore, the differences among them are not necessarily as significant as they appear (i.e. a 4-fold difference between k_{off} values is not reliably for rates slower than 10^{-4} sec^{-1}). The same logic applies to the dissociation constants ($K_D = k_{off}/k_{on}$) calculated from the k_{on} and k_{off} values.

Ric-8A	k_{on} (1/M*s)	SE(k_{on})	k_{off} (1/s)	SE(k_{off})	K_D (M)	SE(K_D)	R_{max} (RU)	SE (R_{max})	χ^2 (RU^2)
R452	3.30E+03	2.05E+02	1.52E-04	4.10E-06	4.62E-08	2.81E-09	239.40	1.30	3.30
pR452	2.66E+03	2.78E+02	1.13E-04	3.60E-06	4.27E-08	4.20E-09	128.10	0.77	0.58
R491	3.19E+03	2.44E+02	3.08E-04	4.20E-06	9.70E-08	7.72E-09	182.30	1.00	1.57
pR491	2.61E+03	4.25E+02	8.94E-05	2.70E-06	3.48E-08	5.20E-09	242.00	1.70	1.05

Table 3-1 BiaCore parameters describing the kinetics of Gαi1 binding to Ric-8A
All kinetics curves within a data set are fitted globally using a 1:1 binding model to generate a single k_{on}, k_{off}, K_D, R_{max} and the standard error (SE) for each parameter, as well as a χ^2 value, a measure of the average deviation of the experimental data from the fitted curve. See Materials and Methods for an explanation of each parameter.

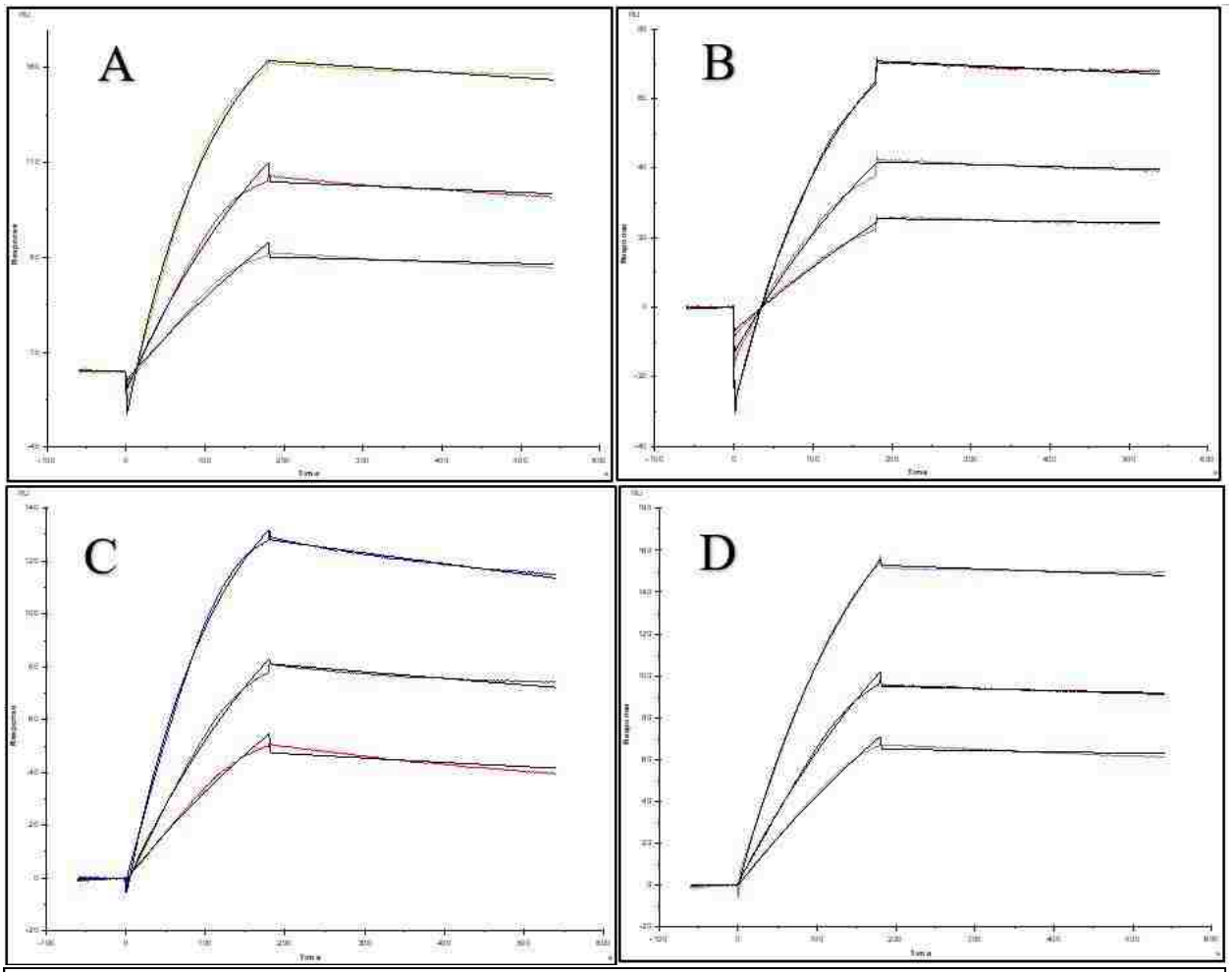

Figure 3-9 BiaCore results showing change in Gαi1 binding affinity to different Ric-8A
All experiments were carried out at room temperature under a constant flow rate (30µL/min). For each of R452 **(A)**, pR452 **(B)**, R491 **(C)**, and pR491 **(D)**, 2.5µM, 1.25µM, and 0.625µM of Gαi1 W258A were applied for 3 minutes for the "on" phase, followed by a 6-minute wash with buffer, thereby completing the "off" phase.

The small χ^2-values of each fit indicated that the 1:1 binding model describes all four Gαi1, Ric-8A interactions reasonably accurately.

$$\chi^2 = \frac{\sum_1^n (r_f - r_x)^2}{n - p}$$

where r_f is the fitted value at a given point, r_x is the experimental value at the same point, n is the number of data points, and p is the number of fitted parameters (86).

3.2.5 R452 Is the Longest Ric-8A Truncation Mutant Crystallized

3.2.5.a R452 and R425 Crystallized Whereas R491, R470 and R401 Did Not

Seeing some phase-separations but no crystal formation up to a month for R491, we turned to C-terminally truncated constructs of Ric-8A. Constructs including R452, R425, and R401 were already available from a previous study (42); R470 was made by simply mutating residue 471 to a stop-codon using the site-directed mutagenesis method discussed in Chapter II. R470 did not crystallize either.

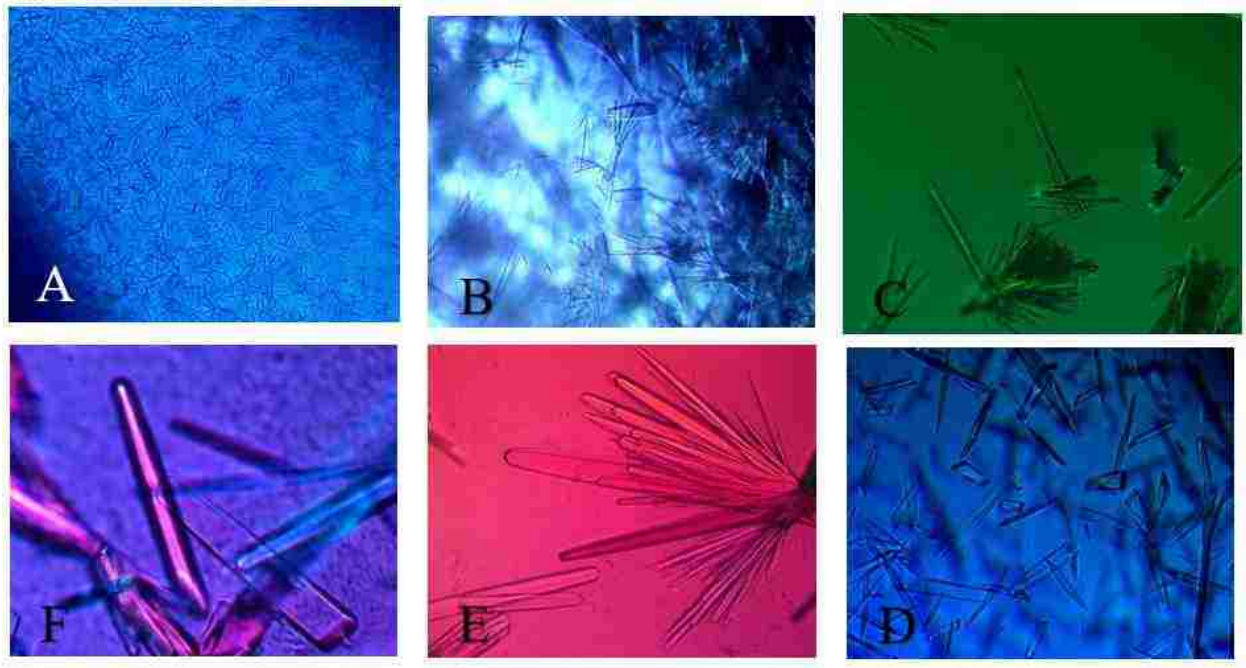

Figure 3-10 Photos of crystals of Ric-8A 1-452
(A), R452 crystallized in initial condition screen, R425 produces needle-shaped crystals of similar morphology. **(B)**, phosphorylation of R452 improves size of the crystals. **(C)**, 10 mg/mL of pR452 forms thicker 2D needle crystals. **(D)**, 25mg/mL of pR452 forms 3-D rods at protein-to-reservoir volume ratio = 3:1. **(E)**, 20mg/mL pR452 forms larger rods in an in-house buffer screening block. **(F)**, 20mg/mL pR452 forms crystals suitable for sulfur-SAD data collection. All photos of crystals were taken using a light microscope (Olympus).

We saw needle-shaped crystals forming for R452 in the initial screen, more specifically, PEGs-II suite from Qiagen. **(Figure 3-10)** After seeing that R452 crystallizes, R425 and R401 were tested

against the same crystallization condition as R452; R425 crystallized but R401 did not, suggesting that R425 might be the shortest construct available to retain packing interactions under the particular crystallization condition. As discussed in section 3.2.1, R401 appeared to be in equilibrium between monomer and a stable homo-dimeric species which could be dissociated by boiling in SDS-PAGE sample buffer for 1 minute, suggesting exposure of hydrophobic core regions due to the C-terminal truncation. **(Figure 3-4)** The R401 dimer formed also might not have the same interactions between the two pR452 molecules in the asymmetric unit described in the following sections regarding pR452 crystal structure. The GEF activities of both R425 and R401 (monomer) were assayed and compared to R452 and R491; R425 appeared to be the shortest Ric-8A construct that retains minimal GEF activity towards Gαi1. **(Figure 3-11)**

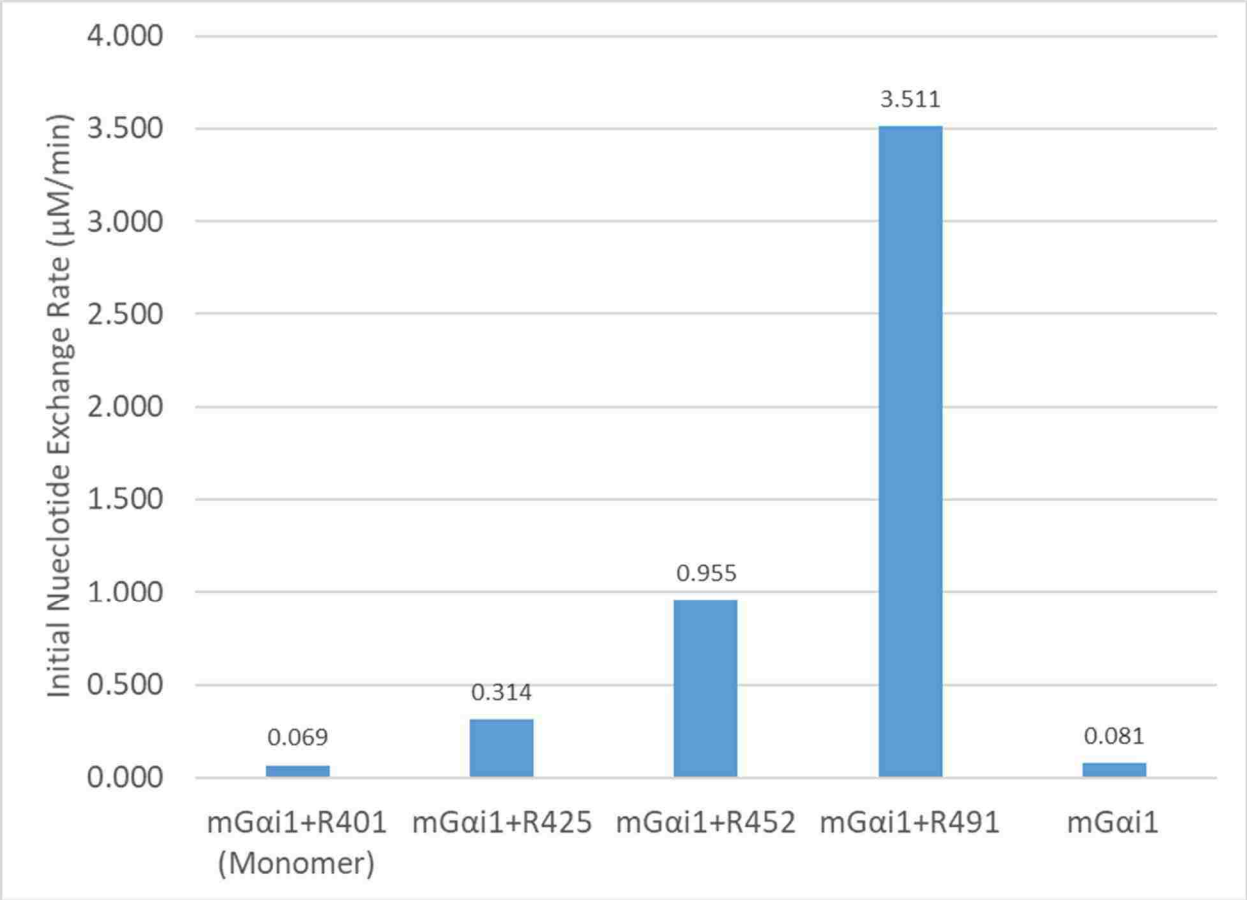

Figure 3-11 GEF activity of Ric-8A truncation mutants on mGαi1 presented in initial rates of GTPγS binding (μM/min). Similar to the "nucleotide exchange" tryptophan fluorescence assay described in Chapter II, 2μM Ric-8A and 20μM GTPγS were added to 2μM mGαi1 to start the reaction.

3.2.5.b R452 and pR452 Crystallization Conditions were Optimized

Purified R452 or pR452 at 20mg/mL crystallized in 0.2M Li_2SO_4, 0.1M common buffers with good buffering capacity from pH7 to pH9 (Tris, HEPES, MES, EPPS, etc.), 20% to 30% polyethylene glycol 3350 (PEG3350). Visible needle crystals were observed 72-hours after plate set-up and they reached maximum sizes after a week in a 20°C incubator. Crystal sizes were optimized for both R452 and pR452 up to 30X10X5 μm^3 plates and 500X50X20 μm^3 plates, respectively, by varying the initial protein-to-reservoir liquor volume ratio. The biggest and best-quality pR452 crystals, from which the merged SAD data set was collected, were grown in a

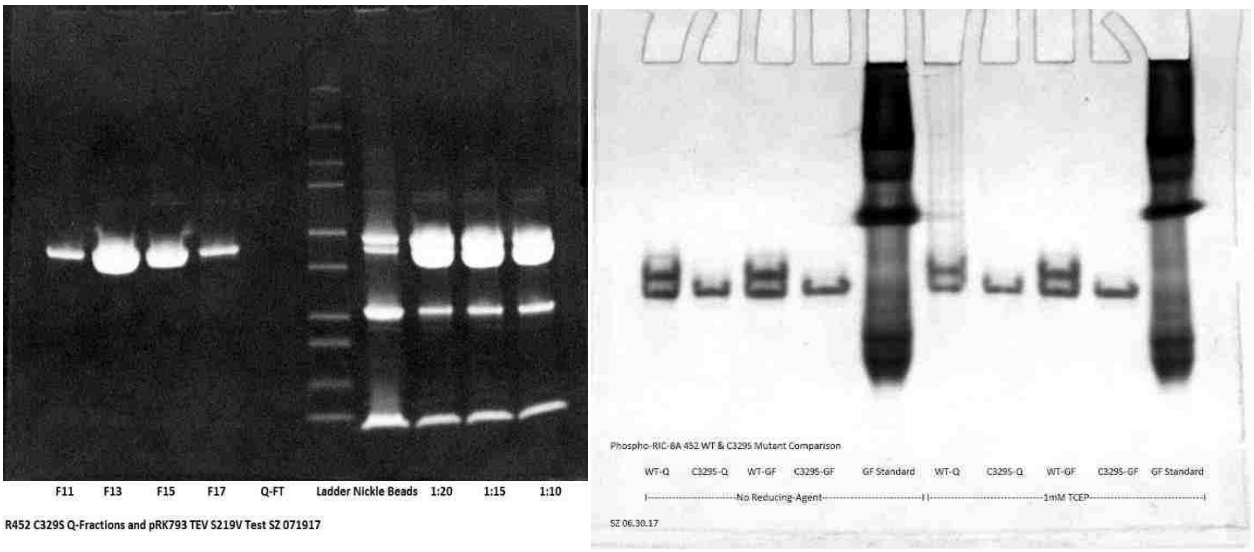

Figure 3-12 Efforts made to improve pR452 protein homogeneity
(Left), SDS-PAGE result showing anion-exchange chromatography-purified Ric-8A 1-452 C329S mutant fractions (Lane 1-5), pRK793 TEV efficiency test (Lane 8-10) showing more protease-digested product with increased protease dosage. **(Right)**, native-PAGE results showing the effect of C329S mutation on sample homogeneity of phospho-Ric-8A 1-452 construct. Lane 1 and 2: Q-column purified WT and C329S Ric-8A, respectively; Lane 3 and 4: Size-exclusion column purified WT and C3289S Ric-8A, respectively; Lane 5: Bio-Rad gel-filtration standard; Samples were resolved in the absence of reducing agent (lane 1-5) and duplicated in 1mM TCEP (lane 6-10)

3:1 = protein: precipitant ratio. **(Figure 3-10)** The crystallization condition and parameters for optimal crystal growth were still unclear. Based on my experience, big crystals with shapes and sizes similar to the largest crystals grew in sporadic conditions (type of buffer, pH, %PEG3350, incubation temperature, etc.) with large variations; there was no obvious trend for crystal optimization for either R452 or pR452 within the range of conditions mentioned above. To approach optimizing the crystals size and quality, a buffer screen block was made to randomly sample conditions within a confined pH and precipitant concentration range (0.1M buffer pH 7 to pH 8.5, 0.2M Li_2SO4, 25% to 30% PEG3350) and the following buffers were tested: Bicine, Bis-Tris-Propane, EPPS, HEPES, TAPS, TES, Tricine, Tris.

As part of extra effort to improve the quality of the crystals, we purchased a new TEV protease expression plasmid (pRK793) for expressing TEV protease and we created a mutant Ric-8A 1-452 construct (C329S). Our old TEV protease bound to anion-exchange columns and co-eluted with Ric-8A. It also formed a ~50 kDa dimer so it eluted at almost the same elution volume as R452 on a size-exclusion column. The new TEV protease cleaved the 6x His-tag with similar efficacy **(Figure 3-12)** and was easier to remove from Ric-8A because it did not bind to anion-exchange column. We mutated C329 to a serine because it is the only rat Ric-8A cysteine not conserved in human Ric-8A. Based on a previous conversation with Celestine Thomas, SDS-PAGE analysis of human Ric-8A does not show double bands as does rat Ric-8A. Therefore, we suspected that C329 is responsible for Ric-8A sample heterogeneity by forming intramolecular disulfide bonds. The C329S mutant expressed and purified similarly to the WT R452 and showed a higher level of sample homogeneity on a native-PAGE **(Figure3-12)**. The C329S mutant crystallized under the same conditions as the wild type protein but crystal quality was comparatively improved in the absence of the reducing agent, tris(2-carboxyethyl)phosphine (TCEP), which was present in 1mM concentration in the WT crystallization condition, suggesting possible crystal packing-disturbing disulfide linkages or conformational heterogeneity within the WT protein sample due to the disulfide-linked cysteines. The mutant phospho-Ric-8A 452 construct (C329S) crystallized under the same condition as the WT pR452 and followed the same pattern in terms of its preference for reducing agents as the non-phosphorylated C329S mutant. However, no further improvement in either the size or quality of crystals was observed for the phosphorylated R452 C329S or the seleno-methionine derivative (pSR452 C329S).

3.2.5.c Seleno-Methionine R452 Crystallized but Was Not Optimized

The derivatized protein (SR452) crystallized in similar conditions as native protein, however, the size and diffraction quality were inferior compared to native protein. To improve crystal size and quality, phosphorylation of SR452 produced phospho-SR452 (pSR452) as judged by anion exchange chromatography but the protein did not crystallize at all under similar conditions as pR452. Initial condition screening of pSR452 was also fruitless.

Although the crystals of SR452 were small, we still hoped to collect low-resolution data sets to obtain phasing information using multi-wavelength anomalous dispersion (MAD) or single-wavelength anomalous dispersion (SAD) methods. However, the available SR452 crystals did not diffract at all at SSRL BL12-2 or NSLS-II FMX possibly due to the small size or inferior quality of these crystals.

3.2.6 Experimental Phasing Using Extrinsic Heavy-Atoms Soaking Methods Was Not Promising

Unfortunately for phasing experiments, phosphorylation of the seleno-methionine derivative not only failed to improve crystal quality as it did for native R452, pSR452 did not crystallize at all under similar conditions, possibly due to oxidation of surface seleno-methionine residues, which could introduce sample heterogeneity. Soaking pR452 crystals with numerous heavy atoms (iodine, lead, platinum, mercury, gold, xenon, bromine) and heavy atom-containing compounds yielded little success in crystal derivatization. 5-Amino-2,4,6-triiodoisophthalic acid (I3C), a compound that contains three iodine atoms, produced derivatized crystals of marginally acceptable quality for x-ray diffraction experiments and a noticeable anomalous signal for single-

wavelength anomalous dispersion (SAD) phasing. (50) Due to the nature of the I3C compound, which not only binds with relatively low affinity to the surface of protein and is also sensitive to X-ray radiation damage, more careful soaking experiments need to be conducted and data collection strategies adjusted to improve the heavy atom incorporation and anomalous signal, respectively, which ultimately translate to phasing power of these I3C derivatives. Co-crystallization with I3C produced deformed crystal-like protein aggregates, which are certainly not suitable for X-ray diffraction experiments.

3.2.7 Decision and Strategy to Use Sulfur SAD Phasing

To get from the diffraction data to a model of the actual protein structure, we were left with few options to obtain phase information for the pR452 data sets. Before I describe our final decision of phasing method used, I would like to briefly introduce the theory of X-ray diffraction and anomalous signal with information from the text book "Biomolecular Crystallography"(46) and "Structure Determination by X-Ray Crystallography" (113).

In an X-ray diffraction experiment, we measure the intensities (I) and the positions of spots (or reflections) that are recorded on the detector. From the position of a reflection we can determine its Miller indices (*h,k,l*) in reciprocal space and assign the intensity to it. This intensity is proportional to the square of the structure factor amplitude, $|F_{hkl}|$. $\mathbf{F}_{hkl}$ is the vector sum of waves from all atoms within the unit cell, defined as

$$\mathbf{F}_{hkl} = F_{hkl}e^{i\alpha_{hkl}} = \sum_{j=1}^{N} f_j e^{2\pi i(hx_j+ky_j+lz_j)} \qquad (11)$$

where the sum is over all atoms in the unit cell, h, k, l are the Miller indices of the structure factor, x_j, y_j, z_j are the positional coordinates of the jth atom, f_j is the scattering factor of the jth atom, and α_{hkl} is the phase of the diffracted X-ray in the direction h, k, l.

The complex exponential function is periodic, and with the above parameters it is limited between -1,1 for its real part and -i, i for the imaginary part. In such cases of periodic functions, we can apply a Fourier transformation (FT) and we obtain for our formula (equation 11) the following FT:

$$\rho_{xyz} = \frac{1}{V}\sum_h \sum_k \sum_l |F_{hk}\ | e^{-2\pi i(hx+ky+lz-\alpha_{hkl})} \qquad (12)$$

where V = volume of the unit cell. In order to perform the FT, we need the complex structure factors F_{hkl} but we only measure the magnitude $|F_{hkl}|$. In terms of physics, this means that we know only the absolute value of the complex vector F_{hkl} but not its phase, α_{hkl}. To obtain phase information without a suitable homology model for molecular replacement, anomalous scattering from heavy atoms can be exploited. Briefly, Friedel's Law (named after Georges Friedel) states that a reflection, $\mathbf{F}_{hkl}$ and the inverse, $\mathbf{F}_{-h-k-l}$ have the same magnitude and inverse phases:

$$|F_{hk}\ | = |F_{\overline{hkl}}| \qquad (13)$$

$$\varphi_{hk} = -\varphi_{\overline{hkl}} \qquad (14)$$

Symmetry-related reflections are called Friedel pairs. When the incident photons with wavelength near the absorption edge of an atom hit the atom, some photons are absorbed and immediately re-emitted at the same energy. The scattered photon gains an imaginary component to its phase and we observe anomalous scattering. Anomalous scattering causes small but measurable differences in intensity of the Friedel pairs, $\mathbf{F}_{hkl}$ and $\mathbf{F}_{-h-k-l}$, differences that are normally absent, thereby breaking Friedel's Law. **(Figure 3-13)**

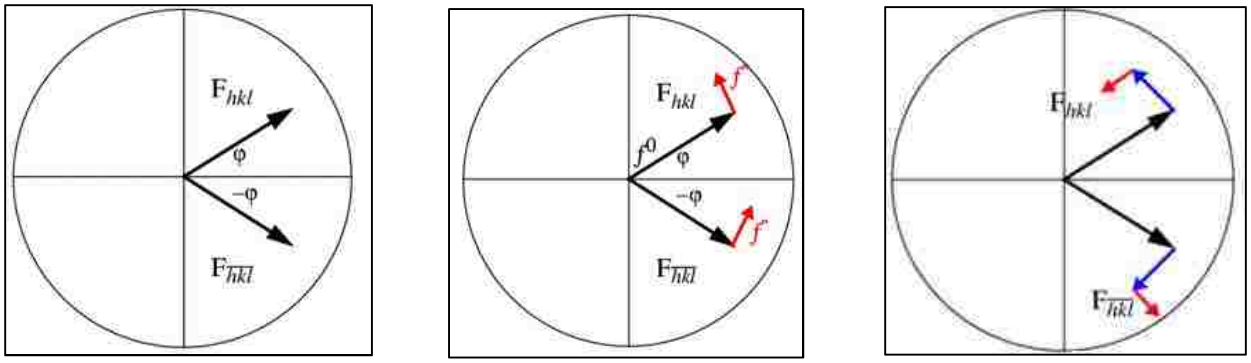

Figure 3-13 Breaking Friedel's Law
On an Argand diagram, $\mathbf{F}_{hkl}$ and $\mathbf{F}_{-h-k-l}$ appear to be reflected across the real axis for any crystal in the absence of anomalous scattering **(left)**. If all atoms scatter equally, then the amplitudes remain equal, **(Equation 13)** but the phase relationship no longer holds **(Equation 14)** because the *f*" (red arrows) imaginary term is always positive **(middle)**. If some atoms scatter anomalously and some do not, then both the amplitude, *f'* (blue arrows), and phase, *f''* (red arrows), relationships are broken, and we are able to measure the differences between $\mathbf{F}_{hkl}$ and $\mathbf{F}_{-h-k-l}$**(right)**. (46)

The scattering factor, *f*, in equation (11) becomes complex:

$$f = f_0 + f' + if'' \qquad (15)$$

where f_o = normal scattering factor, *f'* = **real** anomalous correction factor, and *f''* = **imaginary** anomalous correction factor.

The structure factor equations for the Friedel pairs, $\mathbf{F}_{hkl}$ and $\mathbf{F}_{-h-k-l}$, then become:

$$F_{hkl} = (f_0 + f' + if'')e^{2\pi\,(hx+ky+l\,)} \qquad (16)$$

and

$$F_{\overline{hkl}} = (f_0 + f' + if'')e^{2\pi i(-hx-ky-lz)} \qquad (17)$$

Bijvoet pairs are the pairs of symmetry-related intensities and their inversion-related intensities.

For example, if the unit cell has a two-fold symmetry axis along the *b* axis, *hkl* = *-hk-l*, and

$$|F^{+}| \equiv |F_{hkl}| = |F_{\bar{h}k\bar{l}}| \qquad |F^{-}| \equiv |F_{\overline{hkl}}| = |F_{h\bar{k}l}| \qquad (18)$$

Each *hkl* has true symmetry equivalents. These true symmetry equivalents of a Bragg reflection have equal amplitude even in the presence of anomalous scattering. True symmetry equivalents of one member of a Friedel pair form a set, all of whose members have the same amplitude $|F^+|$; while all symmetry equivalents of the inverse member of the Friedel pair form a second set, whose members share a different amplitude $|F^-|$. For crystals with significant anomalous scattering, the Bijvoet difference, the difference in the measured amplitude for a Bijvoet pair is detectable.

$$\Delta F = |F^+| - |F^-| \qquad (19)$$

Several comprehensive reviews written in the past few years have addressed major issues in sulfur-SAD phasing experiments at the level of both synchrotron hardware and crystallographic software and describe methods to enhance anomalous signals by reducing the systematic errors (5-7, 11, 15, 22, 25, 28). There is no homology model for Ric-8A for use in molecular replacement phasing and neither seleno-methionine derivatization of Ric-8A nor heavy-atom soaking of the pR452 crystals yielded appreciable results. Thus, we attempted to obtain phase information using the anomalous difference arising from 9 native cysteines and 10 native methionines, which make up 4.2% of total Ric-8A amino acids composition. The decision has proven to be a bold yet fruitful adventure for many reasons, some more obvious than the others. For a well-diffracting crystal, the anomalous signals from a sulfur atom within practical X-ray energy range (6.0 keV to 14.0 keV) is comparatively much weaker (i.e. *f"* = 0.72e at 7.0keV) than that from other anomalous signal-generating heavy-atoms such as selenium (i.e. *f"* = 3.85e at 12.7keV) or iodide (i.e. *f"* = 8.53e at 7.0keV). It is especially challenging for protein crystals with modest diffraction quality and relative low sulfur content.

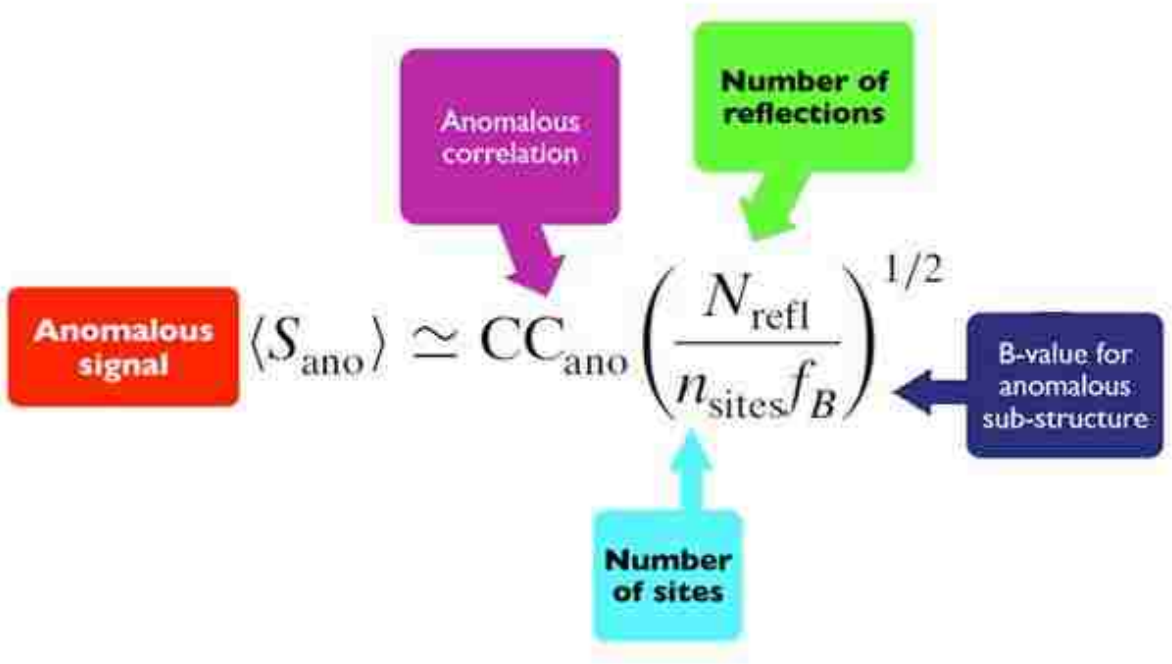

Figure 3-14 Expression used in phenix.plan_sad_experiment to calculate expected anomalous signal
S_{ano} is the expected useful anomalous signal and determines the chance to find a heavy-atom substructure; CC_{ano} is the correlation of observed anomalous differences with ideal one for the structure, therefore, determines phase accuracy and the quality of the resulting electron density map. (15)

We analyzed the anomalous differences measurability of the R452 construct following the pipeline method developed by Thomas Terwilliger and his colleagues. (20) The anomalous signal **(Figure 3-14)** and anomalous correlation, (16)

$$CC_{ano} \equiv \frac{\langle \Delta_{ano} \Delta^{obs}_{ano} \rangle}{\langle \Delta^2_{ano} \rangle^{1/2} \langle (\Delta^{obs}_{ano})^2 \rangle^{1/2}} \quad (20)$$

(where Δ_{ano} is the "useful" anomalous difference from the atoms that make up the target anomalous substructure, Δ^{obs}_{ano} is the observed anomalous difference, which is just the sum of Δ_{ano} and errors such as radiation damage and "not useful" anomalous difference from other atoms)
with specific anomalous substructures can be calculated using the Phenix program, "phenix.plan_sad_experiment", by providing the number and type of anomalously scattering atoms, the

X-ray source energy/wavelength, the target resolution (the number of unique reflections to be measured), and the protein amino acid sequence for calculating anomalous contributions from oxygen, nitrogen, and carbon atoms.(16) f_B is the second moment of the values of the scattering factors,

$$f_B = \frac{\langle f_{h,B}^2 \rangle}{\langle f_{h,B} \rangle^2}$$

Where factors $f_{h,B}$ are the anomalous scattering factors adjusted for the effects of the atomic displacement factor B at the resolution of reflection h and are given by

$$f_{h,B} = f_h'' \exp[-B(\sin^2 \theta_h / \lambda^2)] \quad (15)$$

For the pR452 crystals, the correlation of useful anomalous scattering from sulfur atoms to total anomalous scattering is 0.91. At a target resolution at 3.0 Å, the anomalous signal (S_{ano}) is at most 8 with maxima I/σ up to 100, where the anomalous correlation is 0.55. The estimated probability of finding the sulfur substructures is about 76%, and the estimate figure-of-merit (FOM) of phasing, the expected value (probability-weighted average) of the cosine of the phase error, is 0.33 if all data up to 3.0 Å is used. The probability and figure-of-merit drop to 28% and 0.27, respectively if I/σ is 100 only up to 5.0 Å. These estimations are performed under the assumption that all 19 sulfur atoms are highly ordered, each with 100% occupancy in the crystal lattice, and the data are collected with minimal radiation damage.

```
========================== SAD experiment planning ==========================

   ----------Dataset overall I/sigma required to solve a structure----------


Dataset characteristics:
  Target anomalous signal:    10.0
  Residues: 453
  Chain-type: PROTEIN
  Solvent_fraction:    0.50
  Atoms: 3669
  Anomalously-scattering atom: S
  Wavelength:  1.7700 A
  Sites: 19
  f-double-prime:    0.72
  Resolution:   3.0 A
  B-value for anomalously-scattering atoms:  144

Target anomalous scatterer:
  Atom:  S  f": 0.72  n:   19   rmsF:    3.1  rmsF/rms(Total F) (%):  0.8

Other anomalous scatterers in the structure:
  Atom:  C  f": 0.01  n: 2333   rmsF:    0.6
  Atom:  N  f": 0.02  n:  621   rmsF:    0.6
  Atom:  O  f": 0.04  n:  716   rmsF:    1.2

Normalized anomalous scattering:
  From target anomalous atoms rms(x**2)/rms(F**2):     0.78
  From other anomalous atoms rms(e**2)/rms(F**2):      0.36
  Correlation of useful to total anomalous scattering: 0.91


-------Targets for entire dataset-------  ----------Likely outcome-----------

                                  Anomalous    Useful    Useful
                                Half-dataset  Anom CC  Anomalous
 Dmin    N      I/sigI sigF/F       CC       (cc*_anom)  Signal   P(Substr)   FOM
                        (%)                                          (%)

 6.00   1188    100    0.9       0.38         0.55         4         18        0.25
 5.00   2053    100    0.9       0.38         0.55         5         28        0.27
 3.00   9507    100    0.9       0.38         0.55         8         76        0.33

Note: Target anomalous signal not achievable with tested I/sigma (up to 100 )
for resolutions of  3.00 A and lower. I/sigma shown is value of max_i_over_sigma.
```

Figure 3-15. Result of running "phenix.plan_sad_experiment" for collecting sulfur SAD data from pR452 crystals

Based on the anomalous signal analysis, assuming the reflection data are collected accurately, and the atomic displacement factor (B-factor or temperature factor, which accounts for the fact the atom is on slightly different positions in each unit cell with average position x,y,z) of the sulfur atom is low, pR452 crystals will generate marginally enough anomalous signal at the highest diffraction resolution (3.0Å) we can obtain at synchrotron sources. **(Figure 3-15)** Thus, we expect it to be challenging to solve the phase problem of Ric-8A structure with sulfur SAD even if we manage to collect and merge large number of datasets from a very reliable and precise synchrotron source.

3.2.8 Cryoprotectants and Loops Used for Crystal Harvesting Were Optimized for SAD Data Collection

Two different cryo-protectants were used to harvest the pR452 crystals, a 20% polyethylene glycol (PEG) 400 solution in the mother liquor and an oil-based cryo-solution, Paratone-N, which was also suggested by Tzanko Doukov from SSRL. The oil-based cryo-protectant appeared to cause shrinking of unit cell parameters and the degree of non-isomorphism/shrinkage vary upon the time crystals spend soaked in oil. The crystal, which was used to collect the data set for the "oil" structure, was left in Paratone-N overnight and cryo-frozen the next day. Crystals harvested and cryo-frozen with the 20% PEG-400 cryo-protectant were largely isomorphous with differences in cell parameters within 0.1% among the collected data sets, therefore, were suitable for SAD phasing experiments. The oil soaked crystals, however, vary in their extent of crystal lattice shrinkage in a soaking time-dependent manner, therefore were not suitable for data set merging or SAD phasing based on our experience with BLEND and Phenix scale-and-merge.

As suggested by SSRL beamline scientist, Tzanko Doukov, it was necessary to minimize systematic error from crystal vibrations during the data collection by using a 20μm (nylon fiber diameter) crystal mounting loop to harvest the crystals. The thicker nylon loops effectively decreased the mechanical

vibration caused by cryostream and improved overall quality of data sets collected from similar crystals, eventually helping us merge data from multiple datasets. We also harvested pR452 crystals using MiTeGen MicroLoops E loops, which have an inclined, elongated aperture especially useful for orientating needle- or rod-shaped crystals for effective data collection. We have collected data sets from crystals mounted with these loops at SSRL BL9-2 and BL12-2 in the past and received satisfactory results compared to conventional loops. The pins used to mount the MiteGen microloops were not compatible with the auto-mounting robot at FMX, therefore, crystals harvested using MiteGen loops were not collected at NSLS-II. It is worth mentioning that the MiteGen loop has a feature for easy removal of excess solution from crystal to reduce background scattering from liquid. When harvesting crystals using viscous cryo-protectant such as Parabar 10312(Hampton Research, previously known as Paratone-N), this feature significantly reduced maneuver time compared to conventional nylon loops, for which I had to slowly blot excess cryo-protectant. With proper usage, the MiTeGen loop could prove to be more useful in collecting data sets that require high accuracy since the rigid MiTeGen loop body provides the same benefits a 20μm conventional loop offers in terms of reducing vibration during data collection.

3.2.9 Sulfur-SAD Data Processing and Merging

After 18 SAD data sets of pR452 were collected at NSLS-II FMX, we used two different methods to merge those data sets. BLEND in "analysis mode" first performed multiple pair-wise comparisons of all data sets and then groups the closely "related" data sets into several clusters based on variation in unit cell parameters among data sets. After defining the clusters and plotting them on a dendrogram, the most appropriate data sets to be merged were manually

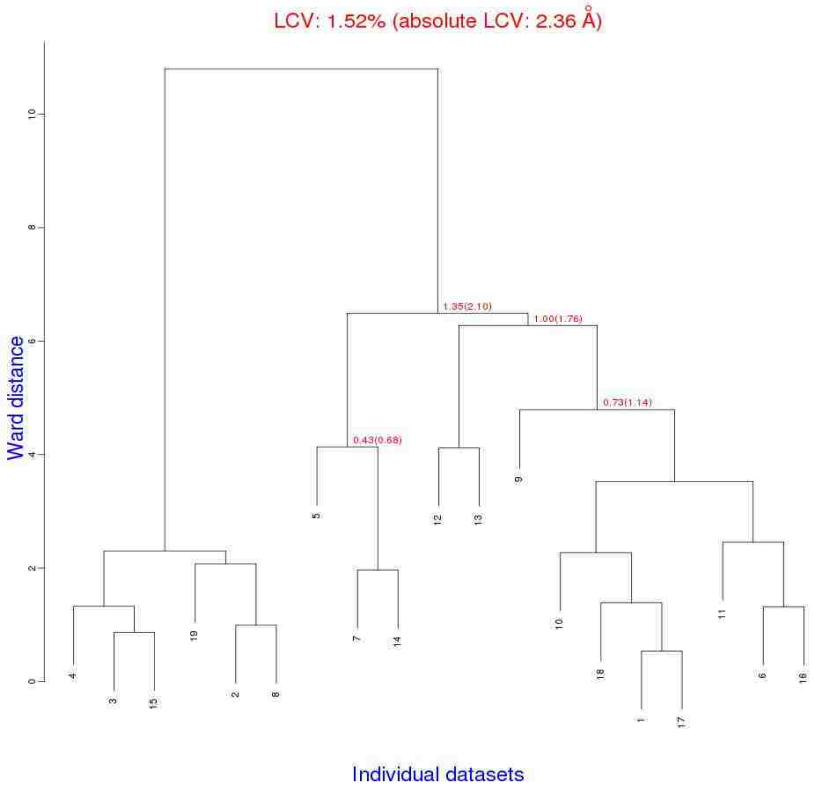

Figure 3-16 Dendrogram generated by BLEND analysis mode showing closely related clusters of data sets from eighteen pR452 data sets
The linear cell variation (LCV) give an indication of cell similarity among all crystals included in the specific cluster; thus, ultimately, they can be associated with isomorphism between different data sets. The dendrogram presents two major clusters, a larger cluster with 1.35% LCV and a smaller cluster. The variability is increased to 1.52% when these two clusters merge into the overall cluster containing all 18 data sets; this is indicative of minor form of non-isomorphism between the small and large clusters of data sets.

chosen based on the result of the cluster analysis. **(Figure 3-16)** BLEND also made suggestions for user to exclude frames that show obvious radiation damage from each data set and using global scaling method to generate a merged data set for each sub-cluster on the dendrogram. The program halted while merging some of the data sets for a prolonged period (>72 hours) without writing any error message or terminating the program. Excluding the problematic data sets from the merging task solved the issue but the resulting merged data do not contain a strong enough anomalous signal for SHELX to determine a good substructure solution. The cause of the

prolonged halt of BLEND programs that eventually led to the exclusion of data sets remains unknown.

All (18-merged) or only the top 2 (2_14 and 2_10) or 3 (2_14, 2_10, and 2_7) datasets ranked by anomalous coefficient were merged by phenix.scaled-and-merged program using the local scaling method **(Table 3-2)**. The highest resolution limit of these merged datasets was 3.4 or 3.0 Å where the resolution at which the overall anomalous signals were maximal. Both BLEND and phenix.scaled-and-merged programs remove radiation damaged frames that would degrade the anomalous signal. All 18 datasets from 14 crystals were successfully merged by Phenix scaled-and-merged program eventually. The resolution limit of the dataset was set at 3.4 Å where the anomalous signal was maximal.

Datasets	18-merged	Top 2 merged (2_10,2_14)	Top 3 merged (2_10,2_14,2_7)
Unit cell dimensions			
a, b, c (Å)	67.1 103.7 141.9	67.1 103.7 141.9	67.1 103.7 141.9
α, β, γ (°)	90 90 90	90 90 90	90 90 90
Resolution range (Å)*	20.00 - 3.4 (3.72 - 3.40)	20.0 -3.00 (3.18-3.00)	20.0 -3.00 (3.18-3.00)
Total reflection	11088284 (2681047)	5821121 (885390)	6861300 (1047918)
Unique reflections*	14109 (1980)	20387 (3258)	20409 (3269)
Redundancy*	785.9 (803.4)	285.5 (271.8)	336.2 (320.6)
Completeness (%)*	99.5 (100)	99.6 (99.8)	99.7 (100)
Mean I/σ (I)*	118.3 (67.1)	65.6 (12.7)	70.1 (14.8)
$CC_{1/2}$	0.994 (1.0)	0.999 (0.996)	1.000 (0.997)
R_{meas} †,*	0.226 (0.373)	0.166 (0.787)	0.168 (0.734)
$R_{p.i.m.}$ †,*	0.008 (0.013)	0.010 (0.047)	0.009 (0.041)
CC_{ano} **	0.58	0.51	0.50

Table 3-2 Statistics of merged datasets for S-SAD phasing

* Data for highest resolution shell are given in brackets. † $R_{meas}=\sum_{hkl}(n/n\text{-}1)^{1/2}\sum_i |I_i(hkl)-\langle I(hkl)\rangle|/\sum_{hkl}\sum_i I_i(hkl)$, where $I_i(hkl)$ is the ith observation of the intensity of the reflection hkl and $\langle I_{hkl}\rangle$ is the mean over n observations. $R_{p.i.m.}=\sum_{hkl}(1/n\text{-}1)^{1/2}\sum_i |I_i(hkl)-\langle I(hkl)\rangle|/\sum_{hkl}\sum_i I_i(hkl)$. Correlation coefficients: $CC = \sum_i((x_i - \langle x\rangle)(y_i - \langle y\rangle))/(\sum_i((x_i - \langle x\rangle)^2(y_i - \langle y\rangle)^2)^{1/2}$, where x_i and y_i are the ith of n observations of quantities whose mean values are $\langle x\rangle$ and $\langle y\rangle$; for $CC_{1/2}$, x_i, and y_i correspond to intensity measurements derived from each of two randomly selected half-data sets from the set of unmerged data; $CC_{ano} = \langle\Delta_{ano}\,\Delta_{ano,obs}\rangle/(\langle\Delta^2_{ano}\rangle^{1/2}\langle\Delta^2_{ano,obs}\rangle^{1/2}$, where Δ_{ano} and $\Delta_{ano,obs}$ are the anomalous structure factor amplitude differences ($F^+ - F^-$), respectively, computed from the anomalously scattering atomic substructure, and the observed anomalous differences. CC_{ano} was calculated using data truncated to d_{min}= 3.4 Å or 3.0 Å for all merged data or top 2/3 merged data, respectively.

3.2.10 Heavy-Atom Substructure Determination

The merged and scaled data was input into the HKL2map(69), a graphical user interface (GUI) for the SHELXC/D/E program suite. SHELXC evaluated the anomalous signal to be significant up to 3.4 Å **(Figure 3-17)**.

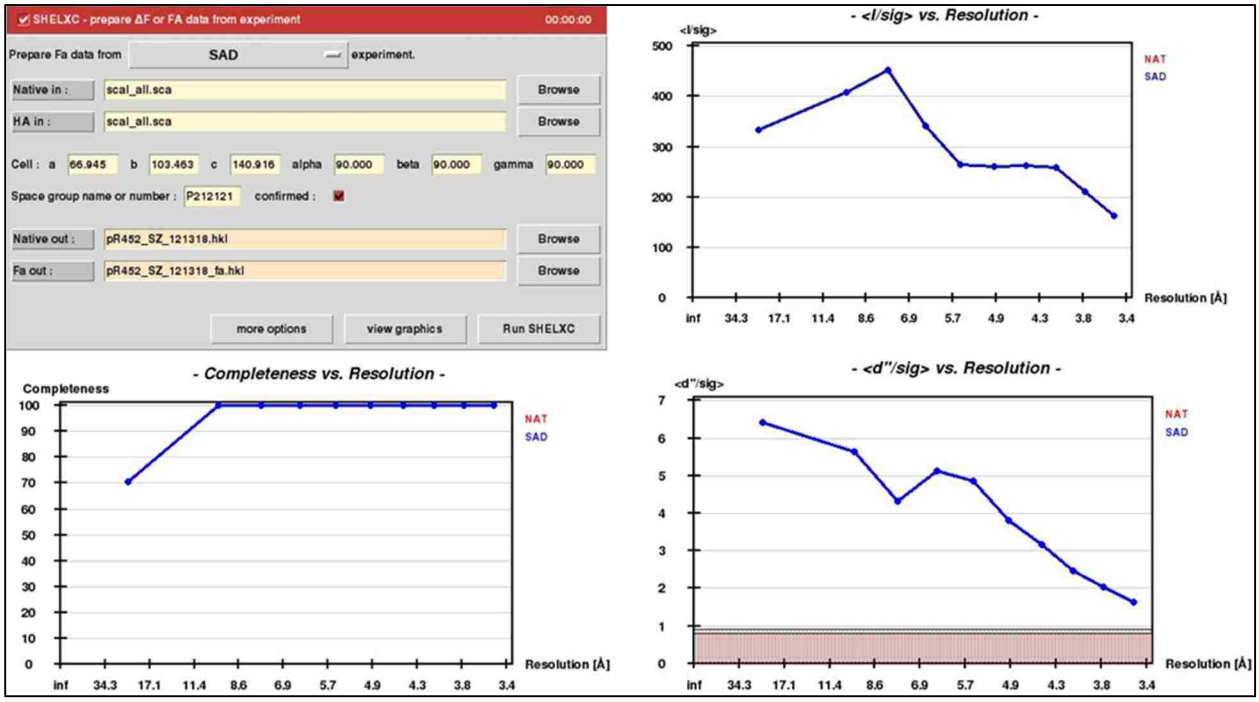

Figure 3-17 Data Analysis using SHELXC
(Top left) SHELXC setup and data input screen. Analysis of the merged data set <I/σ> **(top right)**, completeness **(bottom left)**, and <d''/σ> **(bottom right)** over resolution indicates significant (d''/σ > 1.5) anomalous signal up to 3.4Å.

$$< d''/sig >=< \frac{\Delta F}{\sigma \Delta F} > \quad (21)$$

The substructure search by SHELXD, which gave the highest CC_{all} and CC_{weak}

$$CC = 100 \frac{\left(\sum wE_oE_c \sum w - \sum wE_o \sum wE_c\right)}{\left\{\left[\sum wE_o^2 \sum w - \left(\sum wE_o\right)^2\right]\left[\sum wE_c^2 \sum w - \left(\sum wE_c\right)^2\right]\right\}^{1/2}} \quad (22)$$

(where E_o and E_c are the observed and calculated normalized anomalous difference, respectively) and judge the number of sites by the occupancies (fraction, from 0 to 1, of the sulfur atom occupying a real-space position x,y,z), was performed with up to 10,000 iterations **(Figure 3-18)**. Characteristic bi-modal distribution was observed in the CC_{all} vs. CC_{weak} graph. The best solution had the following values CC_{all}=32.0 and CC_{weak}=11.1. The substructures were successfully determined by SHELXC/D dual-space substructure search. The same merged dataset was also used to search for substructures with Phenix Hybrid Substructure Search (HySS), a likelihood-based method, but could not find the correct sulfur sites.

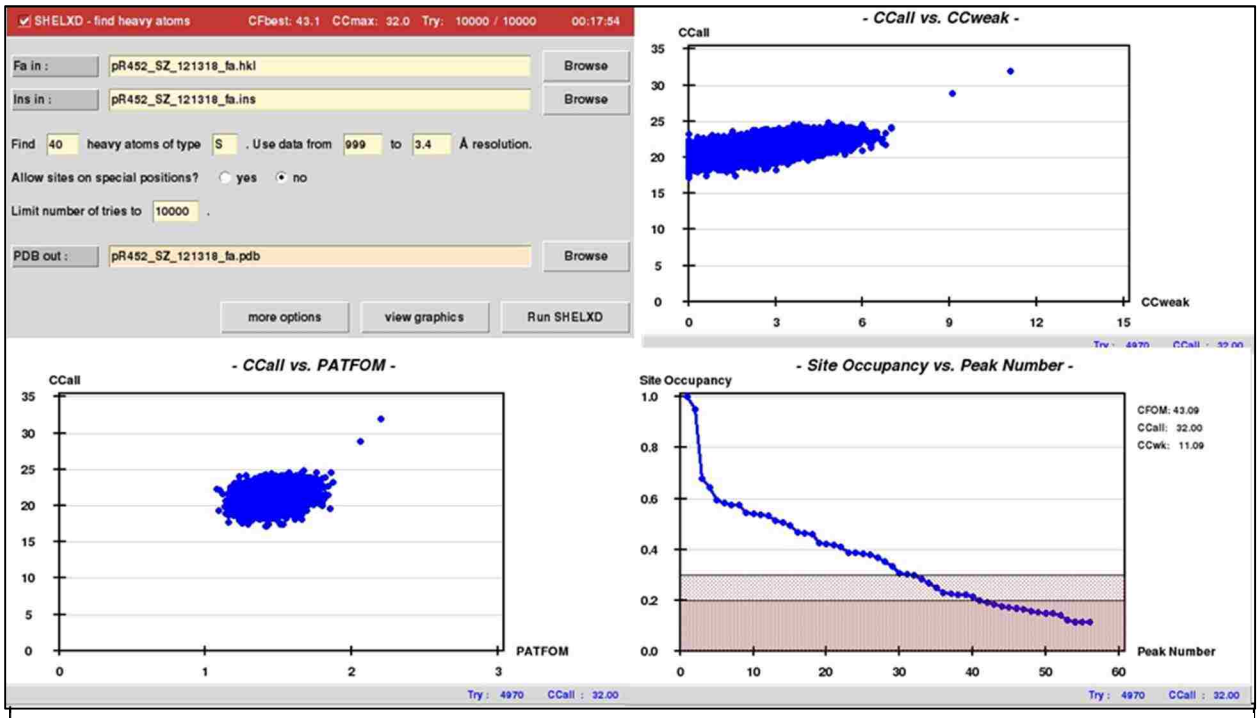

Figure 3-18 Heavy-Atom Substructure Search using SHELXD
(Top left) SHELXD setup and data input screen. Two best substructure solutions with the high CC values **(top right and bottom left)** remote from the rest at the end of approximately 5000 iterations of heavy atom sites searches; the CC values serve as preliminary indicators of correct phase solutions. The solution on the upper right corner of the top right plot (CC_{all} = 32.0 and CC_{weak} = 11.1) was selected for phase-determination and calculating the initial electron density map. The site occupancy vs. Peak Number plot **(bottom right)** shows 30 high-occupancy sulfur sites out of the 40 sites searched in the best solution; occupancy = 0.3 is an empirical cut-off that often proves useful in ambiguous cases.

The substructure determination was only successful when using merged data up to 3.4 Å. Only one substructure solution after SHELXC/D searching with 10,000 tried (default is 1,000) was correct. We did

not obtain any native anomalous substructure other than sulfur atoms from this Ric-8A crystal form from the above software programs we applied.

3.2.11 Determination and Refinement of pR452 Structure

After 38 sulfur sites in the asymmetric unit were obtained by SHELXD, the sulfur substructure and structure factor data were input into Phenix Autosol. Phenix.AutoSol uses SOLVE for phasing, RESOLVE for statistical density modification, phenix.AutoBuild and phenix.refine to generate and refine, respectively, an initial model, and HySS to find additional sulfur sites. Two additional sulfur sites in the substructure were identified by HySS with a FOM of 0.378. The initial crystallographic phases were also determined by AutoSol and followed by iterative phase improvement, which are statistical density modification, optimization of parameters, iteration of positional optimization of anomalous scattering atoms, calculating phases and solvent flattering density modification. The non-crystallogaphic symmetry (NCS) operator was calculated from the given sulfur sites during the phase refinement. A promising solution was obtained from the final AutoSol result where the R factor,

$$R = \frac{\sum ||F_{\text{obs}}| - |F_{\text{calc}}||}{\sum |F_{\text{obs}}|} \qquad (23)$$

map skew (skew of histogram of electron density map), and model-map cross-correlation (measures the similarity between model and electron density map) are 0.2473, 0.10 and 0.79, respectively. Visual inspection of the substructure sites and electron density map under WinCoot also shows continuous electron density resembles a predominantly α-helical polypeptide chain, thereby confirming the validity of the heavy-atom substructure and its handedness. **(Figure 3-19)**

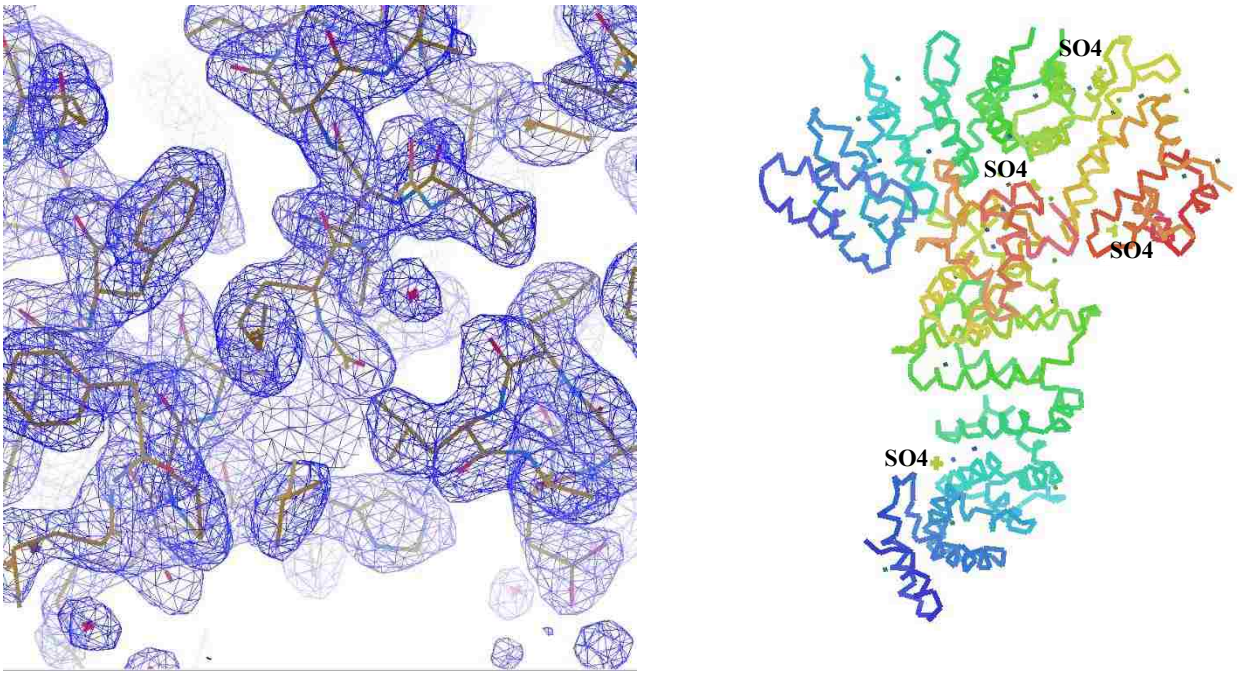

Figure 3-19 Structure of pR452 solved using sulfur SAD
(Left), real-space 2.2Å pR452 electron density map, contoured at 1.5σ, superimposed on the structure of pR452 in the crystal lattice. **(Right)**, structure of pR452 (rainbow) superimposed on the heavy-atom substructure consisting of 40 sulfur sites (green dots) in the asymmetric unit. 4 sulfate molecules are labelled.

The initial model built by phenix.AutoBuild program correctly traced 16% of the structure in the asymmetric unit. After removing all the questionable residues, the main chains were retraced manually with sigma-weighted $2F_o$-F_c map at 3.4Å using WinCoot, initially around the sulfur substructure sites (cysteines and methionines) and the Autobuild model. Two pR452 molecules can be outlined in an asymmetric unit. The starting phases were further refined and extended to 2.2 Å by phenix.refine using a dataset collected at 0.979Å/12.7keV, termed "native" dataset, and the partially-build model from sulfur-SAD phasing. Fragments of additional main chains were constructed after iterations of manual model rebuilding with WinCoot and refinement with phenix.refine program. The registry of the sequence was determined from the residues around the sulfur sites or bulky residues (W, F, Y, etc.) at both chains. The final model confirmed that 40 sulfur sites in the initial sulfur substructures corresponded to the 9 methionine and 9 cysteine residues from each Ric-8A molecule in the asymmetric unit, while the four remaining sites corresponded to sulfate ions from the reservoir solutions (Li_2SO_4). Met-426 was not

located possibility due to its location at the flexible C-terminus of the structure. In addition, the NCS refinement was only carried out in the first few refinement cycles since the 2 molecules in the asymmetric unit are not identical (RMSD of C_α=0.718 between chain A and B). The final refinement statistics, including correlation coefficients, show good agreement between the Ric-8A model and experimental native dataset **(Table 3-3)**.

The crystal structure of pR452 consists of ~425 residues in the final model, which is composed of nine ARM and HEAT repeat domains **(Figure 3-20)**. The phosphorylation sites at S435 and T440 were part of the flexible C-terminal region and not observed in the electron density map. Based on this structural information, insights regarding the biological function of Ric-8A and its complex with Gαi1 will be discussed in the next section.

Data collection	Native	Sulfur SAD	Oil-immersed
Wavelength (Å)	0.979	1.77	0.980
Resolution range (Å)*	31.05 - 2.2 (2.28 - 2.2)	29.1 - 3.41 (3.72-3.40)	39.65 – 2.3 (2.382 – 2.3)
Space group	$P2_12_12_1$	$P2_12_12_1$	$P2_12_12_1$
Unit cell dimensions			
a, b, c (Å)	67.0 103.6 141.5	66.8 103.4 141.8	63.30 100.1 130.0
Total reflections*	324978 (22568)	11088284 (1536621)	977649 (98737)
Unique reflections*	50537 (4980)	25770 (6848)	37176 (3675)
Redundancy*	6.4 (4.5)	785.9 (803.4)	26.3 (26.9)
Completeness (%)*	99.4 (99.2)	99.5 (100)	99.11 (99.19)
Mean I/σ (I)*	15.4 (2.2)	118.3 (67.1)	30.72 (4.55)
Wilson B-factor	32.8	83.3	41.0
R_{meas}†,*	0.10 (0.58)	0.22 (0.37)	0.09 (1.04)
$R_{p.i.m}$†,*	0.04 (0.28)	0.008 (0.013)	0.02 (0.20)
$CC_{1/2}$†	1.0 (0.32)	1.0 (0.98)	1 (0.95)
Anomalous CC† (%)		58.4	
Bijvoet ratio§		1.22	
Refinement			
R_{work}†,*	0.230 (0.373)		0.211 (0.247)
R_{free}†,*	0.276 (0.404)		0.260 (0.338)
CC_{work}†*	0.959 (0.353)		0.957 (0.901)
CC_{free}†*	0.924 (0.263)		0.930 (0.780)
Number of total atoms			
protein	6671		6445
ligands (ions)	20		0
solvent	202		96
total protein residues	843		813
RMS deviations			
bond lengths (Å)	0.005		0.003
bond angles (°)	1.01		0.58
Ramachandran favored (%)††	97		98
Ramachandran allowed (%)††	3		2
Ramachandran outliers (%)††	0		0
Rotomer outliers (%)††	0.14		0
Clash Score††	6.95		6.51
Average B-factor			
Macromolecules	47.3		50.6
sulfate	75.9		N/A
water	42.9		49.91

Table 3-3 pR452 crystal data collection and refinement statistics

*Data for highest resolution shell are given in brackets. † $R_{meas}=\sum_{hkl}(n/n\text{-}1)^{1/2}\sum_i |I_i(hkl)-\langle I(hkl)\rangle|/\sum_{hkl}\sum_i I_i(hkl)$, where $I_i(hkl)$ is the ith observation of the intensity of the reflection hkl and $\langle I_{hkl}\rangle$ is the mean over n observations. $R_{p.i.m.}=\sum_{hkl}(1/n\text{-}1)^{1/2}\sum_i |I_i(hkl)-\langle I(hkl)\rangle|/\sum_{hkl}\sum_i I_i(hkl)$. § $R_{work}=\sum_{hkl}||F_{obs}|-|F_{calc}||/\sum_{hkl}|F_{obs}|$, where F_{obs} and F_{calc} are the observed and calculated structure-factor amplitudes for each reflection hkl. R_{free} was calculated for 5% of the diffraction data that were selected randomly and excluded from refinement. Correlation coefficients: $CC=\Sigma_i((x_i-\langle x\rangle)(y_i-\langle y\rangle))/(\Sigma_i((x_i-\langle x\rangle)^2(y_i-\langle y\rangle)^2)^{1/2}$, where x_i and y_i are the ith of n observations of quantities whose mean values are $\langle x\rangle$ and $\langle y\rangle$; for $CC_{1/2}$, x_i, and y_i correspond to intensity measurements derived from each of two randomly selected half-data sets from the set of unmerged data; For CC_{work} and CC_{free} x_i and y_i refer to observed structure factor amplitudes and structure factor amplitudes computed from the refined atomic model, respectively, for the working data set and the set used to compute R_{free}. $CC_{ano}=\langle\Delta_{ano}\Delta_{ano,obs}\rangle/(\langle\Delta^2_{ano}\rangle^{1/2}\langle\Delta^2_{ano,obs}\rangle^{1/2}$, where Δ_{ano} and $\Delta_{ano,obs}$ are the anomalous structure factor amplitude differences ($F^+ - F^-$), respectively, computed from the anomalously scattering atomic substructure, and the observed anomalous differences. CC_{ano} was calculated using data truncated to d_{min}= 3.4 Å. §Bijvoet ratio $[(\langle|F^{+/-}|\rangle)/(\langle F\rangle)]$, was calculated using James Holton's xtalsize server (http://bl831.als.lbl.gov/xtalsize.html). ††Calculated using MolProbity (Chen et al., 2010). **Anomalous correlation coefficient was calculated using data truncated to d_{min}= 3.4 Å.

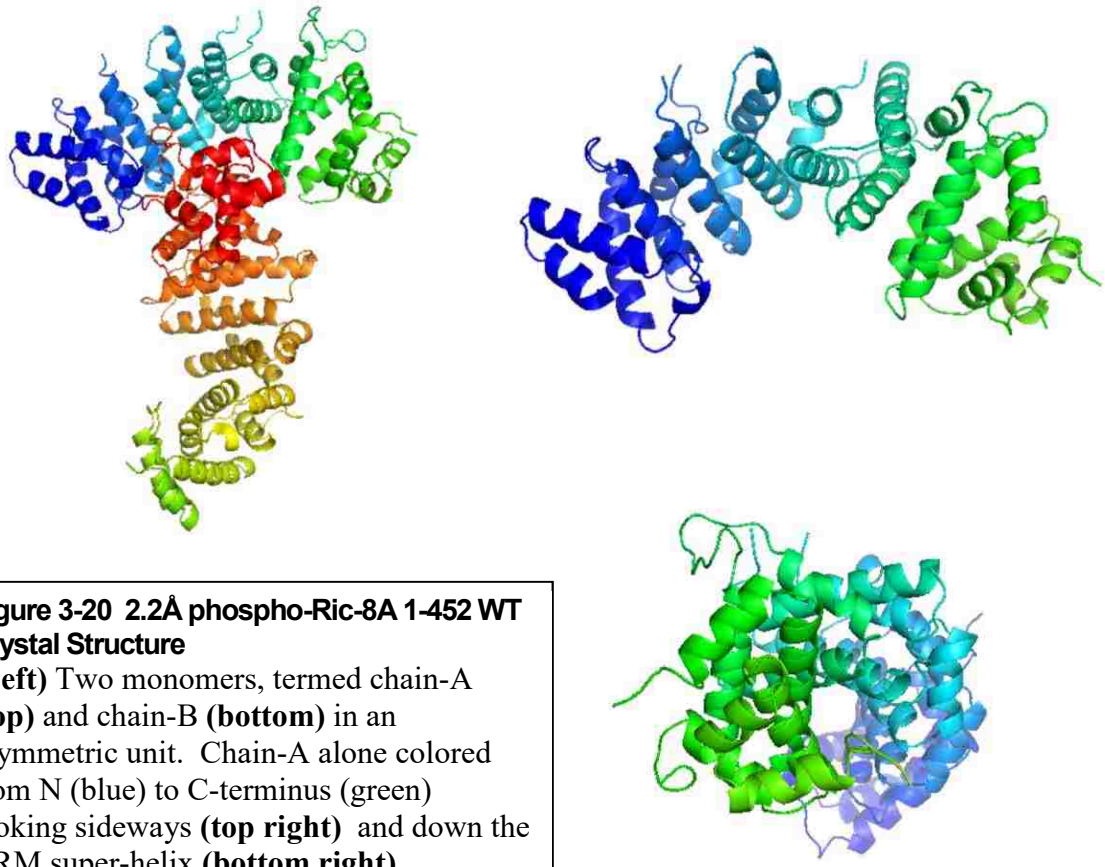

Figure 3-20 2.2Å phospho-Ric-8A 1-452 WT Crystal Structure
(Left) Two monomers, termed chain-A **(top)** and chain-B **(bottom)** in an asymmetric unit. Chain-A alone colored from N (blue) to C-terminus (green) looking sideways **(top right)** and down the ARM super-helix **(bottom right)**

3.2.12 "Oil-Immersed" pR452 Crystal Structure Shows Large Unit-Cell Variance but Small Structural Rearrangements

Experiment performed by Tzanko Doukov from the SSRL showed that immersion of crystals in Paratone-N oil before data collection results in shrinkage along the a, b and c axis of 4Å, 6.5Å and 11.5Å, respectively, an observation which indicated either high water content of the crystals and/or alternative packing of protein molecules in the shrunken crystals. Using the pR452 structure determined from the regular cryo-protectant protected crystals as starting model for molecular replacement, we determined another crystal structure of Ric-8A 452 WT, which showed subtle conformational changes induced by compression and/or dehydration of crystals by oil. Since the second (oil immersed) structure differed slightly from the first (native) structure, molecular replacement (MR) by "phenix.Phaser-MR (simple one-

component interface)" resulted in a near-complete model (LLG = 578.471, TFZ = 25.9). Iterations of manual model building mostly focused on small adjustments of side-chain orientations to improve R_{work} and R_{free} values.

Lattice compaction by Paratone-N soaking resulted in little distortion of the structure itself (RMSD at Cα positions = 0.61Å and 0.66Å for chains a and b, respectively). Rather, symmetry-related molecules within underwent relative translations and reorientations within the lattice that largely preserve the original molecular packing. The crystals used to collect the "oil-immersed" data set with the most unit cell shrinkage were left soaked in Paratone-N in a cold room overnight. ARM repeats in the core region (residues 162 to 282) remained relatively unchanged while helices in the N and C-termini underwent more pronounced shifts in the oil structure. Loop regions were slightly stabilized compared to the unshrunk structure. **(Figure 3-21)**

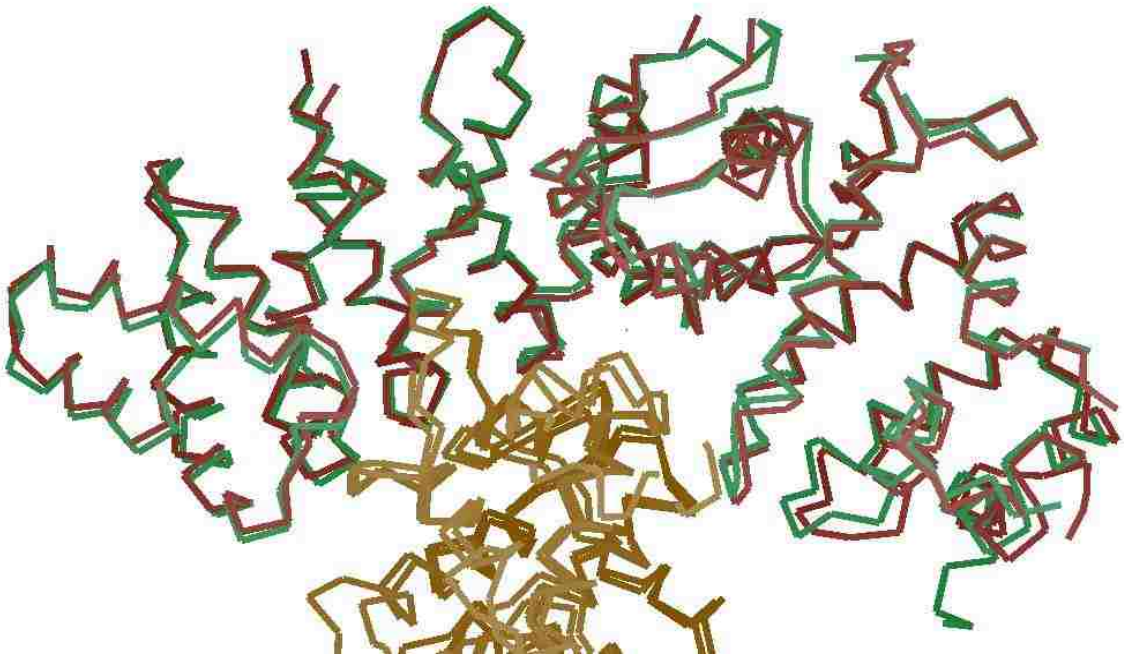

Figure 3-21 Chain-A conformation changes induced by soaking, harvesting, and cryo-protection of Ric-8A crystals in Paratone-N
Crystal structure of chain-A in regular cryo-protectant (red), PEG-400, superimposed on chain-A of "oil-immerse" structure (green) showing unchanged core region. Chain-Bs from both structures are in (coffee).

3.2.13 Structural Analysis of pR452 Crystal Structures

Two slightly different structures of pR452 were determined, a regular cryo-protectant (20% PEG-400) harvested structure and an oil-immersed and cryo-protected (Paratone-N) structure. Data collection and refinement statistics were recorded in **Table 3-3**. Refinement statistics of the initial model built using the merged sulfur SAD data set was not shown because the model was very incomplete and not further refined. In both crystal structures, chain B of the model was more complete than chain A both at the C-terminus and loop regions, therefore, I will be referring to chain B for the remainder of the discussion on pR452 structure.

3.2.13.a Overall Shape, Dimensions, and Residues Built-in/Omitted in the Model

Using the PyMol script, "Draw_Protein_Dimensions.py", an approximate, rectangular minimal bounding box (MBB) was drawn and the dimensions measured. Viewed from one angle, the structure is 93.3Å wide, 50.9Å tall, and 41.4Å deep. **(Figure 3-22)**

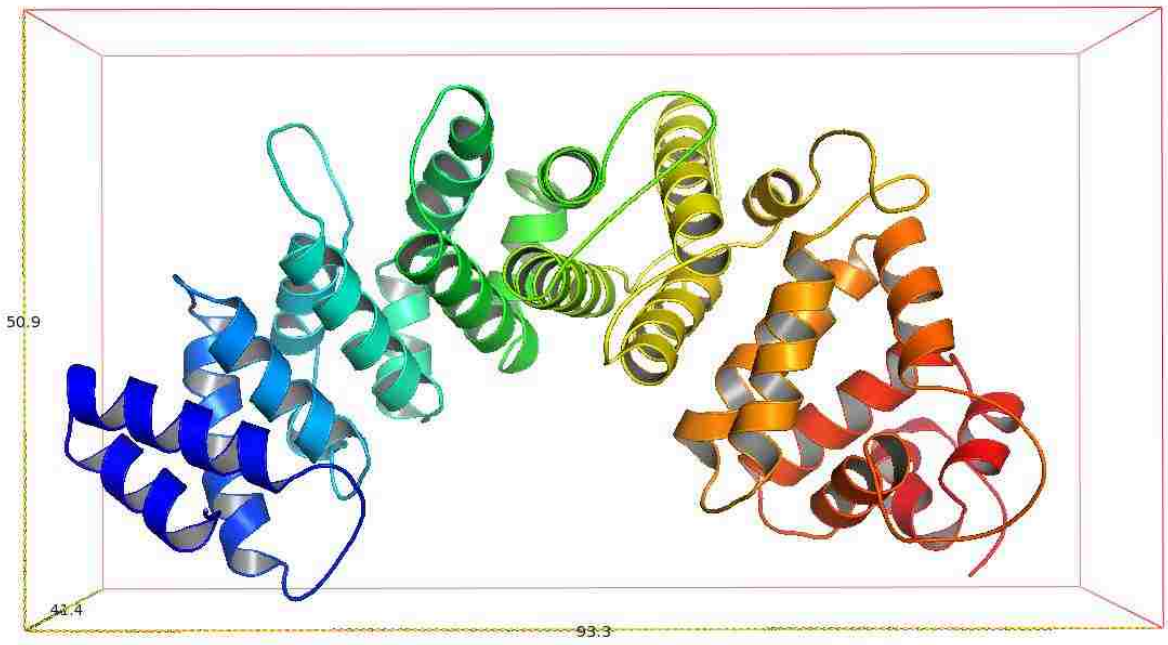

Figure 3-22 Dimensions of pR452 crystal structure
Chain B of pR452 crystal structure enclosed in an approximate minimal bounding box (MBB) to extract the dimensions. The image is generated by PyMol script "Draw_Protein_Dimensions.py". The lengths are in Å.

Based on sequence-based computational analysis, Ric-8A was predicted to comprise mainly Armadillo (ARM) repeats which form a superhelix. (48) The crystal structure of pR452 is mainly α-helical as predicted, yet in contrast to an all ARM repeat protein, comprises both two-helix HEAT motifs and three-helix ARM motifs. **(Figure 3-23)** For the three-helix ARM repeats, the second helix serves as a linker between the nearly antiparallel first and third helix.(76) Using another PyMol script, "draw_rotation_axis.py", a rotation axis was drawn for each adjacent HEAT or ARM repeat pair with the rotation angle and vertical translation distance along rotation

axis calculated. **(Table 3-4)** The rotation angles between adjacent repeat pair are small (20° to 40°) for the first five pairs and larger (60° to 110°) for the last three pairs. The vertical transition distance between repeats of pairs are very similar (9.8Å to 13.3Å) throughout the model. Using the "get_area" command built in PyMol, the buried solvent assessible surface area (SASA) intra- and inter- repeats are calculated. **(Table 3-4, Figure 3-23)** (30) SASA's buried by the structural elements of each repeat (intra-repeat SASA) range from 560Å^2 to 2250Å^2 with the first, second, and last repeats burying the least amount of SASA due to the sizes of these repeats. The last repeat is also the beginning of a highly disordered C-terminus, therefore, comprises secondary structural elements packed far less tightly than preceding repeats. For the same reason, SASA's buried between repeats (inter-repeat SASA) of pairs are quite uniform (1950Å^2 to 2490Å^2) with the exception of the last pair (1550Å^2), suggesting that the entire pR452 structure undergoes very limited dynamic motions except the C-terminus (residue 430-452, of which electron density is not observed).

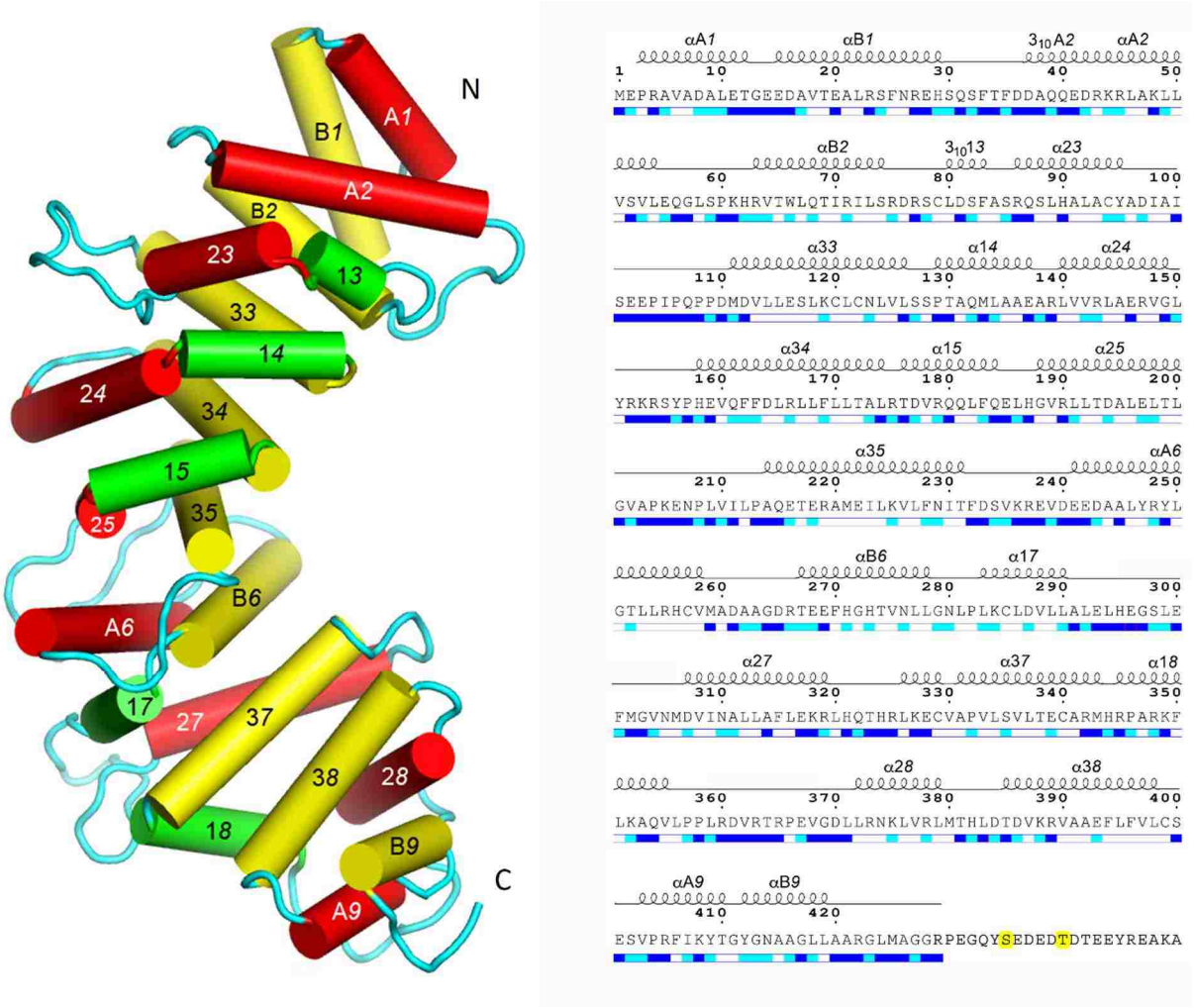

Figure 3-23 HEAT or ARM repeats in the pR452 crystal structure

(Left)pR452 comprises 9 Armadillo/HEAT repeats. HEAT repeats (repeat *1*, *2*, *6*, and *9*) are composed of two helices (labelled A and B); the N-terminal and C-terminal helix of each repeat is colored red and yellow, respectively. Armadillo repeats (repeat *3*, *4*, *5*, *7*, and *8*) comprise three helices (labelled with 1, 2, and 3); the first, second, and third are colored green, red, and yellow, respectively. **(Right),** sequence composition of secondary structural elements. α-helical secondary structure is shown as a series of loops above the amino acid sequence. Helices with 3_{10} hydrogen bonding and geometry are so labeled. Straight-line sections indicate loop segments. No electron density is observed beyond residue 423 (molecule A) and 429 (molecule B). The two phosphorylation sites, S435 and T440, are highlighted in yellow. Blue and cyan bars shown below the amino acid sequence indicate residues that are solvent accessible (blue), partially accessible (cyan) or buried (white). Figure modified from output from ESPript 3.0 server: http://espript.ibcp.fr (30)

Intra-repeat parameters				Inter-repeat parameters			
repeat	residue range	Repeat type	Intra-repeat SASA (Å^2)	transition	Rotation (°)	Center-Center (Å)	Inter-repeat SASA (Å^2)
1	1-36	H	836	-	-	-	
2	37-76	H	953	1→2	39	10.6	2043
3	77-128	A	1415	2→3	22	9.8	1978
4	129-174	A	1338	3→4	31	10.9	2191
5	175-236	A	1695	4→5	34	11.3	2342
6	237-282	H	1200	5→6	40	11.4	2490
7	283-344	A	2250	6→7	78	13.3	1948
8	345-400	A	1791	7→8	61	12.7	2193
9	401-429	H	556	8→9	114	11.7	1551

Table 3-4 pR452 HEAT and ARM repeats
Intra-repeat and inter-repeat parameters including solvent assessible surface area, rotation angle, translation displacement are calculated.

Generally, for structural model refinement of any protein molecule, the electron density at the loop regions that connect α-helices or β-strands is usually more equivocal than the helices. Yet, most of the loops in the pR452 structure were reasonably modeled although with comparably higher B-values than those of helices; no large segments of connecting loops adopt significant alternative conformations in the crystal lattice with the except of the C-terminus. An interesting observation is that all visible loops seem to project towards the convex surface of pR452. The longer loops (>10 residues) connect helical elements intra-repeat, rather than between HEAT or ARM repeats.

Unfortunately for the more sought-after functional assessment of pR452, the phosphorylation sites were not visible in either chain of the two structures due to their location at the C-terminus. According to secondary structure prediction by DISOPRED3 predictor, the unmodelled C-terminal region of pR452 contains a region of ~20 residues that has high probability for adopting

a highly disordered conformation, therefore, also has a high potential to serve as a protein-protein interactive site(21). **(Figure 3-24)** Interestingly, the N-terminal helices are all unexpectedly well-ordered while biochemical data on the N-terminal truncations of Ric-8A suggests crucial GEF-functional motif(s) at the extreme N-terminus(42).

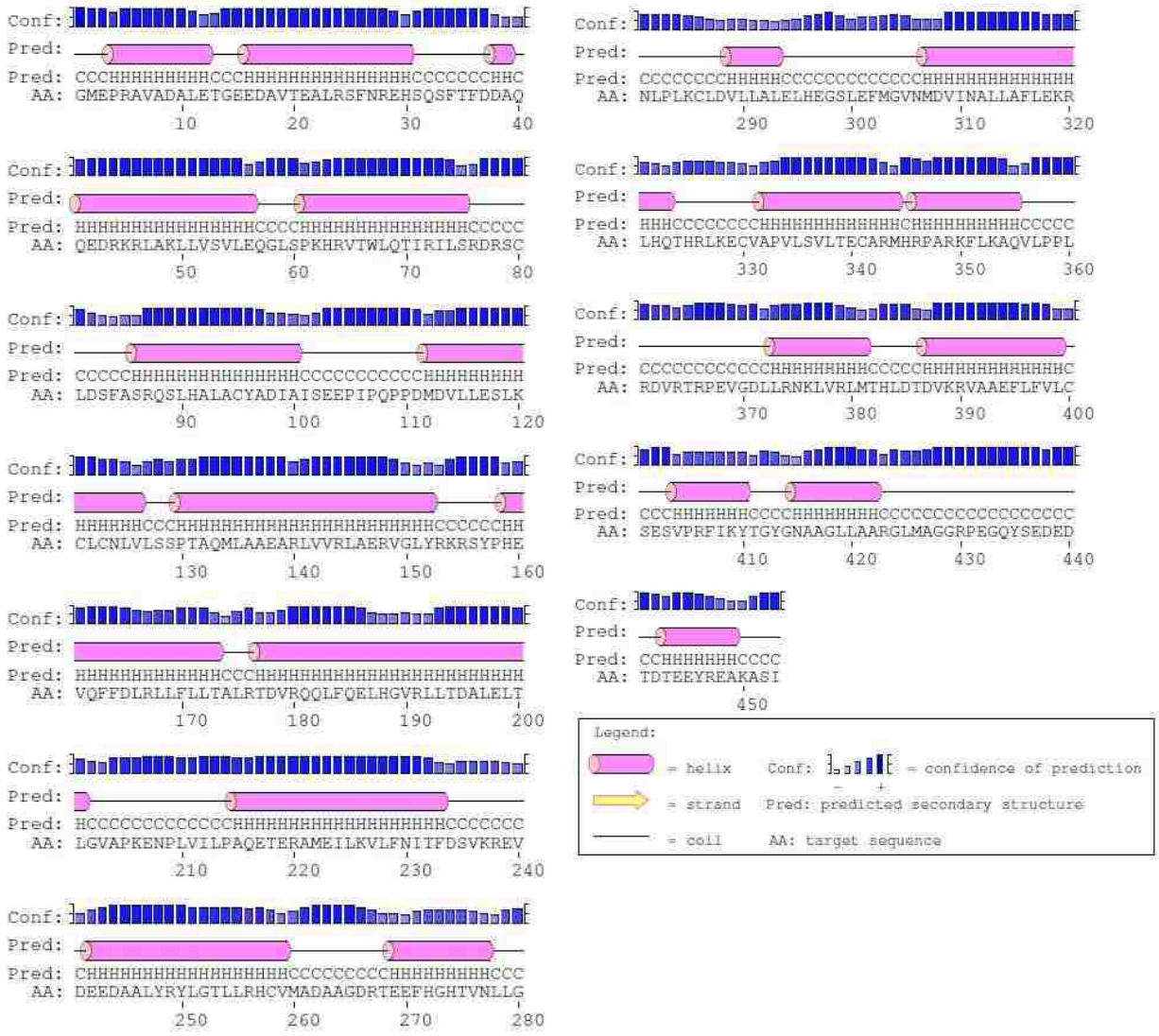

Figure 3-24 DISOPRED3 analysis of predicts composition of Ric-8A 1-452 secondary structure elements

Residues 284-289 in α17 form an unusually long 3_{10} helix and is observed in both chain A and chain B in the asymmetric unit. L283, L286, and L289 are all aligned, and the 3_{10} conformation of this stretch of residues allows those residues all to project into a hydrophobic pocket. **(Figure**

3-25) 3_{10} helices are not uncommon in HEAT/ARM repeat proteins such as importin-β, however, are typically 3-4 residues long to make up one α-helical turn. (83) Although importin-β also contains a long 3_{10} helix, no amount of attention was directed to its function other than stating it as a repeat-connecting helix(83). Without direct structural data of a Ric-8A:Gαi1 complex, we cannot draw any conclusion about the 3_{10} helix either.

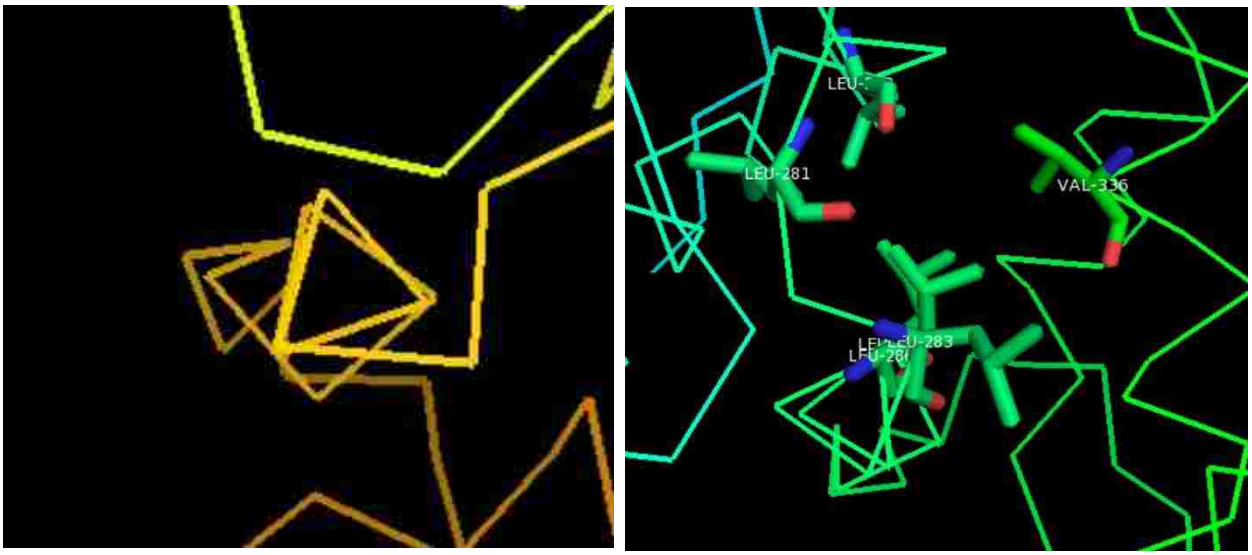

Figure 3-25 A 3_{10} helix on pR452 crystal structure
(Left), "ribbon" presentation of the 3_{10} helix showing three residues per helical turn. **(Right)**, three leucine residues aligned by the 3_{10} conformation and projected into a hydrophobic pocket.

3.2.13.b Crystal-Packing in the Lattice

The two C-shaped molecules of pR452 in the asymmetric unit are related by a 110° rotation and a 29Å translation about an axis that passes obliquely through the ***ab*** plane of the unit cell. This packing interaction arises from an extensive interface formed by α1*8* and αA*9* motifs of molecule B with the C-shaped cavity formed by multiple Armadillo/HEAT repeats of molecule A. The corresponding surface of molecule B forms similar, but less intimate contacts with the α1*8* and αA*9* motifs of a symmetry-related copy of Molecule A. It is interesting that the C-

termini of both molecules of the asymmetric unit appear to be extended. That of chain B projects into a solvent-filled cavity formed by symmetry-related chain A and is disordered beyond residue 429. The C-terminus of Molecule A is disordered beyond residue 423, where it likewise projects into a large cavity between symmetry-related molecules. Thus, no electron density is observed for phospho-Serine 335 and phospho-Threonine 440, which are solvated within the crystal lattice.

3.2.13.c Mapping of Properties on the Structure of pR452

In the absence of direct Ric-8A:Gαi1 complex structural information, amino acid sequence conservation scores, protection factors from hydrogen-deuterium exchange experiments, and the distribution of electrostatic potential, provide clues to the function of residues exposed on the surface of pR452.

Using the CONSURF server (61) to rank the conservation of amino acids for a broad selection of Ric-8A and Ric-8B homologs, we assess the general importance to the function of all members of the Ric-8 family. Generally, residues within the concave surface of pR452, formed largely by the αB and α3 helices of HEAT and Armadillo repeats, respectively, are evolutionarily conserved. **(Figure 3-26)**

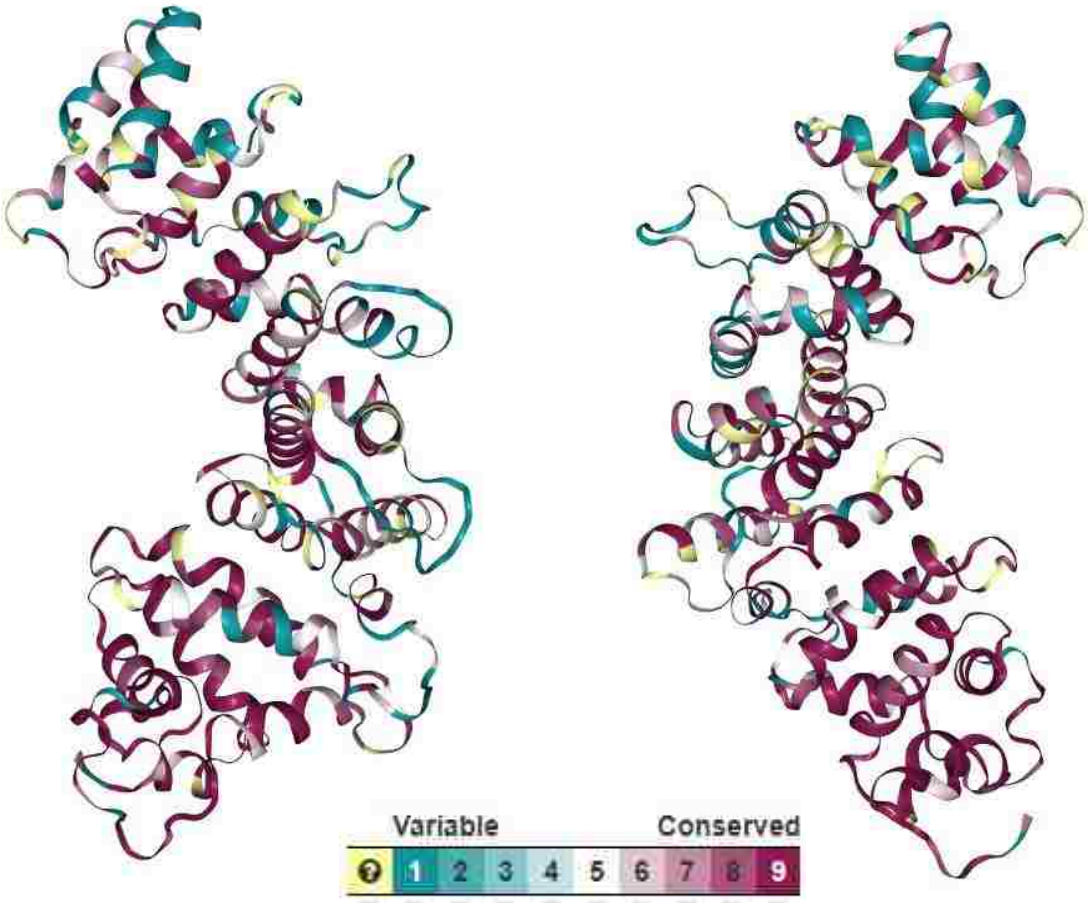

Figure 3-26 pR452 structure viewed from two angles and rendered with amino acid conservation scores calculated by CONSURF server
Yellow residues have unreliable conservation scores due to insufficient data in the multiple sequence alignment.

The electrostatic contact potential map rendered at the molecular surface of R452 reveals dispersed and non-contiguous regions of positive and negative charge density. Exceptions are of negatively charged surface near the N-terminus of the molecule and a striking positively charged surface near the C-terminus **(Figure 3-27)**. The latter arises from a constellation of ten arginine and lysine side chains projecting from α1*8* and αA*9*, all but two of which are highly conserved among Ric-8 homologs. Notably, the conserved Arg345/R348/K349 triad forms the binding site for a sulfate ion from the crystallization buffer and may serve as a recognition site for one of the C-terminal phosphorylated serine or threonine residues.

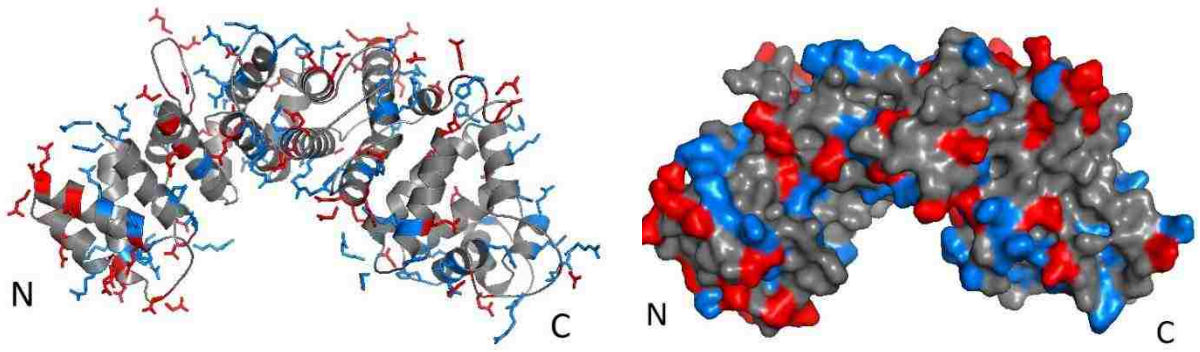

Figure 3-27 Charged residues on pR452
(Left), the charged side-chains are shown as sticks and colored red and blue for negative and positive charges, respectively. **(Right)**, the same color scheme is applied on the electron density surface of pR452.

Now with the actual crystal structure in hand, we mapped the HDX protection profile of Ric-8A by Gαi1 on the structure using the PyMol script, "spectrumany.py". Changes in hydrogen/deuterium exchange (HDX) rates upon Gαi1 binding have been determined for R491, a highly active GEF (10). Two distinct surfaces, the first formed by residues in α2*3*, α1*4* and α1*5*, and the second by residues in α3*7* and α1*8*, are protected to different degrees, by Gαi1 **(Figure 3-28)**. Projection of evolutionary conservation scores of Ric-8A homologs **(Figure 3-26)** onto the structure of pR452 shows that residues that comprise these protected structural elements are not more highly conserved than other positions in the multiple sequence alignment. An exception is the contiguous surface that is partially or wholly encompassed by the V-shaped helical hairpin formed by α3*7* and α1*8* for which the average conservation score exceeds 7 and the mean protection factor is -8%. We propose that this surface, which partly overlaps the positively charged region described above, harbors a Gαi1 binding site, or is otherwise occluded upon Gαi1 binding.

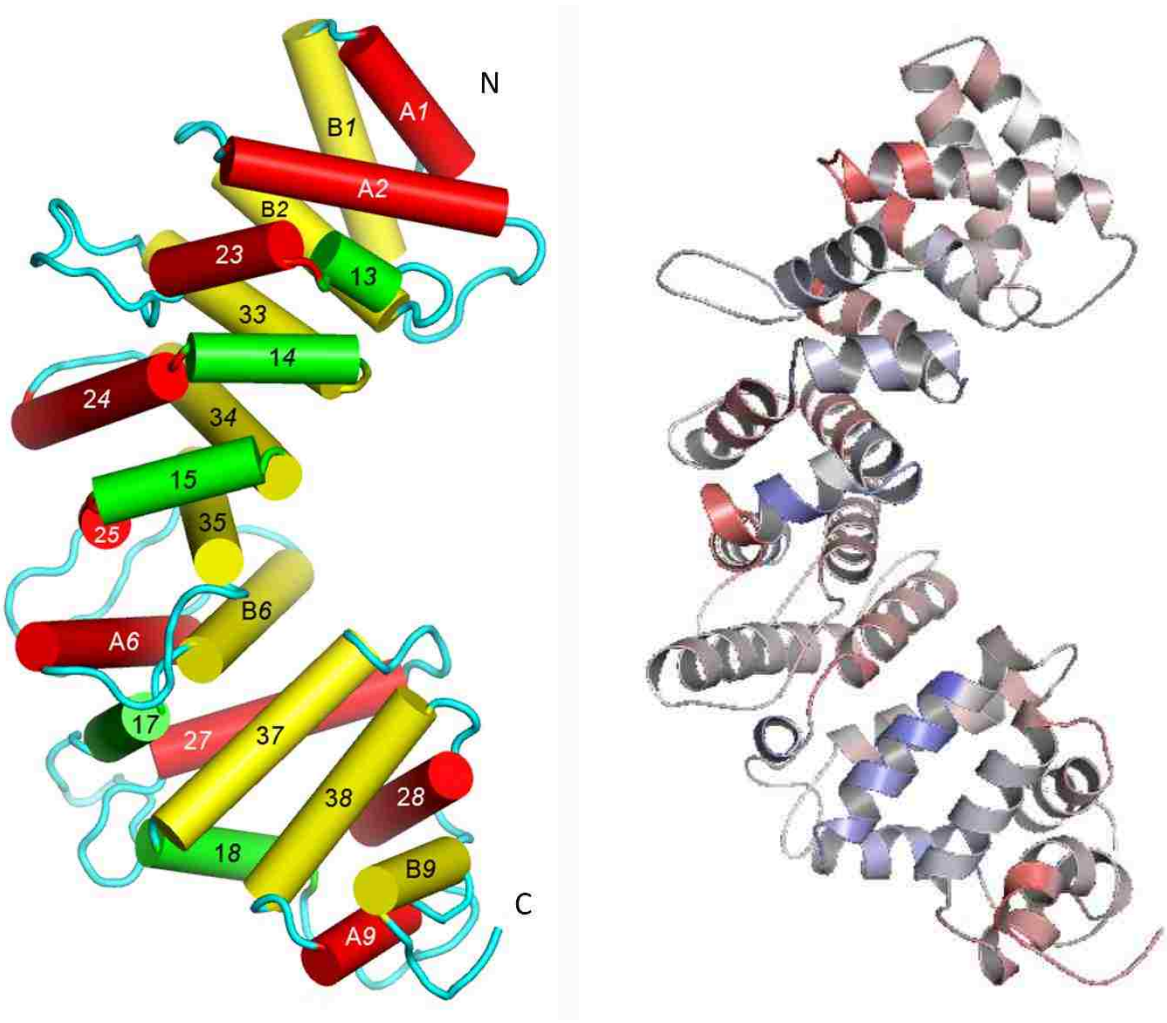

Figure 3-28 Mapping of HDX Protection and Evolutionary Conservation Profiles on the Structure of pR452

Helix key **(left)** is oriented to the same viewing angle as the HDX protection factors-rendered map **(right)** for easy reference. Gradients of blue and red indicate regions that are HDX-protected and deprotected, respectively, by Gαi1-binding.

3.3 Materials and Methods

3.3.1 Protein Expression and Purification

3.3.1.a Myristoylated Gαi1 (mGαi1) and Ric-8A 1-491 WT

Myristoylated Gαi1 (mGαi1) and Ric-8A 1-491 used for nucleotide-binding and steady-state GTPase assays were expressed and purified as described in Chapter II. Expression and purification of full-length Ric-8A (1-530) is discussed in detail in Chapter V.

3.3.1.b Rat Ric-8A 1-452, 1-470, 1-425, 1-401

Rat Ric-8A 1-452 construct, which will be referred as R452 for simplicity, was expressed and purified as described (42) with some alterations. Briefly, the N-terminal hexa-histidine-tagged protein construct **(Figure 2-19)** in pET28a expression vector is expressed in *E. coli* BL21 (DE3)-RIPL cells in TB media containing kanamycin (100mg/L) and induced with 50μM isopropyl β-D-1-thiogalactopyranoside (IPTG) at 20ºC. After cell lysis and fractionation in lysis buffer (50mM Tris, pH 8.0; 250mM NaCl; 5% Glycerol; 2mM β-mercaptoethanol; 2mM PMSF), N-terminally His-tagged Ric-8A is isolated from the soluble faction using a gravity Profinity IMAC(Bio-Rad) column and eluted with elution buffer (50mM Tris, pH 8.0; 250mM NaCl; 5% Glycerol; 2mM β-mercaptoethanol; 2mM PMSF; 300mM Imidazole). The concentrations of imidazole and NaCl in the buffer are reduced by two rounds of dialysis in Q-buffer A (50mM Tris pH 8.0, 5mM β-mercaptoethanol, 50mM NaCl, 5% glycerol); TEV protease is added to the protein sample after the first round of dialysis and the proteolysis reaction proceeds for the duration of the second round of dialysis. The protein sample is further purified by first passing through a fresh IMAC column (Bio-Rad) again to recover TEV-cleaved Ric-8A. The IMAC flow-through is then loaded onto a HiTrap Q XL anion exchange column (GE Healthcare) and

eluted with a NaCl gradient (0mM to 500mM). Tag-less R452 eluted at about 200mM NaCl and is already at high purity after elution from anion exchange column. A final polishing step using a Superdex 200 10/300 GL size-exclusion chromatography column (GE Healthcare) is used to isolate monodisperse, monomeric Ric-8A from aggregated protein and to buffer exchanges the sample into crystallization buffer (50mM HEPES, pH 8.0, 150mM NaCl and 1mM TCEP) right before sample crystallization. Several other Ric-8A truncation constructs including 1-470, 1-425, and 1-401 were expressed and purified in similar fashion as R452.

3.3.1.c Seleno-Methionine Derivative of R452 (SR452)

To obtain important phase information for Ric-8A, which has no suitable homology model in the protein data bank (PDB) for molecular replacement (MR), multiple attempts were made towards crystallizing a seleno-methionine derivative of R452 (SR452). Briefly, the pET28a expression plasmid containing the hexa-His-R452 construct is transformed into either B834(DE3) (Novagen) competent cells or T7 Express Crystal (NEB, discontinued on January 02, 2018) competent cells. The methionine auxotrophic *E. coli* expressing Ric-8A were grown using a media kit, SelenoMethionine Medium Complete (Molecular Dimensions), following the kit protocol. SR452 protein was purified using methods identical to R452.

3.3.2 Phosphorylation and Purification of Phospho-Ric-8A

Purified Casein Kinase II hetero-tetramer (CKII) is purchased from New England Biolabs (Catelog#P6010S). The kinase reaction is carried out by largely following an established protocol(1) with minor alterations. For every 10 mg of R452, powdered adenosine 5′-triphosphate (ATP) disodium salt is first adjusted its pH by mixing with 110µL of 10X reaction buffer (200 mM Tris-HCl, 500 mM KCl, 100 mM $MgCl_2$ pH 7.5 @ 25°C) to reach 10mM ATP

and then the 110µL of mixture were added to 1mL of 10mg/mL Q-column purified R452 in gel-filtration buffer (50mM HEPES, pH 8.0, 150mM NaCl and 1mM TCEP) to achieve final kinase reaction condition (1mM ATP, 20 mM Tris-HCl pH 7.5, 50 mM KCl, 10 mM $MgCl_2$, 50mM HEPES, pH 8.0, 150mM NaCl and 1mM TCEP) without heavily aggregating R452. 3000 units of CKII were then added to the mixture (1110µL) and incubated over-night (>10 hours) at room temperature (~25ºC) R452, which contains two high-affinity CKII phosphorylation site, reach >90% phosphorylation using this method. It is important to dissolve solid ATP in 10X reaction buffer first before adding to Ric-8A due to a large pH shift caused by high concentration of un-buffered ATP (di-sodium salt); R452 precipitates heavily when solution pH drops too rapidly.

Doubly-phosphorylated R452 (pR452) elutes at different NaCl concentration than contaminants, such as nucleotides, CKII or R452, on an anion exchange column. The entire kinase reaction is then re-purified with a high-resolution anion exchange column, Source 15Q (GE Healthcare), followed by a size-exclusion step using Superdex 200 SEC column (GE Healthcare) in crystallization buffer (50mM HEPES, pH 8.0, 150mM NaCl and 1mM TCEP) before crystallization. Samples of purified R452 and pR452 were sent to CBSD Mass Spectrometry Core Facility at University of Montana for LC-TOF-MS (Bruker micrOTOF) analysis. SR452 was phosphorylated and re-purified using the same approach.

3.3.3 Competition Assays with Gαi1 C18 Peptide

C18M1, a modified version of the rat Gαi1 C18 peptide (DAVTDVIIKNNLKDCGLFKK)(42), was purchased from GenScript. C18M1 was soluble in water up to 5.5mM. The peptide competition assays were performed similarly to the "GTP-binding" tryptophan fluorescence assays described in Chapter II. Briefly, 100µM of C18M1 peptide or equal volume of water

(negative control) was pre-incubated with 1μM R491 or 8μM pR452 for 1 hour on ice. Each pre-incubated mixture is then transferred to the quartz fluorescence cuvette (quartz SUPRASIL macro/semi-micro cell, PerkinElmer) with stirring at room temperature. 1μM mGαi1:GDP were added and allowed to equilibrate for 5 minutes before the addition of 10μM GTPγS. Triplicated, 10-minutes time courses of GTPγS binding events were recorded and fit to the same single exponential equation mentioned in Chapter II using SigmaPlot (Systat Software):

$y = a*(1-e^{-kt})$ *(8)*

3.3.4 Steady-State GTPase Assay

All samples (mGαi1, R452, pR452, R530, and pR530) were SEC-purified on a Superdex 200 SEC column (GE Healthcare) so they are effectively buffer exchanged into the assay buffer (50mM HEPES, pH 8.0, 100mM NaCl, 1mM EDTA, 1mM TCEP, and 10mM $MgCl_2$) before experiments. γ-^{32}P-GTP (6000Ci/mmol, 10mCi/ml, 250 μCi) was purchased from PerkinElmer. All samples were pre-warmed in a 30^{o}C water bath for 3-minutes. To start the reaction, 1μM mGαi1:GDP was added to different concentrations (10μM, 5 μM, 2.5 μM, 1.25 μM, 0.625 μM, 0.3125 μM, 0 μM) of different Ric-8A's (R452, pR452, R530, pR530) and 30μM GTP (doped with ^{32}P-GTPγS to >1000cpm/pmol GTP) to reach a 20μL final reaction volume. All reactions were allowed to proceed for 5 minutes and quenched with 180μL of cold 1M NaH_2PO_4 pH 4.0. Immediately after quenching, 200μL of quenched reaction mixture were vigorously mixed with 800μL of a suspension of cold 5% w/w Norit activated charcoal in 50mM NaH_2PO_4 pH 4.0. The 1mL of charcoal mixture were then centrifuged under 10,000 x g for 10 minutes at room temperature. After centrifugation, triplicates of 150μL of clarified supernatant solution were added into scintillation vials containing 10mL of 3a70B scintillation cocktail (RPI) and counted.

To control for residual CKII contamination, which could use GTP as a phosphate source and produce counts not originated from GTPase, a negative control was included for each Ric-8A concentration series at [Ric-8A] = 10μM, [mGαi1] = 0μM, [GTP] = 30μM.

The C18M1 peptide described in section 3.3.3 was incorporated into the steady-state GTPase assay as well. 50μM of C18M1 peptide or water control with 10μM Ric-8A on ice for 1 hour prior to performing the assays.

3.3.5 SPR Binding Assay

Using the BiaCore X100 system (GE Healthcare), we measured the binding kinetics of Gαi1:GDP to Ric-8A by anchoring hexa-Histidine-tagged Ric-8A on a Ni-NTA sensor chip (GE Healthcare) surface and flow difference concentrations of Gαi1 or buffer through the surface at a constant flow-rate and temperature while monitoring association as well as dissociation measured in response units (RU) in real time.

In preparation for the experiments, it was mandatory that all protein samples used in the BiaCore analysis were buffer exchanged into the running buffer (50mM HEPES pH 8.0, 150mM NaCl, 1mM TCEP) by passing them through a Superdex-200 SEC column (GE Healthcare); small buffer components mismatch deterred SPR data quality significantly by introducing large baseline shifts.

Each experiment consisted of three main phases, ligand anchoring and equilibration phase, analyte binding phase (“on” phase), and analyte unbinding phase (“off” phase); all experiments were carried out at room temperature under a constant flow rate (30μL/min). During ligand

anchoring, 0.1μM His-Ric-8A was applied to the Ni-NTA sensor chip surface for 5 minutes followed by a 7-minute wash with buffer to remove unbound/loosely bound ligand molecules. Once the baseline was stable, a range of concentrations (10μM, 5μM, 2.5μM, 1.25μM, 0.625μM) of Gαi1 W258A (analyte) was applied to the ligand-coated sensor chip surface for 3 minutes for the "on" phase, followed by a 6-minute wash with buffer, thereby completing the "off" phase. The Ni-NTA sensor chip surface was regenerated by first stripping the nickel cation with 350mM Ethylenediaminetetraacetic acid (EDTA), followed by double-distilled water (ddH_2O) to remove the EDTA, followed by 0.5mM $NiCl_2$, 3mM EDTA, then back to the running buffer.

Each data set contains multiple curves corresponding to the range of concentrations of analytes binding to the same Ric-8A species (R491, pR491, R452, or pR452; we do not have a His-tagged construct for the full-length Ric-8A). Using BiaCore X100 evaluation software (GE Healthcare), all kinetics curves within a data set are fitted globally using a 1:1 binding model to generate a single k_{on}, k_{off}, K_D, R_{max} and the standard deviation for each parameter, as well as a χ^2 value of the fit for the ligand, analyte pair. (85, 86, 100)

The "on" phase is fitted with the integrate rate equation:

$$R_{(t)} = \left(1 - e^{-(k_{on}*C+k_{off})*t}\right)R_{eq} \qquad (24)$$

And the "off" phase with:

$$R_{(t)} = \left(e^{-k_{off}*t}\right)R_{eq} \qquad (25)$$

where $R_{eq} = \left(\frac{k_{on}*C}{k_{on}*C+k_{off}}\right)R_{max}$ (26)

R_{max} = Maximum possible relative response (RU) if all ligand molecules on the chip are saturate with analyte. A theoretical value that is not attainable for a non-zero k_{off}.

R_{eq} = Relative response (RU) at equilibrium for each "on" curve. Depending on k_{off}, R_{eq} could be smaller or equal to R_{max}.

k_{on} = Pseudo-first order "on" rate in ($M^{-1}s^{-1}$), a C-dependent value if R_{max} is C-dependent

k_{off} = "Off" rate in (s^{-1}), a C-independent value

C = Analyte concentration in (M)

$R_{(t)}$ = Relative response (RU) at time t

t = Elapsed time in seconds

3.3.6 Protein Crystallization and Optimization

3.3.6.a Ric-8A 491

The protein sample in gel-filtration buffer (50mM HEPES pH 8.0, 150mM NaCl, 1mM TCEP) was concentrated to 20mg/mL before setting up initial crystal screens in commercial screening blocks including PEG-I, PEG-II, JCSG-I, JCSG-II, JCSG-III, JCSG-IV, Wizard, Morpheous, ProPlex, etc. (Qiagen, Hampton Research, Molecular Dimensions) The crystal screens were set up on an Intelli-Plate 96 (Art Robbins Instruments) using a Crystal Gryphon robot (Art Robbins Instruments), which rapidly sets up plates containing up to 96 screening conditions under 15 minutes/plate. For each condition, a 0.5µL sitting drop was set up by spotting 0.25µL sample on 0.25µL reservoir solution and sealed with ClearSeal Film (Hampton Research) immediately after plate setup.

3.3.6b Ric-8A Truncation Constructs

R470 and R452 were screened similarly to R491. Screening of R425 and R401 constructs were not started until we saw R452 crystallizing, therefore, these shorter constructs were not screened using the full arsenal of initial screening conditions; instead, PEGs-II suite and an in-house R452 screening suite were used. The in-house R452 screening suite was created using Scorpion Screen Builder (Art Robbins Instruments). It screens around the original crystallization condition (0.1mM Tris pH 8.5, 0.2M Li2SO4, 30% w/v PEG 3350) by only fixing the Li_2SO_4 concentration at 0.2M and varying the pH of buffer (pH 7.0 to pH 8.5), percentage of PEG 3350 (25% to 30% w/v), and the types of pH buffers (Bicine, Bis-Tris Propane, EPPS, HEPES, TAPS, TES, Tricine, Tris) with good buffering capacity at the desired pH range. Seleno-methionine derivatized R452 and R452 C329S mutant, on the other hand, were screened using the full set of initial screening suites mentioned in section 3.2.8a.

3.3.6.c Phospho-Ric-8A 1-452

pR452 as well as pR452 C329S mutant were screened in the same fashion as R491. After seeing no new crystallization conditions besides those for R452, both WT and pR452 C329S proteins become the primary targets for aggressive condition optimization trials. Based on the original condition, we varied the concentration of Li_2SO_4, length and concentration of PEGs, type and pH of 100mM pH buffer by creating in-house screening blocks using the Scorpion Screen Builder (Art Robbins Instruments). We also attempted additive screening and detergent screening using commercial screening suites from Hampton Research. Finally, we varied the incubation temperature (20ºC, 12ºC, and 4ºC), drop size (0.5µL and 1µL) as well as the volume ratio of protein-to-reservoir (i.e. 1-part sample to 2-part reservoir, 1 to 1, 2 to 1, etc.) in the hope of changing the kinetics of nucleation and crystal growth. Larger hanging drops were also set up by

hand on Greiner pre-greased 24 well Combo Plates (Molecular Dimensions). Seeding experiments using conventional seeding methods such as streaking seed crystals into fresh crystallization drops with a cat-whisker or micro-seeding methods such as the seed-beads method described here (112) were performed.

3.3.7 pR452 Experimental Phasing Using Heavy-Atom

Without a suitable homology model to perform molecular replacement, we attempted to solve the phase problem using conventional heavy-atom soaking. I will not go into detail about all the different types of heavy-metals or metal-containing compounds we have tried using different soaking method. In general, we follow established soaking protocols as described(13). Briefly, protein crystals were either slow-soaked by adding heavy-atom-containing mother liquor or cryo-protectant solution (recipe of mother liquor and cryo-protectant solution varies for crystals picked from different wells of crystallization plate, see details in section 3.2.10) of different heavy-atom concentrations to crystals in the drop and incubated for 1 to 24 hours or fast-soaked for 1 to 20 minutes. The soaked crystals were back-soaked into regular cryo-protectant to remove excess heavy-atoms before plunging into liquid nitrogen. For soaking experiments of pR452 crystals in NaBr, back-soaking rapidly reduces heavy-atom incorporation, therefore was skipped; crystals were harvested from soaking solution and flash frozen at the end of soaking experiments.

3.3.8 Crystal Harvesting and Cryo-protection

Due to rapid dehydration and crystallization of the precipitant solutions at room temperature (crystals of Li_2SO_4 form inside the Ric-8A crystallization drop after exposing to air for 5 minutes), all crystals were harvested in a 4^{o}C cold room with minimal time of air exposure. 20μm (nylon fiber diameter) mounted

CryoLoops (Hampton Research) and MicroLoops E loops (MiTeGen) were both used to harvest crystals. Two different cryo-protectants were used to harvest the pR452 crystals, a 20% PEG400 solution in the mother liquor, in which the crystals were grown, and an oil-based cryo-solution, Paratone-N (Hampton Research). To minimize ice build-up on the mounting loop, cryo-freeze techniques discussed in Pflugrath 2015 was employed during crystal harvesting.(24) Briefly, liquid nitrogen used for flash-freezing were kept devoid of ice; magnetic wands used to harvest crystals were kept dry by occasionaly heating and wiping; crystals mounted on loops spent minimal time in air and were plunged rapidly into liquid nitrogen without hovering over the liquid nitrogen.

3.3.9 Data Collection

In a collaborative effort with Brookhaven National Laboratory (BNL, NSLS-II), Tung-Chung Mou and I collected 18 high-multiplicity sulfur-SAD data sets with a low energy X-ray beam (7000eV) at NSLS-II FMX from a group of randomly orientated native pR452 crystals at 100K . These crystals diffracted up to 2.0Å resolution with sulfur anomalous signal extending to at least 3.4Å. We used the helical data collection method at NSLS II FMX, which was equipped with an Eiger16M pixel array detector with a 133Hz framing rate. The helical collection strategy increased the data redundancy and accuracy by collecting multiple 360^{o} cycles of data while moving down the center axis of crystals so that unexposed portions of the rod-shaped crystal are continuously fed through the X-ray beam path to reduce radiation damage. **(Figure 3-29)**

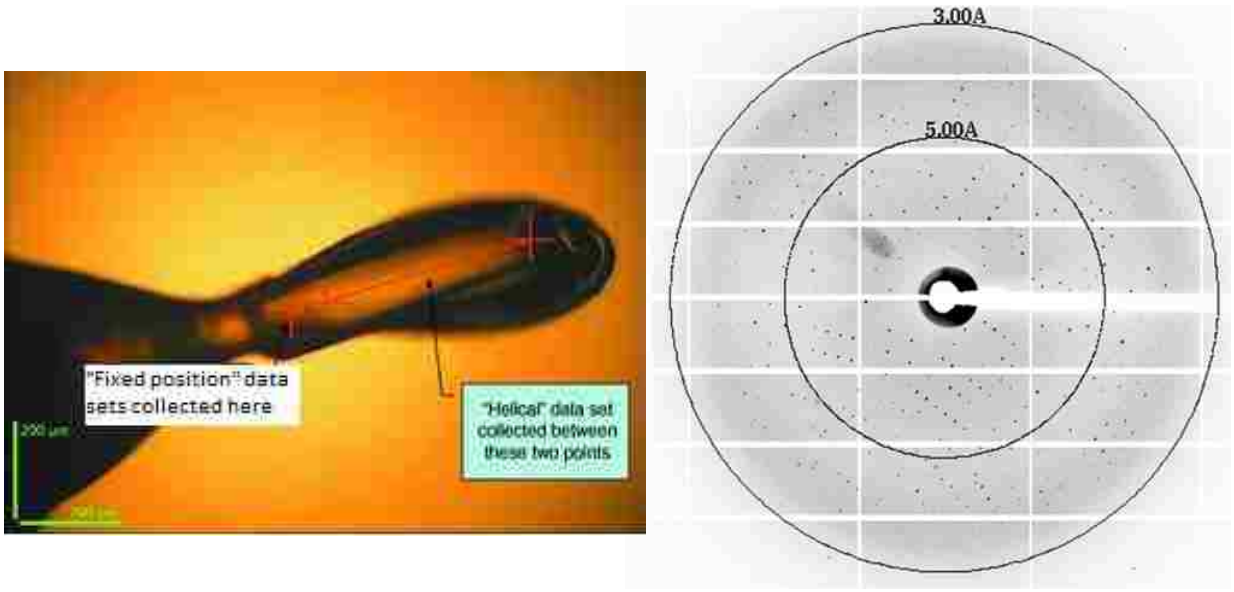

Figure 3-29 Helical data collection mode and typical pR452 crystal diffraction pattern **(Left)**, helical data collection mode using a 10 µm x 10 µm beam avoids irradiation of the crystal at a single volume of the crystal. **(Right)**, typical X-ray diffraction pattern of pR452 crystals.

The crystal-to-detector distance was set to 200 mm to measure diffraction to 2.73 Å resolution. A beam size of 10µm x 10µm was used with a flux of ~5.0 x 10^{12} photons/sec. Each crystal was collected with a thin-slice oscillation range (0.1°-0.2° per image) for a total of 360° to 5760° per dataset at 20% transmission and 0.05 – 0.1 second exposure time depending on the size of crystal and radiation damage. The differences in cell parameters are within 0.1% among these datasets, as a result, data sets collected from multiple isomorphous crystals merged well to enhance the anomalous signal.

The high-resolution "native" and "oil-immersed" data sets were collected at APS 19BM and SSRL BL9-2, respectively **(Table 3-3)**. The "native" data set was collected from one crystal with a 100µm x 100µm X-ray beam tuned at 0.98Å/12.7 keV. The crystal-to-detector distance was set to 175 mm. The crystal was collected with a 0.5° oscillation/frame for a total of 360°. Each frame was exposed for 5 seconds with no attenuation. The "oil-immersed" data set was collected from one crystal with X-ray beam tuned at 0.98Å/12.7 keV. The crystal-to-detector distance was set to 350 mm. The crystal was collected with a 0.2° oscillation/frame for a total of 720°. Each frame was exposed for 2 seconds with ?% attenuation.

3.3.10 Data Processing and Merging

The sulfur-SAD datasets collected at NSLS-II FMX were processed automatically by "fast_dp", an automated XDS-based(44) streamline program developed by NSLS-II scientists, using space group P 2_1 2_1 2_1 and unit-cell cell parameters of a = 66.7 Å, b = 104.0 Å, c = 141.7 Å. Information about the pR452 crystal space group were learned from previous data collection and processing experiences at the Stanford Synchrotron Radiation Lightsource (SSRL). Data sets collected from SSRL were indexed, integrated, and scaled using HKL2000 program suite(87), which contains three programs: "XdisplayF" for visualization of the diffraction pattern, "Denzo" for data reduction and integration, and "Scalepack" for merging and scaling of the intensities obtained by "Denzo" or other programs. The high-resolution "native" and "oil-immersed" data sets were also indexed, integrated, scaled and merged by XDS-based, automated data reduction programs unique to the synchrotron beamlines at which they were collected, APS 19BM and SSRL 9-2, respectively. Both datasets, "native" and "oil-immersed" were optionally processed by HKL2000, which was available either pre-installed on the synchrotron site servers during data collection or on the CBSD Macromolecular X-ray Diffraction Core Facility workstation after datasets were transferred back to Montana. The final decision to use reduced datasets processed by the XDS-based programs was made because HKL2000 routinely rejects weak ($I/\sigma I < 1$) reflections while XDS keeps those reflections and weak reflections could always be rejected during MR and structure refinement cycles.

To create a heavy atom substructure map for phasing, it was necessary to merge multiple sulfur data sets to achieve high signal/noise due to the naturally weak anomalous signal of sulfur atoms. **(Table 3-5)** Using BLEND(33) from the CCP4 program suite, I attempted to scale and merge 18

data sets collected from 14 relatively isomorphous crystals. Simultaneously, Tung-Chung Mou manually performed pair-wise merging of the same 18 data sets using phenix.scaled-and-merged program(16).

Crystal	*Dataset*	*Total range (°)*	*Resolution (Å)**	*Unique reflections*	*Average multiplicity**	*Completeness (%)**	*R_{meas} (%)*†*	*I/σ(I)**	*CC_{ano} @3.5Å*	*% Trans.*	*Oscil. (°)*	*Expo. (s)*
1	1_1	360	30.0-3.27 (3.36-3.27)	15336	12.6 (9.2)	97.1 (71.1)	15.5 (92.6)	12.2 (1.7)		20	0.2	0.05
	1_2	360	30.0-3.24 (3.33-3.24)	15730	13.0 (11.5)	98.0 (82.5)	13.0 (91.3)	14.6 (2.6)		50	0.2	0.05
	1_3	360	30.0-3.39 (3.48-3.39)	13950	12.8 (10.9)	98.7 (91.0)	13.9 (91.4)	13.0 (2.1)		30	0.2	0.05
2	2_1	360	30.0-3.32 (3.40-3.32)	14531	12.0 (10.5)	96.2 (52.6)	18.6 (100.2)	10.1 (1.5)		20	0.2	0.1
	2_2	360	30.0-3.41 (3.50-3.41)	13402	12.6 (8.6)	96.4 (55.3)	15.9 (95.5)	12.0 (1.6)		20	0.2	0.1
7	7_1	1440	30.0-2.86 (2.94-2.86)	22912	50.6 (45.7)	99.1 (88.4)	7.4 (83.5)	50.0 (5.8)	0.43	20	0.2	0.1
8	8_1	1080	30.0-2.70 (2.78-2.70)	27004	13.3 (13.1)	97.7 (93.5)	6.5 (68.5)	27.1 (3.1)		20	0.2	0.1
	8_2	1080	30.0-2.81 (2.88-2.81)	24457	29.7 (20.1)	95.7 (75.1)	11.2 (78.5)	29.4 (4.7)		20	0.2	0.1
9	9_1	1080	30.0-2.77 (2.84-2.77)	24489	34.6 (21.2)	95.4 (89.1)	9.2 (82.8)	38.2 (3.5)	0.35	20	0.2	0.2
10	10_1	2880	30.0-2.97 (3.05-2.97)	21312	80.2 (75.1)	94.2 (73.7)	13.8 (79.2)	40.3 (5.5)	0.50	10	0.2	0.1
13	13_1	1440	30.0-3.25 (3.33-3.25)	15982	46.7 (37.1)	98.7 (84.0)	17.5 (93.0)	21.0 (3.6)	0.22	20	0.2	0.1
14	14_1	5760	30.0-2.97 (3.05-2.97)	22225	134.8 (83.1)	99.7 (90.6)	15.9 (69.7)	42.0 (10.4)	0.53	10	0.2	0.1
15	15_1	3600	30.0-3.37 (3.44-3.37)	14122	100.1 (80.2)	95.6 (75.5)	13.1 (70.5)	34.3 (3.7)	0.25	15	0.2	0.1
17	17_1	360	30.0-2.43 (2.50-2.43)	37043	12.8 (11.4)	99.6 (94.9)	7.3 (76.4)	23.8 (2.7)	0.23	20	0.2	0.1
18	18_1	1080	30.0-3.46 (3.55-3.46)	13414	37.1 (26.4)	97.6 (69.7)	16.2 (92.4)	22.0 (3.5)	0.22	20	0.2	0.1
19	19_1	720	30.0-2.77 (2.84-2.77)	25093	26.6 (24.2)	97.7 (90.5)	11.0 (79.9)	24.4 (3.8)	0.27	20	0.2	0.1
28	28_1	1080	30.0-3.11 (3.19-3.11)	17574	37.8 (28.9)	96.2 (67.7)	13.1 (89.4)	29.9 (3.1)		20	0.2	0.1
34	34_1	1080	30.0-2.81 (2.88-2.81)	24582	38.6 (35.5)	99.5 (94.5)	7.8 (79.5)	44.9 (5.2)	0.33	20	0.2	0.1

Table 3-5 Parameters and statistics of data sets that were merged for Sulfur-SAD phasing

*Data for highest resolution shell are given in brackets. † $R_{meas}=\sum_{hkl}(n/n\text{-}1)^{1/2}\sum_i |I_i(hkl)-\langle I(hkl)\rangle|/\sum_{hkl}\sum_i I_i(hkl)$, where $I_i(hkl)$ is the ith observation of the intensity of the reflection hkl and $\langle I_{hkl}\rangle$ is the mean over n observations. $CC_{ano} = \langle \Delta_{ano}\ \Delta_{ano,obs}\rangle / (\langle \Delta^2_{ano}\rangle^{1/2} \langle \Delta^2_{ano,obs}\rangle^{1/2}$, where Δ_{ano} and $\Delta_{ano,obs}$ are the anomalous structure factor amplitude differences ($F^+ - F^-$), respectively, computed from the anomalously scattering atomic substructure, and the observed anomalous differences.

3.3.11 Heavy-Atom Substructure Searches; and Determination + Refinement of pR452 Structure

The merged and scaled data was input into the HKL2map(69), a graphical user interface (GUI) for the SHELXC/D/E program suite, and Phenix Hybrid Substructure Search (HySS), a likelihood-based method, for sulfur substructures searches.

After the sulfur substructure was determined, the substructure (*.PDB) file and structure factor data file were input into Phenix Autosol for calculation of experimental phases and building of an initial model. Further automated model building was performed using phenix.AutoBuild program. The AutoBuild model was then manually built using WinCoot. The phases were extended to higher resolution using the "native" dataset discussed in section 3.3.9 and the partially-built model from sulfur-SAD phasing. Fragments of additional main chains were constructed after iterations of manual model rebuilding using WinCoot and refinement using phenix.refine.

Using the "oil immersed" dataset discussed in section 3.3.9 and the pR452 structure built from the regular cryo-protectant protected crystals as starting model for molecular replacement (MR) to generate an initial model, another structure of pR452 was determined following manual model rebuilding with WinCoot and refinement of the MR solution.

3.3.12 Structure Validation

MolProbity (43) was incorporated into "phenix.refine" as an add-on feature, therefore, was performed after every iteration of manual model building and refinement to make suggestions for subsequent refinement steps. Final structural models were validated by wwPDB Validation Server (Protein Data Bank).

Chapter IV: Ric-8A SAXS Envelopes

4.1 Introduction

Ric-8A is phosphorylated *in vitro* at five sites (Ser435, Thr440, Ser522, Ser523, and Ser527) near the C-terminus(3). Among them are Ser435 and Thr440 that, when phosphorylated by casein kinase II (CKII) *in vitro*, elevate the function of Ric-8A as a guanine nucleotide exchange factor (GEF) for Gαi1.(3) Using small-angle X-ray scattering (SAXS), the molecular envelopes of Ric-8A and phospho-Ric-8A were determined to see in low-resolution the effect of phosphorylation on Ric-8A. Ric-8A also forms a stable, nucleotide-free complex with Gαi1 *in vitro*; therefore, the low-resolution SAXS envelope of the Ric-8A:Gαi1 complex was also determined readily. By fitting the SAXS envelope of the complex with the crystal structure of pR452 (Chapter III) and Gαi1(95), we hoped to discern large conformational changes induced by complex formation at low resolution and, if possible, the effect(s) of Ric-8A phosphorylation on the complex. While we had large quantities of highly pure protein samples (Ric-8A and Gαi1) which were required for crystallization, the molecular envelopes of Ric-8A and Ric-8A:Gαi1 complex were determined by SAXS with less effort. We tested the hypothesis that the CKII phosphorylation of Ric-8A induces conformational changes, thereby activating Ric-8A to become a more potent GEF for Gαi1:GDP, following the regulation paradigm for many other proteins that are phosphorylated and dephosphorylated inside the cells.

4.1.1 Theory of SAXS

Small-angle x-ray scattering (SAXS) not only enables low-resolution structural determination of protein molecules in solution, but also overcomes the limitation of studying only snapshots of

conformationally dynamic protein molecules that become constrained by a crystal lattice. Limitations of SAXS include the most obvious low-resolution and difficulty in model generation with dynamic protein molecules which sample multiple conformations in solution, therefore, data interpretation can be ambiguous. Nevertheless, SAXS remains a stand-alone, powerful structural tool as well as a good alternative to the high-resolution methods, namely X-ray crystallography, Cryo-electron microscopy (Cryo-EM), and nuclear magnetic resonance (NMR), for visualizing protein molecules.

In a basic SAXS experiment, incident X-rays are scattered by protein molecules tumbling in solution and the scattered X-ray photons hit a detector, similar to X-ray diffraction in X-ray crystallography except the molecules are not periodically packed in a crystal lattice. As a result, almost no intensities can be measured at resolution beyond 10Å. **(Figure 4-1)** The intensity is expressed as a function of the scattering vector q resulting from a photon of wavelength λ scattering off the sample at an angle 2θ (17).

$$q = \frac{4\pi \sin(\theta)}{\lambda} \qquad (27)$$

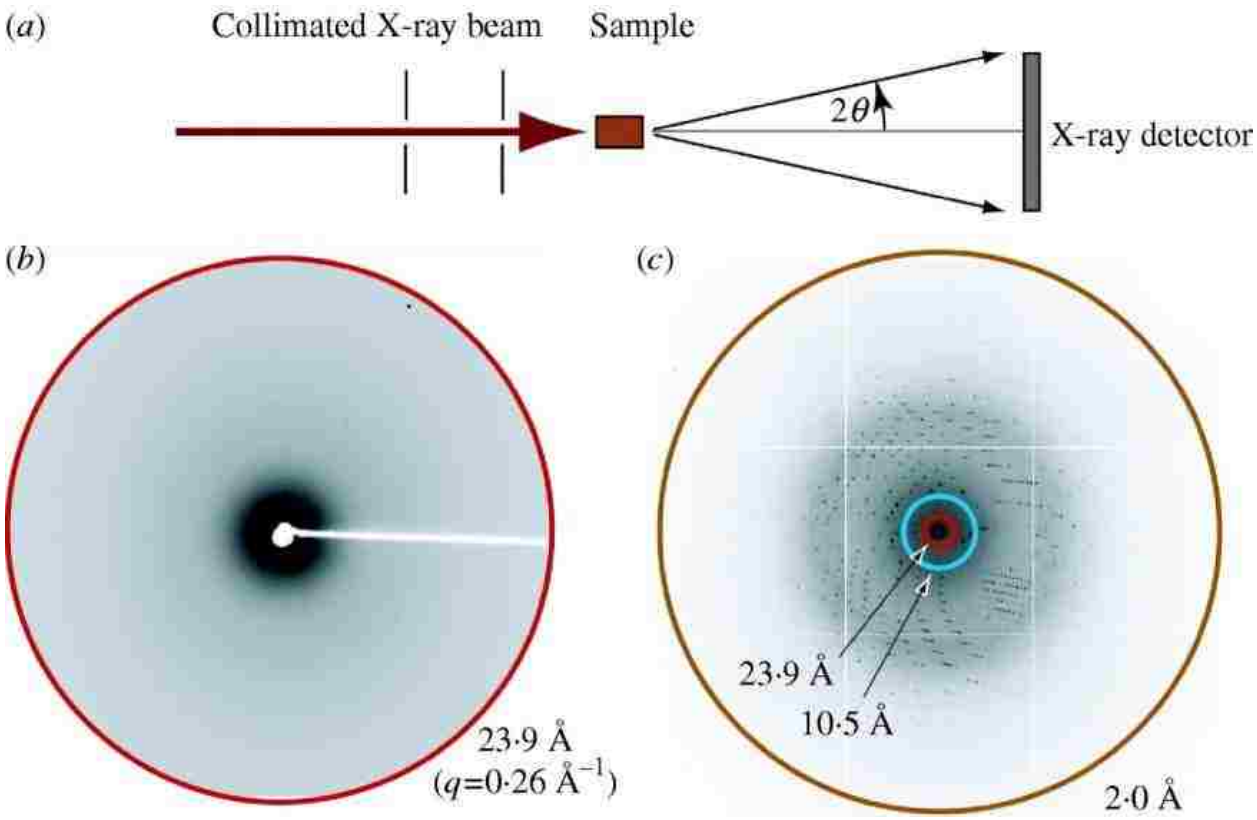

Figure 4-1 X-ray interactions with sample for SAXS or crystallography
(a) Both SAXS and X-ray crystallography involve placing a sample (orange) in the path of a highly collimated X-ray beam (red) and measuring the scattered/diffracted X-rays. The angle of any scattered position with the direct beam is 2θ; **(b)** X-ray scattering pattern from a solution of yeast PCNA; **(c)** diffraction from a nickel superoxide dismutase crystal. The equivalent position of the highest resolution of the SAXS experiment in (b) is indicated as a red circle in (c). The blue circle indicates the highest resolution achievable (q=0.6 Å^{-1}) for SAXS data collection at the "Structurally Integrated Biology for the Life Sciences" (SIBYLS) beamline. Both images collected at beamline 12.3.1 (SIBYLS) at the Lawrence Berkeley National Laboratories. (53)

The scattering pattern is recorded and radially integrated into a one-dimensional SAXS intensity profile. **(Figure 4-3)** Based on the experimental SAXS data, a theoretical intensity profile can be calculated using models that describe spherical or cylindrical particles(17). For monodisperse particles in solution, the theoretical intensity profile for a particle is expressed as

$$I_p(q) = (\Delta\rho)^2 V_p^2 P(q) \quad (28)$$

where $P(q)$ = the form factor, $(\Delta\rho)^2$ = electron contrast, and V_p^2 = particle volume. The total intensity profile is the sum of $I_p(q)$ of all particles,

$$I(q) = \sum I_p(q) \qquad (29)$$

The analysis of the 1-D experimental SAXS profile ultimately yields information about size and shape of the molecules in solution (53).

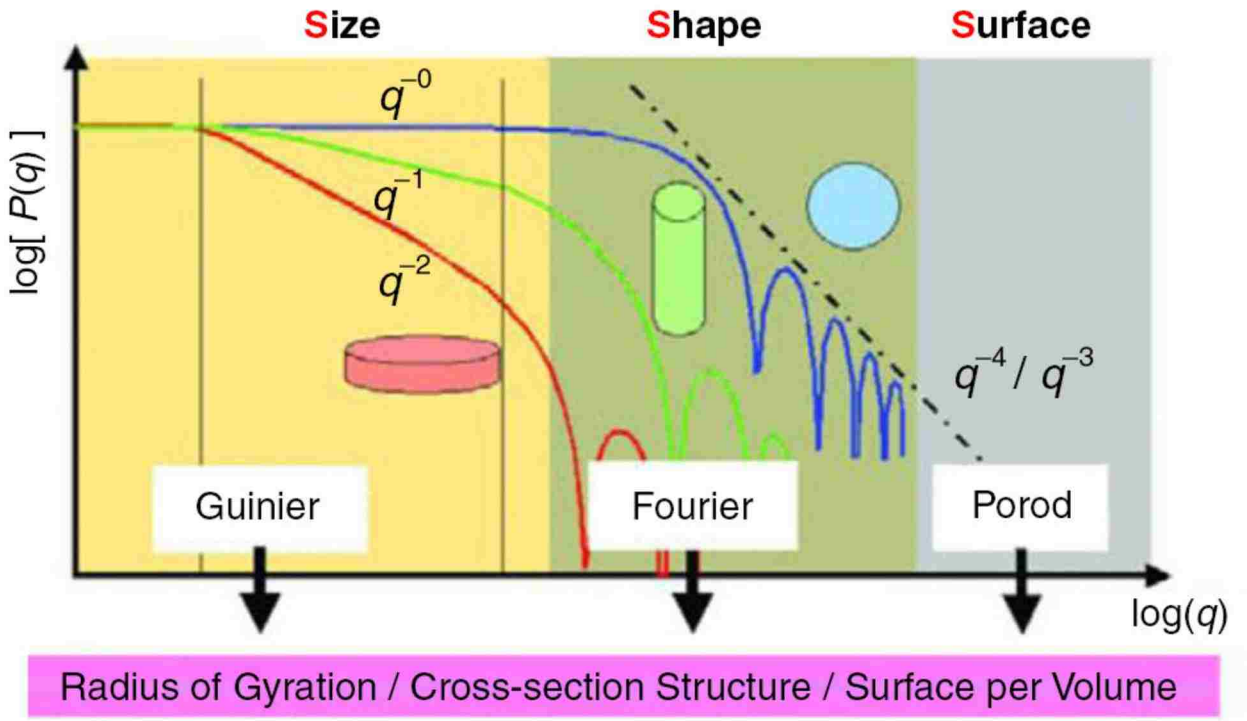

Figure 4-2 Regions of SAXS profile and data that may be extracted from each. (35)

To extract structural information from a SAXS experimental profile, three distinct regions, Guinier, Fourier, and Porod, are analyzed (35) **(Figure 4-2)**. In the Guinier region, R_g, the radius of gyration, is determined by fitting a line through the ln(*I*) vs. s^2 (Guinier) plot (34, 35, 49, 111) **(Figure 4-2, 4-3)**.

$$\ln[I(s)] = \ln[I(0)] - \frac{[sR_g]^2}{3} \qquad (30)$$

In the Fourier region, $\rho(r)$, the pair distribution function, is determined by an indirect Fourier transformation of $P(q)$, the experimental form factor, and plotted against a radius, *r,* to show the distribution of electrons in the molecule (34, 35, 49, 74, 111) **(Figure 4-2, 4-3)**,

$$\rho(r) = \frac{1}{2\pi^2 r}\int_0^\infty qP(q)\sin(qr)dq \qquad (31)$$

In the Porod region **(Figure 4-2)**, the Porod invariant, Q, is determined,

$$Q = \int_0^\infty q^2 I(q)dq \qquad (32)$$

providing surface information such as the surface to volume ratio (*S/V*) and specific surface estimation for compact particles (35, 49).

$$\frac{S}{V} = \frac{\pi(\lim_{q\to\infty} I(q)q^4)}{Q} \qquad (33)$$

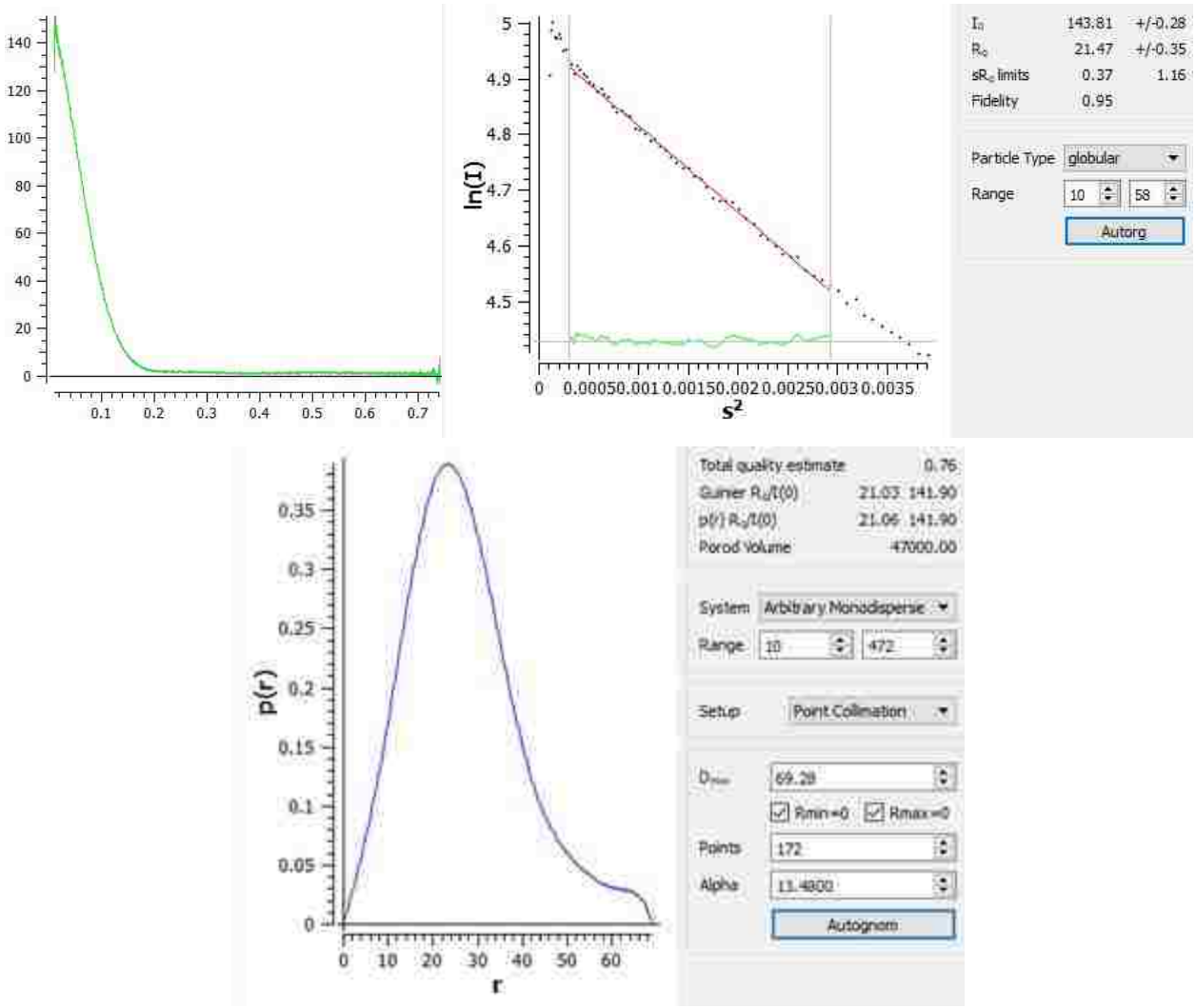

Figure 4-3 SAXS data processing using ATSAS
An integrated, 1-D SAXS intensity profile **(top left)**, plotting I vs. s; the Guinier plot **(top right)**, ln(I) vs. s^2; and the $\rho(r)$ vs. r plot **(bottom)** showing elections distribution. All plots were generated by PRIMUSQT in the ATSAS program suite. ($s = q = 4\pi\sin\theta/\lambda$)

4.2 Results & Discussion

4.2.1 HPLC-SAXS Revealed Overall Shapes of Gαi1, Ric-8A, and Gαi1:Ric-8A Complex

We successfully collected SAXS data sets at the Advanced Photon Source (Argonne, National Laboratory) BIOCAT 18.1 beamline for R491, pR491, and Ric-8A:Gαi1 complex. We also collected high-quality data sets at SSRL for R452 and pR452.

The ATSAS software package was used to analyze and reconstruct 3-D models for the molecular envelopes of protein samples. Each X-ray scattering image was radially averaged to produce a one-dimensional plot of scattering intensity vs. q ($q=4\pi\sin(\theta)/\lambda$). PRIMUSQT was used to estimate molecular weight, maximum particle dimension (D_{max}), and the distance distribution function, $\rho(r)$. 3-D reconstructions of the SAXS data were performed using the *ab initio* modeling programs, DAMMIN and DAMMIF to generate ten dummy atom models. Using DAMAVER, a theoretical Guinier plot of each dummy model was then back-extrapolated and aligned with experimental data to select for the best candidates for building an averaged model. The final averaged molecular envelopes resulted from multiple rounds of refinement with DAMMIN/DAMMIF were visualized using Chimera (UCSF). (66)

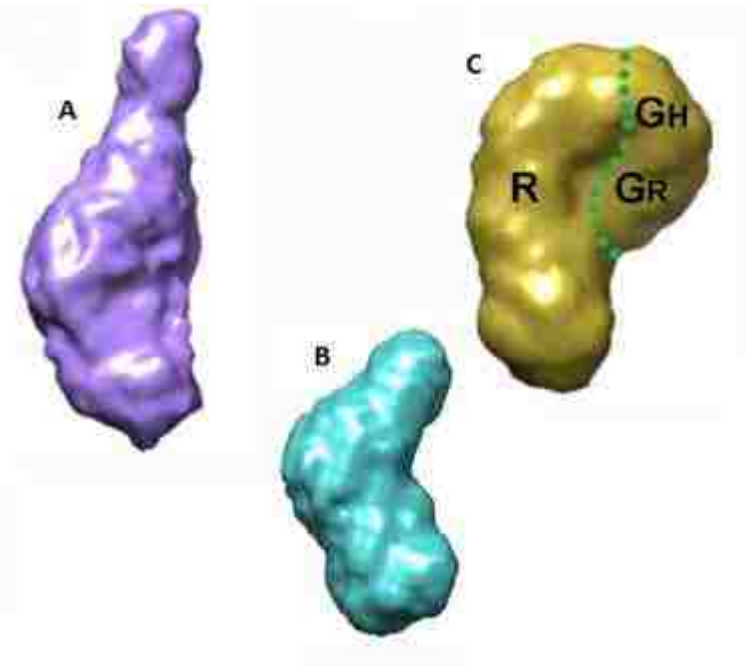

Figure 4-4 HPLC-SAXS Revealed Overall Shapes of Gαi1, Ric-8A, and Gαi1:Ric-8A Complex
SAXS envelopes of **(A)** Ric-8A 491, **(B)** phospho-Ric-8A 491 showing apparent bending of the molecule, and **(C)** Ric-8A 491:Gαi1 complex showing possible location of Gαi1 in the complex.

The model for R491:Gαi1 complex envelope implied large conformational changes including possible Gαi1 domain separation since an intact Gαi1:GDP crystal structure failed to fill confidently the extra density near the top region of R491 in the complex envelope **(Figure 4-4)**. Unpublished evidence provided by SAXS envelopes of R491:nanobodies complex (data not shown) suggested that the protrusion on the R491 envelope is the C-terminus of R491. Taken together, the SAXS envelope of R491:Gα1i complex agreed with the notion that Gαi1 interacts with the C-terminus of Ric-8A.

The SAXS envelope of pR491 showed significant conformational changes compared to R491. The characteristic protrusion, the putative Ric-8A C-terminus, was not observed in the model of pR491. Since the SAXS model was an ensemble average of ten best DAMMIN models, the C-terminus of pR491 might sample multiple conformations, suggesting dynamic motions of Ric-8A C-terminus induced by CKII phosphorylation/activation.

4.2.2 Comparing R452 and pR452 SAXS Envelopes with Normal Mode Analysis

	Ric-8A 1-452	Phos-Ric-8A 1-452
I(0) (cm^{-1}) from Guinier	84.65 ± 0.081	106 ± 0.18
*R*g (Å) from Guinier	29.7 ± 0.57	29.2 ± 0.53
qRg limitation for Guinier analysis	1.17	1.18
I(0) (cm^{-1}) from *P(r)*	84.63	106.2
*R*g (Å) from *P(r)*	30.01	29.59
*D*max (Å) from *P(r)*	101	92
Porod Volume estimate (Å^{-3})	69042.7	69990.9

Table 4-1 SAXS data of R452 and pR452 in solution
The R_g calculated using two different programs/methods, AUTORG for Guinier analysis and AUTOGNOM for pair distribution function analysis, were similar to each other.

Using the same set of programs described in section 4.2.1, SAXS envelopes of both R452 and pR452 were also successfully determined by *ab initio* modelling, however, the differences between the two molecular envelopes were subtle **(Table 4-1, Figure 4-5 A+B, 4-6)**. To further characterize conformational changes on R452 caused by CKII phosphorylation, pR452 crystal structure was converted into coarse-grains model and fitted into the experimental SAXS data of R452 and pR452 in solution by using SREFLEX program in the ATSAS software package. SREFLEX performed a normal mode analysis as described before(12, 66) that included a large domain rigid body refinement and local structural rearrangement. Tung-Chung Mou performed the entirety of the normal mode analysis for R452 and pR452 and generated models for each, **(Figure 4-5 C+D)** therefore, I will refrain from elaborating on the details of the modelling process.

In a comparison of molecular envelopes of pR452 and R452, we saw an apparent bending of the R452 envelope relative to that of pR452, suggesting small domain movements induced by CKII phosphorylation. Superposition of the R452 and pR452 normal mode analysis models by

aligning the first four N-terminal helices confirmed the observation that pR452 is a more elongated molecule than R452 **(Figure 4-6)**. Phosphorylation of R452 might relax the molecule, making the concave surface of R452 slightly more exposed to solvent.

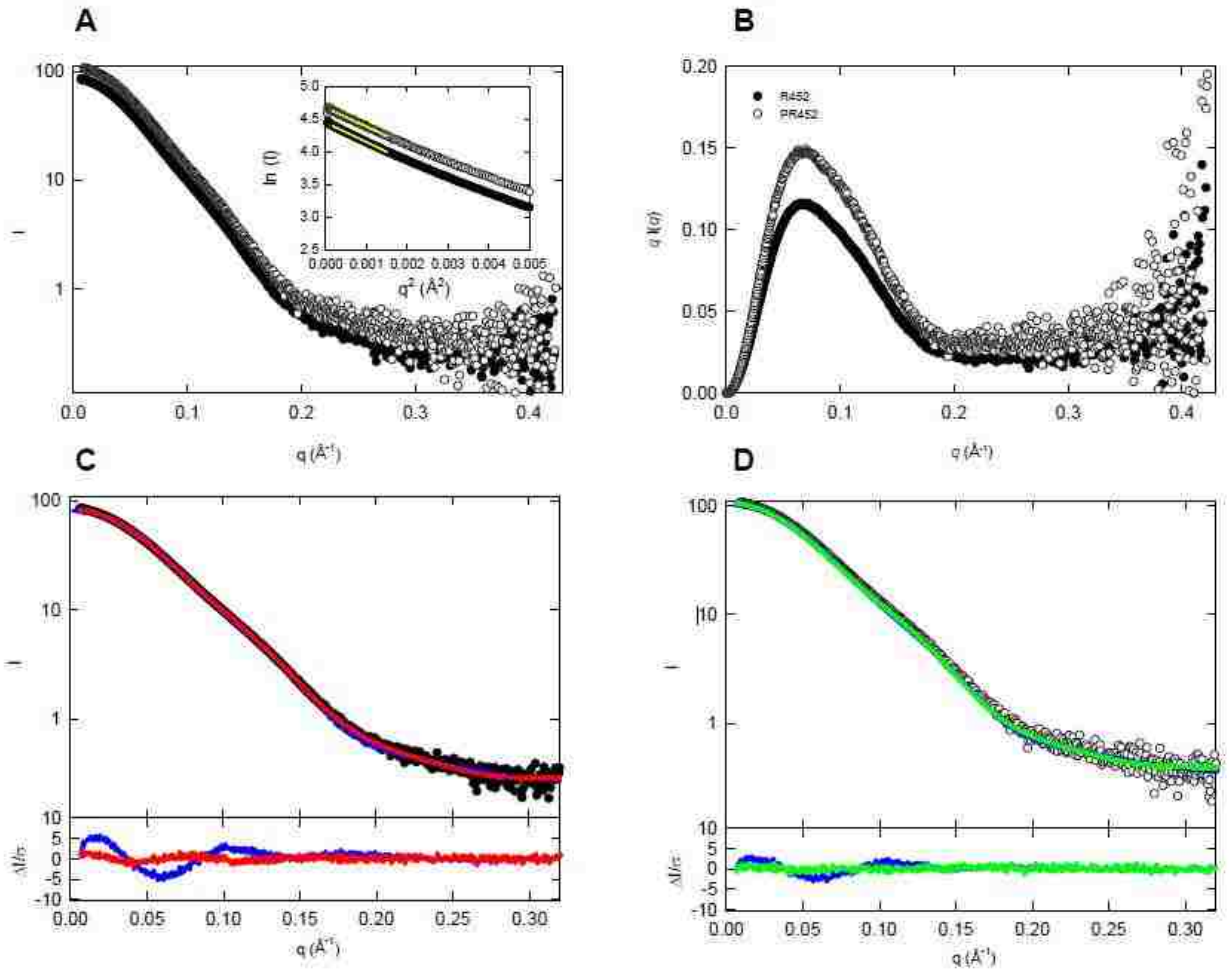

Figure 4-5 Comparing R452 and pR452 SAXS data and pR452 crystal structure-based normal-mode fitted models

(A) Measured scattering data of R452 (closed circle) and pR452 (open circle); Guinier plot for each sample is shown in the inlet; straight-lines are linear fit of the measured data; **(B)** Kratky plot (Fagherazzi et al. 1983) (1) for the same data in (A); **(C) and (D)**, comparison of experimental scattering data with CRYSOL (Svergun et al. 1995) (80) calculated theoretical scattering curves of crystal structure of pR452 (blue), normal-mode fitted R452 model (red), and normal-mode fitted pR452 model (green). The bottom panels of (C) and (D) are the error-weighted residual difference plots $\Delta I/\sigma = [I_{exp}(q) - c*I_{mod}(q)]/\sigma(q)$ versus q. The theoretical scattering profiles of normal-mode pR452 model (green) and R452 model (red) show good agreement to the corresponding SAXS data while the profile for pR452 crystal structure (blue) deviates from the SAXS data of R453 in panel (C).

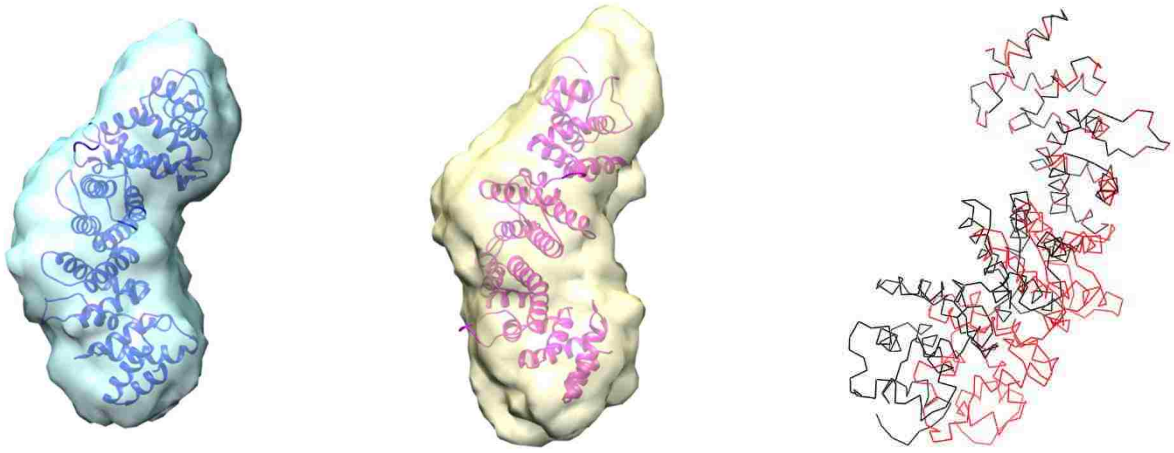

Figure 4-6 Ric-8A conformational changes caused by CKII phosphorylation
(Left and middle), the final SAXS envelopes of R452 (cyan) and pR452 (wheat) are shown in superposition with its respective normal mode analysis model (blue and rose). The superposition of models to SAXS envelopes was carried out by volume fitting function in UCSF Chimera software package. **(Right)**, superposition of the normal mode analysis models of R452 (black) and pR452 (red) by aligning the first four N-terminal helices.

4.3 Materials & Methods

4.3.1 Protein Expression, Purification, and SAXS Samples Preparation

See Chapter III

4.3.2 HPLC-MALS-SAXS at APS 18ID and FPLC-SAXS at SSRL BL4-2

We sent highly purified protein samples in milligram quantities to synchrotron beam-lines for SAXS data collection coupled to size-exclusion chromatography (SEC-SAXS). At APS 18ID, the protein samples (1mg/mL to 10mg/mL) were resolved using a Superdex200 SEC (GE Healthcare) column connected to a high-performance liquid chromatography (HPLC) system (Agilent) in tandem to a DAWN HELEOS II multi-angle light scattering (MALS) detector (Wyatt Technology). As the samples were eluting from the column, they were first continuously injected through the MALS system for light scattering analysis, followed by a capillary that intercepts the X-ray beam. SAXS data collection happened concurrently, therefore, the samples being irradiated were significantly more homogeneous and monodisperse. The background/buffer SAXS were also collected before and after the sample peak eluted from the column so they could be baseline-subtracted from the data to yield actual SAXS from the samples. Sample application, MALS+SAXS data collection, and data processing were handled exclusively by the beamline scientist at 18ID, Srinivas Chakravarthy. At the end of the experimental session, processed MALS data and averaged SAXS profiles were made copies and stored in an external hard drive and transported back to Sprang lab for further analysis. FPLC-SAXS data collected at the Stanford Synchrotron Radiation Lightsource (SSRL) beamline BL 4-2 used BlueIce software with a focused 12 keV X-ray source (0.3mm x 0.3mm beam size)

and recorded on a Pilatus3 X 1M detector at a sample-to-detector distance of 1.7m and over a range of momentum transfer $0.0065<q<0.42Å^{-1}$ [$q=4\pi\sin(\theta)/\lambda$]. The samples were continues flowing through a 1.5 mm quartz capillary sample cell with 1 sec exposure time. To ensure the mono-dispersity of the samples, the sample cell was tandemly connected to an AKTA-FPLC system (GE Healthcare) and a Superdex 200 Increase 1.3/300 column (GE Healthcare) with flow rate at 0.5ml/min. **(Figure 4-7)** Scattering data were radially averaged to produce one-dimensional profiles of scattering intensity vs. q. Data were corrected for background scattering by subtracting the buffer curve from sample curves. Data reduction and analysis were performed using the beamline software SAStool and PRIMUS of the ATSAS suite(4). The program AUTOGNOM was used to generate Guinier curves and pair distribution function, P(r) to the determine maximum particle dimensions (D_{max}) and radius of gyration (R_g) from the scattering intensity curve ($I_{(0)}$ versus q) in an automatic, unbiased manner, and rounds of manual fitting in GNOM were used to verify these values(101). *Ab initio* molecular envelopes were computed by the programs DAMMIN(82). Ten bead models were reconstructed in DAMMIF(47), which were aligned and averaged in DAMAVER(75) with no rejections and a normalized spatial discrepancy of 0.486 ± 0.015 and 0.490 ± 0.019 for R452 and pR452 respectively.

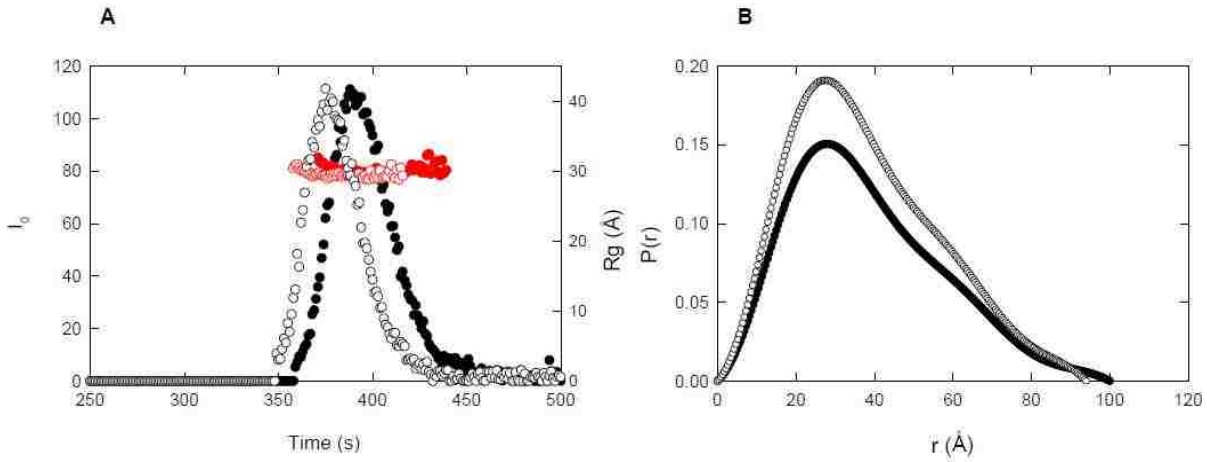

Figure 4-7 FPLC-SAXS data collection at SSRL BL4-2
(A) SEC-SAXS chromatography of R452 (closed circle) and pR452 proteins (open circle). $I(0)$ and R_g were plotted as a function of time as samples passed through a Superdex-200 Increase 1.3/300 column; (B) pair-distribution function of the data sets obtained from fractions under the SEC peaks.

Chapter V: Conclusions, Future Directions, and Preliminary Results

5.1 Conclusions

As important as the GPCR-stimulated Gα nucleotide exchange is, intracellular activation of Gα by Ric-8 implies a more intricate physiological regulatory system in G-protein signaling. Even after more than two decades of extensive research, the molecular mechanism of Ric-8-stimulated Gα nucleotide exchange remains elusive. To gain better understanding of the regulation, we focused on investigating Ric-8A, which acts as a folding chaperone for nascent Gαi1 and catalyzes nucleotide exchange for Gαi1:GDP, in the rat model.

This dissertation focused on two main aspects of the system: **(A)** protein-protein interaction between Ric-8A and Gαi1, and **(B)** 3-D architecture of Ric-8A and its phosphorylated counterpart. To characterize the binding of Ric-8A to Gαi1, a mutagenesis analysis on a putative Gαi1 binding site, suggested by HDX-MS, on Ric-8A was performed. The collection of assays agreed with the hypothesis that the region encompasses Ric-8A residues 454-470 indeed harbors crucial Gαi1 interactive elements.

To visualize Ric-8A at both high/atomic- and low/domain- resolutions, a large fragment Ric-8A (R452), which possesses GEF activity towards Gαi1, was crystallized in two forms, phosphorylated and unphosphorylated. The crystal structure of the phosphorylated form of R452 (pR452) was determined showing a superhelix made of ARM and HEAT α-helical repeats as

predicted by previous computational approaches. Mapping of sequence conservation profile, electrostatic potentials, and HDX protection profile on the structure suggested another putative Gαi1 interactive site (α3*7* and α1*8*) on Ric-8A.

Low-resolution, solution structures of Ric-8A:Gαi1 complex, Apo-Ric-8A, Gαi1:GDP, R452, and pR452 were determined by SAXS. The SAXS envelope of R491:Gαi1 complex suggested that **(A)** Gαi1 very likely interacts with C-terminal regions of Ric-8A and **(B)** in the nucleotide-free Ric-8A:Gαi1 complex, the α-helical domain and Ras-homology domain of Gαi1 might assume dynamic "open" conformations instead of a "closed" conformation as in the nucleotide-bound states. At first glance, R452 and pR452 SAXS envelopes alone did not provide a wealth of information regarding the effect of CKII phosphorylation except that pR452 looks different from R452. By combining information from the crystal structure of pR452 and experimental SAXS data in a normal mode analysis, normal mode structural models of R452 and pR452 in solution were generated. Comparison of the normal mode models to both their experimental SAXS envelopes and each other suggested that R452 is more kinked and less elongated than pR452.

SPR binding results and biochemical assay results suggested that the subtle conformational changes induced by CKII phosphorylation could still activate/enhance the GEF activity of R452. As an exception among the other evidence, the steady-state GTPase assays comparing the effect of R530 or pR530 stimulation on Gαi1 steady-state GTP hydrolysis suggested an aberrant yet interesting inhibitory mechanism under which phosphorylation of full-length Ric-8A might suppress/inhibit the GTPase activity of the Ras-homology domain on Gαi1. The possible pR530

inhibitory activity at high Ric-8A concentration, as we reported in Chapter III, towards the GTPase activity of Gαi1 is interesting because the observation suggests that in addition to acting as the chaperone and GEF, Ric-8A might also stimulate G-protein signaling by locking the activate form, Gαi1:GTP.

5.2 Future Directions and Preliminary Results

The goal of the study is to understand the molecular mechanism under which Ric-8A interacts with Gαi1. Structural information of the rat Ric-8A:Gαi1 complex pair could provide insight into the mode of action for the Ric-8 family of intracellular proteins as Gα chaperones and nucleotide-exchange factors. With the crystal structure of pR452, which includes >80% of all 530 residues of the full-length Ric-8A, and full-length Gαi1 in hand for molecular replacement, future structural studies on the topic should focus more toward the Ric-8A:Gαi1 complex structure.

5.2.1 Gαi1 Ras Domain

In order to eventually obtain a Ric-8A:Gαi1 complex crystal structure that depicts the protein-protein interaction, we attempted to stabilize nucleotide-free Gαi1 in the complex by truncating the helical domain of Gαi1. Based on ideas from Carpenter et al 2016, we designed a Gαi1 helical-domain truncation mutant, termed Rαi1 **(Figure 5-1)** (9). The DNA oligo coding for Rαi1 construct was purchased from IDT and cloned into pDEST15 vector (Gateway System). Rαi1 was expressed and purified using identical methods as the full-length Gαi1 W258A (Figure.) (See Chapter II for details).

---FASTA Protein---

ENLYFQGIDRNLREDGEKAAREVKLLLLGAGESGKSTIVKQMKIIHGGSGGSGGTTGIVETHFTFKDLHFKMFD
VGGQRSERKKWIHCFEGVTAIIFCVDLSDYDRMHESMKLFDSICNNKAFTDTSIILFLNKKDLFEEKIKKSPLTIC
YPEYAGSNTYEEAAAYIQCQFEDLNKRKDTKEIYTHFTCATDTKNVQFVFDAVTDVIIKNNLKDCGLFstop

---FASTA DNA---

GGGGACAAGTTTGTACAAAAAAGCAGGCTTCGAAAATCTTTATTTCCAGGGTATCGACCGCAACCTCCGGG
AGGACGGAGAGAAGGCAGCGCGCGAGGTCAAGCTGCTGCTGCTGGGTGCTGGTGAATCCGGGAAGAGCACA
ATTGTGAAGCAGATGAAAATTATCCACGGTGGGAGTGGCGGGAGCGGAGGTACGACGGGAATTGTGGAAAC
CCACTTTACTTTCAAAGATCTTCATTTTAAAATGTTTGACGTGGGAGGCCAGAGATCAGAGCGGAAGAAGT
GGATTCACTGCTTTGAAGGCGTGACTGCCATCATCTTCTGTGTGGACCTGAGTGACTATGACCGGATGCAT
GAAAGCATGAAGCTGTTCGATAGCATATGTAACAACAAGGCGTTTACGGACACATCCATCATCCTTTTCCT
GAACAAGAAGGACCTCTTCGAAGAGAAGATCAAAAAGAGTCCCCTCACGATATGCTATCCAGAATATGCAG
GCTCAAACACATATGAAGAGGCGGCTGCGTATATCCAGTGTCAGTTTGAAGACCTCAATAAAAGGAAGGAC
ACAAAGGAAATTTACACCCACTTCACTTGCGCCACGGATACGAAGAATGTGCAGTTTGTGTTCGATGCTGT
AACGGACGTCATCATAAAGAATAACCTAAAAGACTGTGGTCTCTTCTAAGACCCAGCTTTCTTGTACAAAG
TGGTCCCC

---Color Code Key---
Red = Stop codons
Grey shaded = TEV site
Cyan shaded = "GS" linker
Yellow shaded = attB1 site
Magenta shaded = attB2 site
Underlined = mutation site
Bold = mutated residue/base

Figure 5-1 FASTA sequence of Rαi1 construct design

Possibly due to the absence of the helical domain to stabilize the bound nucleotide, GDP, the Rαi1:GDP intrinsic guanine nucleotide exchange (in the absence of Ric-8A) appeared to proceed faster than the full-length Gαi1. Rαi1 formed a stable complex with Ric-8A 1-491 and the complex could be isolated by size-exclusion chromatography (SEC). Initial crystallogenesis experiments of Rαi1:GDP and Rαi1:R491 are underway; small rod-shaped crystals were observed in the initial screen (0.5µL 20mg/mL protein + 0.5µL reservoir solution in a sitting drop, 20% w/v PEG3350, 0.2M $CaCl_2$, 48 hours at 4ºC) for Rαi1:GDP but not Rαi1:R491 complex. **(Figure 5-2)** No crystals had formed for the Rαi1:R491 complex.

Unpublished NMR results suggest that Rαi1 becomes completely disordered or assumes rapid dynamic motions in the Rαi1:R491 complex. In either case, our current Rαi1 construct will not be a suitable crystallization target. In the future, the Rαi1 construct should be re-designed and hopefully stabilized for complex crystallization.

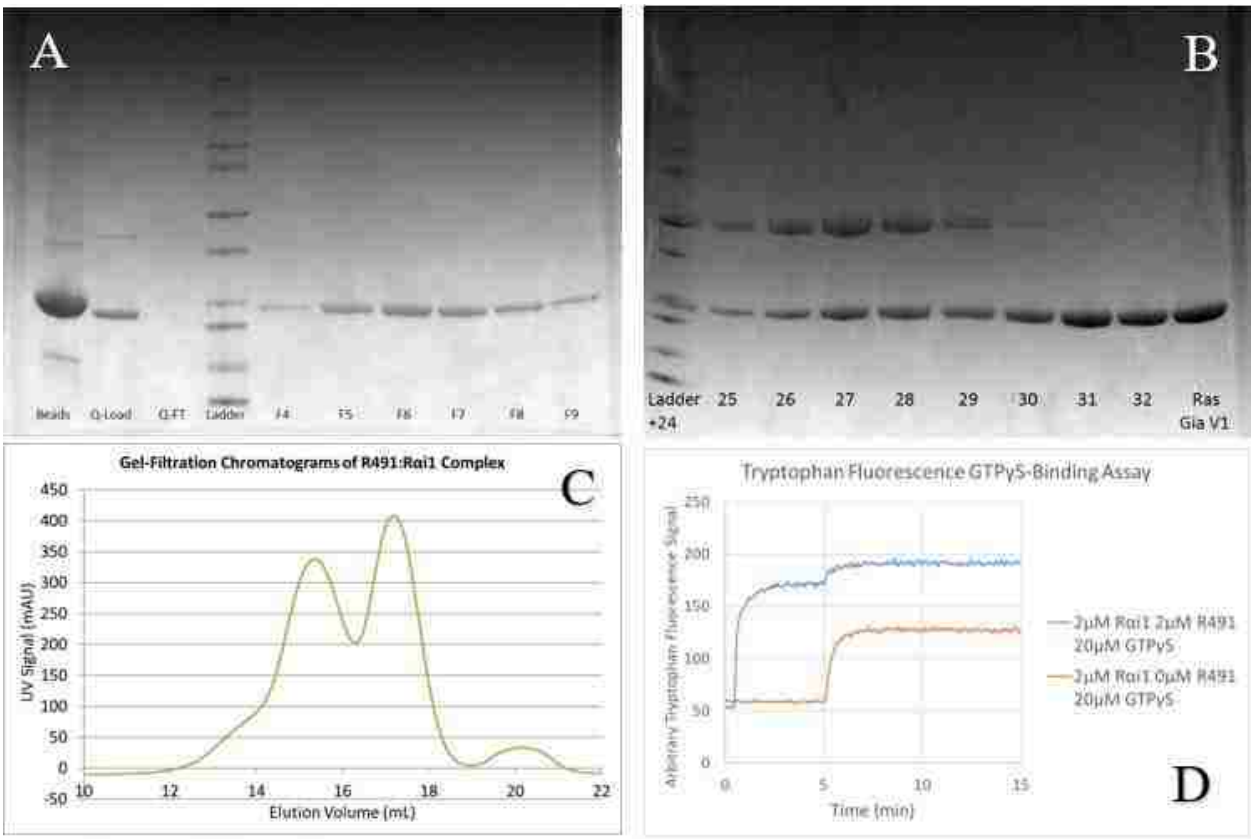
A
Beads
Q-Load
Q-FT
Ladder
F4
F5
F6
F7
F8
F9
B
Ladder +24
25
26
27
28
29
30
31
32
Ras Gia V1
Gel-Filtration Chromatograms of R491:Rqi1 Complex
C
UV Signal (mAU)
Elution Volume (mL)
Tryptophan Fluorescence GTPγS-Binding Assay
Arbitrary Tryptophan Fluorescence Signal
Time (min)
2μM Rqi1 2μM R491 20μM GTPγS
2μM Rqi1 0μM R491 20μM GTPγS
D
E
F

Figure 5-2 Rαi1 purification, Ric-8A complex formation, functional assays, and protein crystallization
SDS-PAGE results of **(A)** samples from Rαi1 purification steps (Lane #1, GST-resin after TEV digestion and elution of Rαi1; lane #2, recovered Rαi1 after TEV digestion; lane #3, Q-column flow-through; lane #4, protein standard; lane #5-10, Q-column-purified fractions of Rαi1) and **(B)** fractions under the gel-filtration chromatogram **(C)** of Rαi1:R491 complex showed Rαi1 expressed and purified similarly to full-length Gαi1 and binds to R491. **(D)** Tryptophan fluorescence GTPγS-binding assay (see Chapter II for materials and methods) results showing rapid intrinsic nucleotide-exchange of Rαi1:GDP for GTPγS; 2μM R491 or negative control were added to 2μM Rαi1:GDP at 0 minutes; 20μM GTPγS were added after 5-minute incubation. Pictures of crystals of Rαi1:GDP were taken using a light microscope (Olympus) **(E)** or a UVEX-M microscope (JANSi) **(F)**.

5.2.2 Full-Length Ric-8A

The rat full-length Ric-8A (Ric-8A 1-530, which will be referred to as R530), when multi-phosphorylated at sites in addition to S435 and T440 (pR530), appears to bind to Gαi1 with higher affinity than the un-phosphorylated protein (3). The previous finding showing reduced GEF activity of the full-length protein compared to R491 were based on experiments conducted with the unmodified, *E. coli*-expressed Ric-8A(42). It will be interesting **(A)** if phosphorylation rescues the GEF activity of R530 to the level of R491 and **(B)** if phospho-Ric-8A 1-530 forms a better complex with Gαi1. No matter what we find out about the modified full-length protein, it remains a never-attempted target for crystallogenesis.

5.2.2.a Protein Expression and Purification

The brief method discussed here was modified based on existing protocol from the Tall lab(1). N-terminally glutathione-S-transferase (GST)-tagged full-length Ric-8A construct in pET21a expression vector was expressed in *E. coli* BL21 (DE3)-pLysS cells in LB media containing carbenicillin (100mg/L) and induced with 30μM isopropyl b-d-thiogalactopyranoside (IPTG) at 17ºC. After cell lysis using an EmulsiFlex-C5 cells disruptor (Avestin) and fractionation in lysis

buffer (20mM HEPES pH 8.0, 150mM NaCl, 5mM Ethylenediaminetetraacetic acid (EDTA), 1mM Dithiothreitol (DTT), and protease inhibitors), GST-fusion Ric-8A 1-530 was protease digested and recovered similarly to Gαi1 W258A(52). Briefly, the GST-fusion protein was isolated from the soluble faction using GST-affinity resins in a glass gravity column. TEV protease was added to the washed GST-affinity resins with protein sample bound. The on-beads proteolysis reaction proceeded in 4ºC overnight. The digested/tagless protein was recovered by eluting the column with anion-exchange buffer A (20mM HEPES pH 8.0, 100mM NaCl, 1mM DTT, 1mM EDTA, and protease inhibitors) and loaded onto a Source 15Q anion-exchange column. High-purity Ric-8A 1-530 was eluted using a salt gradient (100mM to 1M NaCl). CKII kinase reaction to phosphorylate R530 was performed similarly to R452 (see details in Chapter III) with 2.5X the doses of adenosine triphosphate (ATP) and CKII since R530 contains five, instead of two on R452, phosphorylation sites. Purification of pR530 was also accomplished similarly to pR452. **(Figure 5-3)**

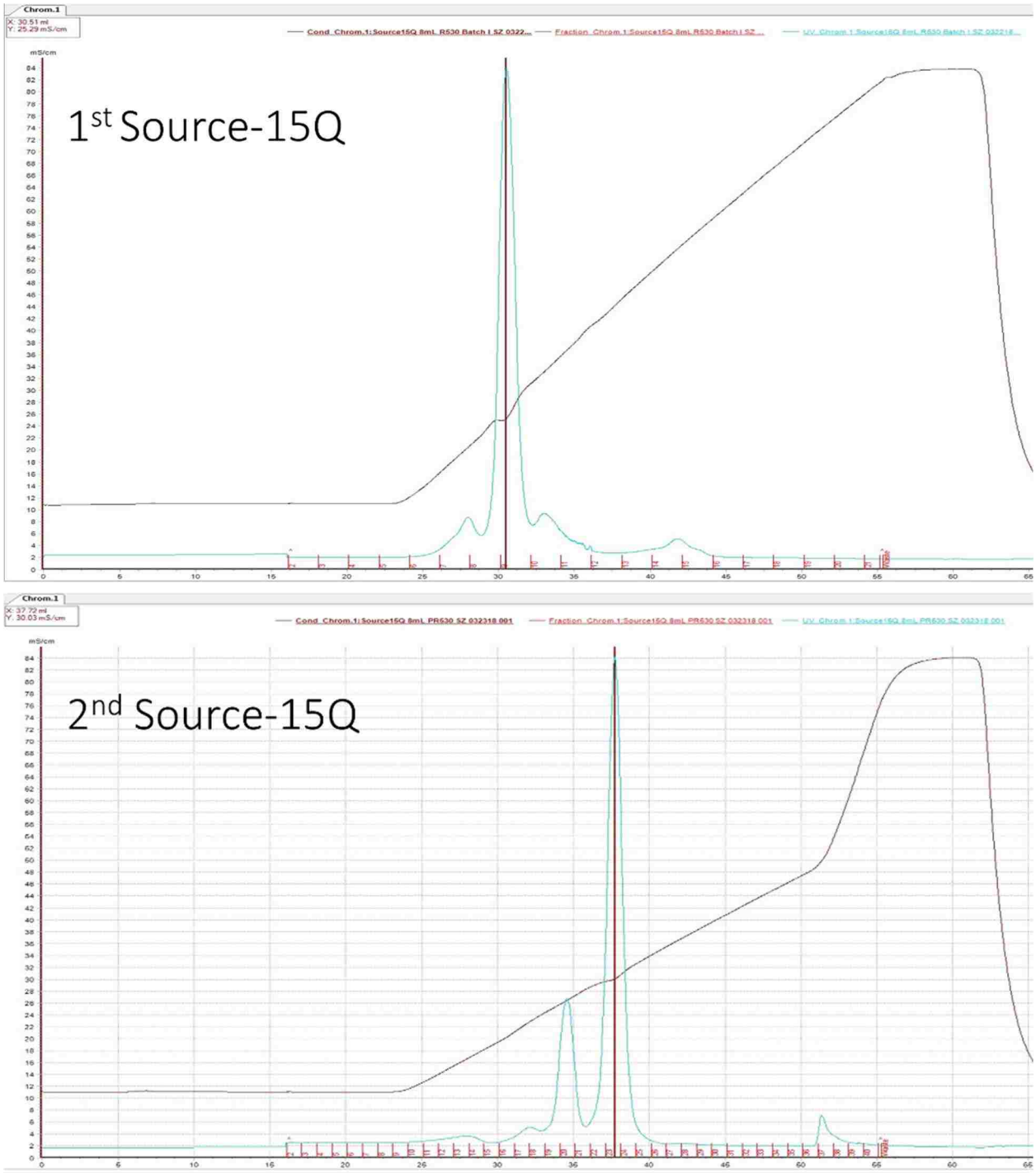

Figure 5-3 Source 15Q anion exchange chromatography results
(Top) Unphosphorylated R530 after on-bead TEV digestion eluted at conductivity~25mS/cm. **(Bottom)** The entire over-night CKII kinase reaction was resolved and pR530 eluted from the column at conductivity~30mS/cm, separated from other protein species (R530 and CKII) in the kinase reaction.

5.2.2b G-protein:Ric-8A Complex Formation and Purification

mGαi1:GDP was expressed and purified as described in Chapter II. To make a complex with pR530, 2X molar excess of mGαi1:GDP was incubated with pR530 on ice overnight and gel-filtered using a Superdex 200 SEC column (GE Healthcare). Although the 100kDa heterodimeric mGαi1:pR530 complex separated well from excess monomeric G-protein, higher-order oligomers of the complex were formed and have been challenging to separate using a Superdex 200 SEC column. The two species of 1:1, mGαi1:pR530 complex resolved well using a HiLoad Superdex 200 16/600 SEC column (GE Healthcare). **(Figure 5-4)** However, the heterodimeric complex and the higher-order oligomer also seemed to be in a temperature and/or concentration-dependent equilibrium between each other (data not shown). We were not confident with the sample homogeneity; therefore, no crystallization trial was set up for the mGαi1:pR530 complex.

Gαi1 W258A:GDP was expressed and purified as described(52). 2X molar excess Gαi1 W258A was incubated with pR530 on ice overnight and gel-filtered with a Superdex 200 SEC column. A single species of 100kDa heterodimeric Gαi1:pR530 complex resolved well from excess monomeric G-protein. Fractions contain the Gαi1:Ric-8A complex were concentrated to 10mg/mL and used for initial crystallization trials set-up.

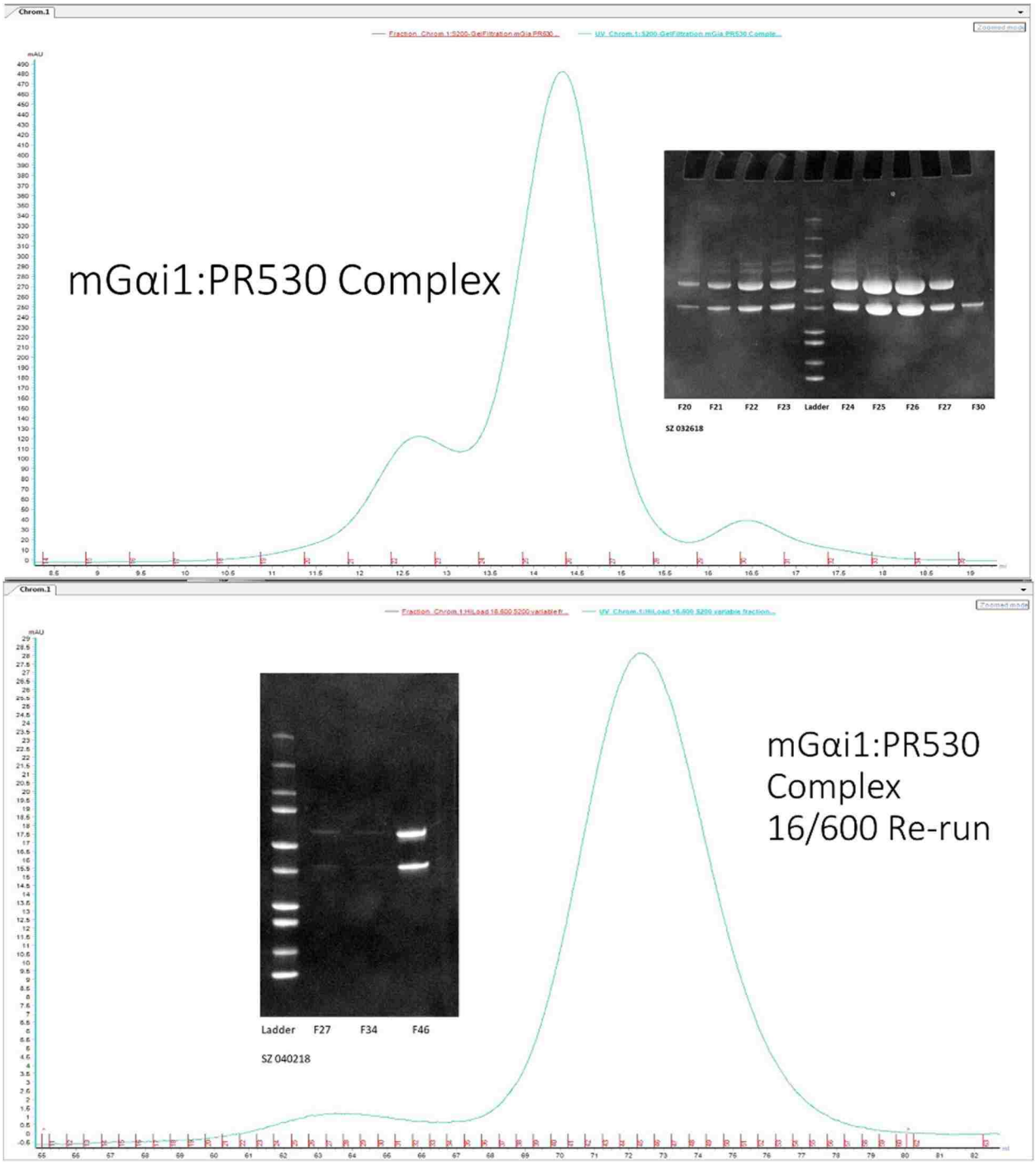

Figure 5-4 Size-exclusion chromatography results of mGαi1:pR530 complex
(Top), mGαi1:pR530 complex resolved using a Superdex 200 SEC column showing higher order oligomeric species (1st peak near 12.7mL) and 1:1 complex (2nd peak near 14.5mL) with small amount of excess unbound mGαi1 (3rd peak near 16.5mL). **(Bottom)**, resolving the 1:1 complex fraction from "top" on a 16/600 SEC column (GE Healthcare) showing good separation of the large oligomer and 1:1 complex. SDS-PAGE analyses of fractions under the curves validated the 1:1 ratio of mGαi1:pR530 in the complex. **(Inlets)**, SDS-PAGE results showing fractions under the curves.

5.2.2.c GEF Activity Assay

The tryptophan fluorescence assays as well as steady-state GTPase assays described in Chapter II and Chapter III were used to test the viability of R530. Both R530 and pR530 were assayed for their GEF activities toward mGαi1. No obvious difference in the initial rate of nucleotide exchange was observed between the two using the tryptophan fluorescence GTPγS-binding assay; however, drastic difference was seen between R530 and pR530 in the steady-state GTPase assay. (See Chapter III for results and discussion) The effect(s) of Ric-8A phosphorylation by CKII on its function towards Gαi1 need to be more characterized more carefully. A study with similar scope to the 2018 publication (29), which used Gαq as the main model instead of Gαi1, should be conducted.

5.2.2.d Protein Crystallization & Optimization

Initial condition screening for both the Apo-pR530 and complex with Gαi1 W258A were accomplished using commercial screening blocks from Hampton Research and Qiagen. Ten different screening suites were used (PEGI-II, JCSG I-IV, Morpheus, Shotgun, Crystal Screen-1, and Proplex) for the initial screen. For each screening condition, two protein-to-reservoir solution ratios (2:1 and 1:1) were setup (See Chapter III for screening plate setup methods) and incubated in a 20^{o}C incubator. Over 3-months, no crystal grew for Apo-pR530, either directly received from Gregory Tall or expressed and purified in Sprang lab; however, a few Gαi1:Ric-8A complex crystals grew at different conditions and/or different time points over the period of 90-days. **(Figure 5-5)** The complex crystals are UV sensitive; SDS-PAGE analysis confirmed the identity of protein samples in the crystals. Samples of the crystals from the initial screening plates were sent to SSRL and screened by Tzanko Doukov. The small crystals that were grew in

"PEG" conditions diffracted to as far as 7Å on BL12-2 using a 10µm X 10µm micro-focused beam; unfortunately, the largest crystals **(Figure 5-5)** did not diffract at all.

Figure 5-5 pR530:Gαi1 complex crystals in the initial screens
Crystallization condition and parameters are labelled above each photo. All photos of crystals were taken using a light microscope(Olympus) the same magnification.

The 2nd and 4th figures **(Figure 5-5)** show crystals grew in presumably identical conditions but differed drastically in sizes. The variation suggest that these crystallization conditions need to be more carefully reproduced and properly controlled in the future. For the complex crystals that diffracted to low resolutions, vigorous optimization trials need to be performed to improve the size and diffraction quality. For the larger crystals that did not diffract at all, seeding experiments, detergents/additives screens, and many other optimization techniques (57) could change the crystal packing. If all attempts fail, we can always try other combinations of Ric-8A:Gαi1 complex using different Ric-8A and Gαi1 constructs.

References

1. Yu W, Yu M, Papasergi-Scott MM, Tall GG. Production of Phosphorylated Ric-8A proteins using protein kinase CK2. Protein Expression and Purification. 2019 Feb;154:98-103.

2. Hilger D, Masureel M, Kobilka BK. Structure and dynamics of GPCR signaling complexes. Nature structural & molecular biology. 2018 Jan;25(1):4-12.

3. Papasergi-Scott MM, Stoveken HM, MacConnachie L, Chan P, Gabay M, Wong D, et al. Dual phosphorylation of Ric-8A enhances its ability to mediate G protein α subunit folding and to stimulate guanine nucleotide exchange. Sci Signal. 2018 May 29,;11(532).

4. Franke D, Petoukhov MV, Konarev PV, Panjkovich A, Tuukkanen A, Mertens HDT, et al. ATSAS 2.8: a comprehensive data analysis suite for small-angle scattering from macromolecular solutions. Journal of Applied Crystallography. 2017 Aug;50(4):1212-25.

5. Liu Q, Hendrickson WA. Contemporary Use of Anomalous Diffraction in Biomolecular Structure Analysis. Methods Mol Biol. 2017;1607:377-99.

6. Weiss MS. Long-Wavelength X-Ray Diffraction and Its Applications in Macromolecular Crystallography. Methods Mol Biol. 2017;1607:401-20.

7. Akey DL, Terwilliger TC, Smith JL. Efficient merging of data from multiple samples for determination of anomalous substructure. Acta Crystallogr D Struct Biol. 2016 Mar;72(Pt 3):296-302.

8. Black LA, Thomas CJ, Nix GN, Terwilliger MC, Sprang SR, Ross JBA. Nanosecond Dynamics of Gαi1 Bound to Nucleotides or Ric-8A, a Gα Chaperone with GEF Activity. Biophysical journal. 2016 Aug 23,;111(4):722-31.

9. Carpenter B, Nehmé R, Warne T, Leslie AGW, Tate CG. Structure of the adenosine A2A receptor bound to an engineered G protein. Nature. 2016 Jul 27,;536(7614):104-7.

10. Kant R, Zeng B, Thomas CJ, Bothner B, Sprang SR. Ric-8A, a G protein chaperone with nucleotide exchange activity induces long-range secondary structure changes in Gα. eLife. 2016 Dec 23,;5.

11. Olieric V, Weinert T, Finke AD, Anders C, Li D, Olieric N, et al. Data-collection strategy for challenging native SAD phasing. Acta crystallographica. Section D, Structural biology. 2016 Mar;72(Pt 3):421-9.

12. Panjkovich A, Svergun DI. Deciphering conformational transitions of proteins by small angle X-ray scattering and normal mode analysis. Phys Chem Phys. 2016 /02/17;18(8):5707-19.

13. Pike ACW, Garman EF, Krojer T, von Delft F, Carpenter EP. An overview of heavy-atom derivatization of protein crystals. Acta Crystallographica Section D. 2016 Mar;72(3):303-18.

14. Syrovatkina V, Alegre KO, Dey R, Huang X. Regulation, Signaling, and Physiological Functions of G-Proteins. Journal of Molecular Biology. 2016 Sep 25,;428(19):3850-68.

15. Terwilliger TC, Bunkóczi G, Hung L-, Zwart PH, Smith JL, Akey DL, et al. Can I solve my structure by SAD phasing? Planning an experiment, scaling data and evaluating the useful anomalous correlation and anomalous signal. Acta Cryst D. 2016 -03-01;72(3):359-74.

16. Terwilliger TC, Bunkóczi G, Hung L, Zwart PH, Smith JL, Akey DL, et al. Can I solve my structure by SAD phasing? Planning an experiment, scaling data and evaluating the useful anomalous correlation and anomalous signal. Acta Crystallographica Section D. 2016 Mar;72(3):359-74.

17. Boldon L, Laliberte F, Liu L. Review of the fundamental theories behind small angle X-ray scattering, molecular dynamics simulations, and relevant integrated application. Nano Rev. 2015 -2-25;6.

18. Dror RO, Mildorf TJ, Hilger D, Manglik A, Borhani DW, Arlow DH, et al. SIGNAL TRANSDUCTION. Structural basis for nucleotide exchange in heterotrimeric G proteins. Science (New York, N.Y.). 2015 Jun 19,;348(6241):1361.

19. Flock T, Ravarani CNJ, Sun D, Venkatakrishnan AJ, Kayikci M, Tate CG, et al. Universal allosteric mechanism for Gα activation by GPCRs. Nature. 2015 Aug 13,;524(7564):173-9.

20. Gábor Bunkóczi, Airlie J Mccoy, Nathaniel Echols, Ralf W Grosse-kunstleve, Paul D Adams, James M Holton, et al. Macromolecular X-ray structure determination using weak, single-wavelength anomalous data. Nature Methods. 2015 Feb 1,;12(2):127-30.

21. Jones DT, Cozzetto D. DISOPRED3: precise disordered region predictions with annotated protein-binding activity. Bioinformatics (Oxford, England). 2015 Mar 15,;31(6):857-63.

22. Liu Q, Hendrickson WA. Crystallographic phasing from weak anomalous signals. Curr Opin Struct Biol. 2015 Oct;34:99-107.

23. Ned Van Eps, Celestine J. Thomas, Wayne L. Hubbell, Stephen R. Sprang. The guanine nucleotide exchange factor Ric-8A induces domain separation and Ras domain plasticity in Gαi1. Proceedings of the National Academy of Sciences. 2015 Feb 3,;112(5):1404.

24. Pflugrath JW. Practical macromolecular cryocrystallography. Acta Cryst F, Acta Cryst Sect F, Acta Crystallogr F, Acta Crystallogr Sect F, Acta Cryst F Struct Biol Cryst Commun, Acta Cryst Sect F Struct Biol Cryst Commun, Acta Crystallogr Sect F Struct Biol Cryst Commun. 2015 -06-01;71(6):622-42.

25. Rose JP, Wang B, Weiss MS. Native SAD is maturing. IUCrJ. 2015 Jul 1,;2(Pt 4):431-40.

26. Blumer JB, Lanier SM. Activators of G Protein Signaling Exhibit Broad Functionality and Define a Distinct Core Signaling Triad. Mol Pharmacol. 2014 -03-01 00:00:00;85(3):388-96.

27. Boularan C, Kamenyeva O, Cho H, Kehrl JH. Resistance to inhibitors of cholinesterase (Ric)-8A and Gαi contribute to cytokinesis abscission by controlling vacuolar protein-sorting (Vps)34 activity. PLoS ONE. 2014;9(1):e86680.

28. Hendrickson WA. Anomalous diffraction in crystallographic phase evaluation. Q Rev Biophys. 2014 Feb;47(1):49-93.

29. Papasergi MM, Patel BR, Tall GG. The G Protein Chaperone Ric-8 as a Potential Therapeutic Target. Molecular Pharmacology. 2014 Nov 19,;87(1):52-63.

30. Robert X, Gouet P. Deciphering key features in protein structures with the new ENDscript server. Nucleic Acids Res. 2014 Jul;42(Web Server issue):320.

31. Chan P, Thomas CJ, Sprang SR, Tall GG. Molecular chaperoning function of Ric-8 is to fold nascent heterotrimeric G protein subunits. Proceedings of the National Academy of Sciences. 2013 Mar 5,;110(10):3794-9.

32. Chishiki K, Kamakura S, Yuzawa S, Hayase J, Sumimoto H. Ubiquitination of the heterotrimeric G protein α subunits Gαi2 and Gαq is prevented by the guanine nucleotide exchange factor Ric-8A. Biochemical and biophysical research communications. 2013 Jun 7,;435(3):414-9.

33. Foadi J, Aller P, Alguel Y, Cameron A, Axford D, Owen RL, et al. Clustering procedures for the optimal selection of data sets from multiple crystals in macromolecular crystallography. Acta Cryst D. 2013 -08-01;69(8):1617-32.

34. Rochette CN. Structural analysis of nanoparticles by small angle x-ray scattering [dissertation]. ProQuest Dissertations Publishing; 2013.

35. Schnablegger H, Singh Y. The SAXS guide: getting acquainted with the principles. 3rd ed. Austria: Anton Paar GmbH; 2013.

36. Chan P, Gabay M, Wright FA, Tall GG. Ric-8B Is a GTP-dependent G Protein s Guanine Nucleotide Exchange Factor. Journal of Biological Chemistry. 2011 Jun 3,;286(22):19932-42.

37. Chan P, Gabay M, Wright FA, Kan W, Oner SS, Lanier SM, et al. Purification of heterotrimeric G protein alpha subunits by GST-Ric-8 association: primary characterization of purified G alpha(olf). The Journal of biological chemistry. 2011 Jan 28,;286(4):2625.

38. Chung KY, Rasmussen SGF, Liu T, Li S, Devree BT, Chae PS, et al. β2 adrenergic receptor-induced conformational changes in the heterotrimeric G protein Gs. 2011 Sep 28,.

39. Gabay M, Pinter ME, Wright FA, Chan P, Murphy AJ, Valenzuela DM, et al. Ric-8 proteins are molecular chaperones that direct nascent G protein α subunit membrane association. Science signaling. 2011 Nov 22,;4(200):ra79.

40. Gerwin H. Westfield, Søren G. F. Rasmussen, Min Su, Somnath Dutta, Brian T. DeVree, Ka Young Chung, et al. Structural flexibility of the Gαs α-helical domain in the β2-adrenoceptor Gs complex. Proceedings of the National Academy of Sciences. 2011 Sep 20,;108(38):16086.

41. Rasmussen SGF, DeVree BT, Zou Y, Kruse AC, Chung KY, Kobilka TS, et al. Crystal structure of the β2 adrenergic receptor-Gs protein complex. Nature. 2011 Jul 19,;477(7366):549-55.

42. Thomas C, Briknarová K, Hilmer J, Movahed N, Bothner B, Sumida J, et al. The Nucleotide Exchange Factor Ric-8A Is a Chaperone for the Conformationally Dynamic Nucleotide-Free State of G[alpha]i1. PLoS One. 2011 Aug 1,;6(8).

43. Chen VB, Arendall 3, W Bryan, Headd JJ, Keedy DA, Immormino RM, Kapral GJ, et al. MolProbity: all-atom structure validation for macromolecular crystallography. Acta crystallographica. Section D, Biological crystallography. 2010 Jan;66(Pt 1):12-21.

44. Kabsch W. XDS. Acta crystallographica. Section D, Biological crystallography. 2010 Feb;66(Pt 2):125-32.

45. Nagai Y, Nishimura A, Tago K, Mizuno N, Itoh H. Ric-8B Stabilizes the Subunit of Stimulatory G Protein by Inhibiting Its Ubiquitination. Journal of Biological Chemistry. 2010 Apr 9,;285(15):11114-20.

46. Rupp B. Biomolecular crystallography. New York, NY: Garland Science; 2010.

47. Daniel Franke, Dmitri I Svergun. DAMMIF, a program for rapid ab-initio shape determination in small-angle scattering. Journal of Applied Crystallography. 2009 Apr 1,;42(2):342-6.

48. Figueroa M, Hinrichs MV, Bunster M, Babbitt P, Martinez-Oyanedel J, Olate J. Biophysical studies support a predicted superhelical structure with armadillo repeats for Ric-8. Protein science : a publication of the Protein Society. 2009 Jun;18(6):1139-45.

49. Roessle M. Basics of X-ray scattering presentation. Luebeck University of Applied Science. 2009.

50. Beck T, Krasauskas A, Gruene T, Sheldrick GM. A magic triangle for experimental phasing of macromolecules. Acta Crystallographica Section D. 2008 Nov;64(11):1179-82.

51. Kinoshita E, Kinoshita-Kikuta E, Matsubara M, Yamada S, Nakamura H, Shiro Y, et al. Separation of phosphoprotein isotypes having the same number of phosphate groups using phosphate-affinity SDS-PAGE. Proteomics. 2008 Aug;8(15):2994-3003.

52. Thomas CJ, Tall GG, Adhikari A, Sprang SR. Ric-8A Catalyzes Guanine Nucleotide Exchange on G i1 Bound to the GPR/GoLoco Exchange Inhibitor AGS3. Journal of Biological Chemistry. 2008 Jun 12,;283(34):23150-60.

53. Putnam CD, Hammel M, Hura GL, Tainer JA. X-ray solution scattering (SAXS) combined with crystallography and computation: defining accurate macromolecular structures, conformations and assemblies in solution. Quarterly Reviews of Biophysics. 2007 /08;40(3):191-285.

54. Sprang SR, Chen Z, Du X. Structural Basis of Effector Regulation and Signal Termination in Heterotrimeric Gα Proteins. In: Advances in Protein Chemistry. Elsevier Science & Technology; 2007. p. 1-65.

55. Abdulaev NG, Ngo T, Ramon E, Brabazon DM, Marino JP, Ridge KD. The Receptor-Bound "Empty Pocket" State of the Heterotrimeric G-Protein α-Subunit Is Conformationally Dynamic. Biochemistry. 2006 October 1,;45(43):12986-97.

56. Greenfield NJ. Using circular dichroism collected as a function of temperature to determine the thermodynamics of protein unfolding and binding interactions. Nat Protoc. 2006;1(6):2527-35.

57. Newman J. A review of techniques for maximizing diffraction from a protein crystal in stilla. Acta crystallographica. Section D, Biological crystallography. 2006 Jan;62(Pt 1):27.

58. Adhikari A. Regulation of guanine nucelotide exchange in inhibitory G protein alpha subunit by activator of G protein signaling 3 and novel regulatory peptides [dissertation]. ; 2005.

59. Afshar K, Willard FS, Colombo K, Siderovski DP, Gönczy P. Cortical localization of the Galpha protein GPA-16 requires RIC-8 function during C. elegans asymmetric cell division. Development. 2005 Oct;132(20):4449-59.

60. David NB, Martin CA, Segalen M, Rosenfeld F, Schweisguth F, Bellaieche Y. Drosophila Ric-8 regulates Galphai cortical localization to promote Galphai-dependent planar orientation of the mitotic spindle during asymmetric cell division. Nature Cell Biology. 2005 Nov 1,;7(11):1083-90.

61. Meytal Landau, Itay Mayrose, Yossi Rosenberg, Fabian Glaser, Eric Martz, Tal Pupko, et al. ConSurf 2005: the projection of evolutionary conservation scores of residues on protein structures. Nucleic Acids Research. 2005 Jul 1,;33(Web Server issue):W302.

62. Siderovski DP, Willard FS. The GAPs, GEFs, and GDIs of heterotrimeric G-protein alpha subunits. International Journal of Biological Sciences. 2005;1(2):51-66.

63. Tall GG, Gilman AG. Resistance to inhibitors of cholinesterase 8A catalyzes release of G i-GTP and nuclear mitotic apparatus protein (NuMA) from NuMA/LGN/G i-GDP complexes. Proceedings of the National Academy of Sciences. 2005 Nov 15,;102(46):16584-9.

64. Afshar K, Willard FS, Colombo K, Johnston CA, McCudden CR, Siderovski DP, et al. RIC-8 Is Required for GPR-1/2-Dependent Gα Function during Asymmetric Division of C. elegans Embryos. Cell. 2004;119(2):219-30.

65. Couwenbergs C, Spilker AC, Gotta M. Control of Embryonic Spindle Positioning and Gα Activity by C. elegans RIC-8. Current Biology. 2004;14(20):1871-6.

66. Eric F Pettersen, Thomas D Goddard, Conrad C Huang, Gregory S Couch. UCSF Chimera--A visualization system for exploratory research and analysis. Journal of Computational Chemistry. 2004 Oct 1,;25(13):1605-12.

67. Grimsley GR, Pace CN. Spectrophotometric determination of protein concentration. Curr Protoc Protein Sci. 2004 Nov;Chapter 3:Unit 3.1.

68. Lanier SM. AGS proteins, GPR motifs and the signals processed by heterotrimeric G proteins. Biology of the cell. 2004 Jun;96(5):369.

69. Pape T, Schneider TR. HKL2MAP: a graphical user interface for macromolecular phasing with SHELX programs. Journal of Applied Crystallography. 2004;37(5):843-4.

70. Rolf Herrmann, Martin Heck, Petra Henklein, Peter Henklein, Christiane Kleuss, Klaus Peter Hofmann, et al. Sequence of Interactions in Receptor-G Protein Coupling. Journal of Biological Chemistry. 2004 Jun 4,;279(23):24283-90.

71. Anita M Preininger, Ned Van Eps, Nan-Jun Yu, Martina Medkova, Wayne L Hubbell, Heidi E Hamm. The myristoylated amino terminus of Galpha(i)(1) plays a critical role in the structure and function of Galpha(i)(1) subunits in solution. Biochemistry. 2003 Jul 8,;42(26):7931-41.

72. Gregory G. Tall, Andrejs M. Krumins, Alfred G. Gilman. Mammalian Ric-8A (Synembryn) Is a Heterotrimeric GÎ± Protein Guanine Nucleotide Exchange Factor. Journal of Biological Chemistry. 2003 Mar 7,;278(10):8356.

73. Established and Emerging Fluorescence-Based Assays for G-Protein Function: Heterotrimeric G-Protein Alpha Subunits and Regulator of G-Protein Signaling (RGS) Proteins [Internet].; 2003 [updated /05/31; cited Jan 2, 2019]. Available from: http://www.eurekaselect.com/63207/article.

74. Svergun DI, Koch MHJ. Small-angle scattering studies of biological macromolecules in solution. Reports on Progress in Physics. 2003 Oct 1,;66(10):1735-82.

75. Volkov VV, Svergun DI. Uniqueness of ab initio shape determination in small-angle scattering. Journal of Applied Crystallography. 2003 -06-01;36(3-1):860-4.

76. Andrade MA, Petosa C, O'Donoghue SI, Müller CW, Bork P. Comparison of ARM and HEAT protein repeats. Journal of Molecular Biology. 2001;309(1):1-18.

77. K G Miller, M D Emerson, J R McManus, J B Rand. RIC-8 (Synembryn): a novel conserved protein that is required for G(q)alpha signaling in the C. elegans nervous system. Neuron. 2000 Aug 1,;27(2):289-99.

78. Luc De Vries, Thierry Fischer, Hélène Tronchère, Greg M. Brothers, Bentley Strockbine, David P. Siderovski, et al. Activator of G protein signaling 3 is a guanine dissociation inhibitor for Gαi subunits. Proceedings of the National Academy of Sciences of the United States of America. 2000 Dec 19,;97(26):14364-9.

79. Miller KG, Rand JB. A role for RIC-8 (Synembryn) and GOA-1 (G(o)alpha) in regulating a subset of centrosome movements during early embryogenesis in Caenorhabditis elegans. Genetics. 2000 Dec;156(4):1649-60.

80. Ross EM, Wilkie TM. GTPASE-ACTIVATING PROTEINS FOR HETEROTRIMERIC G PROTEINS: Regulators of G Protein Signaling (RGS) and RGS-Like Proteins. Annual Review of Biochemistry. 2000 Jul;69(1):795-827.

81. Biacore AB BIACORE Technology Handbook. 1999.

82. Svergun DI. Restoring Low Resolution Structure of Biological Macromolecules from Solution Scattering Using Simulated Annealing. Biophysical Journal. 1999;76(6):2879-86.

83. Vetter IR, Arndt A, Kutay U, Görlich D, Wittinghofer A. Structural View of the Ran–Importin β Interaction at 2.3 Å Resolution. Cell. 1999;97(5):635-46.

84. Hamm HE. The many faces of G protein signaling. The Journal of biological chemistry. 1998 Jan 9,;273(2):669-72.

85. Björquist P, Boström S. Determination of the kinetic constants of tissue factor/factor VII/factor VIIA and antithrombin/heparin using surface plasmon resonance. Thromb Res. 1997 Feb 01,;85(3):225-36.

86. GE Healthcare. BIA Evaluation Software
Handbook
Version 3.0. 1997.

87. Otwinowski Z, Minor W. [20] Processing of X-ray diffraction data collected in oscillation mode. Meth Enzymol. 1997;276:307-26.

88. Sprang SR. G PROTEIN MECHANISMS:Insights from Structural Analysis. Annual Review of Biochemistry. 1997 Jul;66(1):639-78.

89. Tesmer JJ, Sunahara RK, Gilman AG, Sprang SR. Crystal structure of the catalytic domains of adenylyl cyclase in a complex with Gsalpha.GTPgammaS. Science. 1997 Dec 12,;278(5345):1907-16.

90. Tesmer JJG, Berman DM, Gilman AG, Sprang SR. Structure of RGS4 Bound to AlF 4−-Activated G iα1: Stabilization of the Transition State for GTP Hydrolysis. Cell. 1997;89(2):251-61.

91. Kenneth G. Miller, Aixa Alfonso, Minh Nguyen, John A. Crowell, Carl D. Johnson, James B. Rand. A Genetic Selection for Caenorhabditis elegans Synaptic Transmission Mutants. Proceedings of the National Academy of Sciences of the United States of America. 1996 Oct 29,;93(22):12593-8.

92. Sondek J, Bohm A, Lambright DG, Hamm HE, Sigler PB. Crystal structure of a G-protein beta gamma dimer at 2.1A resolution. Nature. 1996 Jan 25,;379(6563):369-74.

93. Mixon MB, Lee E, Coleman DE, Berghuis AM, Gilman AG, Sprang SR. Tertiary and Quaternary Structural Changes in Gialpha Induced by GTP Hydrolysis. Science. 1995 Nov 10,;270(5238):954-60.

94. Wall MA, Coleman DE, Lee E, Iñiguez-Lluhi JA, Posner BA, Gilman AG, et al. The structure of the G protein heterotrimer Gi alpha 1 beta 1 gamma 2. Cell. 1995 Dec 15,;83(6):1047-58.

95. DE Coleman, AM Berghuis, E Lee, ME Linder, AG Gilman, Sprang SR. Structures of active conformations of Gi alpha 1 and the mechanism of GTP hydrolysis. Science. 1994 Sep 2,;265(5177):1405-12.

96. Mumby SM, Linder ME. [20] Myristoylation of G-protein α subunits. In: Methods in Enzymology. United States: Elsevier Science & Technology; 1994. p. 254-68.

97. Remmers AE, Posner R, Neubig RR. Fluorescent guanine nucleotide analogs and G protein activation. J Biol Chem. 1994 May 13,;269(19):13771-8.

98. Sondek J, Hamm HE, Sigler PB, Lambright DG, Noel JP. GTPase mechanism of Gproteins from the 1.7-Å crystal structure of transducin α - GDP AIF − 4. Nature. 1994 Nov 17,;372(6503):276-9.

99. Hamm HE, Sigler PB, Noel JP. The 2.2 Å crystal structure of transducin-α complexed with GTP γ S. Nature. 1993 Dec 16,;366(6456):654-63.

100. O'Shannessy DJ, Brigham-Burke M, Soneson KK, Hensley P, Brooks I. Determination of rate and equilibrium binding constants for macromolecular interactions using surface plasmon resonance: use of nonlinear least squares analysis methods. Anal Biochem. 1993 Aug 01,;212(2):457-68.

101. Svergun DI. Determination of the regularization parameter in indirect-transform methods using perceptual criteria. J Appl Cryst, J Appl Crystallogr. 1992 -08-01;25(4):495-503.

102. Higashijima T, Ferguson KM. [28] Tryptophan fluorescence of G proteins: Analysis of guanine nucleotide binding and hydrolysis. In: Methods in Enzymology. United States: Elsevier Science & Technology; 1991. p. 321-8.

103. Gilman AG. G Proteins: Transducers of Receptor-Generated Signals. Annual Review of Biochemistry. 1987 Jul;56(1):615-49.

104. T Higashijima, K M Ferguson, P C Sternweis, E M Ross, M D Smigel, A G Gilman. The effect of activating ligands on the intrinsic fluorescence of guanine nucleotide-binding regulatory proteins. Journal of Biological Chemistry. 1987 Jan 15,;262(2):752.

105. Ferguson KM, Higashijima T, Smigel MD, Gilman AG. The influence of bound GDP on the kinetics of guanine nucleotide binding to G proteins. J Biol Chem. 1986 06/05/;261(16):7393-9.

106. P C Sternweis, J D Robishaw. Isolation of two proteins with high affinity for guanine nucleotides from membranes of bovine brain. Journal of Biological Chemistry. 1984 November 25,;259(22):13806.

107. Englander SW, Kallenbach NR. Hydrogen exchange and structural dynamics of proteins and nucleic acids. Quarterly Reviews of Biophysics. 1983 Nov 1,;16(4):521-655.

108. Cassel D, Selinger Z. Mechanism of adenylate cyclase activation by cholera toxin: Inhibition of GTP hydrolysis at the regulatory site. PNAS. 1977 -08-01 00:00:00;74(8):3307-11.

109. Earl W. Sutherland. Studies on the Mechanism of Hormone Action. Science. 1972 Aug 4,;177(4047):401-8.

110. Pohl SL, Birnbaumer L, Rodbell M. The glucagon-sensitive adenyl cyclase system in plasma membranes of rat liver. I. Properties. The Journal of biological chemistry. 1971 Mar 25,;246(6):1849.

111. Guinier A. La diffraction des rayons X aux très petits angles : application à l'étude de phénomènes ultramicroscopiques. Ann Phys. 1939;11(12):161-237.

112. Hampton Research. Seed Bead User Guide HR2-320.

113. Mark F.C. Ladd, Rex A. Palmer, Rex Alfred Palmer. Structure Determination by X-Ray Crystallography, Volume 1.

Vitae

Baisen Zeng was born in the city of Shanghai, People's Republic of China, on April 12, 1986, the son of Weiping Zeng and Jinfeng Lu. Baisen moved to California, United States of America in 2001 and graduated from Alameda High School in 2005. He received the degree of Bachelor of Science in Biochemistry and Molecular Biology from University of California, Davis in 2010. As an undergraduate, he worked for Dr. Robert H. Fairclough in the Department of Neurology, School of Medicine at U.C. Davis. Baisen was admitted to the Biochemistry and Biophysics Ph.D. program at the University of Montana in 2011. On February 5, 2015, he married Nan Li who was a graduate student in the Master of Accountancy program at University of Montana. His parents live in Oakland, California.